MOLECULAR SIMULATION OF IONIC LIQUIDS: EFFECTS OF SOLVATION, HUMIDIFICATION, AND CONFINEMENT

By

Matthew W. Thompson

Dissertation

Submitted to the Faculty of the

Graduate School of Vanderbilt University

in partial fulfillment of the requirements

for the degree of

DOCTOR OF PHILOSOPHY

in

Chemical and Biomolecular Engineering

Septamber 30, 2019

Nashville, Tennessee

Approved:

Peter T. Cummings, PhD

Paul E. Laibinis, PhD

Clare M^{c}Cabe, PhD

D. Greg Walker, PhD

DEDICATION

To my family, for their endless support.

ACKNOWLEDGMENTS

I am grateful to the support of many individuals and institutions that make this work possible. First, I would like to express my gratitude for the support of my advisor, Peter T. Cummings. I have never lacked for resources, funding, or advice for the scientific direction of my research. I have also been fortunate to be able to present my research via oral presentations and posters at several conferences across the country. I would also like to thank my committee members Paul Laibinis, Clare McCabe, D. Greg Walker, and Cary Pint for their for their constructive reviews of my research as it progressed.

I am thankful for to the mentorship and support afforded to me by members and alumni of the Cummings and McCabe research groups. I am especially grateful to Christoph Klein, whose expertise and guidance in software development practices has been invaluable to my research and continues to have a lasting impact as a begin my career. Thanks also to Tim Moore, Andrew Summers, Remco Hartkamp, Ray Matsumoto, Alex Yang, and Justin Gilmer for years of productive scientific discussions, collaborative software development, and camaraderie.

I have also been fortunate to work with many exceptional scientists over the course of my PhD, including both experimentalists and computational scientists. There are too many people to list but in particular I would like to thank Naresh Osti, Lukas Vlcek, C. Heath Turner, Katherine Van Aken, Boris Dyatkin, Hsiu-Wen Wang, Doug LeVan, Yury Gogotsi, Paul Kent, Takeshi Egami, Sheng Dai, and David Wesolowski. Each have pushed the limits of their techniques and it has been a pleasure to work with and be advised by them.

TABLE OF CONTENTS

Page

LIST OF TABLES

LIST OF FIGURES

LIST OF ABBREVIATIONS

ACN Acetonitrile

ADF Annular dark-field

AIMD *ab initio* molecular dynamics

APS Advanced Photon Source

AWH Accelerated weight histogram

AWH Accelerated weight histogram

BET Brunauer–Emmett–Teller

BMIM 1-Butyl-3-methylimidazolium

CDCs Carbide-derived carbons

DCM Dichloromethane

DFT Density functional theory

EDLCs Electrochemical double-layer capacitors

EELS Electron energy loss spectroscopy

GAFF General Amber force field

GCMC Grand canonical Monte Carlo

HRMC Hybrid reverse Monte Carlo

ILs Ionic liquids

MC Monte Carlo

MD Molecular dynamics

MeOH Methanol

MoSDeF Molecular Simulation and Design Framework

MSDs Mean squared displacements

NE Nernst-Einstein equation

OPLS-AA Optimized potential for liquid systems — all-atom

ORNL Oak Ridge National Laboratory

PMFs Potentials of mean force

PSDs Pore size distributions

QENS Quasi-elastic neutron scattering

QMD Quenched molecular dynamics

RDFs Radial distribution functions

RMC Reverse Monte Carlo

RTILs Room temperature ionic liquids

SANS Small-angle neutron scattering

SAXS Small-angle X-ray scattering

SMS Synthesis-mimetic simulation

SSA Specific surface area

STEM Scanning transmission electron microscopy

Tf2N bis(trifluoromethanesulfonyl)imide

THF Tetrahydrofuran

VMD Visual molecular dynamics

WHAM Weighted histogram analysis method

XRD X-Ray diffraction

Chapter 1

Introduction

Ionic liquids hold great potential for a number of applications across several industries and applications, from electrochemical energy storage and electrocatalysis to biofuel processing and CO_2 storage. Common to each of these and any future applicaitons is that a molecular-scale understanding of the behavior of ionic liquids is necessary to make intelligent design decisions at the application scale. This includes, but is not limited to, the structure, transport, and thermodynamics of ionic liquids in the bulk phase, at interfaces with solid materials, and in confinement.

The work comprising this thesis is based around using molecular simulations to understand the behavior of ionic liquids at the molecular scale. The primary computational tool is classical atomistic molecular dynamics simulation, although some other techniques are also used. Experimental results are integrated throughout; in some cases, simulations are used to understand experimental results, and in others, simulations predict trends that are later explored in experiment. In Chapter 2, energy storage devices and their components, including ionic liquids electrolytes and several electrode materials, are discussed for context. Chapter 3 reports the development of an atomistic model for porous carbon, including comparisons to several structural properties measured in experiment. The dissolution of ionic liquids in organic solvents is thoroughly examined in Chapter 4 via computational screening techniques supported by neutron scattering experiments. Chapter 5 presents to studies aimed at understanding the effects of added water content of ionic liquid-based supercapacitors. Next, Chapter 6 examines the accuracy of the molecular models commonly used in molecular simulation studies. Some early work on MXenes is described in Chapter 7. Finally, Chapter 8 summarizes the presented results and adds further suggestions for future studies.

Chapter 2

Background

2.1 Energy Storage Devices

Among the grandest challenges of the energy sector is how to efficiently and sustainably store harvested energy in a manner that it can be used later. Nature readily provides large amounts of energy — e.g. in the form of solar irradiation or the kinetic energy of wind — typically much more energy than society demands. A fundamental issue with these energy harvesting technologies, however, is the transience of their sources: the sun does not shine all day nor does the wind blow constantly. Municipal energy grids also have a long-standing interest in storing energy to balance energy demands over the course of a day. Demand is greater during the day than at night, but coal-fired power plants are unable to be turned on or off quickly enough. Global climate change induced by the burning of fossil fuels has pushed many applications, large and small, toward electrification. In comparison to fossil fuels, which can easily be stored in tanks of pressurized gasses or liquids, there is no simple manner in which to store electrical energy.

Many small devices (cell phones, wearable technology, IoT, drones,[1] cars, etc.) are also limited in overall utility by the performance of their energy storage components.[2] Batteries are the most-widely used energy storage devices, now almost ubiquitous in consumer electronics, but are not feasible for storing electrical energy at the grid scale.[3,4] There are also some fundamental aspects of battery technology that limit their use today and raise concerns[5] about their use in future decades as more powerful computing hardware is developed, decentralized technologies mature, and infrastructure in the developing world becomes more electrified.

By contrast, supercapacitors store energy in a fundamentally different manner.[6] They are sometimes referred to as electrochemical capacitors or electrochemical double layer capacitors. The primary charge storage mechanism is the physical adsorption of ions at electrically charged interfaces. There is conventionally no chemical reactions as a part of this process. While Faradaic

reactions are not necessarily slow processes, they establish a rate-limiting step in the charging and discharging of electrochemical devices. A lack of such reactions leaves only the kinetics of the adsorption process, which are much faster, as a limiting step in charge storage. However, the energetics of physical adsorption are much weaker than that of Faradaic reactions. These differences are manifested as the scale of device performance in drastically higher power density compared to batteries but similarly lower energy density. For example, an electric car fueled primarily by commercially available supercapacitors instead of batteries only could have a more powerful engine than what is on the market today, but it would have orders of magnitude less range. Such a car may be interesting to test or race but, like other potential applications of supercapacitors, it would not be functional in its main purpose (a safe and sustainable means of long-range transportation). Ragone plots, such as Fig. 2.1 are used to compare these and other devices.

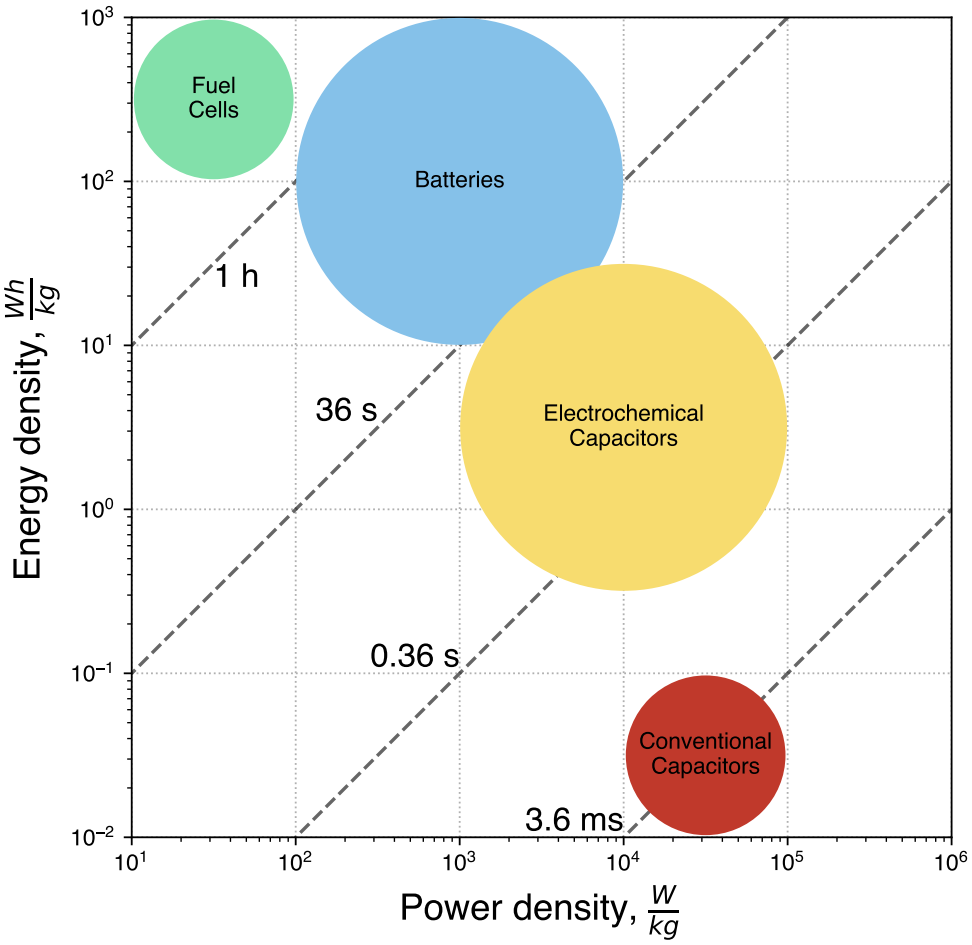

Figure 2.1: Ragone plot comparing the energy and power densities of classes of electrochemical energy storage devices. Diagonal lines approximate the time required to fully charge or discharge a device. For further details and some specific examples of such systems, see refs[2,7–13]

Another difference is their greater stability and lifetimes; batteries exhibit large drops in performance after a few hundred cycles and tend to become nearly unusable after a few thousand. Supercapacitors, however, through tests of millions of charge-discharge cycles, have been shown to retain nearly all of their energy storage capacity.[14–17] Their higher power densities — or, equivalently, shorter charge and discharge times — means they will likely go through more cycles than batteries, but should still be considered stable for longer device lifetimes.

While supercapacitors have found commercial use in some distinct applications[18,19] (regenerative braking, uninterruptible power supplies, and some small consumer electronics) their use is vastly dwarfed by batteries. If supercapacitors are to meet the energy storage challenges of today

and the future, they need to be designed with greatly increased energy density (although further increases in power density could be useful as well). The energy and power density of supercapacitors are characterized as follows:[7]

$$E = \frac{1}{2}CV^2 \tag{2.1}$$

$$P = \frac{V^2}{4R} \tag{2.2}$$

where E and P are energy and power density, respectively, C is the specific capacitance, V is the operating potential window, and R is the resistance of the device. These relationships provide clues to how devices can be designed with greater performance: increases in the potential window increase energy density, decreases in resistance increase power density, and increases in specific capacitance simultaneously increase both.

2.2 Ionic Liquids

Ionic liquids (ILs) are organic salts that exist in the liquid state near ambient conditions.[20–22] They are sometimes referred to as room temperature ionic liquids (RTILs) if their melting point is near or below room temperature. Following this convention, an IL is a salt with a melting point below 100 °C and an RTIL is one with a melting point below room temperature. Their discovery is cited as taking place more than a century ago[23] although they were virtually ignored until the turn of the millennium. Interest from academia and industry has rapidly grown in the past two decades for three primary reasons.

First, the physiochemical properties of ionic liquids are both unique and remarkable. Their strong intermolecular interactions, primarily electrostatic in nature, are a robust driving force that mostly prevents them from escaping liquid state. Ionic liquids are sometimes stated to have no vapor pressure; while this is not strictly true, it is a reasonable approximation.[24] Some works involving rigorous Monte Carlo simulations[25] and careful experiments[26–29] has been done to characterize their vapor pressure, broadly finding negligible vapor near ambient conditions but vapor-

ization without needing to access extreme conditions. This is a notable contrast to conventional electrolytes with low boiling points (water: 100 °C, acetonitrile 82 °C) that can partially vaporize during typical operation if exposed to the atmosphere. This low volatility is an appealing property for relatively safe and environmentally friendly operation.

Ionic liquids are often claimed to be thermally stable to high temperatures (i.e. 400 °C or higher) whereas, in reality, many decompose closer to 200 °C.[30] Much like their volatility, their chemical stability in most operating conditions is both a valid selling point and commonly oversold,[31,32] as operating electrochemical devices at such high temperatures is not typical. For some narrower applications, ionic liquids with legitimately high melting points have been developed.[33]

Second, these properties have manifested themselves in an extensive and growing list of applications at various stages along the technological pipeline.[21,34,35] This includes, but is far from limited to, cellulose dissolution,[36] liquid and gas separation,[27,37–40] chemical[41] and biological sensors, and energy storage.[2,18,42] A popular application in the past few years has been their use as electrolytes in supercapacitors.[2,43–47] Putting aside for a moment the crucial selection of electrode material, these are appealing electrolytes because of a scaling law characteristic of supercapacitors. The energy density of a device is proportional to the capacitance of the system times the square of its operating voltage window. The relationship between energy density (E), the capacitance C, and the operating potential window (V) was described above:

$$E = \frac{1}{2} C V^2. \tag{2.3}$$

This provides an opportunity to exploit the remarkably wide voltage windows of ionic liquids which sometime exceed 4 V in operating conditions or even 6 V in the lab. This is a notable increase over aqueous electrolytes (approximately 1.2 V); despite generally exhibiting a smaller specific capacitance, the overall energy density can be improved.

Third, their chemical structure is amenable to an extremely vast number of potential species. In order to have low melting points and prevent crystallization, ionic liquids are composed of intricate

structures, typically including asymmetric functional groups built off a core structure. A common such structure is the imidazolium cation functionalized with alkyl groups at its two nitrogen atoms. One chain is typically a methyl group and the other is typically longer, sometimes much longer, to inhibit crystallization. The number of neat ionic liquids — those with one cation, one anion, and no other components — was estimated on the order of billions almost two decades ago and estimates of as high as 10^{18} have been suggested since then. Consideration of mixtures of ionic liquids with other ionic liquids or solvents grows this figure by many orders of magnitude. This chemical space is vastly unexplored; even the set of commonly studied species is limited to a select few (on the order of 10 to 1000).

A key feature of ionic liquids is their strong ion pairing.[48,49] In water, conventional electrolytes are solvated by several water molecules and, at molecular length scales, tend not to come in direct contact with other ions, although this is mostly a consequence of water's strong screening overcoming the coulombic interactions of the ions. In ionic liquids, however, whether or not there is a solvent, the molecular structure includes strong ion pairing. This behavior persists even when ionic liquids are dissolved in polar solvents.[50] This inherently limits ionic conductivity as bound ions are poor charge carriers compared to free ions. Watanbe *et al.*[51] pioneered a quantification of this effect in experiment by introducing the concept of ionicity, which compares Λ_{imp}, the conductivity measured by electrochemical impedance, to Λ_{NMR}, a value predicted by molecular diffusivities and assuming no ion pairing. The ratio of these conductivities $\frac{\Lambda_{imp}}{\Lambda_{NMR}}$ defines ionicity and characterizes the extent of ion pairing. In an ideal system this ratio would be unity and smaller values indicate stronger ion pairing effects. In many neat ionic liquids, this pairing manifests itself as nanometer-scale ordering,[52–57] often interpreted as molecular-scale polar and non-polar domains.

However, ionic liquids have some concerning limitations that need to be discussed. The most relevant issue in most applications is their generally slow transport properties in comparison to conventional electrolytes: high viscosity, low molecular diffusivity, and low ionic conductivity. This is largely a consequence of their strong intermolecular attractions but large molecular weights are also a factor. As a result, engineering ionic liquids to exhibit faster transport coefficients is

difficult; while many other properties can be engineered with intelligent organic chemistry, we may already be at the upper limit of transport properties of neat ionic liquids. However, mixing ionic liquids in organic solvents can produce electrolytes with greater transport properties while maintaining many of the appealing physical properties of neat ionic liquids. This parameter space had not been explored much in the literature until a few years ago, but Chapter 4 includes several such contributions.

2.3 Electrode Materials for Supercapacitors

2.3.1 Porous Carbons

At the molecular scale, the charge storage mechanism of supercapacitors is the physical adsorption of ions at the surface of a charged electrode. As with other surface phenomena, the resulting macroscopic properties are believed to scale as the surface area available to partake in such phenomena. Therefore, a common approach toward designing supercapacitors with high energy storage is the use of porous carbons with high specific surface areas. Conveniently, there already exists a rich history, including a century of scientific papers and major components of chemical industries, dedicated to using such materials to promote surface phenomenon for other applications. Many porous materials are well-studied for their ability to adsorb and/or separate gas molecules at high capacity or catalyze industrially relevant chemical reactions, but electrode materials for energy storage must also be electrochemically stable and conducting. Porous carbons fit these requirements and more; certain classes of porous carbons have specific surface areas on the order of hundreds or thousands of square meters per gram of material and, under proper synthesis specifications, they are electrochemically stable to large amounts of cycling. Porous carbons also tend to be less expensive to manufacture than other novel nanostructured materials, and it has been demonstrated in many cases that food or other plant-based biomass otherwise considered waste can viably be used as precursors.

Further, some porous carbons can be engineered toward particular porosities, even some toward

particular pore size distributions. This is particularly relevant in the case of designing supercapacitors in which control over pore sizes and their dispersity is crucial to device design.

2.3.2 Exohedral Electrodes

Non-porous carbon materials are also appealing electrodes for supercapacitor applications. Included are some other carbon allotropes, such as carbon aerogels, fullerene-like carbon onions, and carbon nanotubes (in which ion adsorption is typically exohedral). While the specific surface area of these materials is much lower than that of porous carbons, it is still high, on the order of a few hundred m^2/g. However, nearly the entirety of the exohedral surface is accessible to electrolytes, in contrast to porous carbons which often include inaccessible porous domains. As a result, these materials generally exhibit more electrical conductivity than porous carbons and have been shown to increase the conductivity of electrodes even as an additive to a porous material. Because of these differences, these electrodes are preferred for applications in which power density and fast cycling is desirable.

2.3.3 2–D Materials

The past decade or so of materials research has seen rapid growth in the interest of 2-D materials. These materials are typically one or a few atoms thick in one dimension and several orders of magnitude longer in the other two dimensions. Aspect ratios on the order of 10^3-10^9 are not uncommon. Because of their unique structure, their properties can differ greatly from comparable bulk materials. The seminal 2D material is graphene, defined in a strict sense as single atom-thick layers of sp^2-hybridized carbon, which has seen use or interest in innumerable applications. Other materials, such as hBN, phosphorous black, and metal dichalcogenides like MoS_2, have also seen similar interest. Perhaps the most popular of a second wave of 2-D materials are MXenes. MXenes are a class of 2-D metal carbides with high conductivity and large planar surfaces terminated by redox-active functional groups. They have demonstrated potential as electrodes in Faradaic (batteries), non-Faradaic (supercapacitors) and semi-Faradaic (psuedocapacitors) energy storage devices

in addition to a variety of other applications.

2.4 Confinement Effects

The use of porous carbons in combination with ionic liquids has defined a generation of research into capacitive energy storage. Much of this recent interest in supercapacitors can be traced back to a groundbreaking study from Chmiola *et al.*.[58] They reported a dramatic increase in capacitance as the characteristic pore size of an electrode dropped from a few nanometers (the order of a few ion sizes) to less than a nanometer, or approximately the size of a single ion. Follow-up studies, both experimental[47,59,60] and computational[61–67] in nature, have corroborated this specific finding of high capacitance when ion and pore sizes are comparable, and, more generally, elucidated the effects of ion and pore size on capacitive performance. One important difference is that these computational studies predict oscillations of capacitance with pore size, i.e. multiple decaying peaks at different pore widths, whereas only the first peak has been observed in experiments. This has mostly been attributed to the difficulty of synthesizing porous materials with narrow pore size distributions at arbitrary targets. However, some studies have raised questions about these relationships due to limits in the confidence of porosimetry measurements from adsorption experiments and the Brunauer–Emmett–Teller (BET) equation and density functional theory (DFT) methods used to estimate surface area.[68,69]

A valid criticism of this thrust of research is that, while clear performance increases have been demonstrated, they are insufficient to close the energy density gap with batteries. The greatest increases in capacitance suggested by simulations reflect roughly a doubling of performance. Considering again Fig. 2.1, performance increases of multiple orders of magnitude are needed for supercapacitors to compete with batteries in practical applications. Further, given that there is more academic and industrial backing of battery research, batteries will plausibly continue to grow in their energy (and power) density as well.

Nonetheless, this has opened a growing field of research focused on understanding the structure and dynamics of highly confined (i.e. nanoconfined) electrolytes. Because ionic liquids lack

a solvation shell — or, more strictly speaking, can exist both in solvated and de-solvated states - existing theories (and our intuition) needed to be revised. For example, there was a minor controversy in the literature on the topic of whether ionic liquids behave as dilute electrolytes (i.e. most ions strongly and permanently pair to form neutral supramolecular-like species) or dissociated ions, floating around in solution and interacting with many neighbors but lacking any permanent associations. The overwhelming bulk of evidence from experiments and simulations is consistent with the latter. This topic has not been a primary focus of this thesis, however some work late in Chapter 4 builds on this view of ionic liquid structure.

As with other fluids, things become both more physically complex and practically useful when moving from bulk ionic liquids to those at interfaces and in confinement. Of particular interest to energy storage, as discussed above, is the confinement of ionic liquids in porous carbon consisting of nanometer-sized pores. While some ionic liquid molecules are large, the lack of a solvation shell works in their favor. First, while conventional alkali metal halide ions are small single atoms, their effective size when considering a solvation shell of water molecules is larger. Second, stripping this solvation shell away from an ion is thermodynamically disfavorable process. In neat ionic liquids, there is no large energetic barrier[70] and ionic liquids readily fill pores not much larger than their own molecular sizes. The structure and dynamics of confined ionic liquids have been thoroughly studied with many experimental probes and computational techniques since the landmark study of Chmiola *et al.*[58] While many groups have dedicated much effort and novel experimental[71–79] and computational[63,65,80–83] techniques to understanding the structure and dynamics of confined ionic liquids, many results contradict each other and a comprehensive view remains elusive.[84]

Molecular simulation in general and molecular dynamics (MD) simulation in particular is well-suited to studying ionic liquids in confinement. Any reasonable conception of the electric double layer concerns itself with the length scale of several Angstroms to a few nanometers. These push the boundaries of what first-principles electronic structure calculations can access, yet the molecular structure is too complex[43,85] to be captured by equilibrium models. Coarse-grained molecular models are useful in a limited sense, but the chemistry of ionic liquids is too diverse to feasi-

bly be captured by these simpler models. Instead, recent development[86] of polarizable models that attempt to bridge the gap of expensive *ab initio* molecular dynamics (AIMD) simulations and polarizable MD simulations may prove the most useful in the future, although these models are difficult to derive and the corresponding simulations are more expensive. Thus, most of the work included in this thesis uses molecular dynamics simulations to interrogate many fundamental scientific questions relevant to numerous applications but with a focus on energy storage.

2.5 Bibliography

[1] Dario Floreano and Robert J. Wood. "Science, technology and the future of small autonomous drones". In: *Nature* 521.7553 (2015), pp. 460–466.

[2] Patrice Simon and Yury Gogotsi. "Materials for electrochemical capacitors". In: *Nature Materials* 7.11 (2008), pp. 845–854.

[3] Fernando J. de Sisternes, Jesse D. Jenkins, and Audun Botterud. "The value of energy storage in decarbonizing the electricity sector". In: *Applied Energy* 175 (2016), pp. 368–379.

[4] Bruce Dunn, Haresh Kamath, and Jean-marie Tarascon. "for the Grid : A Battery of Choices". In: *Science* 334.6058 (2011), p. 928.

[5] M. C. McManus. "Environmental consequences of the use of batteries in low carbon systems: The impact of battery production". In: *Applied Energy* 93 (2012), pp. 288–295.

[6] Patrice Simon, Yury Gogotsi, and Bruce Dunn. "Where Do Batteries End and Supercapacitors Begin?" In: *Science* 343.6176 (2014), pp. 1210–1211.

[7] Brian E Conway. *Electrochemical supercapacitors: scientific fundamentals and technological applications*. Springer Science & Business Media, 2013.

[8] Bryan D. McCloskey. "Expanding the Ragone Plot: Pushing the Limits of Energy Storage". In: *Journal of Physical Chemistry Letters* 6.18 (2015), pp. 3592–3593.

[9] Xuehang Wang et al. “Selective Charging Behavior in an Ionic Mixture Electrolyte-Supercapacitor System for Higher Energy and Power”. In: *Journal of the American Chemical Society* 139.51 (2017), pp. 18681–18687.

[10] David Pech et al. “Ultrahigh-power micrometre-sized supercapacitors based on onion-like carbon.” In: *Nature nanotechnology* 5.9 (2010), pp. 651–4.

[11] S. Pohlmann and A. Balducci. “A new conducting salt for high voltage propylene carbonate-based electrochemical double layer capacitors”. In: *Electrochimica Acta* 110 (2013), pp. 221–227.

[12] C. K. Ranaweera et al. “Orange-Peel-Derived Carbon: Designing Sustainable and High-Performance Supercapacitor Electrodes”. In: *C* 3.3 (2017), p. 25.

[13] Vitor L. Martins et al. “Improved Performance of Ionic Liquid Supercapacitors by using Tetracyanoborate Anions”. In: *ChemElectroChem* 5.4 (2018), pp. 598–604.

[14] Andrew Burke. “R&D considerations for the performance and application of electrochemical capacitors”. In: *Electrochimica Acta* 53.3 SPEC. ISS. (2007), pp. 1083–1091.

[15] P. W. Ruch et al. “Aging of electrochemical double layer capacitors with acetonitrile-based electrolyte at elevated voltages”. In: *Electrochimica Acta* 55.15 (2010), pp. 4412–4420.

[16] D. Weingarth, A. Foelske-Schmitz, and R. Kötz. “Cycle versus voltage hold - Which is the better stability test for electrochemical double layer capacitors?” In: *Journal of Power Sources* 225 (2013), pp. 84–88.

[17] Donal B. Murray and John G. Hayes. “Cycle testing of supercapacitors for long-life robust applications”. In: *IEEE Transactions on Power Electronics* 30.5 (2015), pp. 2505–2516.

[18] Masayoshi Watanabe et al. “Application of Ionic Liquids to Energy Storage and Conversion Materials and Devices”. In: *Chemical Reviews* 117.10 (2017), pp. 7190–7239.

[19] R. Kötz and M Carlen. “Principles and applications of electrochemical capacitors”. In: *Electrochimica Acta* 45.15-16 (2000), pp. 2483–2498.

[20] K R Seddon. “Ionic liquids: designer solvents”. In: *The International George Papatheodorou Symposium: Proceedings, ed. S. Boghosian, V. Dracopoulos, CG Kontoyannis and GA Voyiatzis, Institute of Chemical Engineering and High Temperature Chemical Processes, Patras*. 1999, pp. 131–135.

[21] Robin D. Rogers and Kenneth R. Seddon. “Ionic Liquids - Solvents of the Future?” In: *Science* 302.5646 (2003), pp. 792–793.

[22] Robert Hayes, Gregory G. Warr, and Rob Atkin. “Structure and Nanostructure in Ionic Liquids”. In: *Chemical Reviews* 115.13 (2015), pp. 6357–6426.

[23] Paul Walden. “Molecular weights and electrical conductivity of several fused salts”. In: *Bull. Acad. Imper. Sci.(St. Petersburg)* 1800 (1914).

[24] Peter Wasserscheid. “Volatile times for ionic liquids”. In: *Nature* 439.7078 (2006), pp. 797–797.

[25] Neeraj Rai and Edward J. Maginn. “Vapor–Liquid Coexistence and Critical Behavior of Ionic Liquids via Molecular Simulations”. In: *The Journal of Physical Chemistry Letters* 2.12 (2011), pp. 1439–1443.

[26] Luis P.N. Rebelo et al. “On the critical temperature, normal boiling point, and vapor pressure of ionic liquids”. In: *Journal of Physical Chemistry B* 109.13 (2005), pp. 6040–6043.

[27] Martyn J. Earle et al. “The distillation and volatility of ionic liquids”. In: *Nature* 439.7078 (2006), pp. 831–834.

[28] Y. U. Paulechka et al. “Vapor pressure and thermal stability of ionic liquid 1-butyl-3-methylimidazolium Bis(trifluoromethylsulfonyl)amide”. In: *Thermochimica Acta* 439.1-2 (2005), pp. 158–160.

[29] Marisa A A Rocha et al. “High-accuracy vapor pressure data of the extended [CnC 1im][Ntf2] ionic liquid series: Trend changes and structural shifts”. In: *Journal of Physical Chemistry B* 115.37 (2011), pp. 10919–10926.

[30] Marek Kosmulski, Jan Gustafsson, and Jarl B. Rosenholm. “Thermal stability of low temperature ionic liquids revisited”. In: *Thermochimica Acta* 412.1-2 (2004), pp. 47–53.

[31] Cedric Maton, Nils De Vos, and Christian V. Stevens. “Ionic liquid thermal stabilities: Decomposition mechanisms and analysis tools”. In: *Chemical Society Reviews* 42.13 (2013), pp. 5963–5977.

[32] Zhimin Xue et al. “Thermal, electrochemical and radiolytic stabilities of ionic liquids”. In: *Physical Chemistry Chemical Physics* 20.13 (2018), pp. 8382–8402.

[33] Brooks D. Rabideau, Kevin N. West, and James H. Davis. “Making good on a promise: Ionic liquids with genuinely high degrees of thermal stability”. In: *Chemical Communications* 54.40 (2018), pp. 5019–5031.

[34] Natalia V Plechkova and Kenneth R. Seddon. “Applications of ionic liquids in the chemical industry.” In: *Chemical Society reviews* 37.1 (2008), pp. 123–150.

[35] Joan F. Brennecke and Edward J. Maginn. “Ionic liquids: Innovative fluids for chemical processing”. In: *AIChE Journal* 47.11 (2001), pp. 2384–2389.

[36] Richard P. Swatloski et al. “Dissolution of cellose with ionic liquids”. In: *Journal of the American Chemical Society* 124.18 (2002), pp. 4974–4975.

[37] Ann E Visser et al. “Task-specific ionic liquids for the extraction of metal ions from aqueous solutions”. In: *Chemical Communications* 1 (2001), pp. 135–136.

[38] Congmin Wang et al. “Equimolar CO2 capture by imidazolium-based ionic liquids and superbase systems”. In: *Green Chemistry* 12.11 (2010), p. 2019.

[39] Cesar Cadena et al. “Why Is CO 2 So Soluble in Imidazolium-Based Ionic Liquids?” In: *Journal of the American Chemical Society* 126.16 (2004), pp. 5300–5308.

[40] Jessica L. Anderson et al. “Measurement of SO2 solubility in ionic liquids”. In: *Journal of Physical Chemistry B* 110.31 (2006), pp. 15059–15062.

[41] Chengdu Liang et al. “Ionic liquids: A new class of sensing materials for detection of organic vapors based on the use of a quartz crystal microbalance”. In: *Analytical Chemistry* 74.9 (2002), pp. 2172–2176.

[42] Bong Gill Choi et al. “Enhanced Pseudocapacitance of Ionic Liquid/Cobalt Hydroxide Nanohybrids”. In: *ACS Nano* 7.3 (2013), pp. 2453–2460.

[43] Alexei A. Kornyshev and Rui Qiao. “Three-Dimensional Double Layers”. In: *The Journal of Physical Chemistry C* (2014), p. 140625063556000.

[44] François Béguin et al. “Carbons and Electrolytes for Advanced Supercapacitors”. In: *Advanced Materials* 26.14 (2014), pp. 2219–2251.

[45] Cheng Zhan et al. “Computational Insights into Materials and Interfaces for Capacitive Energy Storage”. In: *Advanced Science* 4.7 (2017), p. 1700059.

[46] Wan Yu Tsai et al. “Ordered mesoporous silicon carbide-derived carbon for high-power supercapacitors”. In: *Electrochemistry Communications* 34 (2013), pp. 109–112.

[47] R. Lin et al. “Solvent effect on the ion adsorption from ionic liquid electrolyte into sub-nanometer carbon pores”. In: *Electrochimica Acta* 54.27 (2009), pp. 7025–7032.

[48] Barbara Kirchner et al. *Ion pairing in ionic liquids*. 2015.

[49] Oldamur Hollóczki et al. “On the origin of ionicity in ionic liquids. Ion pairing versus charge transfer”. In: *Phys. Chem. Chem. Phys.* 16.32 (2014), pp. 16880–16890.

[50] Jesse Gatten McDaniel and Chang Yun Son. “Ion Correlation and Collective Dynamics in BMIM/BF 4 Based Organic Electrolytes: From Dilute Solutions to the Ionic Liquid Limit”. In: *The Journal of Physical Chemistry B* 122 (2018), acs.jpcb.8b04886.

[51] Kazuhide Ueno, Hiroyuki Tokuda, and Masayoshi Watanabe. “Ionicity in ionic liquids: correlation with ionic structure and physicochemical properties”. In: *Physical Chemistry Chemical Physics* 12.8 (2010), p. 1649.

[52] José N a Canongia Lopes and Agílio A. H. Pádua. “Nanostructural organization in ionic liquids”. In: *Journal of Physical Chemistry B* 110.7 (2006), pp. 3330–3335.

[53] Olga Russina et al. “Morphology and intermolecular dynamics of 1-alkyl-3-methylimidazolium bis{(trifluoromethane)sulfonyl}amide ionic liquids: structural and dynamic evidence of nanoscale segregation”. In: *Journal of Physics: Condensed Matter* 21.42 (2009), p. 424121.

[54] Olga Russina et al. “Mesoscopic structural heterogeneities in room-temperature ionic liquids”. In: *Journal of Physical Chemistry Letters* 3.1 (2012), pp. 27–33.

[55] Alessandro Triolo et al. “Nanoscale segregation in room temperature ionic liquids”. In: *Journal Of Physical Chemistry B* 111.18 (2007), pp. 4641–4644.

[56] Song Li et al. “Alkyl Chain Length and Temperature Effects on Structural Properties of Pyrrolidinium-Based Ionic Liquids: A Combined Atomistic Simulation and Small-Angle X-ray Scattering Study”. In: *The Journal of Physical Chemistry Letters* 3.1 (2012), pp. 125–130.

[57] Song Li et al. “Distinctive Nanoscale Organization of Dicationic versus Monocationic Ionic Liquids”. In: *The Journal of Physical Chemistry C* 117.35 (2013), pp. 18251–18257.

[58] J. Chmiola et al. “Effect of pore size and surface area of carbide derived carbons on specific capacitance”. In: *Journal of Power Sources* 158.1 (2006), pp. 765–772.

[59] Celine Largeot et al. “Relation between the ion size and pore size for an electric double-layer capacitor”. In: *Journal of the American Chemical Society* 130.9 (2008), pp. 2730–2731.

[60] Nicolas Jäckel et al. “Increase in Capacitance by Subnanometer Pores in Carbon”. In: *ACS Energy Letters* (2016), pp. 1262–1265.

[61] Guang Feng and Peter T. Cummings. “Supercapacitor capacitance exhibits oscillatory behavior as a function of nanopore size”. In: *Journal of Physical Chemistry Letters* 2.22 (2011), pp. 2859–2864.

[62] De-en Jiang, Zhehui Jin, and Jianzhong Wu. “Oscillation of capacitance inside nanopores”. In: *Nano Letters* 11.12 (2011), pp. 5373–5377.

[63] Céline Merlet et al. “On the molecular origin of supercapacitance in nanoporous carbon electrodes”. In: *Nature Materials* 11.4 (2012), pp. 306–310.

[64] S. Kondrat et al. “Effect of pore size and its dispersity on the energy storage in nanoporous supercapacitors”. In: *Energy & Environmental Science* 5.4 (2012), p. 6474.

[65] Svyatoslav Kondrat and Alexei A. Kornyshev. “Pressing a spring: what does it take to maximize the energy storage in nanoporous supercapacitors?” In: *Nanoscale Horizons* 1.1 (2016), pp. 45–52.

[66] Justin N. Neal et al. “Ion distribution and selectivity of ionic liquids in microporous electrodes”. In: *The Journal of Chemical Physics* 146.17 (2017), p. 174701.

[67] Alpha A. Lee et al. “Capacitance-power-hysteresis trilemma in nanoporous supercapacitors”. In: *Physical Review X* 6.2 (2016), pp. 1–11. arXiv: 1510.05595.

[68] N. Jäckel et al. “Anomalous or regular capacitance? The influence of pore size dispersity on double-layer formation”. In: *Journal of Power Sources* (2016), pp. 1–12.

[69] Belén Lobato et al. “Capacitance and surface of carbons in supercapacitors”. In: *Carbon* 122 (2017), pp. 434–445.

[70] Clarisse Pean et al. “Understanding the different (dis)charging steps of supercapacitors: influence of potential and solvation”. In: *Electrochimica Acta* 206 (2016), pp. 504–512.

[71] Ahmet Uysal et al. “Structural Origins of Potential Dependent Hysteresis at the Electrified Graphene/Ionic Liquid Interface”. In: *The Journal of Physical Chemistry C* 118.1 (2014), pp. 569–574.

[72] Ryusuke Futamura et al. “Partial breaking of the Coulombic ordering of ionic liquids confined in carbon nanopores”. In: *Nature Materials* September (2017), pp. 1–20.

[73] John M. Griffin et al. “In situ NMR and electrochemical quartz crystal microbalance techniques reveal the structure of the electrical double layer in supercapacitors”. In: *Nature Materials* June (2015).

[74] Alexander C Forse et al. “NMR Study of Ion Dynamics and Charge Storage in Ionic Liquid Supercapacitors”. In: *Journal of the American Chemical Society* 137.22 (2015), pp. 7231–7242.

[75] Alexander C. Forse et al. “Direct observation of ion dynamics in supercapacitor electrodes using in situ diffusion NMR spectroscopy”. In: *Nature Energy* 2.3 (2017), p. 16216.

[76] Boris Dyatkin and Yury Gogotsi. “Effects of structural disorder and surface chemistry on electric conductivity and capacitance of porous carbon electrodes”. In: *Faraday Discuss.* 172 (2014), pp. 139–162.

[77] Boris Dyatkin et al. “Influence of Surface Oxidation on Ion Dynamics and Capacitance in Porous and Nonporous Carbon Electrodes”. In: *The Journal of Physical Chemistry C* (2016), acs.jpcc.6b01204.

[78] Boris Dyatkin et al. “Ionic liquid structure, dynamics, and electrosorption in carbon electrodes with bimodal pores and heterogeneous surfaces”. In: *Carbon* 129 (2018), pp. 104–118.

[79] Jean Comtet et al. “Nanoscale capillary freezing of ionic liquids confined between metallic interfaces and the role of electronic screening”. In: *Nature Materials* 16.6 (2017), pp. 634–639. arXiv: 1611.08448.

[80] Alexander J. Pak and Gyeong S. Hwang. “Charging Rate Dependence of Ion Migration and Stagnation in Ionic-Liquid-Filled Carbon Nanopores”. In: *The Journal of Physical Chemistry C* (2016), acs.jpcc.6b06637.

[81] Alexander J. Pak and Gyeong S Hwang. “Molecular Insights into the Complex Relationship between Capacitance and Pore Morphology in Nanoporous Carbon-based Supercapacitors”. In: *ACS Applied Materials & Interfaces* 8.50 (2016), pp. 34659–34667.

[82] Alpha A. Lee, Svyatoslav Kondrat, and Alexei A. Kornyshev. “Single-file charge storage in conducting nanopores”. In: *Physical Review Letters* 113.4 (2014), pp. 1–5.

[83] Svyatoslav Kondrat et al. “Accelerating charging dynamics in subnanometre pores”. In: *Nature Materials* 13.4 (2014), pp. 387–393. arXiv: 1311.7529.

[84] Alexander C. Forse et al. “New Perspectives on the Charging Mechanisms of Supercapacitors”. In: *Journal of the American Chemical Society* (2016), jacs.6b02115.

[85] Céline Merlet et al. “The Electric Double Layer has a Life of Its Own”. In: *The Journal of Physical Chemistry C* (2014), p. 140527145351001. arXiv: 1404.0343.

[86] Agílio A. H. Pádua. “Resolving dispersion and induction components for polarisable molecular simulations of ionic liquids”. In: *The Journal of Chemical Physics* 146.20 (2017), p. 204501. arXiv: 1703.01540.

Chapter 3

An Atomistic Carbide-Derived Carbon Model Generated Using ReaxFF-Based Quenched Molecular Dynamics

3.1 Introduction

Porous carbons have been ubiquitous materials for energy applications since the Iron Age (burning charcoal for energy), through the 20th century (separation processes in chemical plants), and may be into the future (energy storage). They have high surface areas (typically hundreds to thousands of square meters of active surface area per gram of material), can be derived from sustainable precursors such as biomass, and, in comparison to other nanomaterials, are inexpensive to produce at scale. In terms of energy storage, carbide-derived carbons have been an exciting substrate with which to probe relationships between ion and pore size because they can be synthesized to specific, narrow porosities.

Molecular simulation is a valuable tool for understanding the molecular phenomena governing these and other energy-relevant systems. In particular, atomistic molecular dynamics (MD) simulations can describe the structure and dynamics of confined ions and how these properties give rise to their behavior in devices. However, these studies necessitate valid structural models of porous carbon. Many nanomaterials have well-defined crystal structures whereas porous carbons are amorphous and include a variety of structural motifs. Additionally, experimental probes tend to be limited to global-averaged properties and therefore have historically been less able to isolate local structure. In this chapter, we employ several experimental probes (X-ray scattering, electron microscopy, and adsorption experiments) to supplement the development of an atomistic model for the *in silico* generation of CDC structures. This work has been featured in an article in *C*[1] (a new MDPI journal) and is supplemented by a GitHub repository[2] that includes input files for implementing the model in LAMMPS. Experimental contributions to this chapter are from Hsiu-Wen Wang of Oak Ridge National Laboratory (ORNL) (*ex situ* X-ray total scattering), Boris Dyatkin

of Drexel University and ORNL (material synthesis, nitrogen adsorption experiments, and *ex situ* X-ray total scattering), and Xiahan Sang and Raymond R. Unocic of ORNL (electron microscopy and spectroscopy).

3.2 Background

Carbide-derived carbons (CDCs) are a class of porous carbons with well-ordered porosities and heterogeneous, short-range graphitic ordering.[3] The most common synthesis approach uses halogen gas (typically Cl_2) to selectively etch out the metal phase of a metal carbide (e.g., TiC,[4] Mo_2C,[5] or $TiAlC_2$[6]) at high temperatures (200 °C–1200 °C).[7] They have high surface areas (typically 1000 $m^2\,g^{-1}$–2000 $m^2\,g^{-1}$) and tunable pore size distributions in the microporous and mesoporous regimes.[4,8–10] These properties, in addition to the chemical, thermal, and electrical stability of carbon, make CDCs an appealing electrode material for electrochemical energy storage[4,11–14] and other applications such as a substrate for gas[4,15–17] and protein[18,19] separation and storage.

Carbide precursor, particle size,[20] and synthesis conditions influence the resulting porosities, carbon bonding and graphitic defects, and surface chemistries of CDCs.[21] Low-temperature synthesis typically yields micropores with narrow pore diameter distributions. In particular, 600 °C–800 °C Cl_2 etching of SiC and TiC yield predominantly sub-nanometer pores;[13] their dimensions match the sizes of electrosorbed ions and yield exceptionally high energy densities as electrochemical capacitors.[22] Different carbide precursors and pore diameters yield slit or cylindrical pore shapes with different curvatures.[8,23] While most carbon ordering in CDCs is a heterogeneous mixture of short-ranged sp^2 and sp^3 bonding, graphitization (and resulting electron transport properties) directly depends on synthesis temperature.[24] Thermal treatment above 1000 °C typically increases the prevalence of graphitic features, such as ribbons, barrels, and nanotubes.[9] These features define concentrations of structural defects (vacancies, Stone–Wales transformations, etc.[25]), pore topography and geometric roughness,[26] and degree of long-range ordering in the [100] and [002] (sheet stacking) directions.[27] In turn, these properties govern the contribution and relative influence of quantum capacitance on total charge storage densities of these materials as electrodes.[28]

Finally, post-Cl_2 treatment methods (H_2 or NH_3 600 °C annealing) and exposure to air introduces various functional groups on pore surfaces.[29] These moieties also influence electrosorption dynamics[30] and capacitance.[31,32] Many of these properties are convoluted and difficult to quantify in experimental systems. Therefore, subsequent optimization of these materials requires a detailed computational model.

Even though nanoporous carbons have non-uniform structure, they are often modeled as slit pores directly in contact with a bulk fluid or electrolyte. Additional models also consider cylindrical, spherical, and other morphologies.[23,33–35] Nonetheless, the slit pore model remains common for the study of porous systems, even for studying advanced properties such as gas adsorption[36,37] and separation,[38] capacitance,[26] and the structure and dynamics of confined ions[39,40] and molecules.[41] In such model systems, parallel sheets of graphene are separated by the characteristic widths of the nanopores found in experiment, typically defined as the peak in the pore size distribution. These models capture, to a first approximation, the effect of confinement on fluid behavior, but leave out many other effects. CDCs and other nanoporous materials have structural heterogeneities such as surface curvature and a distribution of pore widths, which have qualitative and quantitative effects on the performance of CDCs as electrodes in supercapacitors[42,43] or as adsorbents of gas molecules.[44] Furthermore, direct exposure of a nanopore to a bulk fluid ignores entrance effects and dynamics associated with transport through a complex pore architecture.[45] Therefore, to better understand the fundamentals of gas sorption, electric double layer structure, and electrolyte dynamics in CDCs, a structurally valid model for CDCs that captures these effects is needed.

Reverse Monte Carlo (RMC)[46,47] and Hybrid reverse Monte Carlo are approach that has been used to create structurally relevant nanoporous models.[48–51] These models are created in an iterative process of fitting simulated radial distribution functions (RDFs) to those obtained from scattering experiments. While CDC structures have been generated that reproduce experimental RDFs, fits of empirical information to an RDF with an RMC routine have inherent limitations. Some studies added other physical constraints, such as prohibiting the formation of three-membered

rings[51] or moves that would generate non-physical interatomic distances..[49] Structural features on the order of a few nanometers, particularly porosity and surface curvature, are not typically well-captured with RDFs, which usually decay to unity in a few angstroms. Additionally, while RMC is capable of producing robust fits to experimental data, many unique three-dimensional models may be generated from a single, one-dimensional RDF. Subsequently, results derived using RMC cannot formally be considered unique.[52–54] Furthermore, as with many Monte Carlo-based methods, accessible system size may be limited due to the challenges of deploying algorithms to parallel computing architectures. Small systems on the order of a few hundred or thousand atoms are sufficient for capturing short-range features such as bonding, ring formations, and a small number of structural features and pores. Larger system sizes on the order of tens or hundreds of thousands of atoms are needed to better sample a range of structural heterogeneities and pore size distributions.

As an alternative approach, quenched molecular dynamics (QMD) has viably reproduced atomistic models of amorphous and/or porous carbons,[55–57] silica,[58–60] and metals.[61,62] QMD generates metastable structures by lowering the temperature of a system over the course of a simulation. Although this process lacks a direct physical analog (i.e., in practice, CDCs are typically formed via chemical etching), QMD is, nonetheless, capable of generating realistic atomistic models of porous materials. This technique allows quench rate and initial and final temperatures to be modulated in order to control some of the structural properties of the CDC, such as porosities and RDFs. The inherent parallel nature of molecular dynamics simulations allows them to explore large system sizes. Previous QMD results have used force fields such as the Adaptive Intermolecular Reactive Empirical Bond Order (AIREBO),[63] the Environment-Dependent Interatomic Potential (EDIP),[64] the Reactive Summation State (RSS),[55] and the Tersoff potential[65] to generate nanoporous carbon structures for use in molecular simulation. While many impactful studies[51,54,56,57,66–68] have been done with these force fields, the generated structures have often failed to accurately reproduce experimental pore size distributions and always depend, at least in part, on the accuracy of the force field itself. Carbon-based materials, and CDCs in particular, present a unique challenge for these force fields because of their nanoscale heterogeneity. Individual force fields can sufficiently de-

scribe specific structural moeities, such as short-range graphitization at low density,[69] but are often not sufficient to capture the full range of non-ideal features observed in CDCs.[70]

One possible way to increase the accuracy of computationally derived CDC structures is to employ sophisticated reactive force fields, such as ReaxFF.[71,72] ReaxFF uniquely includes three- and four-body, non-bonded van der Waals, and electrostatic interactions in conjunction with a long-range bond order concept, where parameter sets are trained to reproduce a range of first-principles data describing reaction energies as well as reaction barriers. This allows ReaxFF to largely approach the accuracy of first-principles calculations, but at significantly (several orders of magnitude) reduced computational cost, although, we note more costly than other reactive and non-reactive force fields.[54] The use of ReaxFF for the formation of CDC structures is limited, with only a single recent study[73] examining the formation of amorphous carbon structures using QMD. This study examined the carbon hybridization, ring formation, and pore size distribution as a function of density and quench rate, and demonstrated the potential that ReaxFF could be effective in generating model CDCs; however, the study was not explicitly focused on the formation of experimentally relevant CDCs. EDIP, which has been shown to exhibit similar behavior to ReaxFF at low density,[69] has been used to generate CDCs via removal of metal atoms from a carbide lattice and subsequent annealing at the target density, showing close agreement with experimental pore size distributions.

In this chapter, we further explore the use of the ReaxFF force field to develop novel, structurally relevant atomistic models of CDCs. Our combined computational and experimental approach directly compares experimentally derived structural information to properties of models derived from simulation. Here, we examine the effects of quench rate on CDC structure, including a slower rate than was used in prior ReaxFF studies.[73] We also investigate the role of a novel post-quenching compression step as a means to adjust pore size distribution. CDC structure is examined, including pore size distributions, pair distribution functions, and ring sizes. These analyses make comparisons to X-ray scattering, nitrogen sorption, and electron microscopy results. We demonstrate close agreement between experiment and simulation, including pore size distribu-

tions, for our approach. This chapter includes major contributions from experimental collaborators at Oak Ridge National Laboratory and other institutions. This work was been published in the MDPI journal *C* in 2017.[74]

3.3 Computational Methods

3.3.1 Quenched Molecular Dynamics Simulations

Reactive molecular dynamics simulations were performed using the ReaxFF[71,75,76] force field implemented in the LAMMPS[77] simulation package (Version 27-Jul-2013, Sandia National Laboratory, Albuquerque, NM, USA). ReaxFF is a reactive potential that models the breaking and formation of chemical bonds through bond order, which is calculated from interatomic distances and used in calculating a bond energy. Three- and four-body, non-bonded van der Waals, and electrostatic interactions are also included. Parameter sets are developed by fitting to structural and thermodynamic properties to quantum density functional theory (DFT) data. The specific ReaxFF parameter set used in this study was optimized for modeling carbon materials.[72]

Initial configurations were generated by assigning 20,000 carbon atoms to random positions in a periodic simulation cell of length 7.488 nm. This corresponded to a bulk density near 0.95 $\frac{g}{cm^3}$, consistent with previous studies.[51,57] In an attempt to mitigate biases arising from an initial configuration, random positions give the system a fluid-like initial state. Quenched molecular dynamics simulations were performed from an initial temperature of 3500 K to a final temperature of 3000 K. The use of temperature ranges higher than used in experiment is a common approach in ReaxFF studies to bring reaction kinetics into a time scale accessible in molecular simulation.[72,78,79] This temperature range is near the phase transition from liquid carbon to graphite at low pressures reported by experiment.[80,81] While the melting point was not rigorously examined with this force field, the transition appears to occur within the range expected from experiment. In simulations of the lengths considered here, major structural changes do not occur after the system has condensed from a fluid to solid state, so additional quenching below 3000 K was not considered. In order to explore the effects of quench rate, simulations varied from 5 ps to 500 ps in length, giving quench

rates between 1 and 100 $\frac{K}{ps}$. These rates are studied for their effects on the structures and are not to be interpreted physically or compared directly to synthesis parameters. Temperature was controlled using a Nosé–Hoover thermostat with a damping constant of 10 fs. All quenching simulations were performed in the canonical (*NVT*) ensemble and a 0.5 fs time step was used throughout. This is a larger timestep than what is normally used in ReaxFF studies (0.25 fs); however, these systems include only carbon atoms and therefore lack any O-H or C-H vibrations, which are much faster than C-C vibrations and typically constrain the timestep to smaller values.

For select samples, an additional compression step was applied after the quenching step using the *NPT* ensemble. The *NPT* integrator follows the work of Shinoda et al.,[82] combining the work of Martyna et al.[83] and Parrinello and Rahman,[84] as implemented in LAMMPS. The ReaxFF force field was again applied with a time step of 0.5 fs. Isothermal temperature control and isobaric pressure control at 3000 K and 20 000 atm were used with damping constants of 10 fs and 100 fs, respectively. Selection of this pressure is discussed in the Appendix, including a relationship between system density and compression pressure. Like the quenching step, there is no direct physical analog to this step, but it was used to drive structural properties toward the experimental target. Effects of the post-quenching compression step are discussed in context below. For both compressed and non-compressed samples, no additional structural relaxation was performed.

3.3.2 Grand Canonical Monte Carlo Simulations

In order to study the properties of QMD-generated CDC models as adsorbent materials, grand canonical Monte Carlo (GCMC) simulations of nitrogen isotherms were performed with LAMMPS. A single-site nitrogen model was utilized as the fluid and both fluid–fluid and fluid–solid interactions were described with 12–6 Lennard–Jones potentials. A cut-off distance of 15 Å was used with no long-range corrections. Carbon and nitrogen atoms were described using $\varepsilon_C = 28.0\,\mathrm{K}$, $\varepsilon_N = 95.2\,\mathrm{K}$, $\sigma_C = 3.4\,\text{Å}$, and $\sigma_N = 3.75\,\text{Å}$. Lorentz–Berthelot mixing rules[85,86] were used, giving $\varepsilon_{C/N} = 51.6\,\mathrm{K}$ and $\sigma_{C/N} = 3.575\,\text{Å}$. The carbon substrate was fixed in position; only moves involving nitrogen sites were considered. Construction of simulated isotherms for each carbon structure

involved many short simulations of 2×10^6 translation attempts and 2×10^6 insertion/deletion attempts. At a fixed temperature of 77 K, a range of 40 pressures ranging from 1×10^{-6} atm to 1 atm for the bulk fluid were considered. Beginning with a bare carbon structure at the minimum pressure of 1×10^{-6} atm, the aforementioned short simulations were repeated at the same pressure until changes in the number of nitrogen atoms in the system were sufficiently close to zero to be considered at equilibrium. Subsequent pressure values incremented by a small amount and this process repeated until all pressures in the prescribed range were considered.

3.4 Experimental Methods

3.4.1 CDC Synthesis and Annealing

Porous CDC particles were synthesized using a previously described procedure.[7] Silicon carbide (SiC) particles (1.0 µm–5.0 µm diameter, 99.1+ % purity, Alfa Aesar, Haverhill, MA, USA) were placed into a quartz boat and loaded into a tube furnace. The furnace ramped up to 900 °C under flowing Ar gas. Once the system reached this temperature, pure Cl_2 gas flowed over the furnace at a rate of 0.5 L min^{-1} for 4 h and etched away the metal carbide using the following reaction:[87]

$$2\,Cl_2(g) + SiC(s) \longrightarrow SiCl_4(g) + C(s).$$

Subsequently, the system cooled down to 600 °C and H_2 gas annealed the leftover carbon particles for 2 h.[29] Finally, the material cooled down to room temperature under flowing Ar.

The material was placed into a graphite crucible and loaded into a vacuum furnace (Solar Atmospheres, Souderton, PA, USA). The furnace outgassed for 24 h until a high vacuum (1×10^{-6} torr) was reached.[9] Under continuously pulled vacuum, the furnace ramped up at a 10 °C min^{-1} rate up to 700 °C, held at that isothermal condition for 11 h, and, subsequently, cooled to room temperature.[88] This step removed all non-carbon functional groups, impurities, and moieties (adsorbed from air exposure or byproducts of CDC synthesis) from the CDC surface.

3.4.2 Gas Sorption and Porosimetry

Gas sorption measurements were carried out using Quadrasorb sorption analyzer (Quantachrome Instruments, Boynton Beach, FL, USA). Samples (0.050 g–0.075 g) were loaded into glass cells and outgassed at 120 °C for 24 h prior to analysis. The instrument collected gas adsorption and desorption isotherms (adsorbed volume vs. relative pressure) using N_2 adsorbate gas in the 0.000 75 $\frac{P}{P_0}$–0.9995 $\frac{P}{P_0}$ range (P_0 = 760 torr). Measurements were collected at a 77 K isothermal condition using a liquid N_2 coolant bath. The Brunauer–Emmett–Teller equation (BET) was used to calculate the BET specific surface area (SSA) of the CDCs.[89] The equation was calculated using a linear regression for 0.05–0.30 $\frac{P}{P_0}$ values and normalized by the sample mass to obtain $m^2\,g^{-1}$ values.

Quenched Solid Density Functional Theory (QSDFT) data reduction analysis provided information on a secondary (DFT-derived) SSA value, cumulative pore volume $cm^3\,g^{-1}$ values), and pore size distributions (PSDs, pore diameter vs. $\frac{dV}{dr}$ plots).[33] The data reduction used only the adsorption isotherms and assumed slit pore configurations.[90] Quantachrome's Quadrawin software (Version 5, Quantachrome Instruments, Boynton Beach, FL, USA) provided all BET calculations and DFT data modeling kernels and computational analysis.

3.4.3 Ex Situ X-Ray Total Scattering

Synchrotron X-ray total scattering data were collected at the 11-ID-B beamline at the Advanced Photon Source (APS) at Argonne National Laboratory (Lemont, IL, USA). Ground powder samples were loaded into polyimide capillaries (1 mm inner diameter) and measured in transmission mode at ambient conditions (photon energy 58.65 keV, 0.2114 Å) using an amorphous silicon image plate detector (Perkin Elmer, Fremont, CA, USA). Scattering data of a CDCs annealed at 700 °C were collected for a total of 15 min and parasitic scattering from an empty polyimide container (duplicating the assembly without a sample) and an Ni powder standard (99.99%, Sigma Aldrich, Saint Louis, MO, USA) were collected using the same setup. The program Fit2D[91] was used to calibrate the sample to detector distance and detector alignment with data from a CeO_2

powder standard. Raw scattering data was integrated into Q-space spectra, applying a mask and polarization correction during integration. The normalized total scattering patterns, $S(Q)$ were produced in PDFgetX2[92] (Version 1.0, Michigan State University, East Lansing, MI, USA) by subtracting polyimide container scattering, utilizing the appropriate sample composition, and applying standard corrections for the area detector setup.[93] Pair distribution function patterns, PDF G(r), were calculated via Fourier transformation of the total scattering data utilizing a Q range of 1.0 $Å^{-1}$ (Q_{min}) to 26.0 $Å^{-1}$ (Q_{max}) for the Ni dataset, and was fit in PDFgui[94] in the range 1 Å–50 Å to calibrate the instrument Q_{damp} = 0.038(1) and Q_{broad} = 0.021(1) effects on real-space data. The same Q range was used for sample data. Because the diffractometer is only capable of capturing a small portion of such pore signals with the limitation of Q_{min} near 0.5 $Å^{-1}$, a Fourier transform with Q_{min} of 0.5 $Å^{-1}$ will thus result in a weak oscillating signal with a wavelength of approximately 13 Å in the real-space domain from the $\frac{2\pi}{Q}$ inverse relationship. For the purpose of comparing PDFs to QMD-generated models without complications arising from incomplete measurements of pore structures, a Q_{min} value of 1.0 Å was selected.

3.4.4 Abberation Corrected Scanning Transmission Electron Microscopy

The structure of the CDC was characterized using an abberation corrected Nion UltraSTEM (Nion Company, Kirkland, WA, USA) operating at 60 kV. Scanning transmission electron microscopy (STEM) imaging provides[95,96] atomic resolution characterization of the overall CDC morphology following the chlorine heat treatment and subsequent vacuum annealing.

3.5 Results and Discussion

A quenched molecular dynamics routine was used to generate atomistic models for CDCs. Images provide qualitative analyses of sample morphology and structural properties, while quantitative characterization includes pair distribution functions, pore size distributions, ring size distributions, and ring neighbor correlations. Comparisons of QMD-generated CDC models to experimental results are made in appropriate corresponding discussions.

A summary of the models is listed in Table 4.4. Throughout, models generated through simulation named 'QMD-x' where 'x' is the quench rate used to produce it (in units of $1\,\mathrm{K\,ps^{-1}}$–$100\,\mathrm{K\,ps^{-1}}$). A 'c' is appended to the name if a post-quench compression step was included. The experimental sample is referred to as 'Expt.'.

Table 3.1: Summary of sample structures. Models are named 'QMD-x' where 'x' is the quench rate used to produce it (in units of $\mathrm{K\,ps^{-1}}$). A 'c' is appended to the name if a post-quench compression step was included. Q: Quench rate, $\mathrm{K\,ps^{-1}}$; $\bar{p}$: mean pore size, nm; L: Box length, nm; ρ: Particle density, $\mathrm{g\,cm^{-3}}$.

Sample	Q**, K ps** $^{-1}$	$\bar{p}$**, nm**	L**, nm**	ρ**, g cm** $^{-3}$	**Compression**
QMD-100	100	0.50	7.488	0.950	No
QMD-10	10	0.97	7.488	0.950	No
QMD-1	1	1.40	7.488	0.950	No
QMD-10c	10	0.56	6.489	1.467	Yes
QMD-1c	1	0.91	6.733	1.311	Yes

3.5.1 Imaging and Spectroscopy of CDC Structures

Before evaluating QMD-generated CDC structures, we first consider imaging of these structures from experiments. Figure 3.1 shows representative annular dark-field (ADF) STEM images of the CDC structure. They reveal that the CDC structure is composed primarily of high curvature graphene sheets. The STEM images also show regions where the graphene sheets come together along their edges to form slit-like geometric configuration. Moreover, due to the atomic-scale chemical sensitivity of ADF STEM imaging, single atoms with an atomic number greater than carbon are clearly visible in the CDC. Shown in the Appendix, Electron Energy Loss Spectroscopy (EELS) measurements from these brighter atoms confirm that these are silicon atoms, likely the result of incomplete chlorine treatment. Raman spectra were also collected on the experimental CDC sample and presented in The Appendix. Prominent D and G bands, characteristic of disordered carbon, are observed.

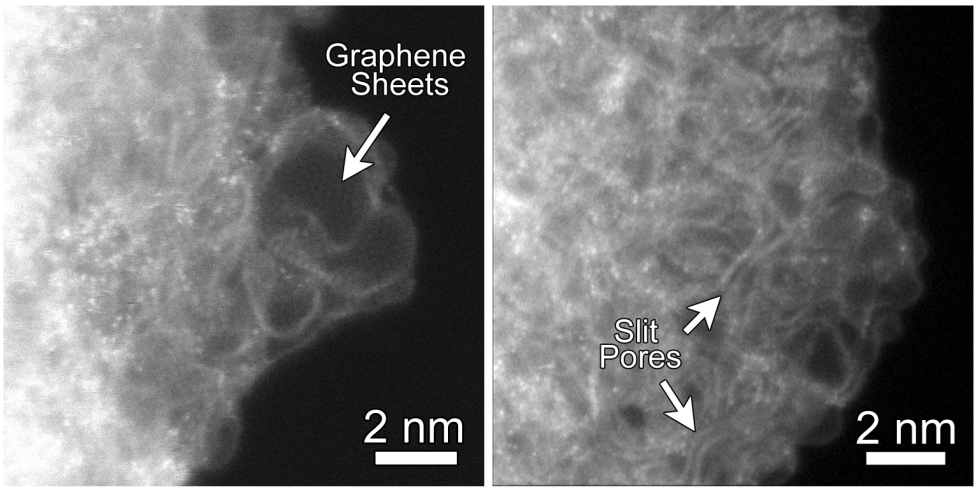

Figure 3.1: Representative Annular Dark-Field (ADF) Abberation-Corrected Scanning Transmission Electron Microscopy (STEM) images of carbide-derived carbons (CDCs) from experiment. CDC samples were subjected to heat treatment at 700 °C for 11 h. Left: regions of highly-curved graphene sheets; Right: regions where the graphene sheets form slit-like configurations. The bright atoms with the CDC structure are residual silicon atoms as confirmed through Electron Energy Loss Spectroscopy (EELS).

3.5.2 QMD-Generated CDC Structures

Snapshots of final-state structures produced with QMD are shown in Figure 3.2 and can be compared to representative STEM images of experimental samples shown in Figure 3.1. Simulation boxes are cubic with characteristic lengths near 7 nm. Therefore, while mesoscale features cannot be analyzed, properties on the order of few Ångstrom can be considered. In particular, we focus on the aggregation of hexagonal and non-hexagonal rings into sheet-like networks and the size distribution of pores. These properties are quantified in Figures 3.3–3.5.

Clear trends with respect to quench rate are observed: faster quenches produce more amorphous structures and slower quenches produce more ordered structures. This is in agreement with prior QMD studies of amorphous carbons.[55,57,73] Shown in Figure 3.2a, a quench rate of $100\,\mathrm{K\,ps^{-1}}$ generates a highly amorphous structure with many stringy domains and few rings. Only a small number of rings are found, as quantified in Figure 3.4, and no specific ring size dominates the distributions. This low quantity prevents the formation of large sheets with graphitic

features, which had been observed in CDCs synthesized at high temperature and that had exhibited prominent graphitic domains. The pore size distribution (Figure 3.3) shows that all porosity is below 1 nm and most pores are approximately 0.5 nm. Despite this, the observed nature of the carbon bonding indicates that these nanopores are not necessarily directly representative of those found in synthesized CDCs.

Slowing the quench rate gives more time for rings to form, as seen in Figure 3.2b, and some networks begin to reach the size of several rings and resemble small graphene-like sheets. Rings are mostly hexagonal, but a number of Stone–Wales and similar defects are observed. Stringy domains are not eliminated but appear at notably smaller frequency. The overall structure remains amorphous, but the greater quality of ring networks generates pores of greater definition. These pores are also larger, as seen in Figure 3.3. Many pores are sub-nanometer, but there is also a broad shoulder between 1 and 2 nm.

As shown in Figure 3.2c, further reducing the quench rate by a factor of 10 to 1 $\mathrm{K\,ps^{-1}}$ generates a more ordered structure. Most carbon atoms assemble into hexagonal rings, which aggregate into large, curved sheets that enclose nanopores. Some sheets collapse onto each other and form domains reminiscent of [002] stacking in graphite, but most sheets are single-layer and comprise pore walls. These pores exhibit a wider size distribution. While a fraction of pores is in the sub-nanometer diameter range, Figure 3.3 shows similar quantities of pores up to 2.5 nm in size. This emergence of larger pores with decreasing quench rate has been observed in previous QMD studies.[57,73,97] It bears repeating that quench rate in simulation lacks a direct physical analog; therefore, this trend cannot directly be attributed to any features of synthesis via halogen etching despite how physically realistic the generated structures may be.

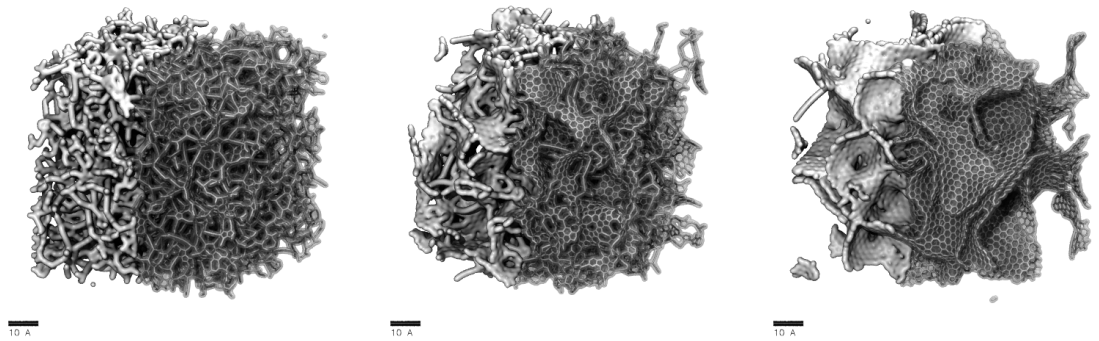

(**a**) QMD-100 (**b**) QMD-10 (**c**) QMD-1

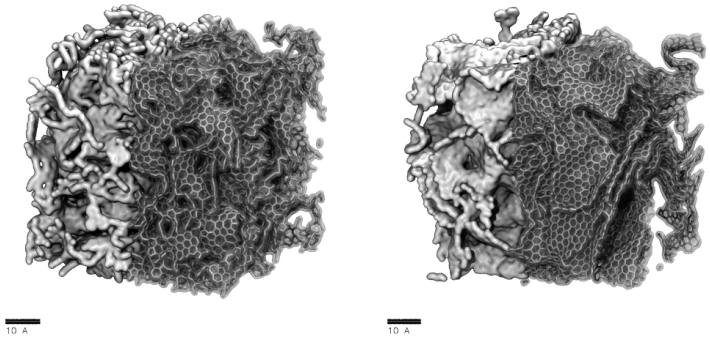

(**d**) QMD-10c (**e**) QMD-1c

Figure 3.2: Sample structures produced via quenched molecular dynamics (QMD) at quench rates and comparison to STEM of Si-CDC from experiment. Simulation boxes are between 6.5 and 7.5 nm in length and include 20,000 atoms. Each scale bar is 10 Å or 1 nm long.

In summary, slower quenches produce structures with physically realistic carbon bonding but larger pores. Because the small pore size of CDCs gives rise to many important physical properties, it is worth attempting to modify the structures generated from slow quenches to have smaller pores. To this end, we applied a post-quench compression step to the QMD-10 and QMD-1 structures via *NPT* simulations at 20 000 atm and 3000 K, generating structures QMD-10c (Figure 3.2b) and QMD-1c (Figure 3.2e).

Comparisons between Figure 3.2b,d and Figure 3.2c,e shows that the compression step qualitatively decreases pore sizes, particularly of larger pores. Some rearrangement is observed in Figure 3.2d, but for the most part, and particularly in Figure 3.2e, pores are modified without collapsing existing pores and/or forming new ones. Qualitative visual observations do not show any alterations of ring bonding. Thus, the combination of ReaxFF with a post-compression step results in

pore size distributions that more closely match experiments as well as a recent study that generated CDCs using the EDIP force field and, rather than QMD, annealing of a system after removal of metal atoms from a carbide lattice.[67] Specifically, this compression step combines properties of QMD-generated models at different quench rates: the local bonding structure is dominated by six-membered rings, but the pore size distribution does not largely extend in the mesoporous regime.

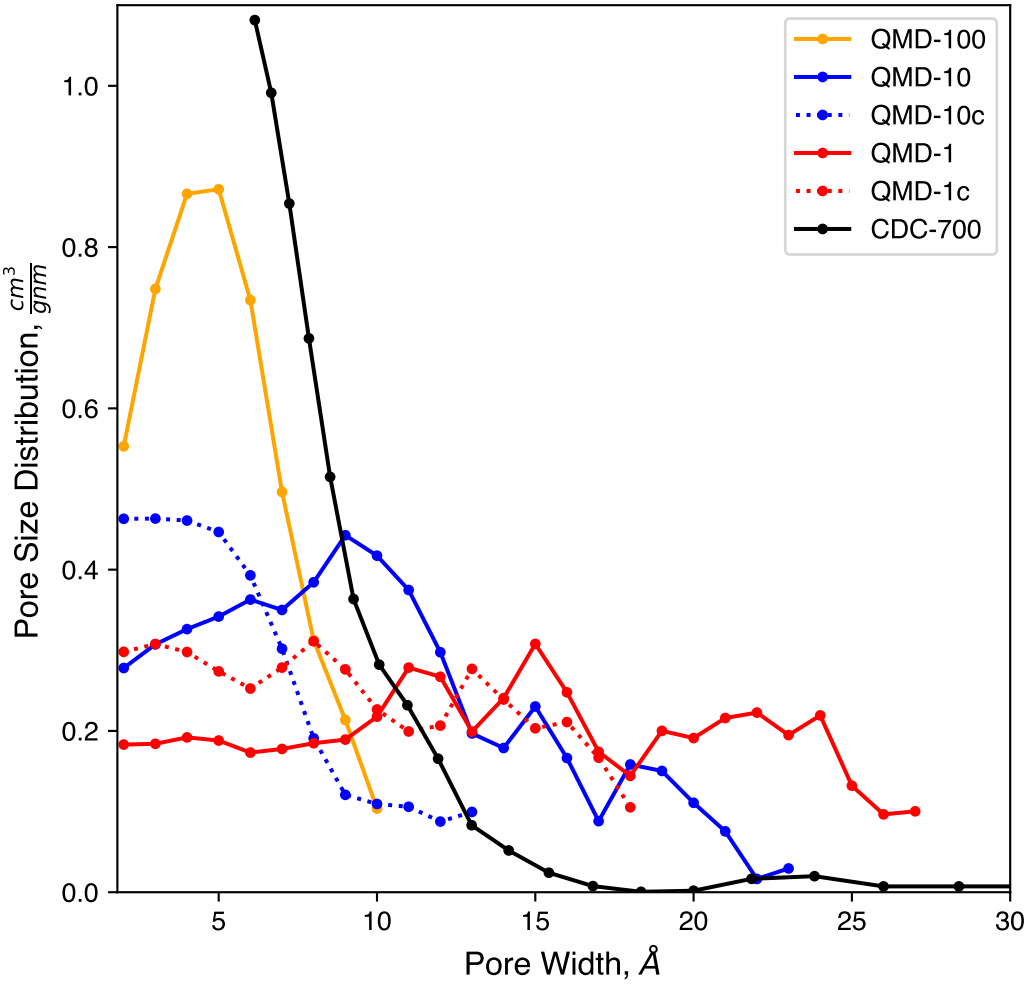

Figure 3.3: Pore size distributions of model samples compared to experiments.

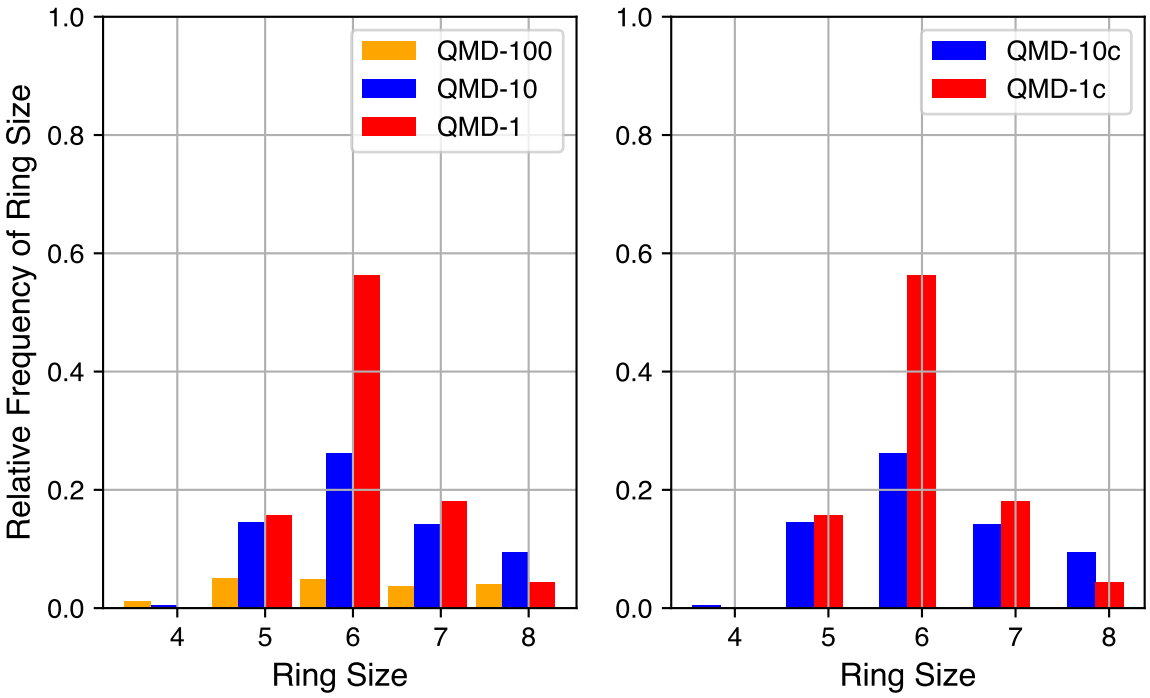

Figure 3.4: Ring size distributions of QMD-generated models.

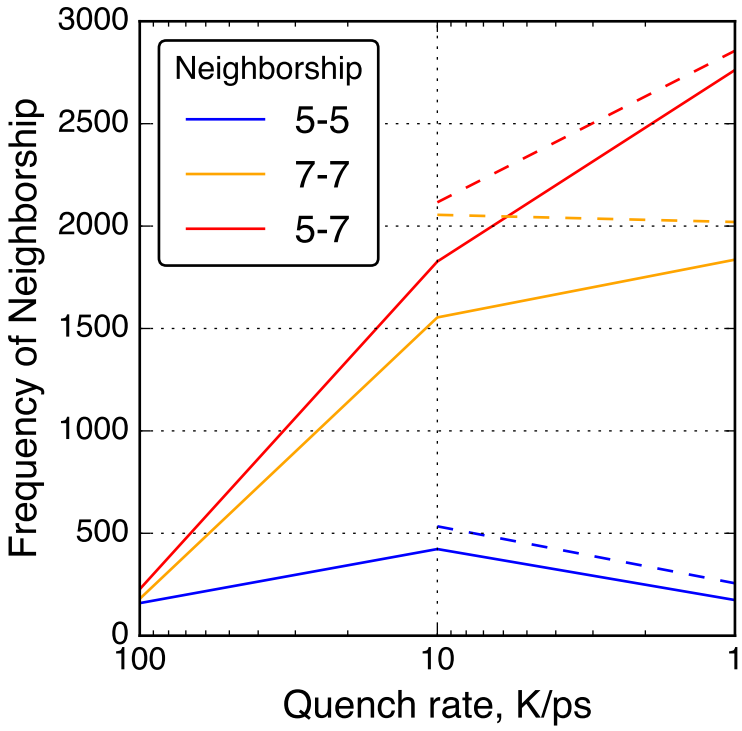

Figure 3.5: Neighbor–neighbor relationships between 5- and 7-membered rings in QMD-generated models. Solid lines connect data from simulations without post-quenching compression and dashed lines connect data from simulations with post-quenching compression.

3.5.2.1 Pore Size Distributions

Pore size distributions of QMD samples are shown in Figure 3.3. Consistent with previous QMD studies,[57,97] the pore size and dispersity increase with slower quench rates. The compression steps (samples QMD-10c and QMD-1c) are shown to quantitatively increase the population of sub-nanometer pores and, to a lesser extent, decrease the dispersity. Although the post-quenching compression step fails to fully reach the monodisperse sub-nanometer target, agreement with the experimental pore size distribution is improved, most notably for QMD-10c.

We note that, while experimental characterization results demonstrate a strong predominance of sub-nanometer pores, a small shoulder at 1–1.5 nm and a small peak between 2.0 and 2.5 nm are observed. As such, the larger pore size distributions observed in some of our or systems may indeed be realistic. However, they may form in higher frequency than in experimentally produced CDCs.

3.5.2.2 Ring Size Distributions

Although a robust quantification of the number of non-hexagonal rings is not currently accessible via empirical characterization of experimental systems, it can be quantified in simulation. The relative quantities of rings of sizes 4 through 8 in QMD-generated structures are shown in Figure 3.4. Ring counts are normalized to the number of hexagonal rings in a fully graphitic sample of the same size (10,000 rings in these 20,000 atom systems). By comparing compressed and non-compressed samples, the compression step is shown to have a small impact on the number of rings but little impact on the distribution. On the left are ring size distributions from samples produced by QMD alone and on the right are ring size distributions from samples that also underwent a post-quench compression step.

The quench rate is shown to have a significant impact on the quantity of ring formation and type of rings formed. At the fastest quench rate, few rings are formed with no particular size dominating the distribution. At the slowest quench rate, the total number of rings approaches the graphitic limit

and hexagonal rings are the most common. The ring size distribution for the samples of medium quench rate mixes properties of the limits: the total number of rings is large and hexagonal rings are the most common, but not by a large margin. For all QMD-generated structures, the number of four-membered rings is negligible and the number of eight-membered rings is non-zero but not significant. For all quench rates, the number of five- and seven-membered rings is similar, indicating that their existence may be structurally coupled.

To further investigate the relationships between non-hexagonal rings, neighbor–neighbor correlations of non-hexagonal rings were analyzed and shown in Figure 3.5. For example, the number of 7-membered rings neighboring a 5-membered rings was counted and shown as a '5-7' neighbor type. With slower quench rate, 5-7 and 7-7 neighbor types increased in quantity while 5-5 neighbor types decreased in quantity. This trend is consistent with common graphene defects such as the Stone–Wales 55-77 defect[98] and the 555-777 divacancy.[43] Other common non-hexagonal defects found in graphene follow a consistent theme of 7-membered rings neighboring each other and 5-membered rings, but rarely 5-membered rings neighboring each other.[99]

3.5.3 Sorptive Loading

Nitrogen isotherms generated from GCMC simulation are shown in Figure 3.6 and compared to a representative experimental isotherm. Characteristic Type I isotherms are observed: most loading occurs at low relative pressures and little change in loading occurs at moderate relative pressures. A partial condensation phase transition is only observed in the QMD-1 sample, which is expected to be the result of mesopores. The loading spikes in experimental samples near $P = P_{vap}$ are the result of larger non-porous features formed from the packing of the CDC nanoparticle and not the result of mesopores found in bulk CDC phases. The lower loadings in compressed samples compared to non-compressed samples is a result of an artificially high density, although the shapes of the isotherms are not noticeably affected.

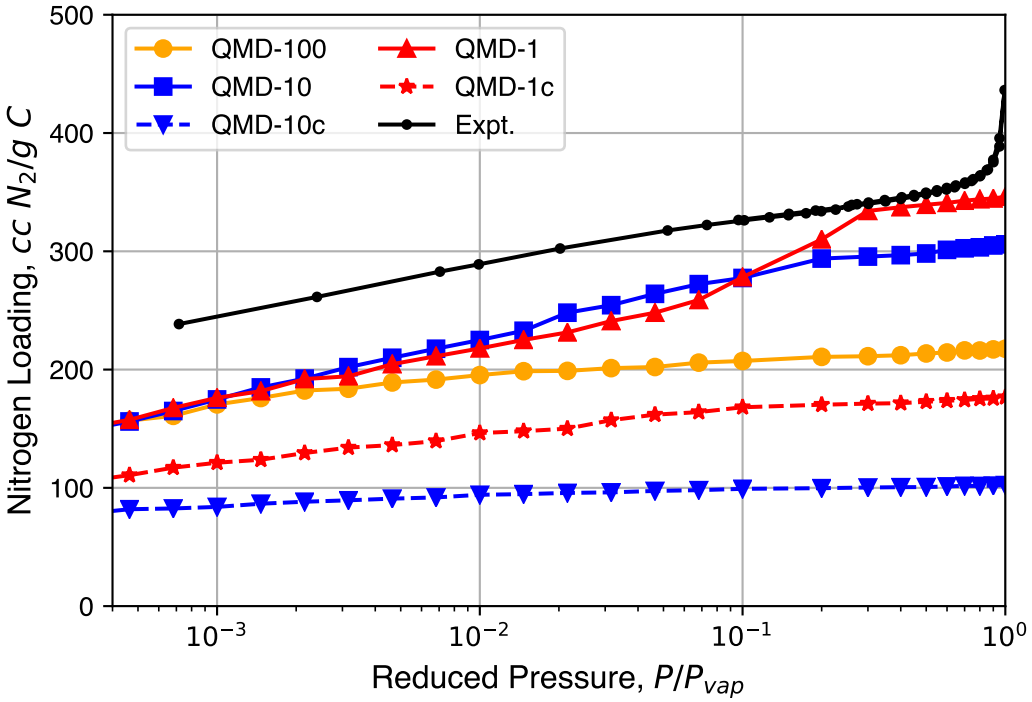

Figure 3.6: Nitrogen isotherms generated from grand canonical Monte Carlo (GCMC) simulation in comparison to experimental isotherms.

3.5.4 X-Ray Total Scattering

Further structural analysis relies on a synchrotron X-ray source for total scattering/pair distribution function analysis. The $S(Q)$ of an annealed CDC sample is shown in Figure 3.7 and compared to simulated data of an ideal graphene sheet of 10×10 unit cells. We note here that the large intensity uptake observed in the low Q region arises from the surface scattering and pore structures present in the CDCs. Comparisons to QMD-generated structures in real space are discussed below. Most of the peaks observed in the experimental sample correspond well to the diffraction pattern of the graphene structure, the exceptions being peaks at $1.4(1)\,\text{Å}^{-1}$ and $1.83(2)\,\text{Å}^{-1}$ ($\sim$3.43 Å and $\sim$4.5 Å in real space). The $1.83(2)\,\text{Å}^{-1}$ peak corresponds to graphite (002) reflection typically observed at $26\,\text{deg}\,2\theta$ with Cu-Kα radiation. This peak, however, is not completely resolved and sits alongside a broad diffuse peak centered at $1.4(1)\,\text{Å}^{-1}$. Such features suggest the presence of poorly coordinated graphene sheets, to which this peak is attributed. In addition, as mentioned in

the experimental section, the large intensity uptake at Q < 1 $Å^{-1}$ by surface and/or pore structure scattering is omitted for subsequent PDF analysis.

The PDF $G(r)$ is related to the RDF $g(r)$ as

$$G(r) = 4\pi r\rho(g(r) - 1); \tag{3.1}$$

therefore, a PDF, unlike an RDF, may fall below zero for some values of r. The length scale over which PDFs provide strong resolution (a few Å), corresponds to carbon atoms separated by a small number of bonds.

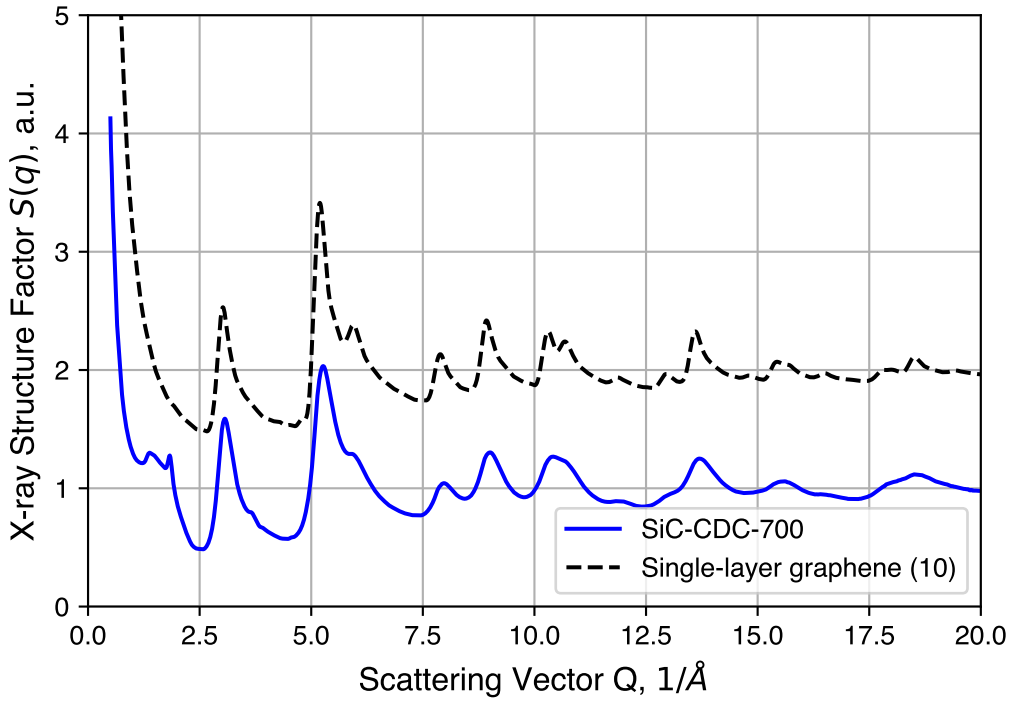

Figure 3.7: Comparison between experimental structure factor of CDC and simulated data of single graphene layer (10 × 10 unit cells).

Pair distribution functions from QMD-generated structures are shown in Figure 3.8. The software package DISCUS[100] (Version 4.2, Michigan State University, East Lansing, MI, USA) used in these calculations in order to include the effects of some biases in the experimental apparatus, including Q_{max}, Q_{damp}, and Q_{broad}. For the local carbon bonding comparisons, only a small isotropic thermal displacement factor is introduced ($B_{iso} = 0.2\,Å^2$, approximately 0.05 Å mean-square dis-

placement) because the QMD-generated structures are large enough to contain the desired static disorder. The overall intensity scale factor is also adjusted to compare with observed PDF. To maintain consistency, all simulated PDFs used the same parameters.

The peaks of these PDFs correspond well to the distances between carbons in an idealized graphene-like structure and follows previous interpretation in which no strong correlation can be observed between different sheets and/or pore walls.[101,102] The first three peaks at 1.43(2), 2.45(2) and 2.83(2) Å correspond to neighbors in a hexagonal ring and peaks at 3.75(5), 4.28(5) and 4.97(8) Å correspond to the location of carbon atoms in neighboring rings. The well-ordered nature of these peaks indicates, as expected, that hexagonal rings are favored. However, significant peak asymmetry and broadening observed at the third and further peaks do indicate the presence of non-hexagonal rings and the resulting sheet curvature effects. Together, these define the extent of structural coherence (approximately 15 Å) in the experimental PDF data. Compared to simulated PDFs, slower quenches provide better agreement with experiment, though QMD-1 is not able to totally capture graphitic ordering at distances greater than $\sim$5 Å. Consistent in both experimental and simulated PDFs is the general feature in peak broadening and the lack of graphite [002] correlation near 3.43 Å, the latter indicating a lack of sheet–sheet stacking despite other graphitic properties.

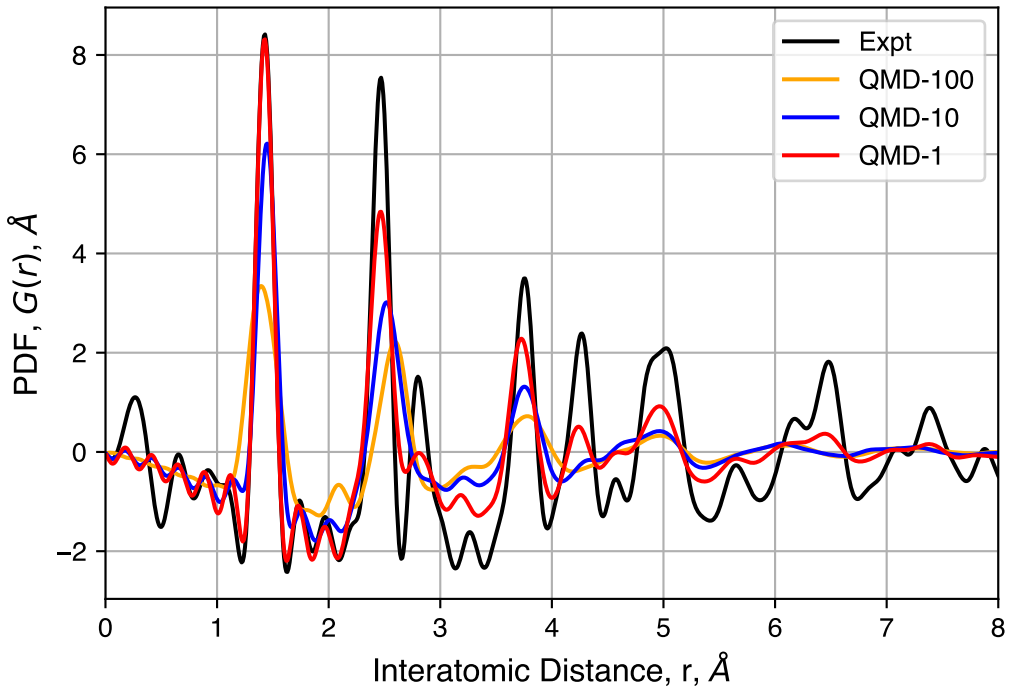

Figure 3.8: Experimental and simulated pair distributed functions (PDFs) for three QMD-generated structures. Corrections used in the DISCUS software result in some noise in the region of $r < 1\,\text{nm}$, whereas a corresponding radial distribution function (RDF) would have only zero values.

3.5.5 Effects of Initial Density

We consider the effects of initial density on the final structure. The QMD-10c sample, which has an initial density of 0.95 g cm^{-3}, was considered as a reference. Simulations were performed with identical inputs with the exception of the initial density. Values of 0.8 and 0.9 g cm^{-3} were considered. After compression, these two systems reached densities of 1.56 and 1.55 g cm^{-3}, respectively, as compared to 1.467 g cm^{-3} for the system originally at 0.95 g cm^{-3}.

The pore size distributions of each of sample, before and after compression at 20 000 atm, are shown in Figure3.9. Pore size distributions of samples compressed at other pressures are shown in The Appendix. For all un-compressed samples, the distribution is broad, covering the range 0.3 nm–2.0 nm. There is also a small increase in the mean pore size as the density decreases. The compressed samples, however, exhibit similar pore size distributions. Each has a peak near 0.5 nm

and a shoulder that disappears near 1.0 nm. The uniformity of these distributions suggested that the initial density does not strongly impact the porosity of the structure after compression, for these relatively high density systems, as quench rate is likely to be the dominant factor for structural evolution.

We also consider the pair distribution functions of these samples, shown in Figure 3.10. For samples with a range of initial densities, compression has a small impact. Peak heights are not noticeably changed, but compression shifts each peak slightly to the left. This is attributed to the high pressure needed to increase the density of each sample and not differences in the nature of the carbon bonds. Comparisons of samples before and after compression show that density has no noticeable impact on the pair distribution functions. In summary, compression is shown to have negligibly small impacts on short-range carbon interactions while driving most of the pore size distribution below 1 nm.

We should note, however, that they are still quite small compared to experiments.

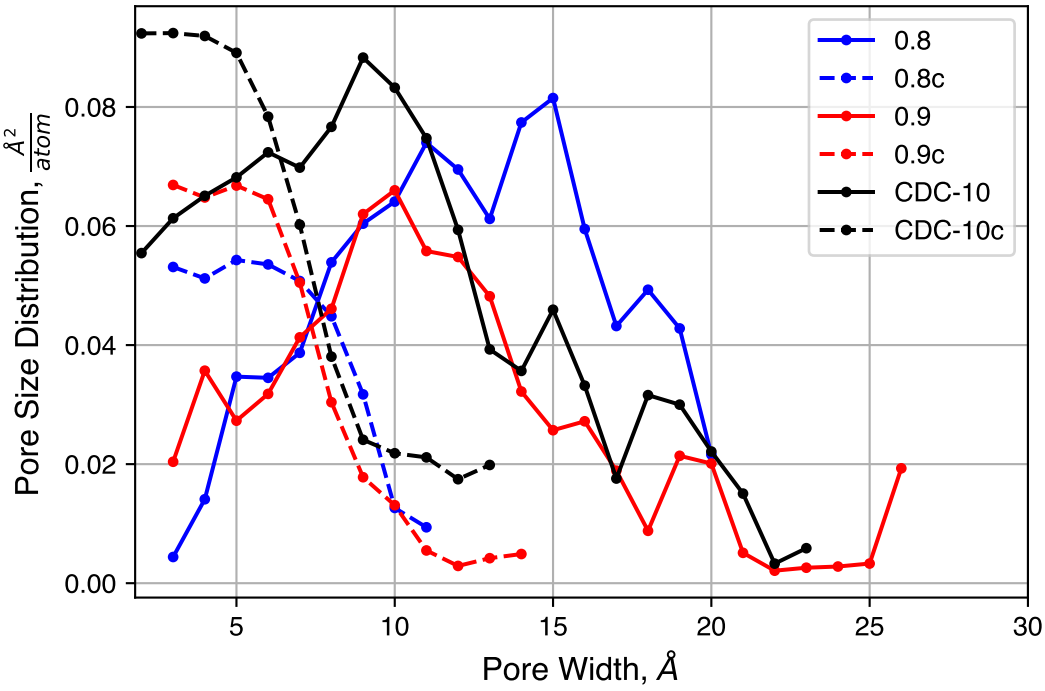

Figure 3.9: Pore size distributions of samples with decreased initial density, before and after compression.

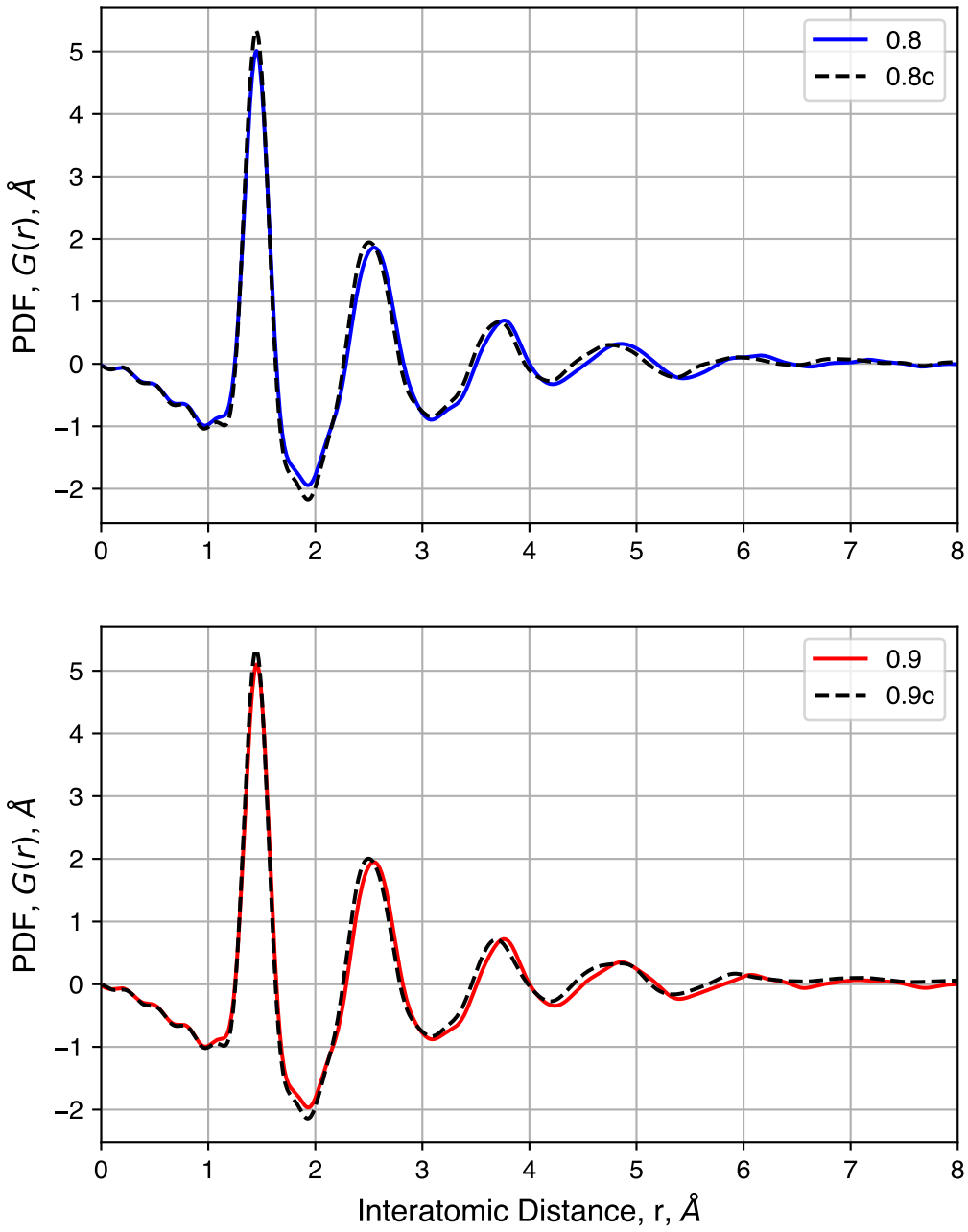

Figure 3.10: Pair distribution functions of samples with decreased initial density, before and after compression.

As shown in Figure 3.1, experimental samples include a variety of highly amorphous domains and features such as graphitic slit pores and single, isolated graphene sheets, in addition to other heterogeneous nanoscale domains. As a result, experimental samples will show localized variation in structure and density. Furthermore, experimental CDC samples could be thought of as a col-

lection of individual structures comprising larger particles. The models generated here represent a separate collection of structures that may overlap with those found in experiments. Thus, prudent studies of the behavior of CDCs should consider the collective behavior of a range of nanoscale structures to better understand the resulting physical properties observed in experiments.

3.6 Conclusions

The use of the ReaxFF reactive force field in generating an atomistic model for carbide-derived carbons was explored using a quenched molecular dynamics (QMD) scheme. The effects of quench rate and system compression were explored. Comparisons were made to an experimental carbide-derived carbon (CDC) material with similar structural properties. These models that use ReaxFF and employ a post-quenching compression step provide clear improvement upon prior CDC models generated using QMD in terms of local bonding and pore size distribution and also closely match those recently published using a process involving removal of metal atoms from a carbide and subsequent annealing.[67]

Slower quench rates and a compression step yield good agreement with experimental pore size distributions (PSDs), pair distribution functions (PDFs), and qualitative morphological features in abberation-corrected scanning transmission electron microscopy (STEM) images. The sorptive behavior closely matches CDCs and typical nanoporous adsorbents. The prevalence of non-hexagonal rings and their neighbor correlations are also explored. System compression, after the quenching step, is shown to decrease average pore size toward a sub-nanometer distribution without disrupting short-range features such as ring size. Overall, QMD-10c and QMD-1c are presented as viable atomistic models for CDCs.

This work provides the framework for use of these structures as model adsorbents and electrodes in molecular simulation of adsorption and electrochemical capacitors, respectively. Specifically, use of these models introduces non-idealities such as pore size dispersity, surface curvature, and non-hexagonal rings.

3.7 Future Work

I will conclude this chapter by describing a few other models that coupld be explored: synthesis-mimetic simulation, templating porosities, and hybrid reverse Monte Carlo.

All existing models in the literature, the above work included, work around the physical process by which CDCs are synthesized and instead attempt to match the properties of the resulting structure. Another approach is so-called synthesis-mimetic simulation (SMS) in which simulations try to actually model the process by which some experimental synthesis takes place. For example, Black *et al.* generated amorphous silica surfaces in simulations with a scheme that follows experimental treatment of silica surfaces with piranha (H_2SO_4 and H_2O_2)[103] This reaction happens quickly on a lab scale and was therefore feasibly accessible with reasonable molecular models (in that case, the reactive force field ReaxFF[71]). The synthesis of CDCs via chemical etching, however, takes place on the time scale of a few hours for a characteristic length on the scale of a micron. A reasonably sized molecular model of 5 nm would take several nanoseconds to etch in simulation. The 500 ps simulations in the above work took two full days on modern supercomputing architecture using highly parallelized software running on 48 cores. However, while a given ReaxFF force field parameter set can sufficiently capture the physical properties it is tuned to, it is less trustworthy for exploring new chemical processes, such as this chlorination reaction that has not been given much attention in other theoretical studies. A rigorous treatment of the reaction would require extremely expensive AIMD simulations. These take approximately 1 min per 1 fs step per atom per core used; a 500 ps simulation on the same number of CPU cores as above (48) would take approximately 400 years, so more CPU core would be needed and the system size and simulation length would need to be drastically reduced. Other recent advancements in computational chemistry attempt to bridge this gap of chemical accuracy and computational cost but have not, to my knowledge, focused on carbon-carbon interactions. All in all, an SMS approach to CDCs would provide valuable insight into how the chlorination reaction guides the physical properties of the carbon structure, but some model development and/or significant investment of computational resources are necessary for it to be a tractable approach.

A limitation of QMD, HRMC, and other techniques is that their focus on short-range structural properties only assures good agreement with respect to short-range properties (on the order of a few Angstroms) and some slightly longer scales (a few nanometers). Past some intermediate distance, agreement with experiment becomes uncontrolled. One example of this is the connectivity of pore structures. It is difficult to characterize with experiment but the high loadings of adsorbed gasses, electrolytes, or other fluids implies that at least most of the pore volume inside of CDC particles is accessible. There is some evidence that characteristic pore paths on the order of hundreds of microns are readily accessed by electrolyte.[104] Conversely, there is no guarantee that pores in model CDCs are connected at all. It is easy to conceive of porous structures that perfectly match experimentally measured pore size distributions yet consist of distinct and separate pores that are not connected at all. Pore accessibility is often induced artificially by slicing a sample across a PBC boundary, see the structures of Palmer *et al.* commonly used by Merlet, Sallane, and co-workers[105–111] and a similar model used by Pak *et al.*[35] In addition to fundamentally improving the accuracy of a model at small scales, studying process crucial to energy storage (ion adsorption, desorption, and exchange in individual pores, diffusive behavior in larger particles, and filling capabilities in tortuous materials) requires models with more realistic pore networks at larger slaces. A simple approach to this may be templating a QMD or HRMC process with solid components, i.e. rigid rods, that bias the system toward containing some amount of longer, inter-connected networks. This ideas is inspired by many porous carbon synthesis techniques that use zeolites or mesoporous silica as temporary templates for well-controlled carbon structures.

Lastly, as discussed above, an alternative to QMD is HRMC, which attempts to reconstruct an atomistic structure via many Monte Carlo moves that drive the system toward a target objective. This can be thought of as reverse engineering at the molecular scale. The primary appeal of this technique is that the target can be an defined arbitrarily with any objective function (or, in HRMC jargon, error norm). The simplest is attempting to minimize the error between an RDF computed on-the-fly and a target RDF that can be generated from experimental data or otherwise by any other desired theoretical method. For better convergence and model accuracy, it is often useful

to add other terms that constrain the system to some physically reasonable configurations.[54] (This distinguishes HRMC from simple RMC.) Different approaches, such as adding an overall potential energy term,[51] its square[112] or other terms that drive C-C-C angles toward 120° instead of 60° and under-coordination have been explored. These ideas can be expanded upon to include terms that refine structure on larger length scales, such as fitting to small-angle X-ray or neutron sacttering (SAXS[8] or SANS) data or calculating on-the-fly some metric that characterizes the global connective of the pores. It is difficult to perscribe in detail such an objective function, but it would be invaluable in efforts to accurately model nanoporous carbons.

3.8 Bibliography

[1] Matthew W. Thompson et al. "An Atomistic Carbide-Derived Carbon Model Generated Using ReaxFF-Based Quenched Molecular Dynamics". In: *C* 3.4 (2017), p. 32.

[2] Matthew W Thompson. *qmd*. \url{https://github.com/mattwthompson/qmd}. 2018.

[3] Volker Presser, Min Heon, and Yury Gogotsi. "Carbide-Derived Carbons - From Porous Networks to Nanotubes and Graphene". In: *Advanced Functional Materials* 21.5 (2011), pp. 810–833.

[4] Ranjan Dash et al. "Titanium carbide derived nanoporous carbon for energy-related applications". In: *Carbon* 44.12 (2006), pp. 2489–2497.

[5] Alar Jänes et al. "Nanoscale fine-tuning of porosity of carbide-derived carbon prepared from molybdenum carbide". In: *Carbon* 47.1 (2009), pp. 23–29.

[6] Elizabeth N. Hoffman et al. "Micro and mesoporosity of carbon derived from ternary and binary metal carbides". In: *Microporous and Mesoporous Materials* 112.1-3 (2008), pp. 526–532.

[7] Yury Gogotsi et al. "Nanoporous carbide-derived carbon with tunable pore size". In: *Nature Materials* 2.9 (2003), pp. 591–594.

[8] Giovanna Laudisio et al. “Carbide-derived carbons: A comparative study of porosity based on small-angle scattering and adsorption isotherms”. In: *Langmuir* 22.21 (2006), pp. 8945–8950.

[9] Sebastian Osswald, John Chmiola, and Yury Gogotsi. “Structural evolution of carbide-derived carbons upon vacuum annealing”. In: *Carbon* 50.13 (2012), pp. 4880–4886.

[10] Miloslav Nič et al., eds. *IUPAC Compendium of Chemical Terminology*. Research Triagle Park, NC: IUPAC, 2009.

[11] J. Chmiola. “Anomalous Increase in Carbon Capacitance at Pore Sizes Less Than 1 Nanometer”. In: *Science* 313.5794 (2006), pp. 1760–1763.

[12] J. Chmiola et al. “Effect of pore size and surface area of carbide derived carbons on specific capacitance”. In: *Journal of Power Sources* 158.1 (2006), pp. 765–772.

[13] J. Chmiola et al. “Monolithic Carbide-Derived Carbon Films for Micro-Supercapacitors”. In: *Science* 328.5977 (2010), pp. 480–483.

[14] R. Lin et al. “Solvent effect on the ion adsorption from ionic liquid electrolyte into sub-nanometer carbon pores”. In: *Electrochimica Acta* 54.27 (2009), pp. 7025–7032.

[15] T. X. Nguyen, J.-S. S. Bae, and Suresh K. Bhatia. “Characterization and adsorption modeling of silicon carbide-derived carbons”. In: *Langmuir* 25.9 (2009), pp. 2121–2132.

[16] Volker Presser et al. “Effect of pore size on carbon dioxide sorption by carbide derived carbon”. In: *Energy & Environmental Science* 4.8 (2011), p. 3059. arXiv: caps17.

[17] Cekdar Vakifahmetoglu et al. “Enhanced hydrogen and methane gas storage of silicon oxycarbide derived carbon”. In: *Microporous and Mesoporous Materials* 144.1-3 (2011), pp. 105–112.

[18] Gleb Yushin et al. “Mesoporous carbide-derived carbon with porosity tuned for efficient adsorption of cytokines”. In: *Biomaterials* 27.34 (2006), pp. 5755–5762.

[19] Saujanya Yachamaneni et al. “Mesoporous carbide-derived carbon for cytokine removal from blood plasma”. In: *Biomaterials* 31.18 (2010), pp. 4789–4794.

[20] C. Portet et al. “High power density electrodes for Carbon supercapacitor applications”. In: *Electrochimica Acta* 50.20 (2005), pp. 4174–4181.

[21] Yury Gogotsi and Volker Presser. *Carbon Nanomaterials*. Ed. by Yury Gogotsi and Volker Presser. 2nd. CRC Press, 2013.

[22] Patrice Simon and Yury Gogotsi. “Capacitive Energy Storage in Nanostructured Carbon–Electrolyte Systems”. In: *Accounts of Chemical Research* 46.5 (2013), pp. 1094–1103.

[23] H Kurig et al. “The suitability of infinite slit-shaped pore model to describe the pores in highly porous carbon materials”. In: *Carbon* 100 (2016), pp. 617–624.

[24] P. M. Vora et al. “Correlating magnetotransport and diamagnetism of <math display="inline"> <mrow> <mi>s</mi> <msup> <mi>p</mi> <mn>2</mn> </msup> </mrow> </math> - bonded carbon networks through the metal-insulator transition”. In: *Physical Review B* 84.15 (2011), p. 155114.

[25] Alexander J. Pak, Eunsu Paek, and Gyeong S. Hwang. “Tailoring the performance of graphene-based supercapacitors using topological defects: A theoretical assessment”. In: *Carbon* 68.512 (2014), pp. 734–741.

[26] Lidan Xing et al. “On the atomistic nature of capacitance enhancement generated by ionic liquid electrolyte confined in subnanometer pores”. In: *Journal of Physical Chemistry Letters* 4.1 (2013), pp. 132–140.

[27] Kristin Faber et al. “In-depth investigation of the carbon microstructure of silicon carbide-derived carbons by wide-angle X-ray scattering”. In: *Journal of Physical Chemistry C* 118.29 (2014), pp. 15705–15715.

[28] Cheng Zhan et al. “Quantum Effects on the Capacitance of Graphene-Based Electrodes”. In: *The Journal of Physical Chemistry C* (2015), p. 150917101153000.

[29] Cristelle Portet et al. “Impact of synthesis conditions on surface chemistry and structure of carbide-derived carbons”. In: *Thermochimica Acta* 497.1-2 (2010), pp. 137–142.

[30] Boris Dyatkin et al. “Capacitance, charge dynamics, and electrolyte-surface interactions in functionalized carbide-derived carbon electrodes”. In: *Progress in Natural Science: Materials International* 25.6 (2015), pp. 631–641.

[31] J.-K. Ewert et al. “Enhanced capacitance of nitrogen-doped hierarchically porous carbide-derived carbon in matched ionic liquids”. In: *Journal of Materials Chemistry A* 3.37 (2015), pp. 18906–18912.

[32] Katja Pinkert et al. “Role of Surface Functional Groups in Ordered Mesoporous Carbide-Derived Carbon/Ionic Liquid Electrolyte Double-Layer Capacitor Interfaces”. In: *ACS Applied Materials & Interfaces* 6.4 (2014), pp. 2922–2928.

[33] Gennady Yu Gor et al. “Quenched solid density functional theory method for characterization of mesoporous carbons by nitrogen adsorption”. In: *Carbon* 50.4 (2012), pp. 1583–1590.

[34] Svyatoslav Kondrat and Alexei A. Kornyshev. “Pressing a spring: what does it take to maximize the energy storage in nanoporous supercapacitors?” In: *Nanoscale Horizons* 1.1 (2016), pp. 45–52.

[35] Alexander J. Pak and Gyeong S Hwang. “Molecular Insights into the Complex Relationship between Capacitance and Pore Morphology in Nanoporous Carbon-based Supercapacitors”. In: *ACS Applied Materials & Interfaces* 8.50 (2016), pp. 34659–34667.

[36] Alberto Striolo et al. “Water Adsorption in Carbon-Slit Nanopores”. In: *Langmuir* 19.20 (2003), pp. 8583–8591.

[37] Qinyu Wang and J. Karl Johnson. “Molecular simulation of hydrogen adsorption in single-walled carbon nanotubes and idealized carbon slit pores”. In: *Journal of Chemical Physics* 110.1 (1999), pp. 577–586.

[38] Roger F. Cracknell, David Nicholson, and Nicholas Quirke. “A grand canonical Monte Carlo study of Lennard-Jones mixtures in slit shaped pores”. In: *Molecular Physics* 80.4 (1993), pp. 885–897.

[39] Yadong He et al. “Dynamic Charge Storage in Ionic Liquids-filled Nanopores: Insight from a Computational Cyclic Voltammetry Study”. In: *The Journal of Physical Chemistry Letters* (2014).

[40] Svyatoslav Kondrat et al. “Accelerating charging dynamics in subnanometre pores”. In: *Nature Materials* 13.4 (2014), pp. 387–393. arXiv: 1311.7529.

[41] Minoru Miyahara and Keith E. Gubbins. “Freezing/melting phenomena for Lennard-Jones methane in slit pores: A Monte Carlo study”. In: *The Journal of Chemical Physics* 106.7 (1997), pp. 2865–2880.

[42] Guang Feng et al. “The importance of ion size and electrode curvature on electrical double layers in ionic liquids”. In: *Phys. Chem. Chem. Phys.* 13.3 (2011), pp. 1152–1161.

[43] Brandon C. Wood et al. “First-Principles-Inspired Design Strategies for Graphene-Based Supercapacitor Electrodes”. In: *The Journal of Physical Chemistry C* 118.1 (2014), pp. 4–15.

[44] Jeremy C. Palmer et al. “Simulating local adsorption isotherms in structurally complex porous materials: A direct assessment of the slit pore model”. In: *Journal of Physical Chemistry Letters* 2.3 (2011), pp. 165–169.

[45] P.R. Bandaru et al. “Charge transfer and storage in nanostructures”. In: *Materials Science and Engineering: R: Reports* 96 (2015), pp. 1–69.

[46] R. L. McGreevy and L. Pusztai. “Reverse Monte Carlo Simulation: A New Technique for the Determination of Disordered Structures”. In: *Molecular Simulation* 1.6 (1988), pp. 359–367.

[47] Simon Duane et al. “Hybrid Monte Carlo”. In: *Physics Letters B* 195.2 (1987), pp. 216–222.

[48] Jorge Pikunic et al. “Structural Modeling of Porous Carbons: Constrained Reverse Monte Carlo Method”. In: *Langmuir* 19.20 (2003), pp. 8565–8582.

[49] Per Zetterström et al. “Reverse Monte Carlo studies of nanoporous carbon from TiC”. In: *Journal of Physics: Condensed Matter* 17.23 (2005), pp. 3509–3524.

[50] Jeremy C. Palmer et al. “Detailed structural models for activated carbons from molecular simulation”. In: *Carbon* 47.12 (2009), pp. 2904–2913.

[51] Amir H. Farmahini, George Opletal, and Suresh K. Bhatia. “Structural Modelling of Silicon Carbide-Derived Nanoporous Carbon by Hybrid Reverse Monte Carlo Simulation”. In: *The Journal of Physical Chemistry C* 117.27 (2013), pp. 14081–14094.

[52] P. Jedlovszky et al. “Investigation of the uniqueness of the reverse Monte Carlo method: Studies on liquid water”. In: *The Journal of Chemical Physics* 105.1 (1996), pp. 245–254.

[53] A.K. Soper. “Empirical potential Monte Carlo simulation of fluid structure”. In: *Chemical Physics* 202.2-3 (1996), pp. 295–306.

[54] Jeremy C. Palmer and Keith E. Gubbins. “Atomistic models for disordered nanoporous carbons using reactive force fields”. In: *Microporous and Mesoporous Materials* 154 (2012), pp. 24–37.

[55] Yunfeng Shi. “A mimetic porous carbon model by quench molecular dynamics simulation.” In: *The Journal of chemical physics* 128.23 (2008), p. 234707.

[56] R. Powles, N. Marks, and D. Lau. “Self-assembly of sp2-bonded carbon nanostructures from amorphous precursors”. In: *Physical Review B* 79.7 (2009), pp. 1–11.

[57] Jeremy C. Palmer et al. “Modeling the structural evolution of carbide-derived carbons using quenched molecular dynamics”. In: *Carbon* 48.4 (2010), pp. 1116–1123.

[58] Stephen H. Garofalini. “Molecular dynamics simulation of the frequency spectrum of amorphous silica”. In: *The Journal of Chemical Physics* 76.6 (1982), p. 3189.

[59] Lev D Gelb and Keith E. Gubbins. “Pore Size Distributions in Porous Glasses: A Computer Simulation Study”. In: *Langmuir* 15.2 (1999), pp. 305–308.

[60] David A. Litton and Stephen H. Garofalini. “Modeling of hydrophilic wafer bonding by molecular dynamics simulations”. In: *Journal of Applied Physics* 89.11 I (2001), pp. 6013–6023.

[61] Mark D Kluge, John R Ray, and Aneesur Rahman. “Amorphous-silicon formation by rapid quenching: A molecular-dynamics study”. In: *Physical Review B* 36.8 (1987), pp. 4234–4237.

[62] Kejian Ding and Hans C. Andersen. “Molecular-dynamics simulation of amorphous germanium”. In: *Physical Review B* 34.10 (1986), pp. 6987–6991.

[63] Steven J. Stuart, Alan B. Tutein, and Judith a Harrison. “A reactive potential for hydrocarbons with intermolecular interactions”. In: *The Journal of Chemical Physics* 112.2000 (2000), pp. 6472–6486.

[64] N A Marks. “Generalizing the environment-dependent interaction potential for carbon”. In: *Physical Review B* 63.3 (2000), p. 035401.

[65] J. Tersoff. “Modeling solid-state chemistry: Interatomic potentials for multicomponent systems”. In: *Physical Review B* 39.8 (1989), pp. 5566–5568. arXiv: arXiv:1011.1669v3.

[66] Xi Mi and Yunfeng Shi. “Topological defects in nanoporous carbon”. In: *Carbon* 60 (2013), pp. 202–214.

[67] Carla de Tomas et al. “Structural prediction of graphitization and porosity in carbide-derived carbons”. In: *Carbon* 119 (2017), pp. 1–9.

[68] Sabine Schweizer et al. “Molecular Modeling of Microporous Structures of Carbide-Derived Carbon Based Supercapacitors”. In: *The Journal of Physical Chemistry C* (2017), acs.jpcc.6b12774.

[69] Carla de Tomas, Irene Suarez-Martinez, and Nigel A. Marks. “Graphitization of amorphous carbons: A comparative study of interatomic potentials”. In: *Carbon* 109 (2016), pp. 681–693.

[70] Sascha Welz, Michael J. McNallan, and Yury Gogotsi. “Carbon structures in silicon carbide derived carbon”. In: *Journal of Materials Processing Technology* 179.1-3 (2006), pp. 11–22.

[71] Adri C. T. van Duin et al. “ReaxFF: A Reactive Force Field for Hydrocarbons”. In: *The Journal of Physical Chemistry A* 105.41 (2001), pp. 9396–9409.

[72] Sriram Goverapet Srinivasan, Adri C. T. van Duin, and P. Ganesh. “Development of a ReaxFF Potential for Carbon Condensed Phases and Its Application to the Thermal Fragmentation of a Large Fullerene”. In: *The Journal of Physical Chemistry A* 119.4 (2015), pp. 571–580.

[73] Raghavan Ranganathan et al. “Generation of amorphous carbon models using liquid quench method: A reactive molecular dynamics study”. In: *Carbon* 113 (2017), pp. 87–99.

[74] Matthew W. Thompson et al. “Scalable Screening of Soft Matter: A Case Study of Mixtures of Ionic Liquids and Organic Solvents”. In: *The Journal of Physical Chemistry B* 123.6 (2019), pp. 1340–1347.

[75] H. M. Aktulga et al. “Parallel reactive molecular dynamics: Numerical methods and algorithmic techniques”. In: *Parallel Computing* 38.4-5 (2012), pp. 245–259.

[76] Kimberly Chenoweth, Adri C. T. van Duin, and William A. Goddard. “ReaxFF Reactive Force Field for Molecular Dynamics Simulations of Hydrocarbon Oxidation”. In: *The Journal of Physical Chemistry A* 112.5 (2008), pp. 1040–1053. arXiv: 0311084 [physics].

[77] Steve Plimpton. “Fast Parallel Algorithms for Short-Range Molecular Dynamics”. In: *Journal of Computational Physics* 117.1 (1995), pp. 1–19.

[78] Kimberly Chenoweth et al. “Initiation Mechanisms and Kinetics of Pyrolysis and Combustion of JP-10 Hydrocarbon Jet Fuel”. In: *The Journal of Physical Chemistry A* 113.9 (2009), pp. 1740–1746.

[79] Fidel Castro-Marcano et al. “Combustion of an Illinois No. 6 coal char simulated using an atomistic char representation and the ReaxFF reactive force field”. In: *Combustion and Flame* 159.3 (2012), pp. 1272–1285.

[80] F.P. Bundy. “Pressure-temperature phase diagram of elemental carbon”. In: *Physica A: Statistical Mechanics and its Applications* 156.1 (1989), pp. 169–178.

[81] F.P. Bundy et al. “The pressure-temperature phase and transformation diagram for carbon; updated through 1994”. In: *Carbon* 34.2 (1996), pp. 141–153.

[82] Wataru Shinoda, Motoyuki Shiga, and Masuhiro Mikami. “Rapid estimation of elastic constants by molecular dynamics simulation under constant stress”. In: *Physical Review B* 69.13 (2004), p. 134103.

[83] Glenn J Martyna, Douglas J Tobias, and Michael L Klein. “Constant pressure molecular dynamics algorithms”. In: *The Journal of Chemical Physics* 101.5 (1994), pp. 4177–4189. arXiv: 0502063v2 [arXiv:hep-ph].

[84] M. Parrinello and A. Rahman. “Polymorphic transitions in single crystals: A new molecular dynamics method”. In: *Journal of Applied Physics* 52.12 (1981), pp. 7182–7190. arXiv: arXiv:1011.1669v3.

[85] H. A. Lorentz. “Ueber die Anwendung des Satzes vom Virial in der kinetischen Theorie der Gase”. In: *Annalen der Physik* 248.1 (1881), pp. 127–136.

[86] Daniel Berthelot. “Sur le mélange des gaz”. In: *Compt. Rendus* 126 (1898), pp. 1703–1706.

[87] Wan Yu Tsai et al. “Ordered mesoporous silicon carbide-derived carbon for high-power supercapacitors”. In: *Electrochemistry Communications* 34 (2013), pp. 109–112.

[88] Boris Dyatkin and Yury Gogotsi. “Effects of structural disorder and surface chemistry on electric conductivity and capacitance of porous carbon electrodes”. In: *Faraday Discuss.* 172 (2014), pp. 139–162.

[89] Stephen Brunauer, P H Emmett, and Edward Teller. “Adsorption of Gases in Multimolecular Layers”. In: *Journal of the American Chemical Society* 60.2 (1938), pp. 309–319.

[90] Johnathon N. Caguiat, Donald W. Kirk, and Charles Q. Jia. “Uncertainties in characterization of nanoporous carbons using density functional theory-based gas physisorption”. In: *Carbon* 72 (2014), pp. 47–56.

[91] A. P. Hammersley et al. “Two-dimensional detector software: From real detector to idealised image or two-theta scan”. In: *High Pressure Research* 14.4-6 (1996), pp. 235–248.

[92] Xiangyun Qiu, Jeroen W. Thompson, and Simon J. L. Billinge. “PDFgetX2 : a GUI-driven program to obtain the pair distribution function from X-ray powder diffraction data”. In: *Journal of Applied Crystallography* 37.4 (2004), pp. 678–678.

[93] Peter J. Chupas et al. “Rapid-acquisition pair distribution function (RA-PDF) analysis”. In: *Journal of Applied Crystallography* 36.6 (2003), pp. 1342–1347.

[94] C L Farrow et al. “PDFfit2 and PDFgui: computer programs for studying nanostructure in crystals”. In: *Journal of Physics: Condensed Matter* 19.33 (2007), p. 335219.

[95] Ondrej L Krivanek et al. “Atom-by-atom structural and chemical analysis by annular dark-field electron microscopy.” In: *Nature* 464.7288 (2010), pp. 571–574.

[96] P M Voyles et al. “Atomic-scale imaging of individual dopant atoms and clusters in highly n-type bulk Si.” In: *Nature* 416.6883 (2002), pp. 826–829.

[97] Lev D Gelb and K E Gubbins. “Characterization of Porous Glasses: Simulation Models, Adsorption Isotherms, and the Brunauer-Emmett-Teller Analysis Method”. In: *Langmuir* 14.8 (1998), pp. 2097–2111.

[98] A. J. Stone and D. J. Wales. “Theoretical studies of icosahedral C60 and some related species”. In: *Chemical Physics Letters* 128.5-6 (1986), pp. 501–503.

[99] Jannik C. Meyer et al. “Direct imaging of lattice atoms and topological defects in graphene membranes”. In: *Nano Letters* 8.11 (2008), pp. 3582–3586.

[100] Th. Proffen and R. B. Neder. “DISCUS : a program for diffuse scattering and defect-structure simulation”. In: *Journal of Applied Crystallography* 30.2 (1997), pp. 171–175.

[101] V. Petkov, R. G. Difrancesco, S. J. L. “Local structure of nanoporous carbons”. In: *Philosophical Magazine B* 79.10 (1999), pp. 1519–1530.

[102] Alexander C. Forse et al. “New Insights into the Structure of Nanoporous Carbons from NMR, Raman, and Pair Distribution Function Analysis”. In: *Chemistry of Materials* 27.19 (2015), pp. 6848–6857.

[103] Jennifer M. Black et al. “Topological defects in electric double layers of ionic liquids at carbon interfaces”. In: *Nano Energy* 15 (2015), pp. 737–745.

[104] Boris Dyatkin et al. “High capacitance of coarse-grained carbide derived carbon electrodes”. In: *Journal of Power Sources* 306 (2016), pp. 32–41.

[105] Céline Merlet et al. “On the molecular origin of supercapacitance in nanoporous carbon electrodes”. In: *Nature Materials* 11.4 (2012), pp. 306–310.

[106] Céline Merlet et al. “Highly confined ions store charge more efficiently in supercapacitors”. In: *Nature Communications* 4.1 (2013), p. 2701.

[107] Clarisse Péan et al. “On the dynamics of charging in nanoporous carbon-based supercapacitors”. In: *ACS Nano* 8.2 (2014), pp. 1576–1583.

[108] Clarisse Péan et al. “Confinement, desolvation and electrosorption effects on the diffusion of ions in nanoporous carbon electrodes”. In: *Journal of the American Chemical Society* (2015), p. 150929003048004.

[109] Clarisse Pean et al. “Multi-scale modelling of supercapacitors: From molecular simulations to a transmission line model”. In: *Journal of Power Sources* (2016), pp. 1–6. arXiv: 1603.06640.

[110] Ryan M Burt et al. “Capacitance of Nanoporous Carbon-based Supercapacitors is a Trade-off between the Concentration and the Separability of the Ions”. In: *The Journal of Physical Chemistry Letters* (2016), acs.jpclett.6b01787.

[111] Clarisse Pean et al. “Understanding the different (dis)charging steps of supercapacitors: influence of potential and solvation”. In: *Electrochimica Acta* 206 (2016), pp. 504–512.

[112] G. Zollo and F. Gala. “Atomistic modeling of gas adsorption in nanocarbons”. In: *Journal of Nanomaterials* 2012 (2012).

Chapter 4

Structure, Dynamics, and Thermodynamics of Solvated Ionic Liquids

Ionic liquids have many appealing physical properties, from their thermal, chemical, and electrochemical stability to their vast chemical functionality that enable utility in numerous applications. Across many applications, however, the inherently slow dynamics of ionic liquids provide some limitations. As electrolytes in energy storage devices, for example, the low molecular diffusivity of ionic liquids can limit the rate-handling capabilities and power densities of electrical devices.[1] In heterogeneous catalysis, slow dynamics as solvent can impact the rates at which reagents are transferred to and reaction products removed from a catalytic surface. Relevant to energy applications broadly, their slow dynamics (and large non-polar constituencies) result in relatively low ionic conductivities for a class of molecules that are purely ionic.

Therefore, for applications in which transport properties are particularly important, ionic liquids are sometimes dissolved in organic solvents. This chapter includes a years-long investigation into the impacts of mixture concentration and solvent properties on the dynamics of ions in such mixtures. This work has been published in three peer-reviewed manuscripts,[2–4] another currently in review[5] and one more in progress.

4.1 Background

A major drawback of using ionic liquids in energy-relevant applications is their inherently slow dynamic properties.[6–11] Compared to conventional electrolytes such as aqueous electrolytes based on alkali metal halides, ionic liquids have lower ionic conductivity,[12] which limits their rate handling capabilities in the case of supercapacitors.[1] They also exhibit low molecular diffusivity,[13–15]and high viscosity,[16] which similarly limits their potential uses in other applications. One approach to mitigating these slow dynamics is by dissolving ionic liquids in organic solvents such as acetonitrile and propylene carbonate.[2,17–22] This solvation significantly enhances transport

properties, thus increasing power density and possibly rate-handling capabilities. Energy density can be impacted by a narrowed electrochemical window, but some studies indicate that the voltage window is still wide - sometimes even as wide as the neat ionic liquids themselves - but consistently much wider than aqueous electrolytes.[23–26] Pech *et al.* compared four different supercapacitor designs, each using a solvated RTIL and a different electrode, and found that they exhibited three to five orders of magnitude greater power density than Li-ion batteries, with varied energy density performance.[27] Lewandowski *et al.* studied four ionic liquids solvated in acetonitrile and propylene carbonate and found that, compared to their neat state, they exhibited slightly decreased energy density ($\sim$5-30% less) but greatly increased power density, up to an order of magnitude in improvement.[28] Other studies[25,29] have offered similar comparisons of the dynamic performance of supercapacitors based on neat and solvated RTILs, again showing that solvation greatly increases power density. A review article by Zhong *et al.* provides a comprehensive (if somewhat outdated) summary of the performance of many supercapacitors and comparisons between aqueous and organic electrolytes.

These preliminary studies each indicate that ionic liquids in organic solvents can be used to design supercapacitors with high power density and energy density. To date, however, relationships between solvent properties and device performance are poorly understood, largely due to practical scope limitations. With nanoscale materials that push the known limits of energy and power density, it is easier to conceive of interesting electrolytes than rigorously synthesize, characterize, and fully understand the property-performance relationships relevant to device design. Most electrochemical studies[28,30] select acetonitrile or a carbonate-based solvent such as propylene carbonate and comparatively little work has been done to thoroughly explore novel solvents[31,32] or understand connections between physiochemical properties of the solvent and electrolytes and device performance. Solvent selection appears to be a matter of what is on hand or what is traditionally used and less about what produces ionic liquid mixtures with optimal properties. This chapter encompasses a set of studies aimed at exploring these relationships using molecular simulation, neutron experiments, and a screening approach. We consider only one ionic liquid, 1-butyl-3-

methylimidazolium bis(trifluoromethanesulfonyl)imide ([$BMIM^+$][TF_2N^-]), but 22 unique (neutral) solvents (*vide infra*). Future studies, perhaps guided by enhancements in computational performance, may evaluate a greater set of ionic liquids as well.

The work included in this chapter encompasses several manuscripts, two of which have been been published in peer-reviewed journals,,[2,3] two more that are currently in review,[4,5] and another that is in the early stages of preparation.

4.2 Methods

4.2.1 Scope of Study

The initial set of systems investigated how cation diffusivity was impacted by two mixture properties: solvent concentration and chemical identity of the solvent. Four mixtures were used to study each trend, for a total of seven unique physical statepoints (one system covered both).

Ionic liquid were dissolved in four solvents: acetonitrile (ACN), dichloromethane (DCM), methanol (MeOH), and tetrahydrofuran (THF). These solvents are all polar (ionic liquids tend to phase separate in non-polar species[33–37]) but represent a range of physiochemical properties, summarized in Table 4.1. The same ionic liquid, 1-butyl-3-methylimidazolium bis(trifluoromethanesulfonyl)imide ([$BMIM^+$][TF_2N^-]) was used throughout and the composition was held fixed at 0.50 mass fraction in order to best compare across solvents of different sizes. Additionally, four mixture concentrations (0.25, 0.50, 0.75, and 1.0 mass fraction ionic liquid) in acetonitrile were considered to examine the effect of composition alone. Identical systems were used in experiments and simulations.

Table 4.1: Solvents used in the first study and some physical properties. The same four solvents were used in MD simulations and QENS experiments.

Solvent	**Abbreviation**	**Dipole moment, Debye**	**Dielectric constant**
Acetonitrile	ACN	3.92	37.5
Methanol	MeOH	2.87	32.7
Tetrahydrofuran	THF	1.75	7.58
Dichloromethane	DCM	1.60	8.93

A second set of systems, studied with molecular simulations only, is summarized below and described in detail *vide infra*.

Table 4.2: Solvents used in the expanded study and some physical properties.

Solvent	**Dipole moment, Debye**	**Dielectric constant**
Acetonitrile	3.92	37.5
Butyronitrile	69.12	20.7
Adiponitrile	3.76	
Benzonitrile	4.18	26
Methanol	1.69	32.7
Ethanol	1.69	24.5
Butanol	1.66	17.8
Octanol	1.76	10.3
Dichloromethane	1.60	8.93
1,2-dichloroethane	0.87	10.36
Chlorobenzene	1.60	
Ethylene carbonate	4.81	95.3
Propylene carbonate	4.94	64
Acetone	2.91	20.7
Cyclohexanone	2.90	18.2
Dimethylsulfoxide	3.96	46.7
N,N-dimethylformamide	3.86	36.7
Dimethylacetamide	3.72	37.8
Tetrahydrofuran	1.63	7.58
Glyme	2.68	42.5
Diglyme		
1,4-Dioxane		2.2

4.2.2 Force Fields

Throughout this chapter, ionic liquid molecules were described with the popular CL&P force field of Canongia Lopes & Pádua *et al.*.[38–40] This force field was derived from the even more popular OPLS-AA force field of Joregensen and many co-workers[41–43] which largely reproduces many physical properties of organic molecules. This design choice of the CL&P authors allows it to stand on the shoulders of giants; by using common functional forms and matching parameters when chemically sensible, the two force fields can be mixed - applied to separate components in a single system - with reasonable confidence in the accuracy of the resulting properties. We chose to do just this; all solvent molecules were described with the OPLS-AA force field and the cross-interactions between them and ionic liquid molecules were inferred by GROMACS according to traditional Lorentz–Berthelot mixing rules.[44,45] For all simulations, partial charges on ionic liquid molecules were scaled by a factor of 0.8.[46]

4.2.3 Classical Molecular Dynamics Simulations

As this story has evolved, two sets of molecular dynamics simulations were collected. In the first part, atomistic classical molecular dynamics (MD) simulations of bulk of ionic liquid mixtures were performed in the software package GROMACS 5.1.[47] Initial configurations were generated via PACKMOL[48] For each system, the initial cubic box length was 7 nm. 200 ion pairs of $[BMIM^+][TF_2N^-]$ were added and then solvent molecules were added such that that mass fraction of ionic liquid in each box was 0.50. Ionic liquid concentrations and final box sizes are summarized in Table 1. Steepest-descent energy minimization was performed for 1000 steps to relax any initial unfavorable interactions as PACKMOL does not include energetic considerations. Then, NPT simulation was performed for 30 ns with a 1 fs timestep. The reference temperature and pressure were 300 K and 1 bar, respectively. Temperature was controlled with the v-rescale thermostat and pressure was controlled with the Berendsen barostat. Data was sampled from the final 10 ns of each trajectory, ensuring that only equilibrium states were sampled. Diffusion coefficients were

calculated via the 3-D mean-square displacement relationship using GROMACS's built-in tools as <r2> = 6Dt. Selections of the solvent, total IL, and cation were considered.

In the second set of simulations, each followed a similar routine with small differences minimal enough to not be expected to affect the interpretation of the results. The same force fields as before were used, system sizes were similar, and systems were controlled with the same reference temperature and pressure of 300 K and 1 bar. The barostat was changed to Parrinello-Rahman, 2000 steps of energy minimization were performed, and a more rigorous equilibration routine was added. Previously, there were no issues with vapor-liquid equilibria expanding the box to a gas phase, so a single *NPT* simulation was sufficient. Here, to keep these systems in the liquid phase during equilibration, we began with a 100 ps *NVT* simulation followed up by a 1 ns simulation at 10 bar and then a a 1 ns simulation at 1 bar. Finally, the production run remained at 30 ns in length but a timestep of 1.5 fs was used and the entire trajectory was used in statistical analysis (instead of only the final 10 ns).

4.2.4 Free Energy Calcuations

Two sets of free energy calculations were carried out as part of this story. Both attempt to reconstruct the same free energy profile but employ different methods. Free energy methods, in general, attempt to calculate the free energy associated with a thermodynamic transition across some reaction coordinate. This reaction coordinate can be a simple variable such as intermolecular distance or an arbitrarirly complex set of collected variables. In this case our reaction coordinate is the intermolecular separation of a single cation and a single anion in solvent at infinite dilution. This characterizes the thermodynamics of ion dissociation in solution, or equivalently, the solvation energy of this ionic liquid in solvent.

The first set of calculation uses the weighted histogram analysis method WHAM[49,50] method to determine a free energy profile. First, a set of configurations along the path of the reaciton coordinate must be generated; in this case that means a set of configurations in which a single ion pair is separated by different distances, from directly in contact (center-of-mass spacing of

approximately 0.5 nm) to sufficiently large distances that their interactions have decayed to small values. For most molecluar models approximately 2-3 nm is considered sufficient as it exceeds the cutoff values of typical pair potentials. The pull code in GROMACS 5.1[47] was used to generate the discrete configurations starting from two ions in a paired state to 3.5 nm in separation. At each of these configurations, a spring along the reaction coordinate was used to bias the configurations in place during short sampling simulations. From each of these simulations, histograms of frequency along this path were generated; in this case that corresponds to histograms of interatomic positions. The `wham` module within GROMACS was used to collect these histogram and invert them into a free energy profile.

A second of free energy calculations used the recent Accelerated Weight Histogram (AWH) method of Lidmar *et al.*[51] as implemented in GROMACS by Lindahl *et al.*.[52] AWH builds on the same principles of WHAM but is both more robust and simpler to implement. Instead of building set of N discrete configurations, applying springs to bias each configuration in place, and sampling from these N simulations, AWH involves running only one simulation. AWH adaptively guides the simulation along the reaction coordinate, generating the free energy profile on-the-fly and periodically directing the system toward under-sampled regions. Note that while traditional WHAM simulations involve many simulations with different springs, these springs typically have the same force constant. Effectively, AWH does in a single long simulation what WHAM alone would take tens or perhaps hundreds of shorter simulations. This is not necessarily an inherently cheaper method, but in practice can be much cheaper by more intelligently sampling the thermodynamic space.

4.3 Experimental Methods

4.3.1 Quasi-Elastic Neutron Scattering

Quasi-elastic neutron scattering (QENS) experiments were conducted by Naresh C. Osti and Eugene Mamontov of Oak Ridge National Laboratory (ORNL). These experiments utilized the

BASIS backscattering spectrometer[15] at ORNL. The scattering of neutrons are particular sensitive to hydrogens, moreso than other atomic species. The selected ionic liquid anion contains no hydrogens but the cation contains many. In order to isolate the behavior of the cations, deuterated solvents were used.

In short, QENS experiments involve directing a neutron beam at a sample and detecting the scattered neutrons. In the regime of the so-called elastic approximation, there is a small amount of energy transferred to the sample. The amount of energy can be computed from differences in the wave vectors of the scattered neutrons, as measured from the detector, and incoming neutrons. The frequency, of scattered neutrons, as a function of energy gained or lost during scattering can be used to back out diffusivities of the sample using Lorentzian fits. QENS is commonly used for studying slow dynamic processes in viscous fluids but is particularly useful compared to other methods, i.e. NMR, because it can detect molecular motion in confined systems.

Table 4.3: Solvents used in the second set of QENS experiments and some physical properties. Note these are a subset of the solvents used in the computational screening study, see Table 4.2.

Solvent	**Abbreviation**	**Dipole moment, Debye**	**Pure solvent diffusivity,** $10^{-10}\mathrm{m}^2\,\mathrm{s}^{-1}$
dichloromethane	DCM	1.60	15.7
octanol	Octanol	1.68	0.4
butanol	BuOH	1.66	2.7
tetrahydrofuran	THF	1.75	8.5

4.3.2 Ionic Conductivity Measurements

Conductivity experiments on the same samples were conducted by Katherine L. Van Aken of Drexel University. Conductivity of the [$BMIM^+$][TF_2N^-] in four solvents was measured using an EP357 Conductivity isoPOD (eDAQ, USA) which was first calibrated with a $0.1\,\mathrm{mol\,dm^{-3}}$ solution of KCl. The different concentrations of [$BMIM^+$][TF_2N^-] in each four solvents were determined by calculating mass fraction [$BMIM^+$][TF_2N^-] in a total solution volume of 0.75 mL.

Table 4.4: Summary of cation diffusivities as predicted by QENS and MD.

Solvent	D_{MD}	D_{QENS}
Acetonitrile	9.367	11.8
Methanol	7.764	6.39
Tetrahydrofuran	3.414	5.12
Dichloromethane	3.396	2.99

Representative snapshots of MD systems are provided in Fig. 4.1 and Fig. 4.2.

4.4.1 Concentration-Dependent Ion Dynamics

We first consider the relationship between mixture composition and ion diffusivities. Our results indicate that cation diffusivity depends strongly and monotonically on mixture composition. A summary, including results from both MD simulations and QENS experiments, is presented in Fig. 4.3. Cation diffusivity is greater in all mixtures than in a neat ionic liquid and and increases smoothly as the composition of ionic liquid decreases. We interpret this on the basis that solvents disrupt the strong ion-ion interactions that produce slow dynamics, allowing for greatly enhanced ion mobility. There is also some contribution from the simple nature of a solute diffusing in a solvent medium (small organic solvents) that is more mobile than another (bulky ionic liquids).

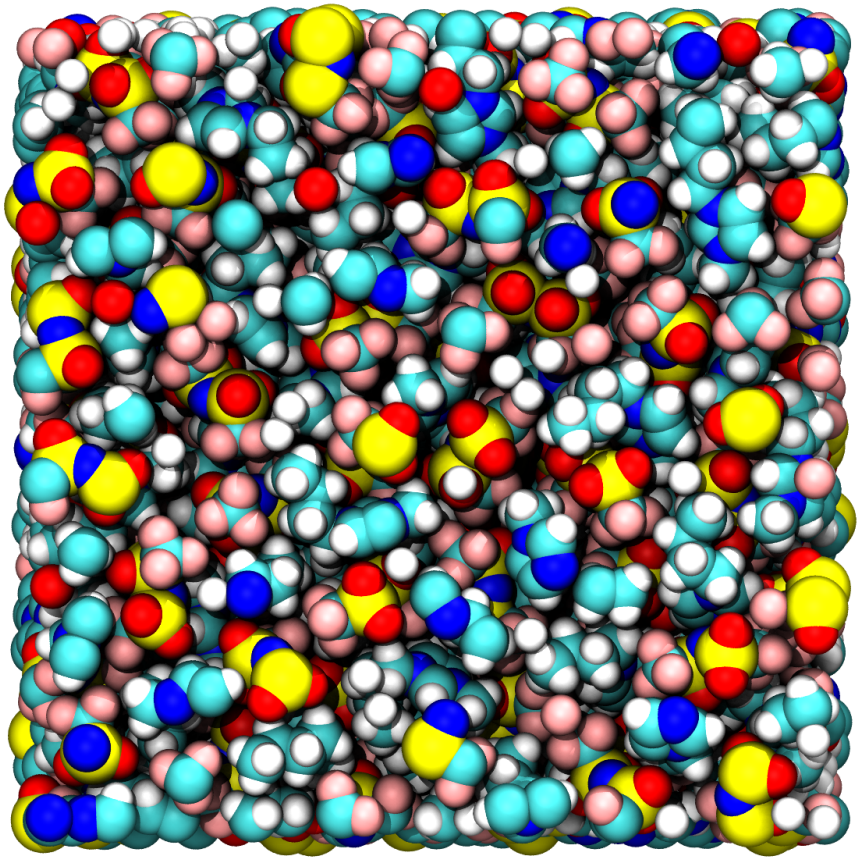

Figure 4.1:]

Representative snapshot of bulk [$BMIM^+$][TF_2N^-] rendered using Visual Molecular Dynamics (VMD).[53,54] The cubic box is approximately of length 4.6 nm. Atoms are drawn with spheres scaled approximately to their Van der Waals radii. Colors roughly follow traditional CPK coloring: hydrogen (white), carbon (cyan), nitrogen (blue), oxygen (red), fluorine (pink), sulfur (yellow).

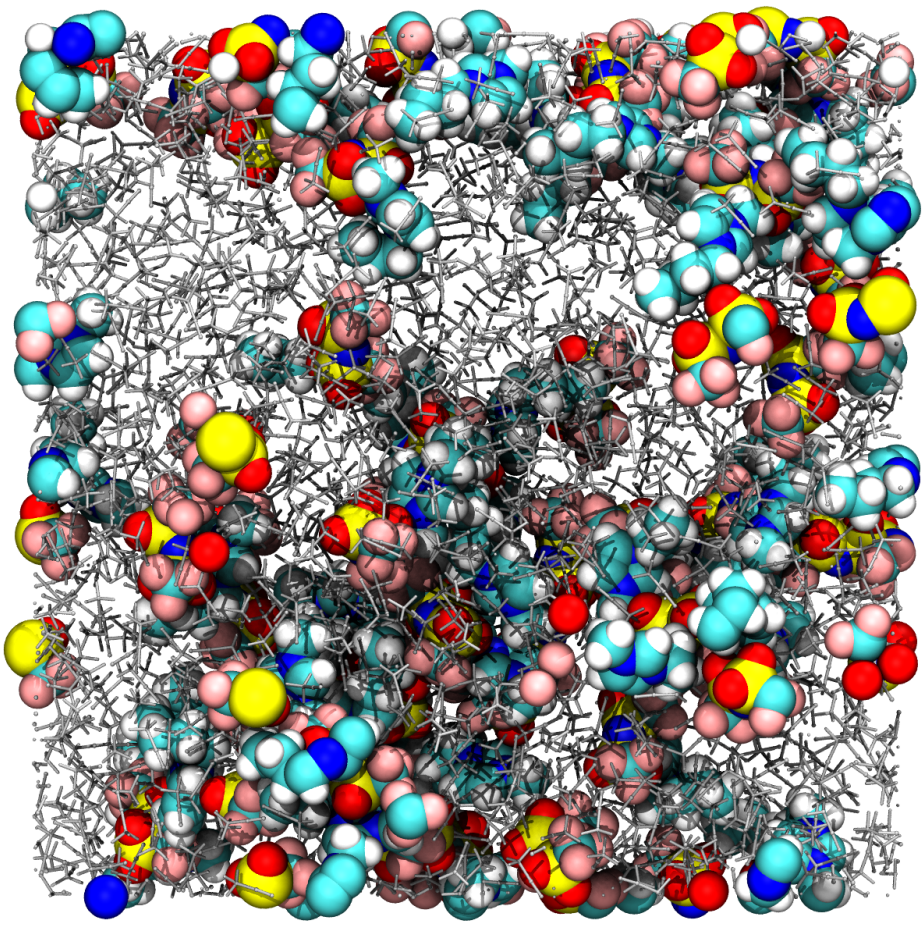

Figure 4.2: Representative snapshot of [$BMIM^+$][TF_2N^-] solvated in acetonitrile at an ionic liquid mass fraction of 0.25. Box lengths are approximately 5.4 nm. Ionic liquid molecules are represented the same as in Fig. 4.1 but, to highlight the structure of the ionic liquid molecules, solvent molecules are drawn with thin silver cylinders representing their bonds.

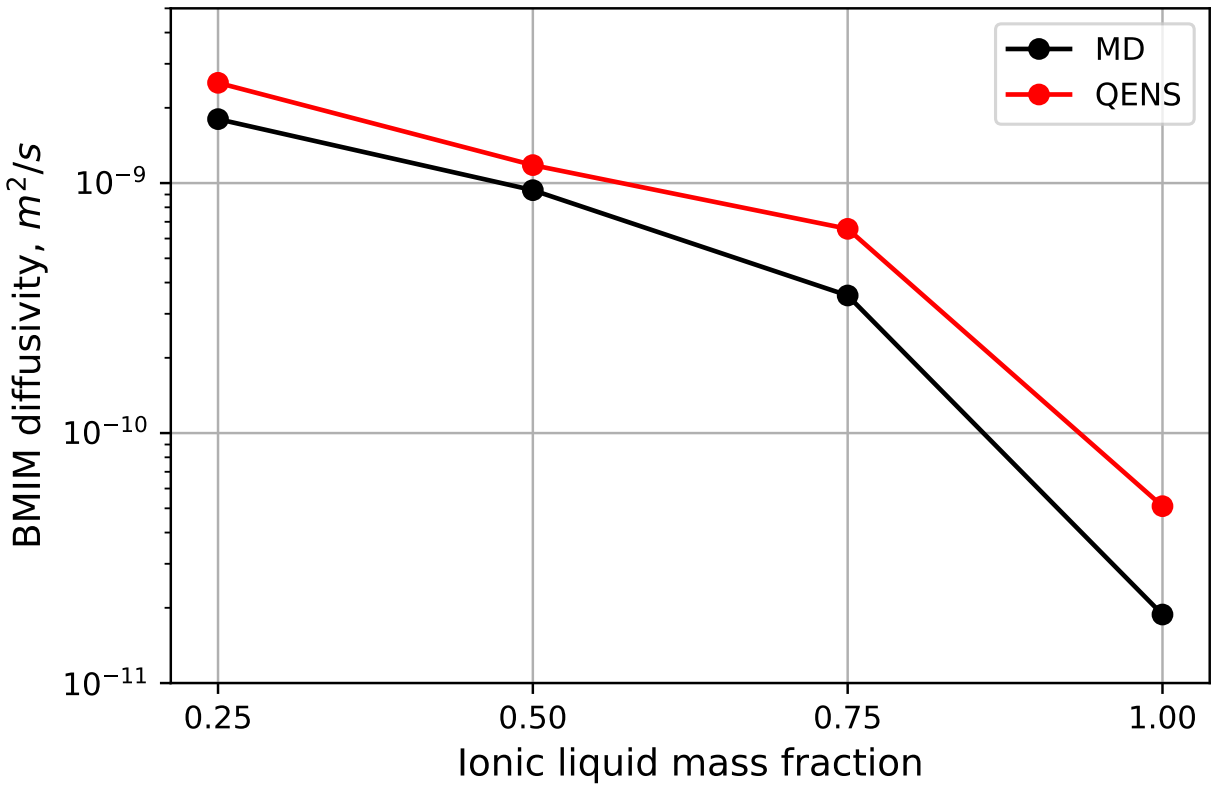

Figure 4.3: [BMIM$^+$] diffusivity in acetonitriles as a function of ionic liquid composition, as predicted by MD (black spheres) and measured by QENS (red spheres).

4.4.2 Solvent-Dependent Ion Dynamics

In an attempt to determine how to best promote ion mobility via selection of solvent, we also investigated how solvation in each of the four solvents affects ion dynamics. It is not generally useful to plot a smooth, continuous variable against a categorical variable, so we selected a solvent property in order to investigate possible trends. We chose the polarity of the solvent, measured by the dipole moment in units of Debye. Fig. 4.4 shows cation diffusivity in these four solvents as a function of the dipole moment of the solvent, using reference values. With this available data, it was concluded that solvent polarity governs ion mobility in these mixtures. We hypothesize that, similar to concentration effects, this is because solvents of greater polarity are more capable of screening the coulombic interactions between ions, freeing them up to diffuse in a more mobile manner.

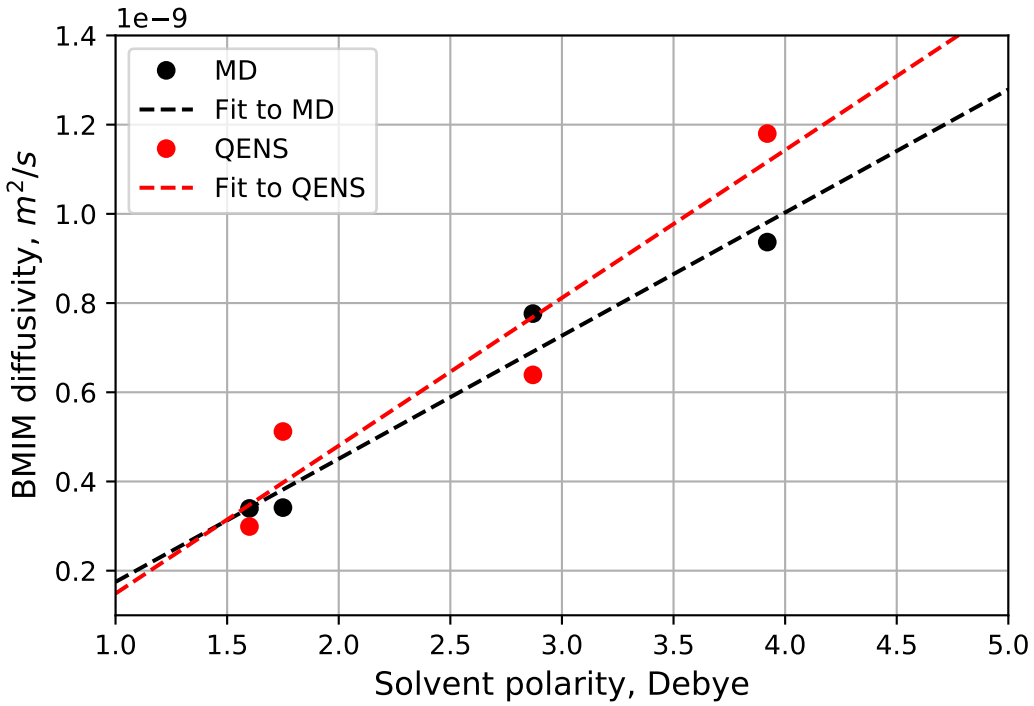

Figure 4.4: [BMIM$^+$] diffusivity in select solvents at 0.50 mass fraction, as predicted by MD (black spheres) and measured by QENS (redspheres). Dashed lines indicate linear fits to each set of data.

4.4.3 Free Energies of Ion Solvation

In order to understand these trends, we turned to free energy calculations. The WHAM method was used to generate potentials of mean force (PMFs), which in this case attempt to describe the free energy associated with interatomic separation. Studying free energy along this reaction coordinate is a viable proxy for thermodynamics of solvation and desolvation. The same force fields used in the bulk simulations were used here. The systems, however, included only a single ion pair in order isolate the effect of solvent and not the interactions with other ions. These PMFs, up to a separation of 3 nm, are shown in Fig. 4.5. There is a clear correlation between energy barriers and ion dynamics; solvents with lower solvation energies produce mixtures with greater ion diffusivity. From lower to greater cation diffusivity, the order of solvents is THF ~DCM < MeOH < ACN and from and from higher to lower energies the order is DCM > THF > MeOH > ACN. These results provide thermodynamic data supporting the hypothesis that screening ion-ion interactions is responsible for the enhancement of ion mobility in organic solvents.

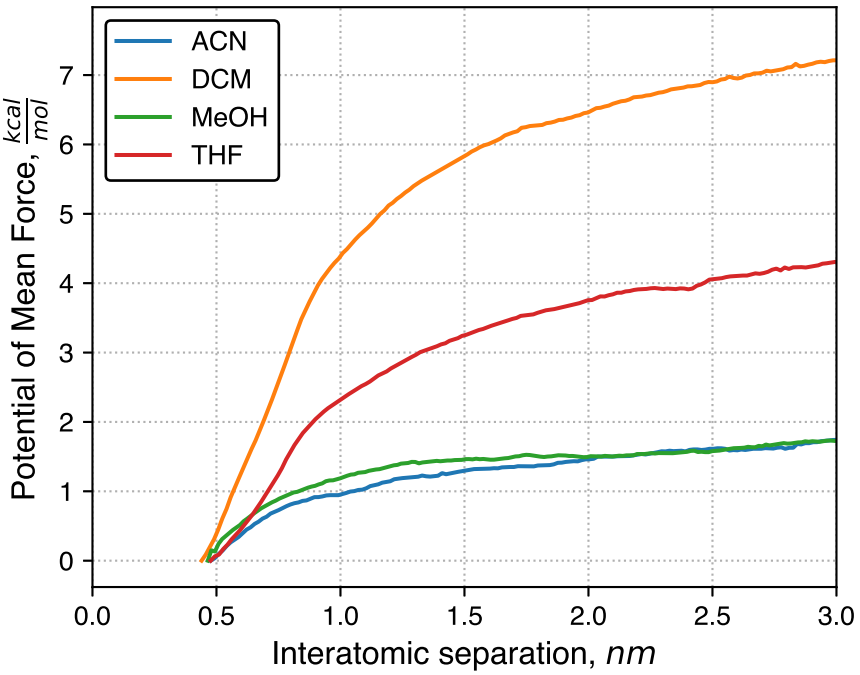

Figure 4.5: Free energy profiles, expressed as potentials of mean force (PMFs), as a function of the cation-anion, derived from MD simulations. A single [$BMIM^+$][TF_2N^-] ion pair was mixed in each solvent at infinite dilution. The energy scale is defined such that the minimum energy is zero. The energy associated with separating an ion pair correlates with the dipole moment of the solvent.

4.5 Results of Computational Screening

A limitation of the above work is the small scope of study. While the trends were smooth and consistent with a reasonable physical interpretation, each conclusion was drawn from a limited (4) number of samples. This is common in science given the cost of collecting large amount of data. It is useful, whenever possible, to interrogate observed physical phenomena by gathering more data and evaluating whether or not prior trends hold true.

There has been a major push in the past few years to move molecular simulation toward automated screening. Many scientific findings are improved by finer stepping-through within a parameter space and replacing discrete, disparate points in this parameter space with smoother curves. This is especially true for chemistry given the vastness of the possible physical statepoints in chemical space. While this sort of grand screening is difficult to do in most experimental probes (at best, most systems experiments have a linear scale-up of cost as a function of statepoints, although some

fields have made use of robots to challenge this) there are fewer fundamental limitations for the automated screening of this space to be done with computational models.

The portion of chemical space encompassed by systems containing ionic liquids is vast and largely unexplored. The number of neat ionic liquids - those with one cation, one anion, and no other components - was estimated on the order of billions almost two decades ago[55] and estimates of as high as 10^{18} have been suggested.[56] Consideration of mixtures of ionic liquids with other ionic liquids or solvents grows this figure by many orders of magnitude.[56] Unsurprisingly, most existing literature, even review papers, covers an extremely small subset of this space. The scale of this problem necessitates computational approaches; even modest ventures into this space are not feasible to do with experiments alone. Synthesis at high purities can be difficult for ionic liquids, especially novel ones, and to date, only a small fraction of possible ionic liquids have been synthesized at all. Additionally, the amount of characterization necessary to understand their structure, dynamics, and thermodynamics via experiments is virtually intractable. Computational screening can provide preliminary searches through this space, providing predictions of molecular and macroscopic physical properties that experiments can later examine. Efforts in this direction have already begun.[57–61]

To accomplish this screening approach for our solvent systems, we have employed the Molecular Simulation and Design Framework (MoSDeF) software suite.

4.5.1 Revisiting Concentration-dependent Ion Dynamics

Bulk diffusivities were computed from mean squared displacements (MSDs) using the same Einstein relation used above. It is useful to evaluate individual components of each system. Therefore, in addition to the mixture as a whole, we consider the solvent, each ion, and the overall ionic liquid as selections. We previously isolated cation dynamics from our molecular dynamics simulations because the QENS experiments exclusively track the cations (the $[TF_2N^-]$ anion has no hydrogens but the $[BMIM^+]$ cation has several). For the case of $[BMIM^+][TF_2N^-]$, which was used in both that study and this one, the cation and anion exhibit nearly identical bulk diffusivities.

Therefore, the cation, anion, and overall ion dynamics can be interpreted interchangeably with each other, though this relationship should not be regarded as a general feature of ionic liquids. Here we will consider the overall ion dynamics.

Two diffusivities were computed for each selection: one from an MSD of the entire 30 ns trajectory and another when slicing it into 20 sections, each 1.5 ns slice comprising a shorter MSD, and averaging the diffusivities from each slice. This was done to gather statistics on the sampling error for each diffusivity. The two methods produce similar results and are further discussed in the Appendix.

First, we revisit one of the two major conclusions of our prior work, which is a monotonic increase in cation diffusivity as the composition of solvent is increased. This result is consistent with intuition given the slow dynamics of neat ionic liquids relative to the pure organic solvents, but the structural and energetic complexity of these interactions should cast doubt on how strongly such physiochemical relationships should hold. That being said, we observe, using our larger parameter set, the same trend as before, summarized in Fig. 4.6.

It is worth noting that this trend is monotonic over the entire composition range, and no plateaus or discontinuities are obesrved. Given the tendency for many ionic liquids to phase separate into nanostructural domains[62–64] in neat and in polar solvents and completely phase separate in non-polar species,[33–37] this observation implies that the transition from dilute ions and/or ion pairs to neat ionic liquids is smooth and lacks any discontinuous transition, i.e. there is no critical composition at which pairs move from dense ionic liquid phases to dissociated ion pairs. Chemical intuition would suggest polar solvents are better than non-polar solvents at dissolving ionic liquids and these results support that idea.

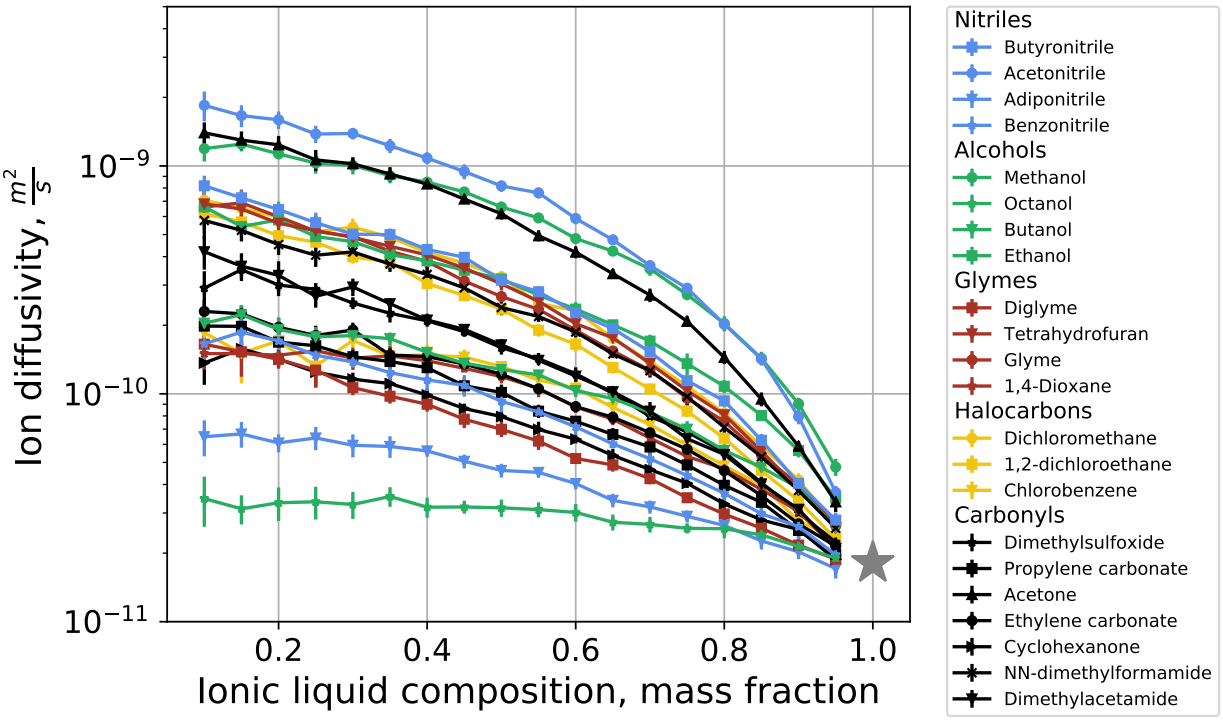

Figure 4.6: Ion diffusivity as a function of mixture composition. Mixtures are grouped by the chemical family of the solvent, which is used to color the lines and markers. Error bars are included as vertical lines, though many are smaller than the width of the dots. Straight line segments are drawn connecting data points with common solvents. The grey star indicates the diffusivity of the neat ionic liquid.

4.5.2 Revisiting Solvent-Dependent Ion Dynamics

Next, we revisit the relationship between solvent polarity and ion diffusivity that was the focus of our prior study.[2] Previously, we considered acetonitrile, methanol, dichloromethane, and tetrahydrofuran and found that solvents with greater solvent polarity produced mixtures that exhibited greater ion diffusivity. A more rigorous summary of our larger data, which considers 22 solvents, set is presented in Fig. 4.7.

While a general trend of increasing solvent polarity as a function of dipole moment is observed for subsets of the data, there exists no strong correlation when considering the entire data set. One could isolate the solvents we previously used as see they do not generally follow the same trend as this data set. Mixtures with acetonitrile (D = 3.92) exhibited the largest diffusivity of all solvents, but mixtures with DMSO (D = 3.96) and propylene carbonate (D = 4.94) each exhibited slower diffusivity than acetonitrile despite their similar and higher molecular dipole moments, respectively. Further, mixtures with methanol (D = 2.87 D) and acetone (D = 2.91 D) exhibited high diffusivity with lower polarity. These results imply that solvent polarity is not the only contribution to ion transport in ion liquid mixtures and in order to better inform design of ionic liquid mixtures with enhanced transport properties, other solvent properties must be considered.

Note that solvent polarity is only one solvent property; others could be better predictors of the properties of ionic liquid-solvent mixtures. We first chose to look at a simple solvent property, molecular weight, for the possiblity it correlates better with ion diffusivity than polarity. Shown in Fig. 4.8, this relationship appears to be much stronger: solvents with greater molecular weight tend to produce mixtures with slower ion diffusivity.

We next looked at correlations with the dielectric constant of the solvents. We used the built-in tools of GROMACS[47] to estimate the dielectric constants for each of the 22 unique solvents studied. Specifically, the dielectric constants are estimated by computing the dipole-dipole correlation function which determines the total dipole moment of the system.[65] Using the total dipole moment,

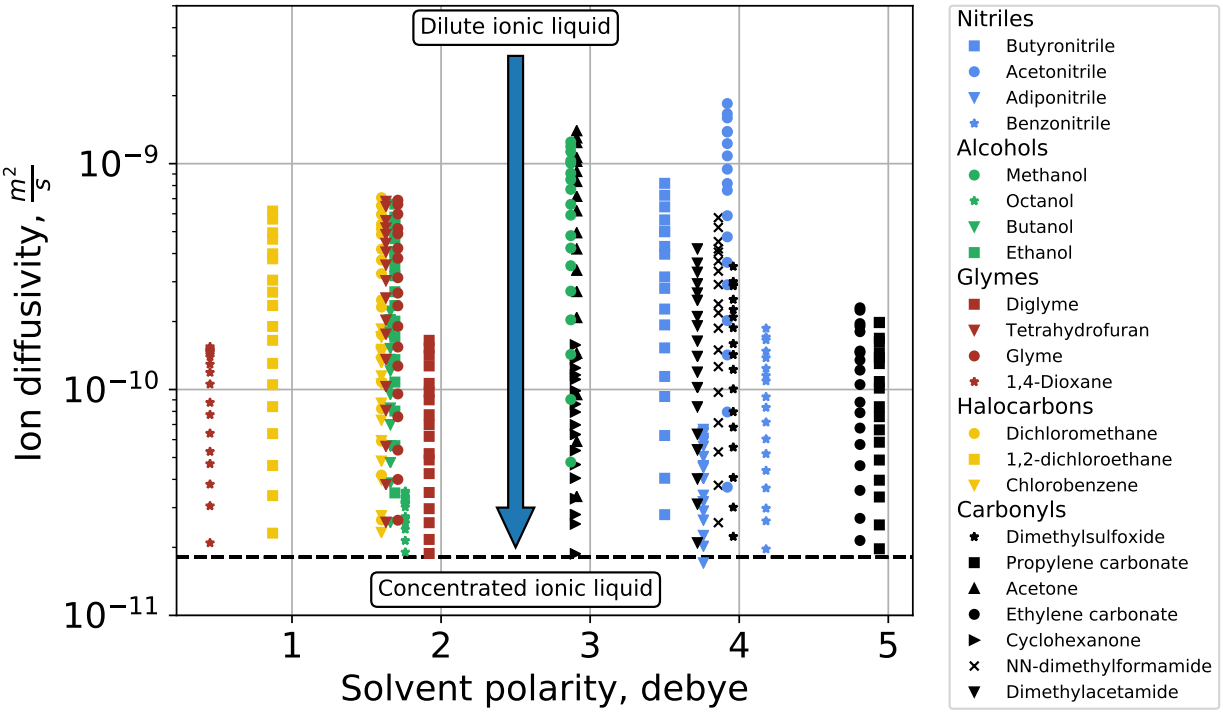

Figure 4.7: Ion diffusivity as a function of solvent polarity. Data points are arranged from top to bottom in order of increasing ionic liquid composition — for any species, the highest diffusivity corresponds to the most dilute mixture mixture and the lowest value corresponds to the most concentrated (0.1 and 0.95 mass fraction). The dashed horizontal line indicates the ion diffusivity of the neat ionic liquid.

the dielectric constants are calculated with the following equation:

$$\frac{\varepsilon - 1}{3}\frac{2\varepsilon_{rf} + 1}{2\varepsilon_{rf} + \varepsilon} = \frac{\langle M^2 \rangle}{9\varepsilon_0 V k_B T} \tag{4.1}$$

where ε_0 is the vacuum permittivity, V is the volume, k_B is Boltzmann's constant, T is temperature, $\langle M^2 \rangle$ is the total dipole moment, and ε_{rf} is the dielectric permittivity of the continuum. Ion diffusivities are plotted as a function of solvent dielectric constants in Fig. 4.9. A stronger trend than other solvent properties is observed.

Next, we investigated the relationship between ion diffusivity and solvent diffusivity, computed from pure solvent simulations. In Fig. 4.10, we observe a more robust trend between ion diffusivity D_{ion} and pure solvent diffusivity $D_{solvent}$. Note that these solvent diffusivities are extracted from independent simulations of pure solvent, not the solvent component of the ionic liquid mixture simulations. This result is intuitively reasonable; sluggish ionic liquid molecules are more likely to exhibit increased molecular diffusivity in an environment of molecules with faster motion. The results are consistent with a Stokes-Einstein picture of ion mobility. According to Stokes-Einstein theory, D_{ion} should scale as the inverse of the solvent viscosity $\eta_{solvent}$ - i.e., $D_{ion} \sim \eta_{solvent}^{-1}$. However, liquid diffusivity generally scales inversely with viscosity, so in particular for these solvents, $D_{solvent} \sim \eta_{solvent}^{-1}$, thus leading to $D_{ion} \sim D_{solvent}$, as we observe from the simulation results.

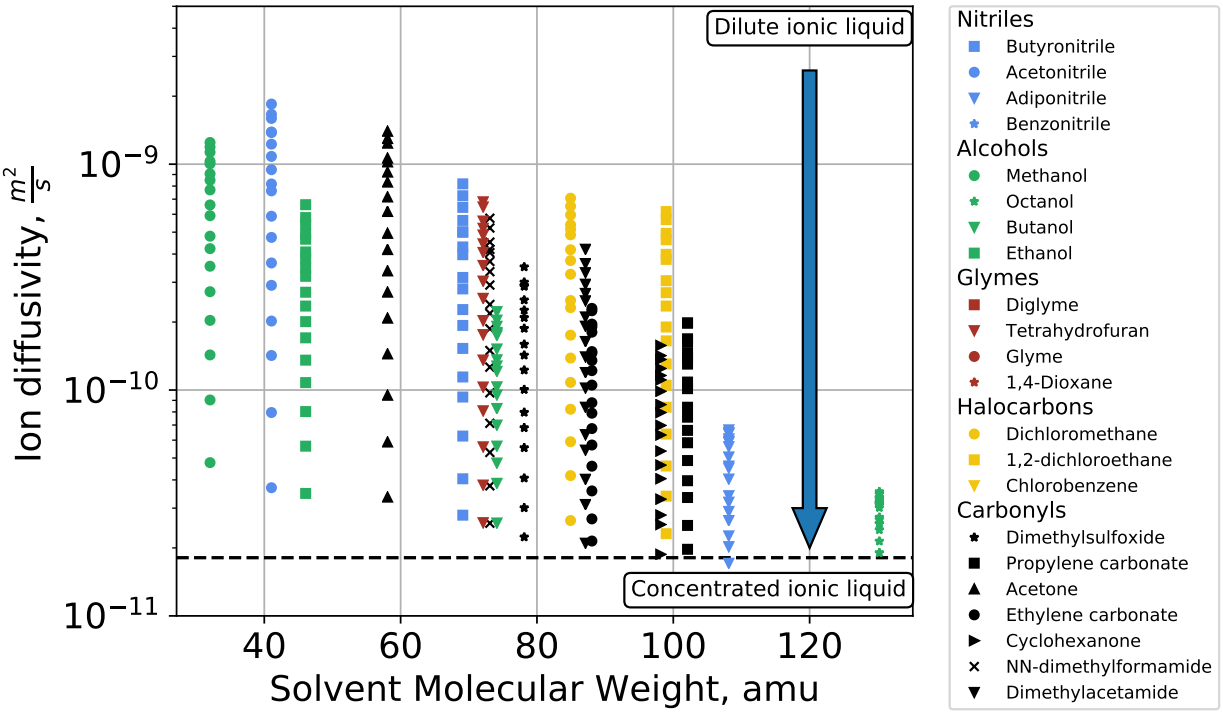

Figure 4.8: Ion diffusivity as a function of solvent molecular weight. Data points are arranged from top to bottom in order of increasing ionic liquid composition. The dashed line indicates the ion diffusivity of the neat ionic liquid.

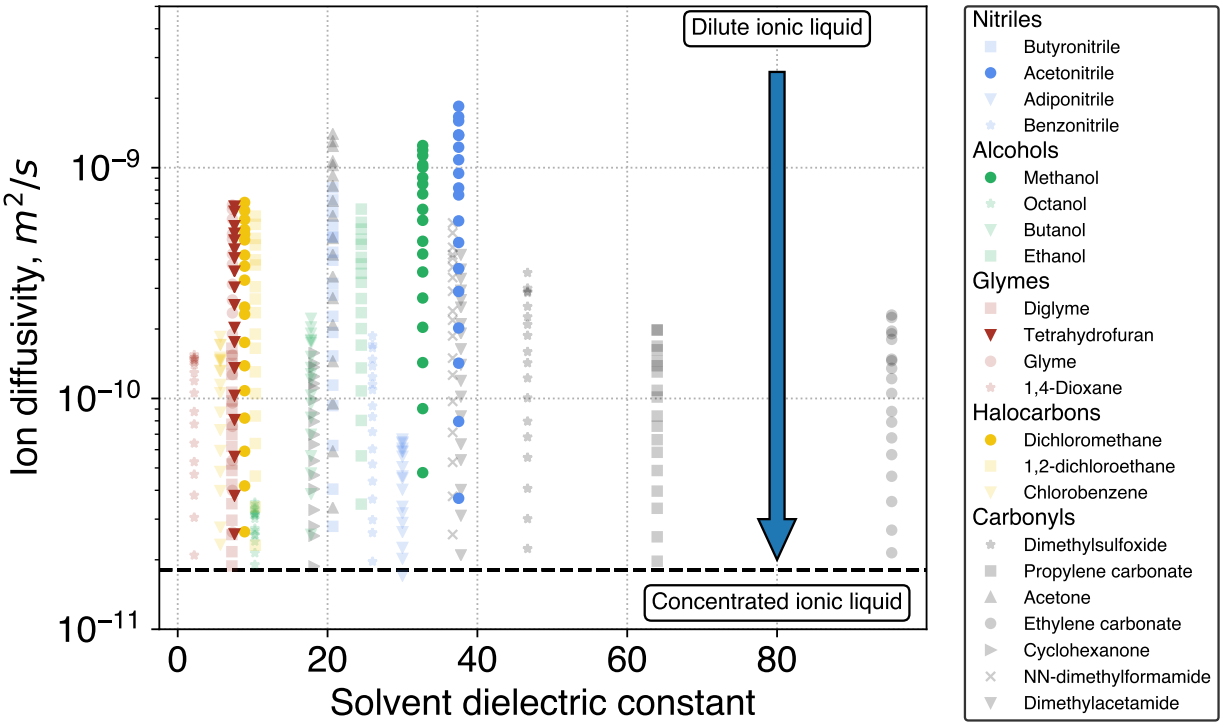

Figure 4.9: Ion diffusivity as a function of solvent dielectric constant. Data points are arranged from top to bottom in order of increasing ionic liquid composition — for any species, the highest diffusivity corresponds to the most dilute mixture mixture and the lowest value corresponds to the most concentrated (0.1 and 0.95 mass fraction). The dashed horizontal line indicates the ion diffusivity of the neat ionic liquid.

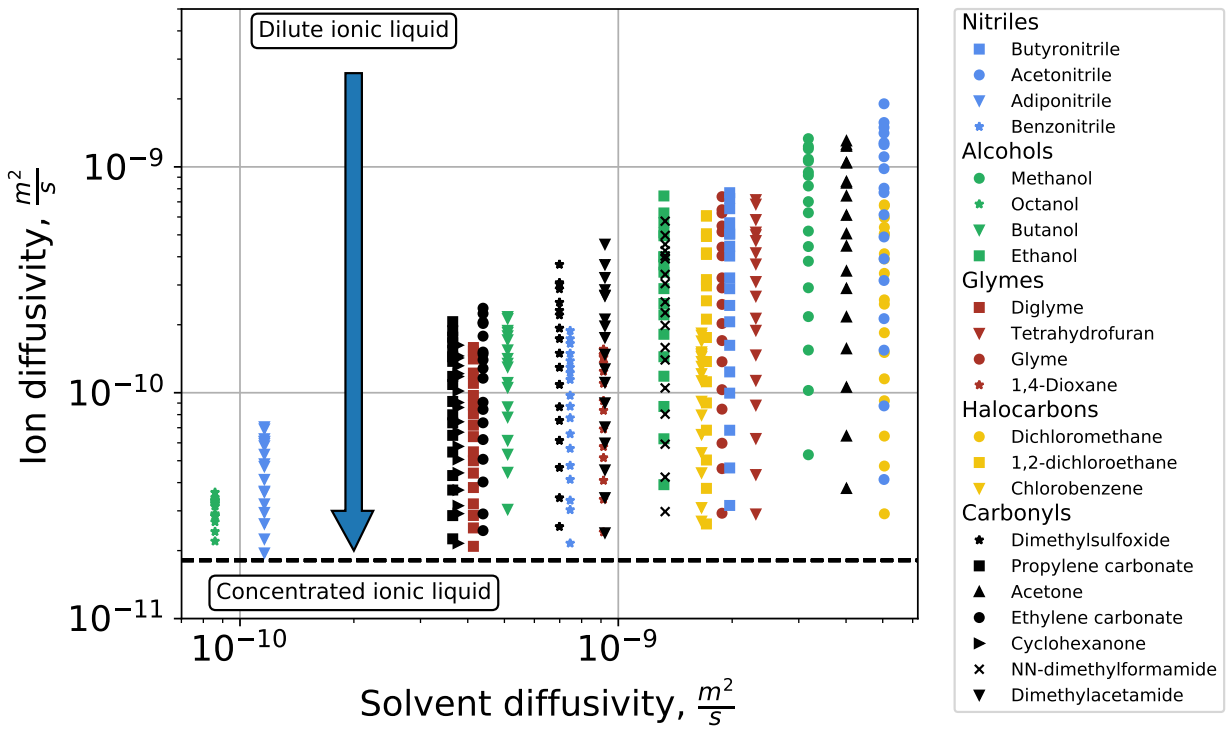

Figure 4.10: Ion diffusivity as a function of pure solvent diffusivity. Data points are arranged from top to bottom in order of increasing ionic liquid composition. The dashed line indicates the ion diffusivity of the neat ionic liquid.

4.5.3 Ionic Conductivity

Next, we consider the ionic conductivities of these mixtures in an effort to investigate how solvent properties impact bulk electrical performance. In accordance with previous works, we began by estimating the conductivity by using the ideal ionic conductivity as a proxy. This can be computed from known values via the Nernst-Einstein (NE) equation:

$$\sigma_{NE} = \frac{N}{k_B V T}(q_+^2 D_+ + q_-^2 D_-) \tag{4.2}$$

where N is the number of ion pairs, k_B is Boltzmann's constant, V is the volume of the system, T is absolute temperature, q_+, q_- are molecular charges and D_+, D_- the diffusivities of the positive and negative ions, respectively.

A more rigorous method for computing the ionic conducivity is the the Einstein-Helfand (EH) equation:

$$\sigma_{EH} = \frac{1}{6V k_B T} \lim_{t\to\infty} \frac{d}{dt} \langle [\vec{M}_J(t) - \vec{M}_J(0)]^2 \rangle \tag{4.3}$$

where translational dipole moment is defined as:

$$\vec{M}_J(t) = \sum_i q_i r_i(t) \tag{4.4}$$

and r_i is the center of mass position of ion i and q_i is the charge of ion i. Furthermore, $\langle [\vec{M}_J(t) - \vec{M}_J(0)]^2 \rangle$ is equal to $\frac{\sum_i [\vec{M}_J(t) - \vec{M}_J(0)]}{N}$. Unlike the NE equation, the EH equation considers the effects of correlated ion motions on conductivity..[66–69] Where σ_{NE} can be thought of an ideal ionic conductivity, it is reasonable to consider σ_{EH} a more direct measure of ionic conductivity, i.e. what would be measured in an experimental setup. Nonetheless, NE is a sufficient approximation to use for the purpose of qualitatively evaluating trends and is commonly employed in the literature.[10,70,71]

A summary of the relationship between ideal ionic conductivity and mixture composition is presented in Fig. 4.11. In agreement with prior works, including our own,[2] the maximum con-

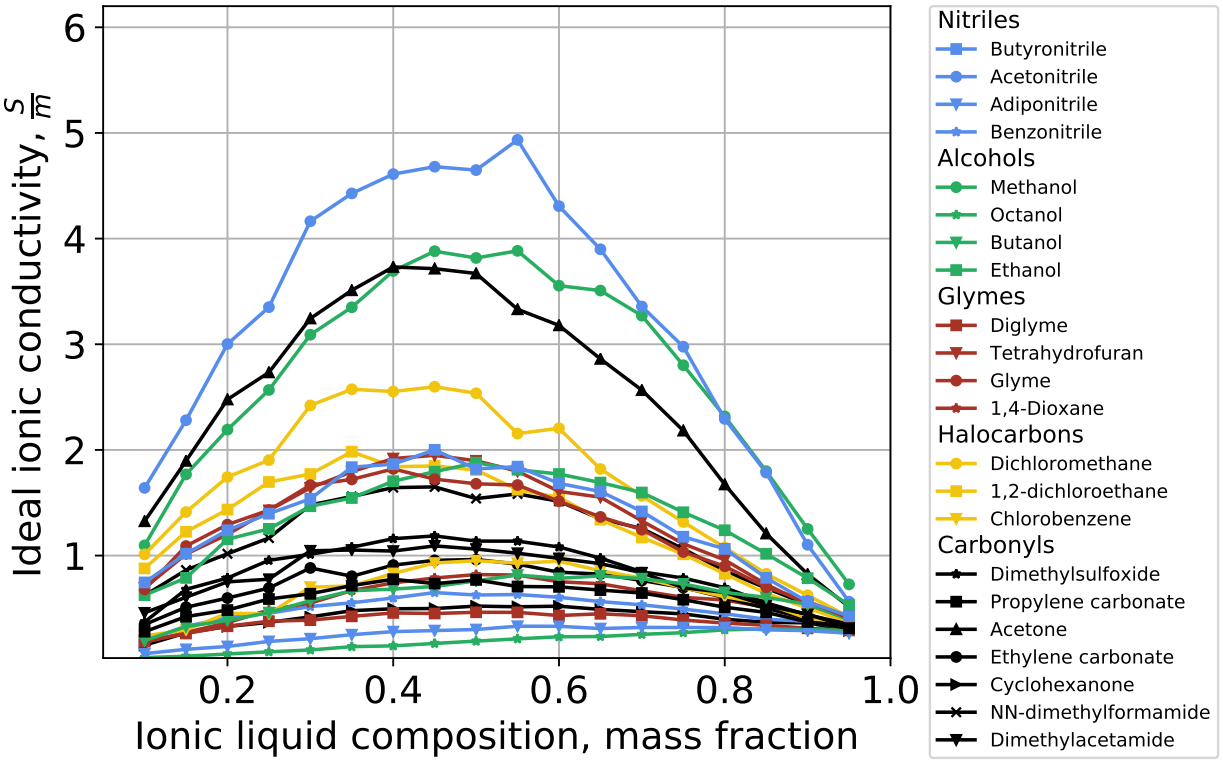

Figure 4.11: Ideal ionic conducivity as a function of ionic liquid composition. Ideal ionic conductivity is highest at intermidate ionic liquid compositions.

ductivity is observed at intermediate compositions. This is due to the counterplay between faster ion dynamics resulting from greater solvation and, by definition, the decrease in ionic density that results in fewer charge carriers: neat ionic liquids exhibit moderate conductivity; however, in the limit of infinite dilution, ion dynamics approach bulk solvent dynamics, but the capacity to carry charge is inherently lost. In most solvents, conductivity maxima are observed near equimass compositions of ionic liquid and solvent. Notable here is that acetonitrile-based mixtures exhibit the greatest conductivity of any mixture over the entire range. This implies that acetonitrile should remain a popular solvent for electrochemical applications. However, these results indicate the existence of viable alternatives if acetonitrile is to be avoided.

Next, we look at the ionic conductivity estimated through the EH formalism, shown in Fig. 4.12. The noise in the data is a consequence of the calculation methods: NE is a per-molecule method that allows for averaging over each atom in the system whereas EH is a global measure of the

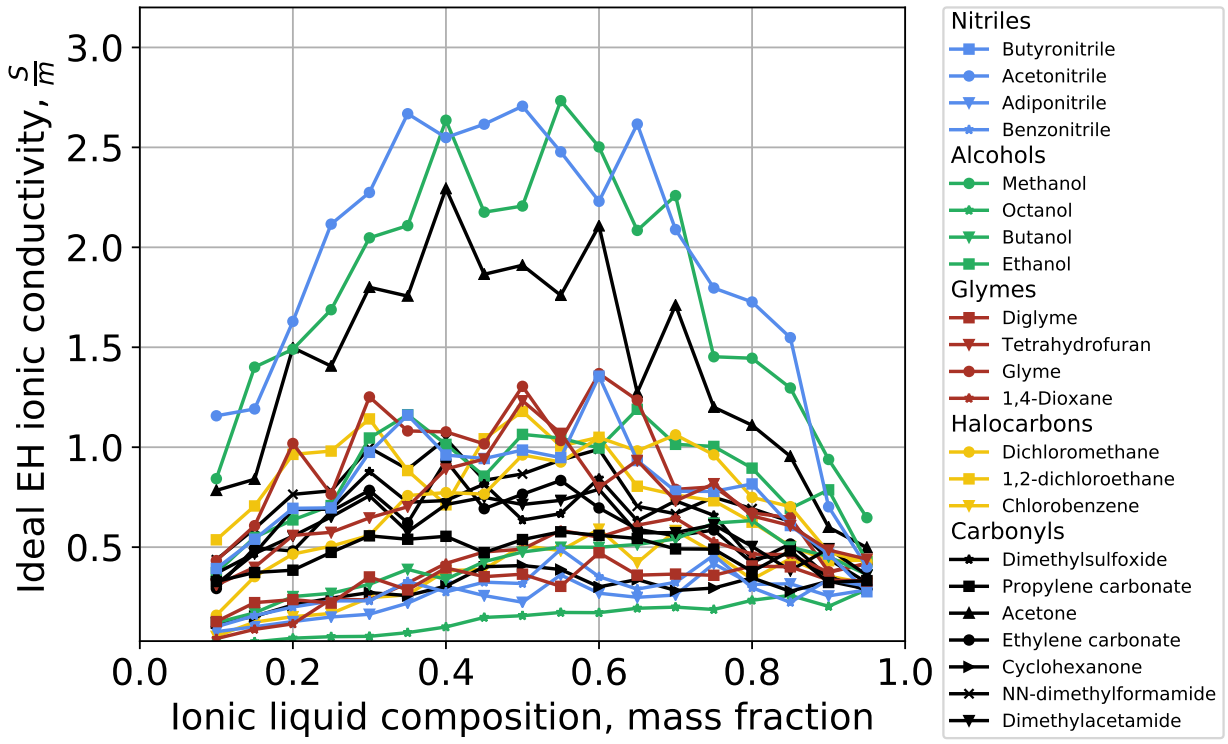

Figure 4.12: Einstein-Helfand conductivity as a function of ionic liquid composition. Like Nernst-Einstein, the Einstein-Helfand conductivity is highest at intermediate compositions.

entire systems and thereforce produces noiser statistics. The EH conductivities follow the same trend as NE conductivities with maxima located roughly in the range of 0.3-0.6 mass fraction [$BMIM^+$][TF_2N^-]. The solvent mixtures with the highest ionic conductivities as calculated by EH are those containing acetonitrile, methanol, and acetone. These are the same solvents that produced mixtures with the highest ideal ionic conductivity, as measured by NE earlier. While there are quantitative differences between these two methods, the qualitative conclusions are similar.

However, it can be useful to quantatively compare the methods using the ratio α, defined as

$$\alpha = \sigma_{NE}/\sigma_{EH} \tag{4.5}$$

where σ_{NE} and σ_{EH} are the conductivities calculated by Nernst-Einstein and Einstein-Helfand, respectively. Consistent with similar studies, this ratio is less than 1.0 for most systems; equivalently, $\sigma_{NE} > \sigma_{EH}$. The Einstein-Helfand formalism is considered more rigorous and is believed to

produce more accurate esimates of ionic conductivity, so we take NE conductivities as an overestimate. This error is typically attributed to the assumption that ion motion is decorrelated; see earlier discussions of ionicity as reported by both simulations and experiments. It is worth pointing out, despite the large amount of noise in this data, that some groupings according to the chemical families of each solvent. The lowest α values are obseved for some halocarbons (yellow) and glymes (red), implying ion pairing is stronger in these than other solvents.

There are a small number of mixtures in Fig. 4.13 with $\alpha > 1$. While this is not commonly observed in ionic liquids, Salanne *et al.* found it in viscious mixtures of the molten salts LiF and BeF_2.[69] They attributed this observation to cooperative motion as promoted by channel-like structures formed in the solvent. Rather than hindering their motion, this view implies that the correlated nature of ions can actually improve conductivity. Although the σ_{EH} data, and therefore α values, are somewhat noisy, it is evident that the most common cases of $\alpha > 1$ occur with two of the most viscous solvents, adiponitrile and diglyme. This is consistent with the interpretation of Salanne *et al.*, however, given the inherently slow dynamics of these mixtures it is difficult to take advantage of this effect in viscous solvents compared to solvents with lesser viscosity. This may be useful in other applications in which design contraints force the use of viscous solvents or it is desirable to have viscous solvents but higher ionic conductivity.

These conclusions from computational screening were evaluated by, and supported by, experimental conductivity measurements. A comparison between simulation predictions and experimental results for a subset of the studied solvents is presented in Fig. 4.14. We selected acetone, dichloromethane, and methanol, which were among the solvents that produced mixtures with the highest conductivity. The trends observed in experiment are consistent with our simulation results: a moderate composition of approximately 0.4 to 0.6 mass fraction ionic liquid produces mixtures with the highest conductivity. In addition, the relative conductivity of $[BMIM^+][TF_2N^-]$ in acetone, dichloromethane, and methanol at low mass fractions, derived from the computational studies, ($\sigma_{acetone} > \sigma_{methanol} > \sigma_{dichloromethane}$ is also seen experimentally. Interestingly, in the simulations there is a crossover from $\sigma_{acetone} > \sigma_{methanol}$ to $\sigma_{acetone} < \sigma_{methanol}$ occurring at an

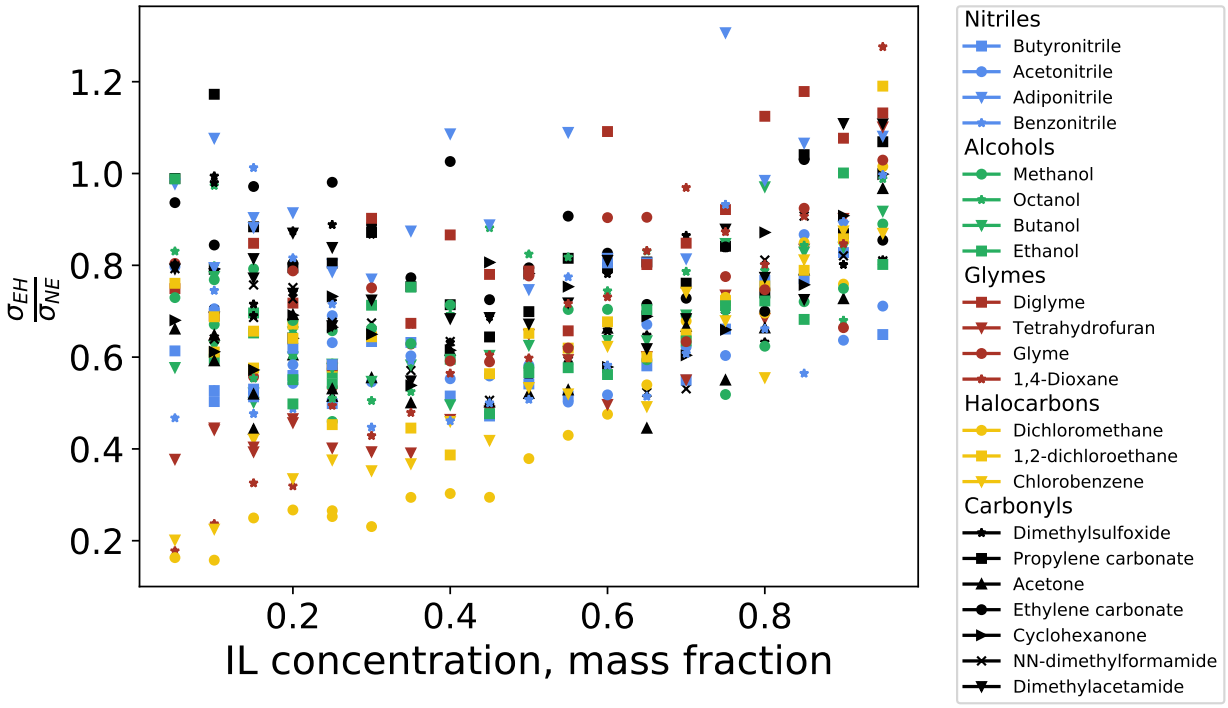

Figure 4.13: A ratio of Einstein-Helfand conductivity and Nernst-Einstein conductivity.

ionic liquid mass fraction of 0.4; the experiments also suggest a similar crossover, though occurring at higher mass fraction. Discrepancies between values from experimental measurements and simulation data are likely the result of inaccuracies in the force field.

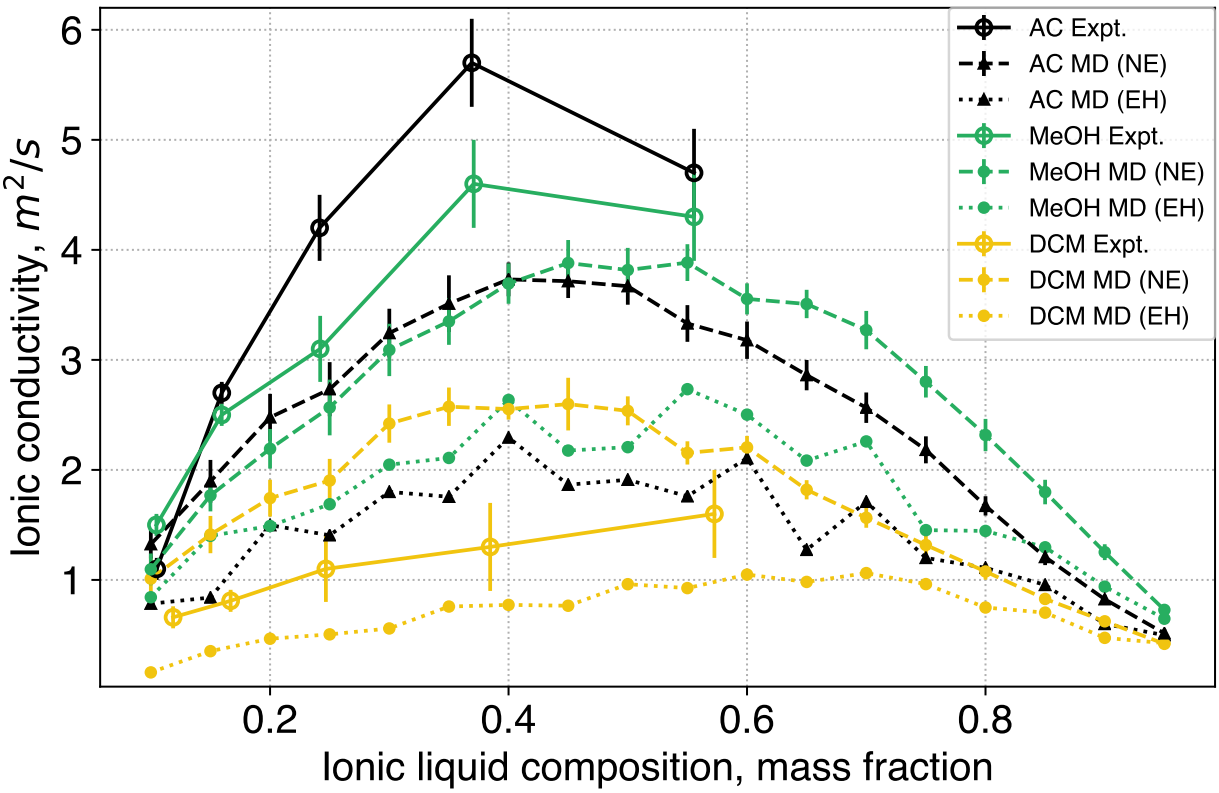

Figure 4.14: Comparison between simulation predictions (solid lines) and experimental measurements (dashed lines) of the ionic conducivity of select mixtures as a function of composition.

4.5.4 Liquid Density

We begin structural evaluation of these ionic liquid-solvent systems by considering their density as a function of composition. Figs. 4.15 and 4.16 shows that these densities change monotonically and smoothly as a function of composition. They appear to roughly follow a simple mixing rule for all compositions outside of the dilute ionic liquid range. All solvents have lesser bulk densities than that of the ionic liquid, and the densities of all mixtures fall between that of the the pure solvent and ionic liquid components. After converting from thinking about liquid density to specific volume (on a mass or molar basis), we consider a simple mixing rule to define an ideal density of mixing:

$$\hat{V}_{expected} = x_{IL}\hat{V}_{IL} + x_{solvent}\hat{V}_{solvent} \tag{4.6}$$

where $\hat{V}_i$ and x_i refer to the specific volume of the bulk liquid and the the composition of component i, respectively. These variables can be considered on a mass or molar basis. One can also define the excess density of mixing

$$\hat{V}_{excess} = \hat{V}_{measured} - \hat{V}_{expected} \tag{4.7}$$

which characterizes deviations from ideal liquid behavior. Negative excess volumes can be interpreted as thermodynamically favorable interactions between species and positive values the opposite. Summaries for this data set are included in Figs. 4.17 and 4.18. Numerical values (on the order of $1\,\mathrm{cm^3\,mol^{-1}}$ are similar to existing works.[72–75]) For most mixtures the strongest deviation from ideal mixing is observed at intermediate compositions of approximately 0.1 - 0.2 mol fraction. All mixtures exhibit negative excess molar volumes, indicating their mixing is thermodynamically favorable. There are some differences among solvents, particularly clear when grouping solvents by chemical family. The most favorable mixing is observed in some nitriles, alcohols, and acetone. It is worth noting that solvents producing the greatest abvolute values of $\hat{V}_{excess}$ also tend to produce the fastest transport properties (see Figs. 4.6, 4.11 and 4.12).

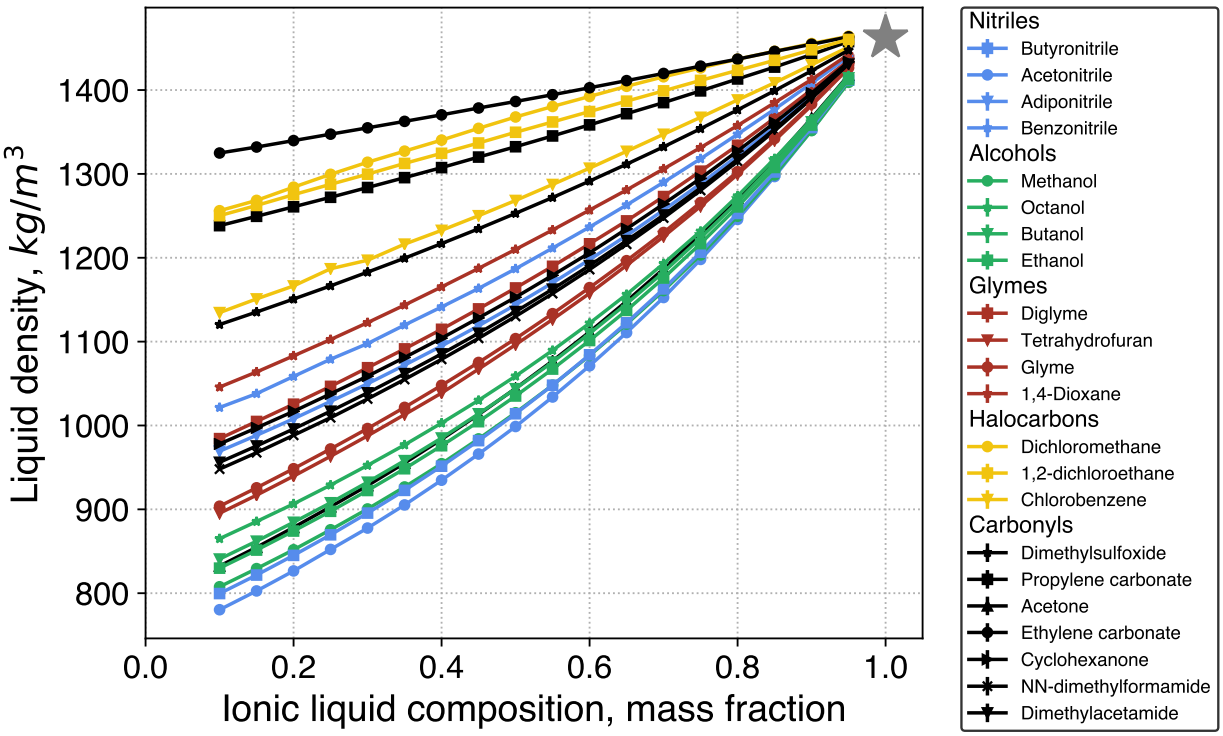

Figure 4.15: Liquid density, ρ, of ionic liquid-solvent mixtures as a function of ([BMIM$^+$][TF$_2$N$^-$]) mass fraction.

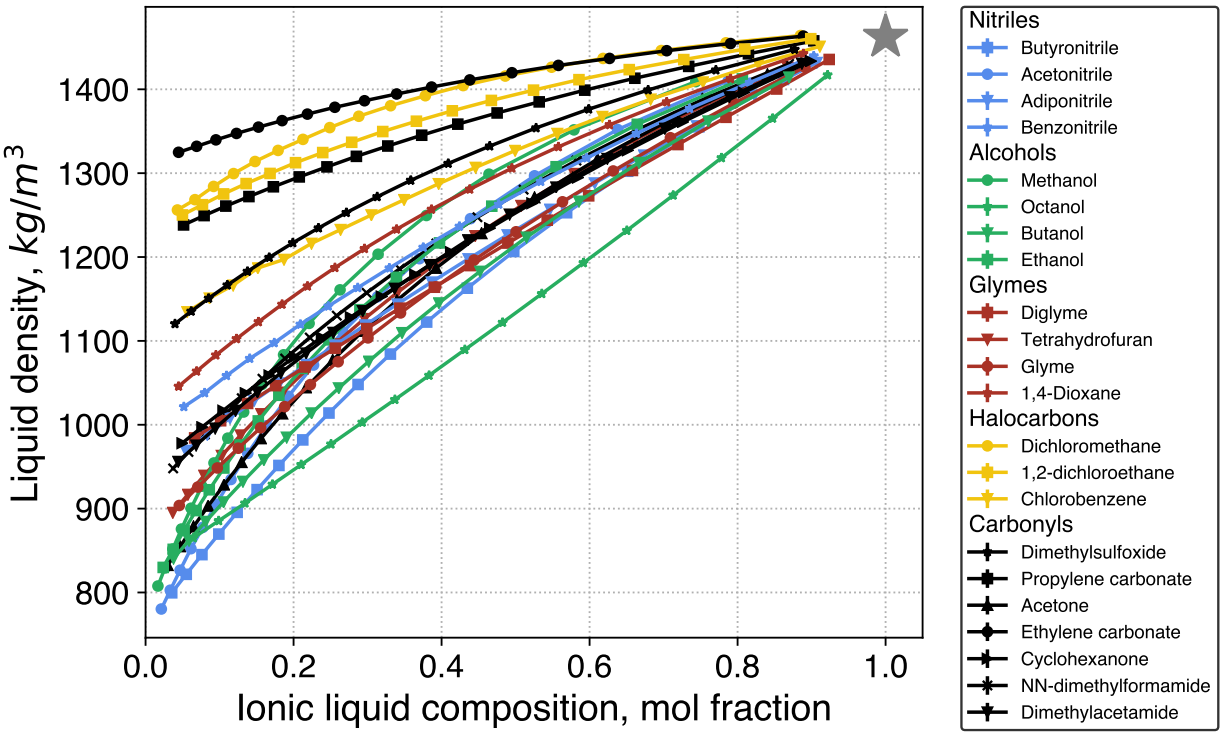

Figure 4.16: Liquid density, ρ, of ionic liquid-solvent mixtures as a function of ([BMIM$^+$][TF$_2$N$^-$]) mol fraction.

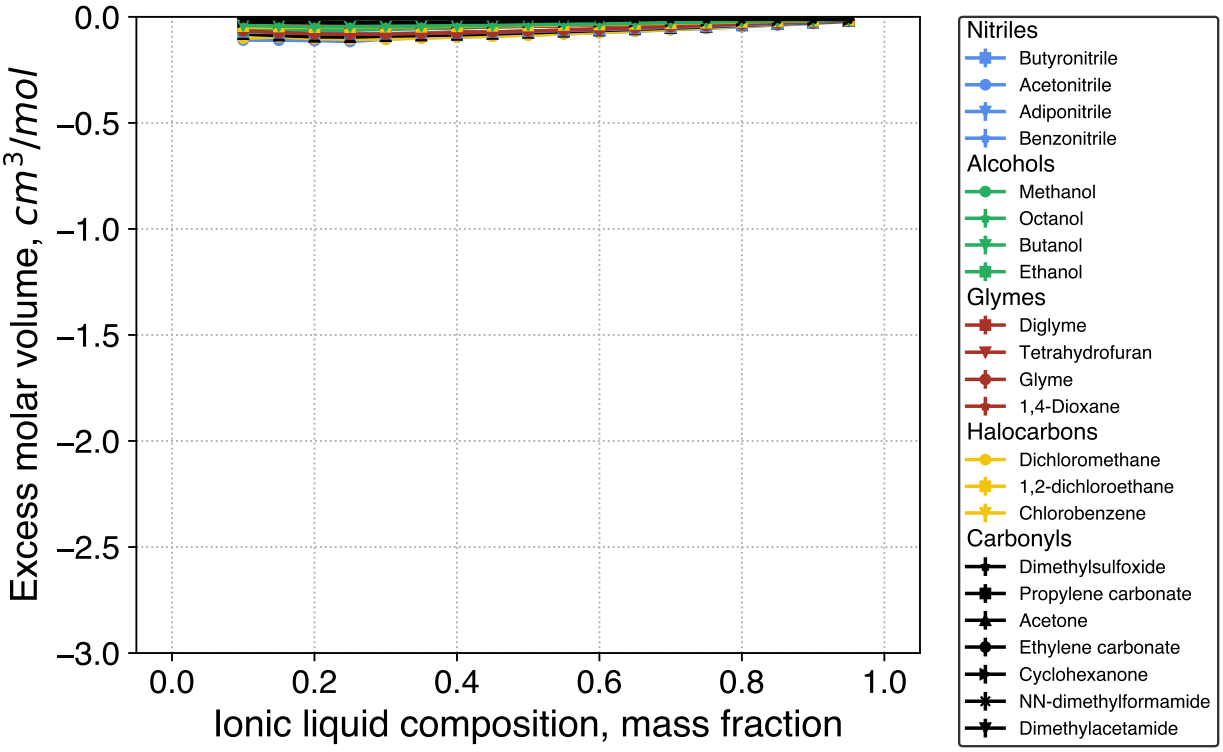

Figure 4.17: Excess molar volume, $\hat{V}_{excess}$, as a function of [BMIM$^+$][TF$_2$N$^-$] mass fraction.

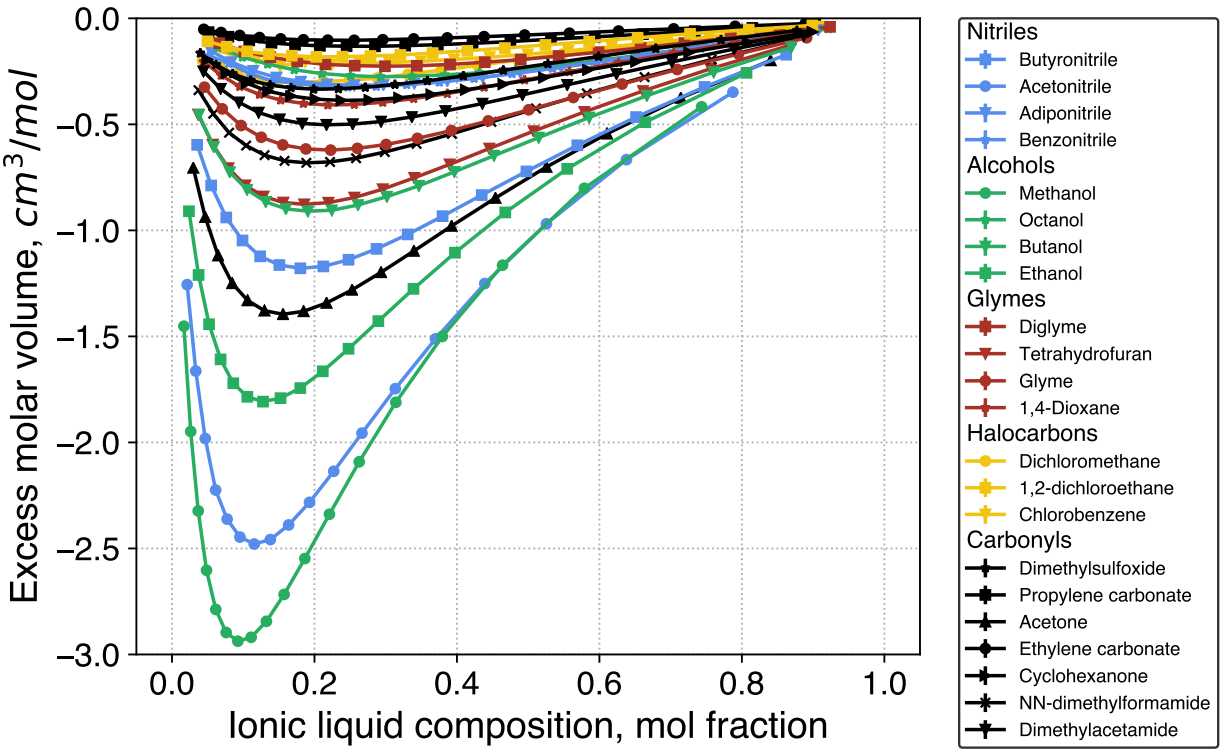

Figure 4.18: Excess molar volume, $\hat{V}_{excess}$, as a function of [$BMIM^+$][TF_2N^-] mol fraction.

4.5.5 Radial Distribution Functions

Next we consider the local structure as defined by radial distribution functions (RDFs), focusing on pairs of cations and anions. In lieu of presenting hundreds of such plots or a single plot with 396 curves, we present summaries in Fig. 4.19 and Fig. B.3. We track the location and magnitude of the first peak, r_{peak1} and $g_{max} = g(r_{peak1})$, respectively. These correspond to the common cation-ion pairing structure characteristically observed in ionic liquids. The distances in r space this is observed, r_{peak1}, are largely insensitive to the properties of the solvent and appear to mostly be a function of the selection of ionic liquid, which was held constant in this study. In contrast, we observe that heights of these peaks, g_{max}, depend strongly on the properties of the solvent and the composition of the mixture. Most notably, these values spike in the limit of low ionic liquid composition. While the numerical values are somewhat inflated by the nature of normalizing RDFs to dilute components, they indicate strong structuring of ionic liquid molecules. There is also considerable variance in this behavior among different solvents. Mixtures in carbonyl-containing compounds (i.e. propylene carbonate, ethylene carbonates, and dimethyl sulfoxide) display nearly identical g_{max} values over all composition ranges and do not exhibit this spike at low concentrations. Mixtures in halocarbons and glymes together make up the most structured systems and mixtures in nitriles, alcohols, and other glymes have this spike but of lesser magnitude. This demonstrates that different chemical families of solvents give rise to substantially different ion structures in these mixtures. In particular, halocarbons and glymes drive ions to pair strongly whereas other solvents promote populations of free ions not bound to a neighboring counter-ion. This indicates varying capacities of different solvents to screen charges: some solvents, particularly carbonates, robustly screen ion-ion interactions, whereas others are much less effective.

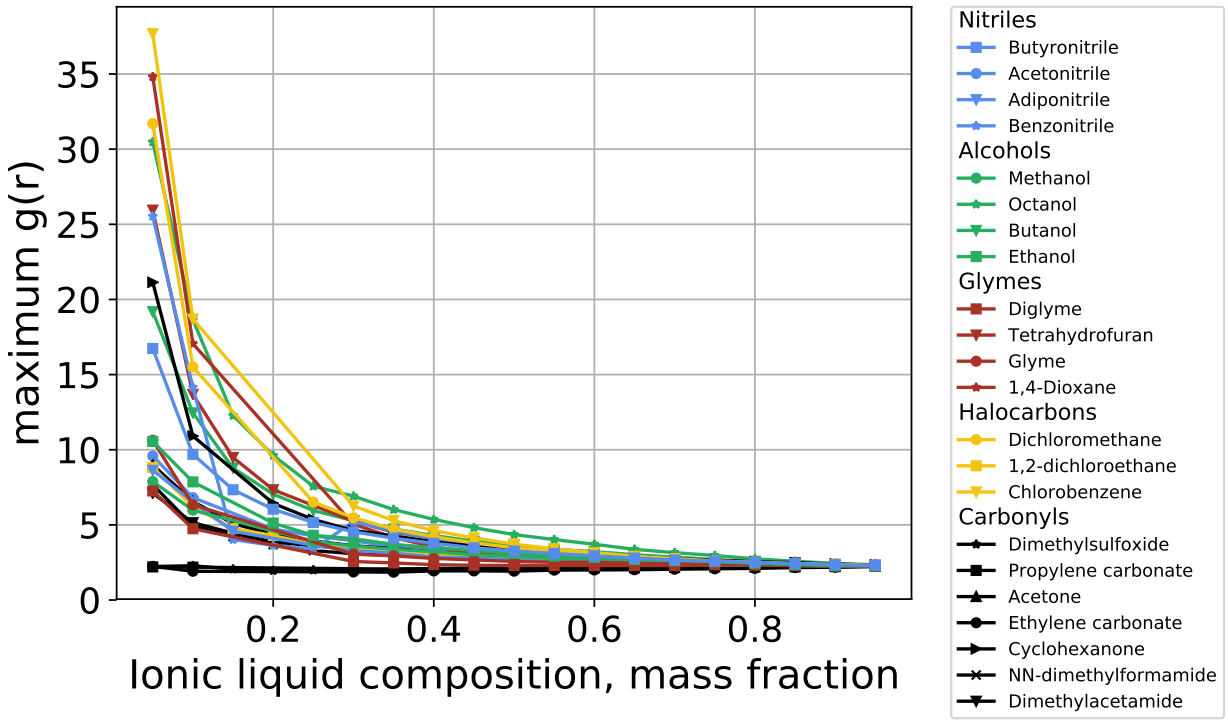

Figure 4.19: Location of the first peak of the RDF, $g_{max}(r_{peak1})$ as a function of ion concentration, colored by the chemical family of the solvent.

4.5.6 Coordination Numbers

The coordination number (N_C(r)) characterizes the molecular structure of a liquid by quantifying the local structure around a molecule in terms of its average number of neighbors as a function of intermolecular distance. It is defined as

$$N_C(r_C) = 4\pi \int_0^{r_C} r^2 g(r) \rho dr \tag{4.8}$$

where $N_C(r)$ is the coordination number of some interatomic pair at some cutoff distance r_C, ρ is the bulk density of these pairs, $g(r)$ is the corresponding radial distribution function, and r is the intermolecular separation. Throughout we use $r_C = 0.8nm$, which corresponds to the location of the first well in a typical RDF, in order to focus on the nearest-neighbor ions. We also consider only cation-anion pairs — co-ions exhibit much less coordination — and no direct correlations with solvent molecules. A summary of the coordination numbers of these systems is presented

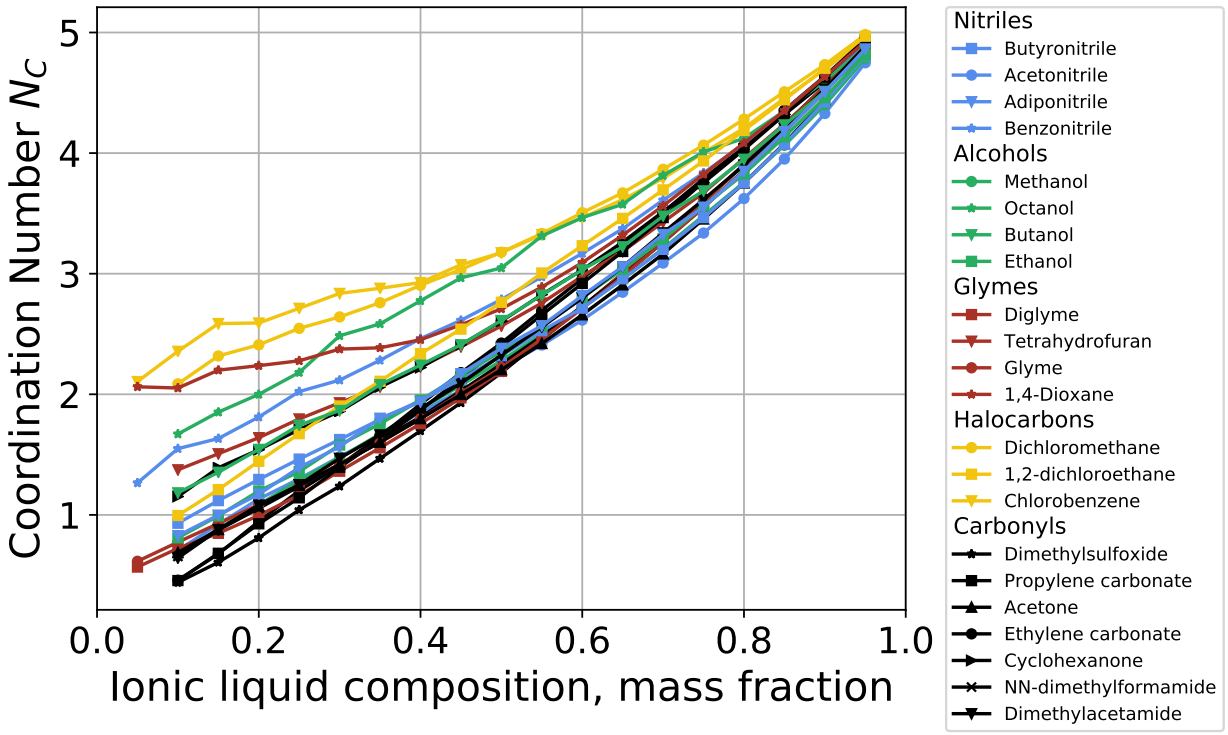

Figure 4.20: Coordination numbers, N_C, as a function of [BMIM$^+$][TF$_2$N$^-$] mass fraction. Only cation-anion ([BMIM$^+$][TF$_2$N$^-$]) pairs are considered.

in Fig. 4.20. In all solvents, there is a monotonic increase in N_C as a function of ionic liquid composition, which is characteristic of the nature of concentrated electrolytes. It is worth pointing out, however, all systems exhibit non-zero coordination numbers at low concentration, indicating that all ions are neighbored by some population of ions, even in very dilute systems. Similar to the solvents that displayed especially large $g_{max}(r)$, N_C varies greatly among different solvents. At low concentrations, it is greater than 2 for some solvents and closer to 0.5 for others. At high concentrations, solvent effects become less relevant and these curves converge toward a bulk value near 5.

4.5.7 Ion Correlations

Ion correlations were computed for all 396 state points. We first analyzed the pairing lifetimes of ions in solution as the ionic liquid composition is increased, shown in Fig. 4.21. We show ionic

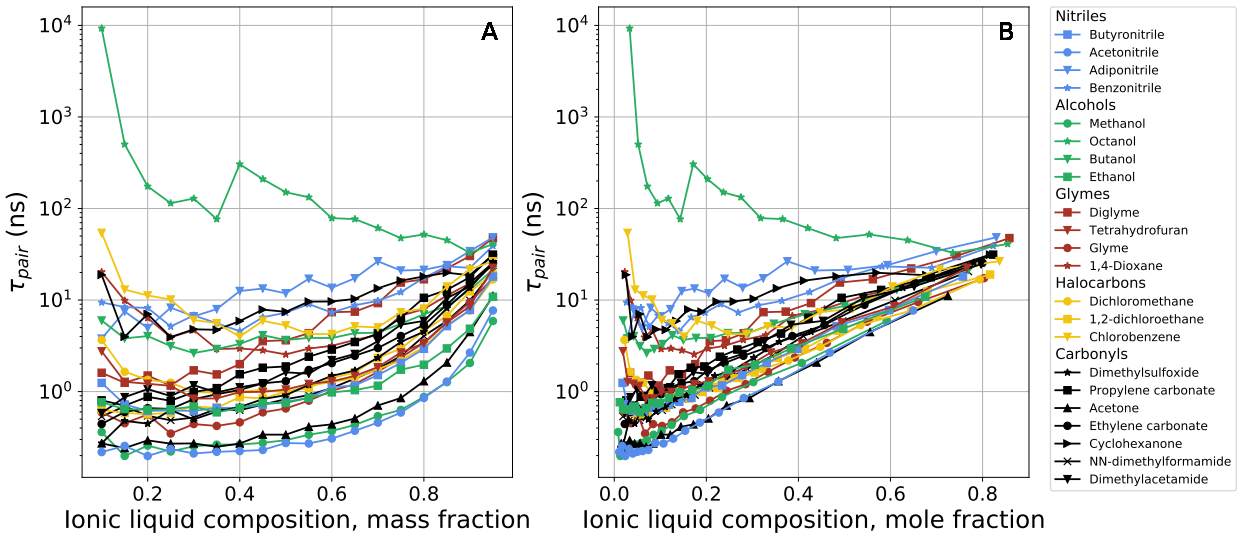

Figure 4.21: Ion pair lifetimes, τ_{pair}, as a function of a) mass fraction composition and b) mole fraction composition. Straight line segments are drawn to connect data points of common solvents.

liquid composition in both units of mole fraction and mass fraction in order to better highlight the trends with τ_{pair}. With the exception of octanol, which is one of the most viscous solvents studied, τ_{pair} of most systems exhibit similar concentration dependence. In general, as concentration increases from intermediate compositions toward the neat regime, τ_{pair} increases. This is an intuitive result; given that ionic liquids have strong self-correlations and inherently slow dynamics, it is not surprising that an increase in ionic liquid composition results in longer pairing lifetimes. Recall Zhang *et al.* found a strong correlation between τ_{pair} and transport properties for a set of 29 neat ionic liquids at a range of temperatures. There is, however, some amount of non-monotonic behavior at low compositions. In particular, τ_{pair} increases dramatically in the dilute limit for chlorobenzene, dichloromethane, dioxane, and cyclohexanone. These are some solvents we previously noted as promoting strongly-structured ion pairs in solution. Other commonly-studied solvents such as acetonitrile and propylene carbonate also show this behavior, but at a greatly lesser magnitude. We attribute this largely to the interplay between the strong ion-ion interactions and the ability of solvent molecules to screen them. In solvents that are less able to screen these interactions, ions exist more often in a paired state, whereas in solvents that effectively screen them, the ions are stable as free ions in solution.

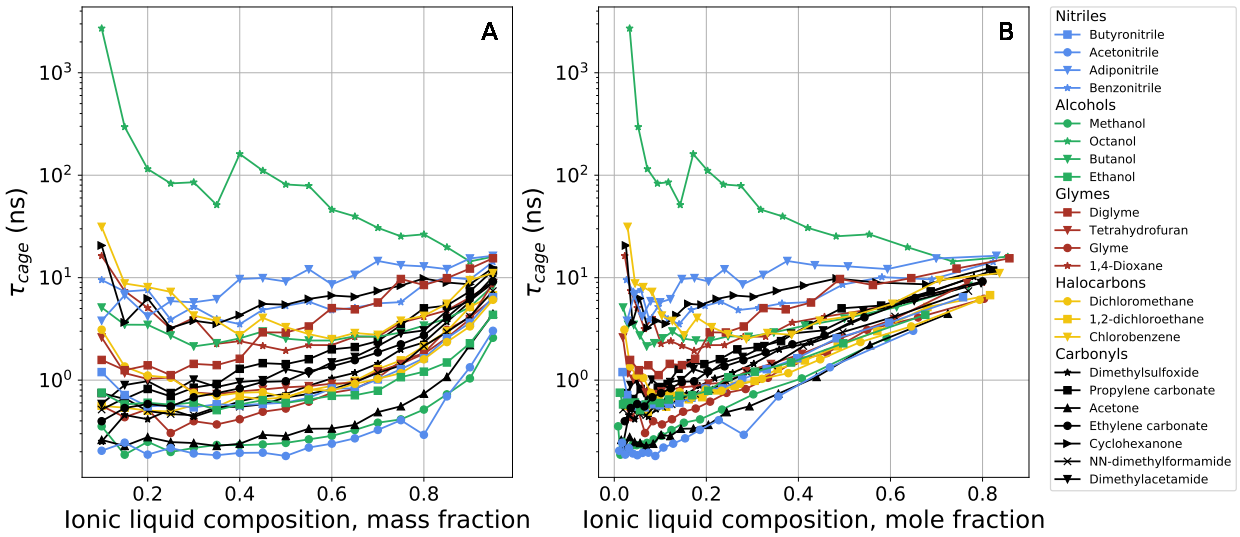

Figure 4.22: Ion cage lifetimes, τ_{cage}, as a function of a) mass fraction composition and b) mole fraction composition. Straight line segments are drawn to connect data points of common solvents.

Next, we analyze the lifetime of ion casges, τ_{cage}, over the range of ionic liquid compositions, shown in Fig. 4.24. These values are qualitatively similar to τ_{pair}, exhibiting a similar parabolic concentration-dependence. Like τ_{pair}, the majority of τ_{cage} values have a minimum at intermediate compositions and increase toward both the limit of dilute and neat ionic liquids. Their values are similar at low concentration, $\tau_{cage} \approx \tau_{pair}$, although differences between caging and pairing lifetimes are observed at other concentrations. As composition increases, τ_{cage} increases slower, resulting in $\tau_{cage} < \tau_{pair}$. Zhang *et al.* also observed this relationship for their set of neat ionic liquids. This is largely a consequence of the definition of caging in a solvated system; in the limit of infinite dilution, pairs and cages become equivalent. However, as more ions are added to a system, cages are composed of more ions and there are more chances for a cage to "break" by losing a single ion.

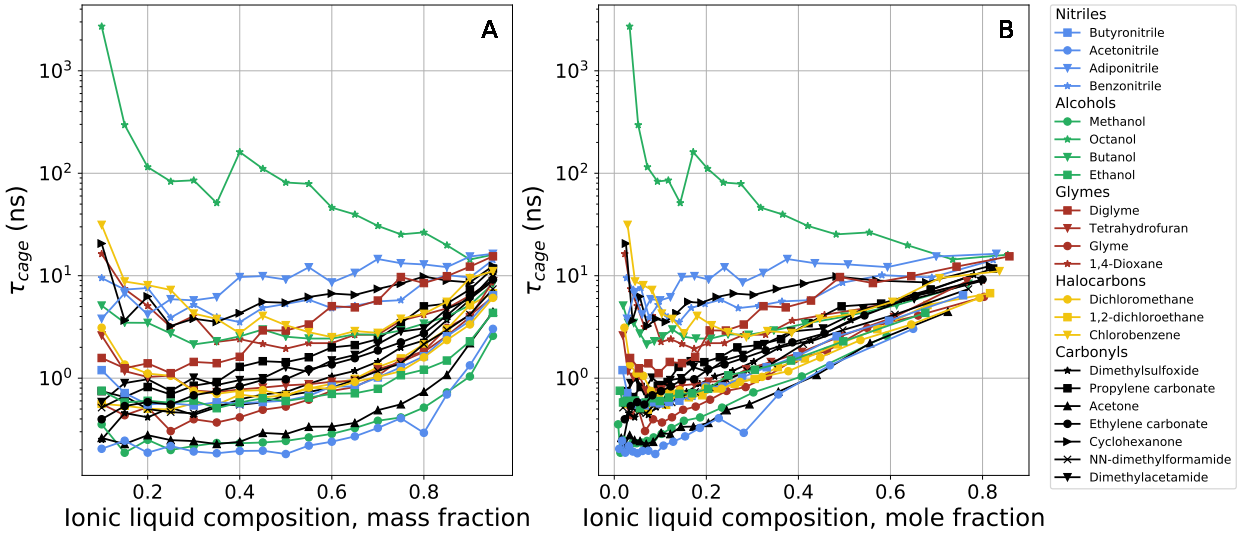

Figure 4.23: Ion cage lifetimes, τ_{cage}, as a function of a) mass fraction composition and b) mole fraction composition. Straight line segments are drawn to connect data points of common solvents.

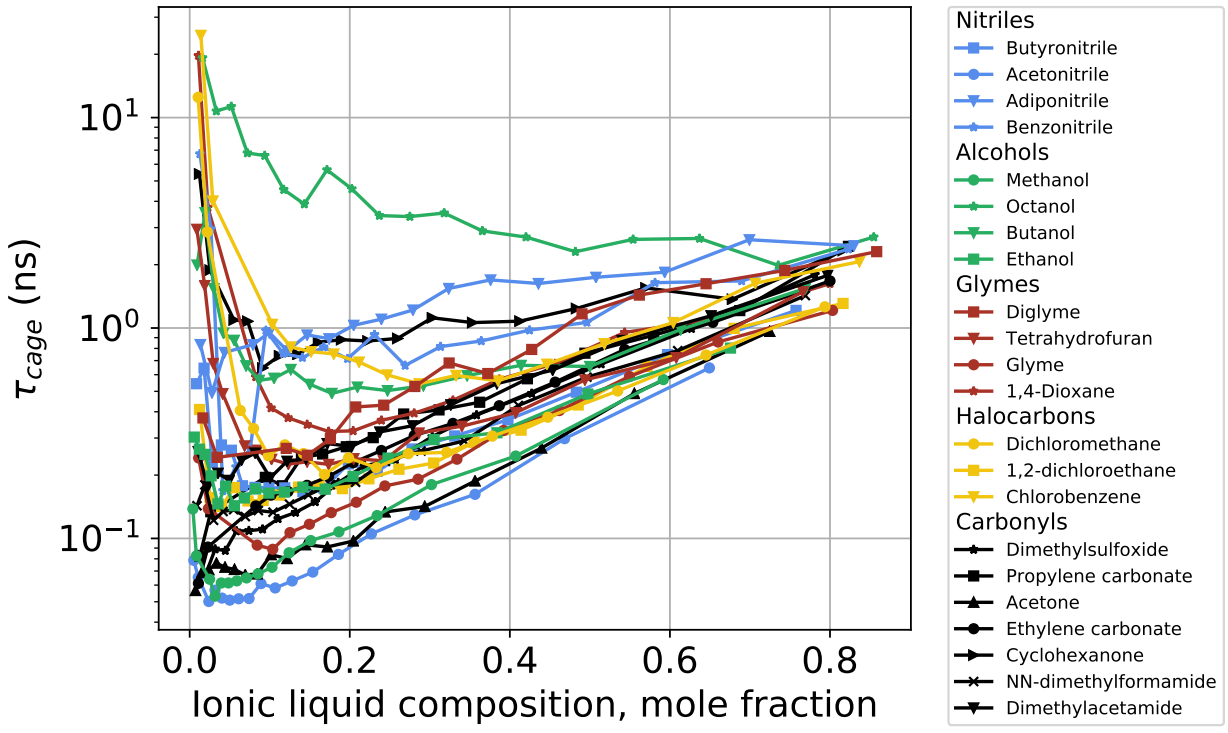

Figure 4.24: Ion cage lifetimes, τ_{cage}, as a function of mixture composition. Straight line segments are drawn to connect data points of common solvents.

4.5.8 State of Ions in Pairs

While we can compute the pairing properties above, we can also extract information about the paired states of ions, if they are in pairs or free ions. Fig. 4.25 displays the fraction of ions that are unpaired in each solvent as a function of [$BMIM^+$][TF_2N^-] mass fraction. We first observe that each solvent displays a linear decrease in fraction of free ions as the composition of [$BMIM^+$][TF_2N^-] increases. We also observe that the differences in free ions between solvents is greatest near the dilute regime of [$BMIM^+$][TF_2N^-]. As the ionic liquid composition increases towards the neat limit, the fractions of free ions converge. To further describe these differences in free ions between solvents, the slopes of each curve were calculated and are shown in the supplementary information. The slope of free ions versus composition for a significant portion of solvents is roughly between -0.8 to -0.9, and at the neat limit of [$BMIM^+$][TF_2N^-], most ions exist in a paired state. There are several solvents including chlorobenzene, dichloromethane, octanol, and 1,4-dioxane, that exhibit lower slopes. As such, a smaller fraction of ions in these solvents are free at low compositions of ionic liquid. Through these structural analyses, we suspect that some solvents such as dimethylsulfoxide, methanol, and acetonitrile are effective at screening ion-ion interactions, resulting in a lower prevalence of ion pairing. Consistent with this view, these solvents also exhibit a higher fraction of free ions. Furthermore, the solvents suspected to be less effective at screening ion-ion interactions such as octanol, chlorobenzene, dichloromethane, and 1,4-dioxane, display a lower fraction of free ions in solution.

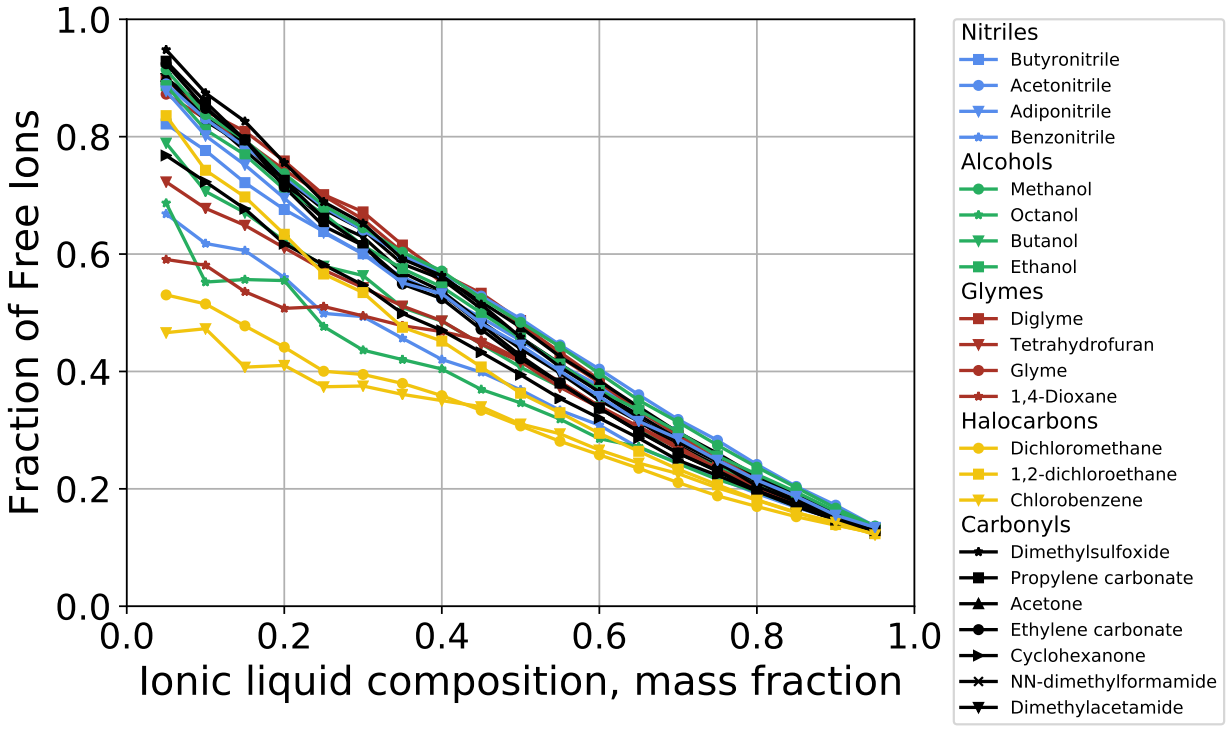

Figure 4.25: The fraction of free ions in each solvent as a function of [$BMIM^+$][TF_2N^-] composition.

4.5.9 Free Energy Calculations

To supplement existing transport and structural characterizaiton of these systems, we next investigate the thermodynamics of ion-ion pairing interactions in these solutions by computing PMFs between [$BMIM^+$] and [TF_2N^-]. Here, a PMF is defined as the reversible work required to bring two molecules to separation r from infinite distance. The general formalism of a PMF is

$$\phi(\varepsilon) = -ln \int \pi_0(x)\delta(\varepsilon - \varepsilon(x))dx,$$

where π_0 is the equilibrium distribution of the system and ε is the reaction coordinate. Here, the reaction coordinate is the intermolecular separation r. The PMFs of a single ion pair in each solvent are displayed in displayed in Fig. 4.26. The minima of these free energy curves are also summarized in Table 4.5. The PMF of of chlorobenzene approaches the most negative values, meaning it requires more energy to separate a pair of [$BMIM^+$][TF_2N^-] in this solution. Equivalently, chlorobenzene is a poor solvent in terms of screening ion-ion interactions. In other solvents

(octanol, dichloromethane, tetrahydrofuran, and benzonitrile) the PMFs also suggest that the interactions between [$BMIM^+$][TF_2N^-] ions are poorly screened. Recall that these solvents exhibited characteristics of strong ion pairing as when looking at pair lifetimes (Fig. 4.21) and coordination numbers (Fig. 4.20), which we attributed to the inability of these solvents to screen ion-ion interactions. By comparison, the PMFs of in propyelene carbonate, ethylene carbonate, acetonitrile, among several other solvents, are much less negative, showing that these solvents are more effective at screening ion-ion interactions. Overall, the ion-ion PMFs in solvents at infinite dilution provides further evidence that the ability for solvents to screen ion-ion interactions significantly impacts the prevalence of ion pairing, which drives many structural and dynamical properties of these mixtures.

Solvent	PMF Peak Minimum ($\frac{kJ}{mol}$)
Propylene carbonate	-3.16
Ethylene carbonate	-5.15
Acetonitrile	-6.74
Ethanol	-11.24
1,2-dichloroethane	-12.28
Dimethylsulfoxide	-13.12
Methanol	-13.54
Adiponitrile	-15.81
Glyme	-18.88
Acetone	-19.13
Dimethylacetamide	-19.67
NN-dimethylformamide	-20.97
Butyronitrile	-24.30
Butanol	-27.74
Diglyme	-36.07
Cyclohexanone	-41.87
Tetrahydrofuran	-48.02
Benzonitrile	-49.34
Dichloromethane	-62.56
Chlorobenzene	-79.79
Octanol	-94.28
1,4-dioxane	-164.89

Table 4.5: Table of solvents and PMF peak minima values ($\frac{kJ}{mol}$). Solvents are listed from least negative minima to most negative minima.

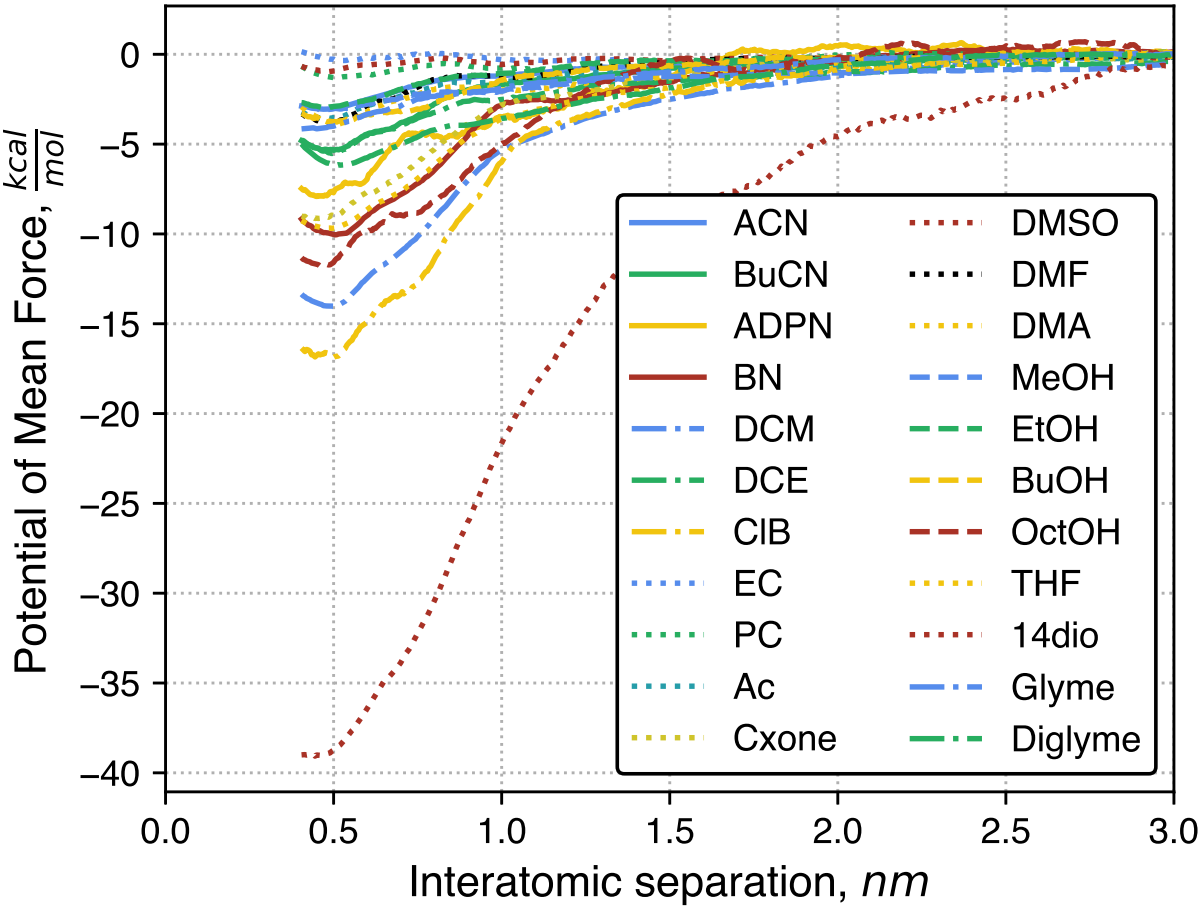

Figure 4.26: PMFs of [BMIM$^+$][TF_2N^-] in various solvents at infinite dilution. The curves have been adjusted to decay to zero energy.

4.5.10 Dielectric Constants

We next compare ion pairing with the dielectric constants of the solvents. Consistent with the general picture of screening coulombic interactions, trends between the molecular polarizability of solvents and various properties of solvated ionic liquids have previously been reported. For instance, Osti *et al.* suggested solvent dipole moment as being an accurate predictor of ion dynamics for [$BMIM^+$][TF_2N^-] solvated in 4 various solvents.[2] From our previous study, we reported from a greatly expanded parameter space that solvent diffusivity is a more accurate predictor of ion dynamics in comparison to solvent dipole moment. McDaniel *et al.* similarly looked at ion pairing and the dielectric strength of solvents for solutions of [$BMIM^+$][BF_4^-] in 4 different solvents. It was reported from this study that solutions containing solvents with with lower dielectric strength exhibit longer ion pair lifetimes. To investigate the relationship between these two properties, we used the built-in tools of GROMACS[47] to estimate the dielectric constants for each of the 22 unique solvents studied. Specifically, the dielectric constants are estimated by computing the dipole moment for all frames of a simulation trajectory. The ion pair lifetimes are plotted as a function of solvent dielectric constants in Fig. 4.27. Upon looking at a portion of the solutions simulated by McDaniel *et al.*, the trend between ion pair lifetime and solvent dielectric constants holds well. 1,2-dichloroethane has the lowest dielectric constant out of the three solvents McDaniel *et al.* tested, and exhibits the highest τ_{pair}. Following the trend, acetonitrile has the highest dielectric constant and has the lowest τ_{pair}. Additionally, there are other solvent systems with chlorobenzene and diglyme that follow this trend. The relationship between dielectric constant and τ_{pair} is less clear however when the entire chemical space of solvents is considered. Octanol has a higher dielectric constant compared to 1,2-dichloroethane, but the ions in these systems have a much higher τ_{pair}. This is simililarly the case for systems containing dimethylesulfoxide, propylene carbonate, and ethylene carbonate. Overall, the monotonic decrease in τ_{pair} for systems containing 1,2-dichloroethane, acetone, and acetonitrile indicate that solvent dielectric constants play a relevant role in ion pairing. Despite this, the other systems do not fit this trend, signifying there are additional solvent properties and competing interactions within these systems that influence ion

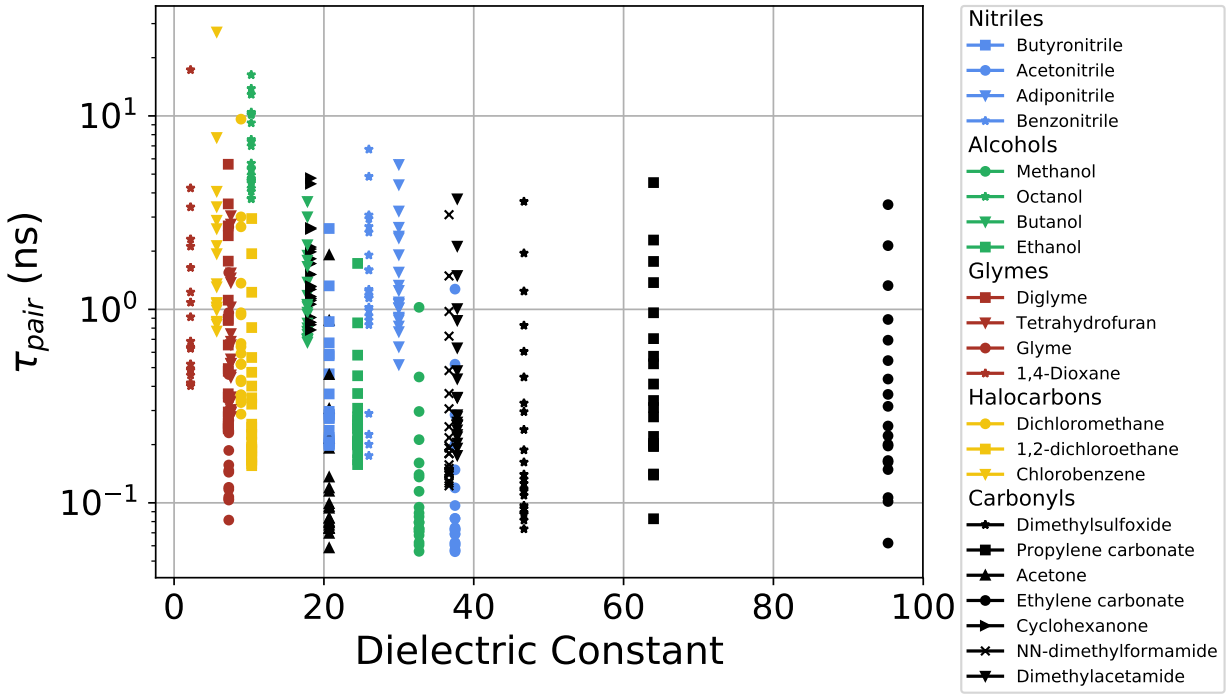

Figure 4.27: Ion pair lifetimes, τ_{pair}, of [BMIM$^+$][TF$_2$N$^-$] solvent solutions as a function of solvent dielectric constant.

pairing.

4.5.11 Connecting Structure and Dynamic Properties

To better understand the implications of the pairing and caging properties τ_{pair} and τ_{cage}, we attempt to connect these structural properties to transport properties. Previously-computed ion diffusivities are plotted against τ_{pair} in Fig. 4.28. As with ionic liquid composition, two distinct trends are observed between ion diffusivity and pair lifetimes. The same solvents that showed a more monotonic trend between τ_{pair} and ionic liquid composition, such as acetonitrile and propylene carbonate, show a roughly monotonic decrease in ion diffusivity as τ_{pair} increases. As such, it appears that ion pairing in these solutions negatively affects the ion dynamics. Similar trends have been observed by Zhang *et al.* for various ionic liquids using non-polarizable force fields[71] and by McDaniel *et al.* for [BMIM$^+$][BF$_4^-$] in four solvents at various concentrations using the SAPT polarizable force field.[18] Also shown in Fig. 4.28 is that solutions with solvents that have the shortest

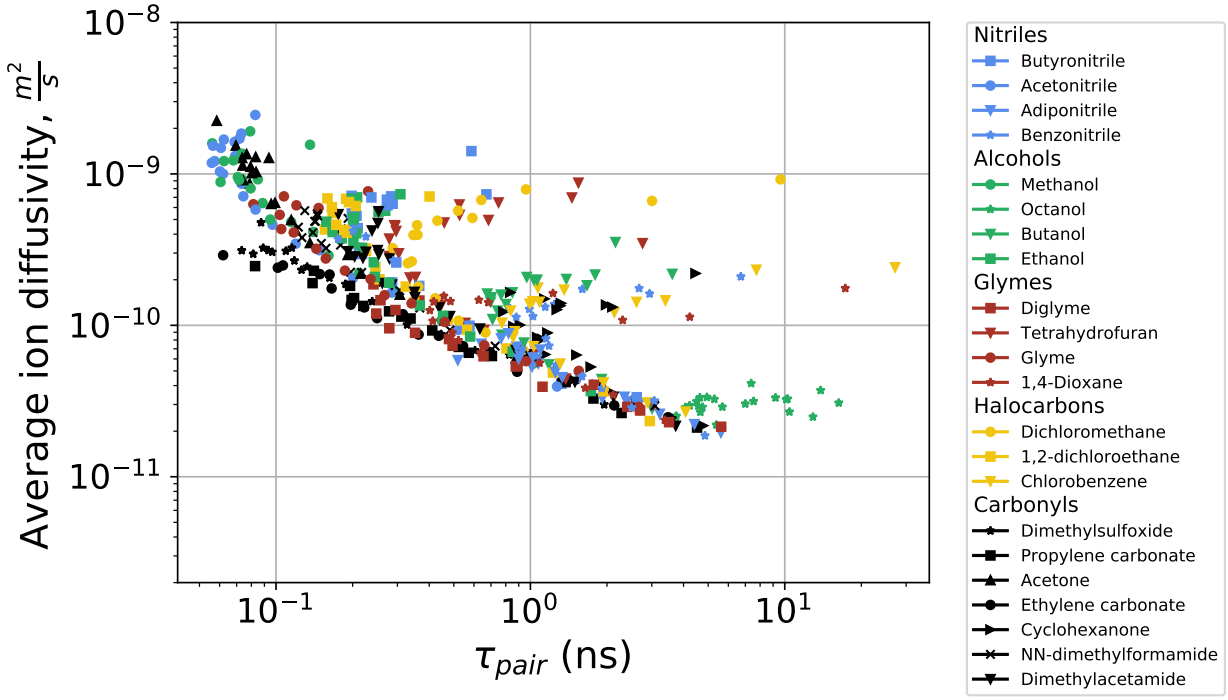

Figure 4.28: Average ion diffusivity of [BMIM$^+$][TF$_2$N$^-$] as a function of ion pair lifetimes, τ_{pair}.

ion pair lifetimes also exhibit the highest ion diffusivities. For example, we previously reported that acetonitrile solutions exhibited the highest diffusivites from this data set;[3] ion pairing analyses now indicate that the same acetonitrile solutions also exhibit the shortest ion pair lifetimes. Consistent with previous structural analyses, from screening over many solvents we observe that some solutions, such as those containing 1,4-dioxane and chlorobenzene, do not follow this monotonic trend in Fig. 4.28. When revisiting Fig. 4.21, the systems with strongly non-monotonic curves also experienced the highest initial decrease in τ_{pair} as a function ionic liquid composition. The ions in these systems are paired in large quantity and for long times at low ion compositions, but this pairing does not appear to affect the diffusivity of these ions. In general, however, we would expect the longer ion pairing lifetimes of these systems to negatively impact conductivity.

4.6 Additional QENS Experiments

While QENS cannot access the scope of our data set (22 solvents at 18 compositions for a total of 396 mixtures), there is a conflict between our recent[3] and earlier[2] results that should be investigated with experiments. We brought out screening results to our experimental collaborators (Naresh C. Osti and Eugene Mamontov at ORNL) who devised a comparatively simple set of experiments to isolate the effect of solvent diffusivity from solvent polarity. They selected four solvents with nearly identical dipole moments (d, Debye) but greatly varying diffusivities (D, $\mathrm{m^2\,s^{-1}}$): dichloromethane ($d = 1.60$ D, $D = 15.7 \times 10^{-10}\,\mathrm{m^2\,s^{-1}}$), octanol ($d = 1.68$ D, $D = 0.4 \times 10^{-10}\,\mathrm{m^2\,s^{-1}}$), butanol ($d = 1.66$ D, $D = 2.7 \times 10^{-10}\,\mathrm{m^2\,s^{-1}}$), and tetrahydrofuran ($d = 1.75$ D, $D = 8.5 \times 10^{-10}\,\mathrm{m^2\,s^{-1}}$). These properties are summarized again in Table 4.3. Because concentration effects are well-understood, here we only considered equimass (0.50 mass fraction) mixtures of [$BMIM^+$][TF_2N^-] in each solvent. If solvent polarity dominated mixture properties we would see little correlation against solvent diffusivity if solvent diffusivity dominated mixture properties we would expect to see a strong correlation. We see the later, summarized below in Fig. 4.29. The trend is stronger with the MD results than QENS data but both show a strong dependence of cation diffusivity on pure solvent diffusivity.

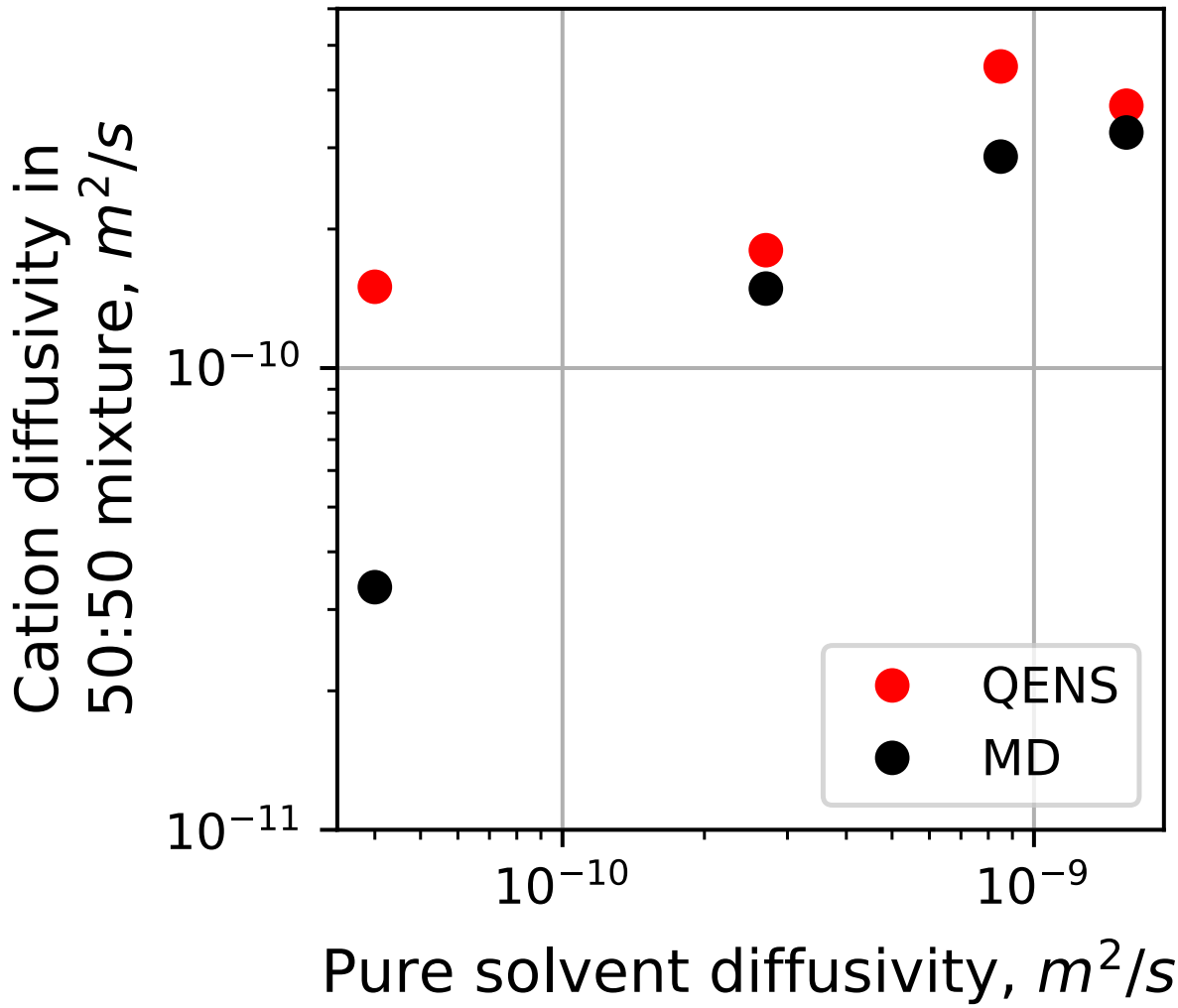

Figure 4.29: Ion diffusivity as a function of pure solvent diffusivity for selected solvents with similar polarity.

4.7 Conclusions

In this chapter, we have used neutron scattering experiments, conductivity measurements, free energy calculations, and hundreds of molecular dynamics simulations to better understand the proeprties of ionic liquids dissolved in organic solvents. This study began with a set of QENS experiments suggesting two trends: ion diffusivity increases as its composition in the mixture decreases and solvents with greater polarity better promote these diffusivity enhancements. MD simulations supported each conclusion and free energy calculations helped explain the latter by connecting bulk transport to local energetics of ions during dissolution. Then, we revisisted these conclusions with new computational tools that enabled screening over more solvents and mixture compositions. The trend with concentration was re-affirmed but some doubt was cast on the observed relationship with solvent polarity. We evaluated other solvent properties and found that pure ion diffusivity was the best predictor of ion diffusivities in mixtures. Finally, we tested this finding with a new set of QENS experiments and found that solvent diffusivity impacts ion diffusivity in mixtures more than the solvent polarity.

It is worth revisiting some of our initial motivations, which is that mixtures in the few commonly-used solvents (acetonitrile and propylene carbonate in particular) may not be optimal electrolytes for applications demanding faster dynamics. The sum of this work assserts that, for all composition ranges, mixtures in acetonitrile exhibit the fastest ion mobility. Short of proposing a novel solvent for absolutely peak dynamics, we find that other proposed solvents exhibit viable alternatives. This is still useful given that other factors (i.e. toxicity concerns, material costs, or environmental regulations) often constrain design of applications in practice. Further, elucidating which molecular interactions have the strongest impact on mixture properties could aid in the design of application-specific mixtures; in the case of energy storage it is desirable to strongly screen ion-ion interactions but other applications may seek to tune molecular interactions in a different manner.

4.8 Future work

While the work of this chapter is a major contribution to the understanding of ionic liquids in more diverse chemistries, it is trivially small compared to the amount of work that needs to be done. Most obviously, only one ionic liquid was considered, whereas the design of novel electrolytes necessitates studying combinations of ionic liquids in solvents - likely even mixtures of salt as well.[76,77] Effects of temperature and pressure should also be considered, as many applications require operation away from normal ambient conditions. Each added physical dimension drastically increases the cost of any study; progress in this direction, while valuable, will still be slow no matter the progress made in computational screening tools (or even potential analogs in experimental setups using robots). The difference is that we are beginning to be limited by our own capacity to intelligently process and analyze large quantities of data. Years or decades ago we were limited by computational resources or the viability of molecular force fields; while these still specify the bounds of what we can accomplish with molecular simulation, the boundary has moved drastically outward.

The most straightforward extension of this work is to collect more experimental data. While it is infeasible to consider the scope of our computational screening study in either QENS or NMR experiments, any increase in the volume of available experimental data adds rigor to these results. Perhaps more data will verify our results or perhaps important differences will emerge — most likely a combination of each will occur, but it is valuable in any case. As an alternative to gathering more diffusivity data, measuring some hundreds of conductivity data would be feasible. The downside, however, is that ionic conductivity is a less direct characterization of the transport behavior of electrolytes at the molecular scale.

A topic worth revisiting is the use of scaled charges on ionic liquids, particularly in dilute solutions. While an approximation, their use in neat ionic liquids is well-studied[46,78,79] and can produce reasonable physical properties if used with care.[80] Further, there is some theoretical and physically sensible basis to this approach, as electronic structure calculations frequently produce structures with less than the formal integer charge. This is typically understood as the manifestation

of charge transfer effects or electronic polarization.

It is less clear, however, that this is valid for mixtures in neutral species, as was done throughout this chapter. To my knowledge, this issue has not thoroughly been explored computationally (in theoretical calculations or simulations). This issue is compounded by some difficulties comparing to transport data from experiment. Since ionic liquids are relatively new as a popular topic of study, there is a limited set of data to pull from. Much of this data deals with neat ionic liquids and a sizable portion of the data considering solvents chooses water or non-polar solvents, which have limits due to miscibility issues and were considered in the scope of this study. Unfortunately, of the three transport properties considered (molecular diffusivity, viscosity, and ionic conductivity), there is no property that is simple to measure experimentally and reliably compute from simulations. Viscosity and conductivity measurements are relatively straightforward to do, provided the compounds are available, but diffusivity data generally requires expensive QENS or NMR experiments. Conversely, backing out diffusivity values from simulation is straightforward but more involved methods are required for viscosity (long simulations analyzed with tricky autocorrelation functions) and conductivity (due to pairing effects in ionic liquids) (*vide supra*). Further, molecular diffusivity is the only measurement that isolates the dynamics of a single species (provided the propert scattering lengths or isotopes are available in QENS and NMR, respectively), whereas viscosity and conductivity are comprehensive properties of the overall mixture. On this basis, it may not be feasible to produce a general and transferrable force field for ionic liquid mixtures, but the hypothesis can be tested on a limited set of data. We are currently exploring the possibility that NMR experiments can be done in sufficient volume to properly investigate the validity of charge scaling in these molecular models.

There is also a growing need for the development of general force fields. There exist some viable general force fields for simple organic species (OPLS[42] and GAFF[81]) which provide generally good agreement with theoretical calculations and experimental measurements of several physical properties.[43] The development and open distribution of these force fields has accelerated a generation of research by allowing researchers to commonly skip over the process of deriving new

models for simple chemical systems. There is a similar need for the development of new general force fields for ionic liqiuds. The popular CL&P force field, used throughout this thesis, is useful for the set of chemistries it covers. It is the most popular ionic liquid force field to date, perhaps because it was one of the first published but also because it covers more moeities than any other (five and four unique types of cations and anions, respectively, for some several thousand combinations of ionic liquids when considering different aklyl chian lengths). However, only some of its "out of the box" physical properties are in good agreement with experimental measurements. By comparison, the KPL force field of Ludwig *et al.*[82–84] provides excellent agreement with density, diffusivity, and enthalphy of vaporizaiton measurements but covers a much smaller number of ionic liquids (a single cation and anion for a total of approximately 5 unique ionic liquids). To enable the investigation of novel ionic liquid-based electrolytes, it is imperative that CL&P is revised to be more physiochemically accurate, KPL expanded to cover more chemistries, entirely new force fields developed, or perhaps a combination thereof.

4.9 Bibliography

[1] Cheng Zhong et al. “A review of electrolyte materials and compositions for electrochemical supercapacitors”. In: *Chemical Society Reviews* 44.21 (2015), pp. 7484–7539.

[2] Naresh C. Osti et al. “Solvent Polarity Governs Ion Interactions and Transport in a Solvated Room-Temperature Ionic Liquid”. In: *The Journal of Physical Chemistry Letters* 8.1 (2017), pp. 167–171.

[3] Matthew W. Thompson et al. “Scalable Screening of Soft Matter: A Case Study of Mixtures of Ionic Liquids and Organic Solvents”. In: *The Journal of Physical Chemistry B* 123.6 (2019), pp. 1340–1347.

[4] Naresh C. Osti et al. “Microscopic Dynamics in an Ionic Liquid Augmented with Organic Solvents”. In: *The Journal of Physical Chemistry C* (2019), acs.jpcc.9b05119.

[5] Ray Matsumoto, Matthew W. Thompson, and Peter T. Cummings. “Investigating the Structure of Solvent-Ionic Liquid Mixtures Through Molecular Dynamics Screening”. In: (2019).

[6] Cesar Cadena and Edward J. Maginn. “Molecular simulation study of some thermophysical and transport properties of triazolium-based ionic liquids”. In: *Journal of Physical Chemistry B* 110.36 (2006), pp. 18026–18039.

[7] Hiroyuki Tokuda et al. “Physicochemical Properties and Structures of Room-Temperature Ionic Liquids. 3. Variation of Cationic Structures”. In: *The Journal of Physical Chemistry B* 110.6 (2006), pp. 2833–2839.

[8] Akihiro Noda, Kikuko Hayamizu, and Masayoshi Watanabe. “Pulsed-gradient spin-echo 1H and 19F NMR ionic diffusion coefficient, viscosity, and ionic conductivity of non-chloroaluminate room-temperature ionic liquids”. In: *Journal of Physical Chemistry B* 105.20 (2001), pp. 4603–4610.

[9] Hiroyuki Tokuda et al. “Physicochemical properties and structures of room temperature ionic liquids. 1. Variation of anionic species”. In: *Journal of Physical Chemistry B* 108.42 (2004), pp. 16593–16600.

[10] Carlos Rey-Castro and Lourdes F Vega. “Transport properties of the ionic liquid 1-ethyl-3-methylimidazolium chloride from equilibrium molecular dynamics simulation. the effect of temperature”. In: *Journal of Physical Chemistry B* 110.29 (2006), pp. 14426–14435.

[11] Oleg Borodin. “Polarizable Force Field Development and Molecular Dynamics Simulations of Ionic Liquids”. In: *The Journal of Physical Chemistry B* 113.33 (2009), pp. 11463–11478.

[12] Hongjun Liu and Edward J. Maginn. “Effect of ion structure on conductivity in lithium-doped ionic liquid electrolytes: A molecular dynamics study”. In: *Journal of Chemical Physics* 139.11 (2013).

[13] Amrish Menjoge et al. “Influence of water on diffusion in imidazolium-based ionic liquids: A pulsed field gradient NMR study”. In: *Journal of Physical Chemistry B* 113.18 (2009), pp. 6353–6359.

[14] Timothy I. Morrow and Edward J. Maginn. “Molecular Dynamics Study of the Ionic Liquid 1-n-Butyl-3-methylimidazolium Hexafluorophosphate”. In: *The Journal of Physical Chemistry B* 107.34 (2003), pp. 9160–9160.

[15] Eugene Mamontov, Huimin Luo, and Sheng Dai. “Proton Dynamics in N,N,N,N-Tetramethylguanidinium Bis(perfluoroethylsulfonyl)imide Protic Ionic Liquid Probed by Quasielastic Neutron Scattering”. In: *The Journal of Physical Chemistry B* 113.1 (2009), pp. 159–169.

[16] Jonathan G. Huddleston et al. “Characterization and comparison of hydrophilic and hydrophobic room temperature ionic liquids incorporating the imidazolium cation”. In: *Green Chemistry* 3.4 (2001), pp. 156–164.

[17] Wenjing Li et al. “Effect of water and organic solvents on-the ionic dissociation of ionic liquids”. In: *Journal of Physical Chemistry B* 111.23 (2007), pp. 6452–6456.

[18] Jesse Gatten McDaniel and Chang Yun Son. “Ion Correlation and Collective Dynamics in BMIM/BF 4 Based Organic Electrolytes: From Dilute Solutions to the Ionic Liquid Limit”. In: *The Journal of Physical Chemistry B* 122 (2018), acs.jpcb.8b04886.

[19] Alexander Stoppa et al. “Structure and dynamics of 1-n -alkyl-3- n -methylimidazolium tetrafluoroborate + acetonitrile mixtures”. In: *Journal of Physical Chemistry B* 116.25 (2012), pp. 7509–7521.

[20] Betul Uralcan et al. “Concentration Fluctuations and Capacitive Response in Dense Ionic Solutions”. In: *The Journal of Physical Chemistry Letters* (2016), pp. 2333–2338. arXiv: 1604.03995.

[21] Jenel Vatamanu et al. “A comparative study of room temperature ionic liquids and their organic solvent mixtures near charged electrodes”. In: *Journal of Physics: Condensed Matter* 28.46 (2016), p. 464002.

[22] Alpha a. Lee et al. “Dynamics of Ion Transport in Ionic Liquids”. In: *Physical Review Letters* 115.10 (2015), p. 106101.

[23] Makoto Ue et al. “Electrochemical Properties of Quaternary Ammonium Salts for Electrochemical Capacitors”. In: *Journal of Electrochemical Society* 144.8 (1997), pp. 2684–2688.

[24] Alan B McEwen et al. “Electrochemical Properties of Imidazolium Salt Electrolytes for Electrochemical Capacitor Applications”. In: *Journal of The Electrochemical Society* 146.5 (1999), pp. 1687–1695.

[25] V. Ruiz et al. “Ionic liquid–solvent mixtures as supercapacitor electrolytes for extreme temperature operation”. In: *RSC Advances* 2.13 (2012), p. 5591.

[26] D. Weingarth et al. “A reliable determination method of stability limits for electrochemical double layer capacitors”. In: *Electrochimica Acta* 103 (2013), pp. 119–124.

[27] David Pech et al. “Ultrahigh-power micrometre-sized supercapacitors based on onion-like carbon.” In: *Nature nanotechnology* 5.9 (2010), pp. 651–4.

[28] Andrzej Lewandowski et al. “Performance of carbon–carbon supercapacitors based on organic, aqueous and ionic liquid electrolytes”. In: *Journal of Power Sources* 195.17 (2010), pp. 5814–5819.

[29] Eléonore Mourad et al. “Biredox ionic liquids with solid-like redox density in the liquid state for high-energy supercapacitors”. In: *Nature Materials* 16.4 (2016), pp. 446–453.

[30] Won Je Cho et al. “Supercapacitive properties of activated carbon electrode in organic electrolytes containing single- and double-cationic liquid salts”. In: *Electrochimica Acta* 89 (2013), pp. 807–813.

[31] Kazumi Chiba et al. “Electrolyte Systems for High Withstand Voltage and Durability I. Linear Sulfones for Electric Double-Layer Capacitors”. In: *Journal of The Electrochemical Society* 158.8 (2011), A872.

[32] Christoph Schütter et al. “Toward new solvents for EDLCs: From computational screening to electrochemical validation”. In: *Journal of Physical Chemistry C* 119.24 (2015), pp. 13413–13424.

[33] Laurie Ropel et al. “Octanol–water partition coefficients of imidazolium-based ionic liquids”. In: *Green Chem.* 7.2 (2005), pp. 83–90.

[34] Urszula Domańska, Zuzanna Żołek-Tryznowska, and Marek Królikowski. “Thermodynamic Phase Behavior of Ionic Liquids”. In: *Journal of Chemical & Engineering Data* 52.5 (2007), pp. 1872–1880.

[35] Urszula Domańska, Andrzej Marciniak, and Marek Królikowski. “Phase equilibria and modeling of ammonium ionic liquid, C2NTf2, solutions”. In: *Journal of Physical Chemistry B* 112.4 (2008), pp. 1218–1225.

[36] Joanna Łachwa et al. “Changing from an unusual high-temperature demixing to a UCST-type in mixtures of 1-alkyl-3-methylimidazolium bis{(trifluoromethyl)sulfonyl}amide and arenes”. In: *Green Chemistry* 8.3 (2006), pp. 262–267.

[37] Yuki Kohno and Hiroyuki Ohno. “Ionic liquid/water mixtures: From hostility to conciliation”. In: *Chemical Communications* 48.57 (2012), pp. 7119–7130.

[38] José N. Canongia Lopes and Agílio A. H. Pádua. “CL&P: A generic and systematic force field for ionic liquids modeling”. In: *Theoretical Chemistry Accounts* 131.3 (2012), p. 1129.

[39] José N. Canongia Lopes, Johnny Deschamps, and Agílio A. H. Pádua. “Modeling Ionic Liquids Using a Systematic All-Atom Force Field”. In: *The Journal of Physical Chemistry B* 108.6 (2004), pp. 2038–2047.

[40] José N. Canongia Lopes and Agílio A. H. Pádua. “Molecular Force Field for Ionic Liquids Composed of Triflate or Bistriflylimide Anions”. In: *The Journal of Physical Chemistry B* 108.43 (2004), pp. 16893–16898.

[41] William L Jorgensen and Nora A. McDonald. “Development of an all-atom force field for heterocycles. Properties of liquid pyridine and diazenes”. In: *Journal of Molecular Structure: THEOCHEM* 424.1-2 (1998), pp. 145–155.

[42] William L. Jorgensen, David S. Maxwell, and Julian Tirado-Rives. “Development and testing of the OPLS all-atom force field on conformational energetics and properties of organic liquids”. In: *Journal of the American Chemical Society* 118.45 (1996), pp. 11225–11236.

[43] Carl Caleman et al. “Force Field Benchmark of Organic Liquids: Density, Enthalpy of Vaporization, Heat Capacities, Surface Tension, Isothermal Compressibility, Volumetric Expansion Coefficient, and Dielectric Constant”. In: *Journal of Chemical Theory and Computation* 8.1 (2012), pp. 61–74.

[44] H. A. Lorentz. “Ueber die Anwendung des Satzes vom Virial in der kinetischen Theorie der Gase”. In: *Annalen der Physik* 248.1 (1881), pp. 127–136.

[45] Daniel Berthelot. “Sur le mélange des gaz”. In: *Compt. Rendus* 126 (1898), pp. 1703–1706.

[46] Xiuyun Zhang et al. “How the Orientation of Graphene Is Determined during Chemical Vapor Deposition Growth”. In: *The Journal of Physical Chemistry Letters* 3.19 (2012), pp. 2822–2827.

[47] Mark James Abraham et al. “Gromacs: High performance molecular simulations through multi-level parallelism from laptops to supercomputers”. In: *SoftwareX* 1-2 (2015), pp. 19–25.

[48] L. Martínez et al. “PACKMOL: A package for building initial configurations for molecular dynamics simulations”. In: *Journal of Computational Chemistry* 30.13 (2009), pp. 2157–2164. arXiv: NIHMS150003.

[49] Shankar Kumar et al. “The weighted histogram analysis method for free-energy calculations on biomolecules. I. The method”. In: *Journal of Computational Chemistry* 13.8 (1992), pp. 1011–1021. arXiv: NIHMS150003.

[50] Benoît Roux. “The calculation of the potential of mean force using computer simulations”. In: *Computer Physics Communications* 91.1-3 (1995), pp. 275–282.

[51] Jack Lidmar. “Improving the efficiency of extended ensemble simulations: The accelerated weight histogram method”. In: *Physical Review E - Statistical, Nonlinear, and Soft Matter Physics* 85.5 (2012), pp. 1–5.

[52] V. Lindahl, J. Lidmar, and B. Hess. “Accelerated weight histogram method for exploring free energy landscapes”. In: *Journal of Chemical Physics* 141.4 (2014). arXiv: 1407.7415.

[53] William Humphrey, Andrew Dalke, and Klaus Schulten. “{VMD} – {V}isual {M}olecular {D}ynamics”. In: *Journal of Molecular Graphics* 14 (1996), pp. 33–38.

[54] John Stone. “\em An Efficient Library for Parallel Ray Tracing and Animation”. MA thesis. Computer Science Department, University of Missouri-Rolla, 1998.

[55] K R Seddon. “Ionic liquids: designer solvents”. In: *The International George Papatheodorou Symposium: Proceedings, ed. S. Boghosian, V. Dracopoulos, CG Kontoyannis and GA Voyiatzis, Institute of Chemical Engineering and High Temperature Chemical Processes, Patras*. 1999, pp. 131–135.

[56] Robin D. Rogers and Kenneth R. Seddon. “Ionic Liquids - Solvents of the Future?” In: *Science* 302.5646 (2003), pp. 792–793.

[57] Xiaochun Zhang, Zhiping Liu, and Wenchuan Wang. “Screening of ionic liquids to capture CO 2 by COSMO-RS and experiments”. In: *AIChE Journal* 54.10 (2008), pp. 2717–2728. arXiv: 0201037v1 [arXiv:physics].

[58] Amitesh Maiti. “Theoretical Screening of Ionic Liquid Solvents for Carbon Capture”. In: *ChemSusChem* 2.7 (2009), pp. 628–631.

[59] Samantha E. McLeese et al. “Design of ionic liquids via computational molecular design”. In: *Computers and Chemical Engineering* 34.9 (2010), pp. 1476–1480.

[60] Arunprakash T. Karunanithi and Amirhossein Mehrkesh. “Computer-aided design of tailor-made ionic liquids”. In: *AIChE Journal* 59.12 (2013), pp. 4627–4640.

[61] K. G. Sprenger, Vance W. Jaeger, and Jim Pfaendtner. “The general AMBER force field (GAFF) can accurately predict thermodynamic and transport properties of many ionic liquids”. In: *Journal of Physical Chemistry B* 119.18 (2015), pp. 5882–5895.

[62] José N a Canongia Lopes and Agílio A. H. Pádua. “Nanostructural organization in ionic liquids”. In: *Journal of Physical Chemistry B* 110.7 (2006), pp. 3330–3335.

[63] Giacomo Saielli, Alessandro Bagno, and Yanting Wang. “Insights on the isotropic-to-Smectic a transition in ionic liquid crystals from coarse-grained molecular dynamics simulations: The role of microphase segregation”. In: *Journal of Physical Chemistry B* 119.9 (2015), pp. 3829–3836.

[64] Alessandro Triolo et al. “Nanoscale segregation in room temperature ionic liquids”. In: *Journal Of Physical Chemistry B* 111.18 (2007), pp. 4641–4644.

[65] David Van Der Spoel, Paul J. Van Maaren, and Herman J.C. Berendsen. “A systematic study of water models for molecular simulation: Derivation of water models optimized for use with a reaction field”. In: *Journal of Chemical Physics* 108.24 (1998), pp. 10220–10230.

[66] C Schröder, M Haberler, and O Steinhauser. “On the computation and contribution of conductivity in molecular ionic liquids”. In: *Journal of Chemical Physics* 128.13 (2008).

[67] Mo Chen et al. “Molecular dynamics simulations of the ionic liquid 1-n-butyl-3-methylimidazolium chloride and its binary mixtures with ethanol”. In: *Journal of Chemical Theory and Computation* 10.10 (2014), pp. 4465–4479.

[68] Florian Dommert and Christian Holm. “Refining classical force fields for ionic liquids: Theory and application to [MMIM][Cl]”. In: *Physical Chemistry Chemical Physics* 15.6 (2013), pp. 2037–2049.

[69] Mathieu Salanne et al. “Conductivity-viscosity-structure: Unpicking the relationship in an ionic liquid”. In: *Journal of Physical Chemistry B* 111.18 (2007), pp. 4678–4684.

[70] W Zhao et al. “Are There Stable Ion-Pairs in Room-Temperature Ionic Liquids? Molecular Dynamics Simulations of 1-n-Butyl-3-methylimidazolium Hexafluorophosphate”. In: *Journal of the American Chemical Society* 131.43 (2009), pp. 15825–15833.

[71] Yong Zhang, Akihito Otani, and Edward J. Maginn. “Reliable Viscosity Calculation from Equilibrium Molecular Dynamics Simulations: A Time Decomposition Method”. In: *Journal of Chemical Theory and Computation* 11 (2015), pp. 3537–3546.

[72] Manish S Kelkar, Wei Shi, and Edward J. Maginn. “Determining the accuracy of classical force fields for ionic liquids: Atomistic simulation of the thermodynamic and transport properties of 1-ethyl-3-methylimidazolium ethylsulfate ([emim][EtSO4]) and its mixtures with water”. In: *Industrial and Engineering Chemistry Research* 47.23 (2008), pp. 9115–9126.

[73] Eric T. Fox et al. “Physicochemical properties of binary ionic liquid-aprotic solvent electrolyte mixtures”. In: *Journal of Physical Chemistry C* 117.1 (2013), pp. 78–84.

[74] Pablo B. Sánchez et al. “Cosolvent effect on physical properties of 1,3-dimethyl imidazolium dimethyl phosphate and some theoretical insights on cellulose dissolution”. In: *Journal of Molecular Liquids* 265 (2018), pp. 114–120.

[75] V. K. Sharma, S. Solanki, and S. Bhagour. “Thermodynamic Properties of Ternary Mixtures Containing Ionic Liquid and Organic Liquids: Excess Molar Volume and Excess Isentropic Compressibility”. In: *Journal of Chemical & Engineering Data* 59.4 (2014), pp. 1140–1157.

[76] Heiko Niedermeyer et al. “Mixtures of ionic liquids”. In: *Chemical Society Reviews* 41.23 (2012), p. 7780.

[77] Yifei Xu et al. “A Dual Ionic Liquid-Based Low-Temperature Electrolyte System”. In: *Journal of Physical Chemistry B* 122.50 (2018), pp. 12077–12086.

[78] Mathieu Salanne. “Simulations of room temperature ionic liquids: from polarizable to coarse-grained force fields”. In: *Phys. Chem. Chem. Phys.* 17.22 (2015), pp. 14270–14279. arXiv: 1505.07860.

[79] Oldamur Hollóczki et al. “On the origin of ionicity in ionic liquids. Ion pairing versus charge transfer”. In: *Phys. Chem. Chem. Phys.* 16.32 (2014), pp. 16880–16890.

[80] Igor Leontyev and Alexei Stuchebrukhov. “Accounting for electronic polarization in non-polarizable force fields”. In: *Physical Chemistry Chemical Physics* 13.7 (2011), pp. 2613–2626.

[81] Junmei Wang et al. “Development and testing of a general amber force field”. In: *Journal of Computational Chemistry* 25.9 (2004), pp. 1157–1174.

[82] Thorsten Köddermann, Dietmar Paschek, and Ralf Ludwig. “Molecular Dynamic Simulations of Ionic Liquids: A Reliable Description of Structure, Thermodynamics and Dynamics”. In: *ChemPhysChem* 8.17 (2007), pp. 2464–2470. arXiv: 1408.1149.

[83] Thorsten Köddermann, Dirk Reith, and Ralf Ludwig. “Comparison of force fields on the basis of various model approaches - How to design the best model for the [CnMIM][NTf2] family of ionic liquids”. In: *ChemPhysChem* 14.14 (2013), pp. 3368–3374.

[84] Jan Neumann et al. “Revisiting imidazolium based ionic liquids: Effect of the conformation bias of the [NTf2] anion studied by molecular dynamics simulations”. In: *Journal of Chemical Physics* 148.19 (2018).

Chapter 5

Effects of Added Water Content on the Structure and Dynamics of Confined Electrolytes

In carefully-controlled experiments and computer models, the content of water in confined fluids can be controlled, even completely removed. However, it is difficult to keep components completely dry and interactions with water are a relevant topic for safety considerations in devices at the application level. Therefore, it is necessary to study the effects of humidification on supercapacitor-like systems. A fundamental understanding is necessary to inform device design, either to avoid undesired effects or perhaps leverage them advantageously. In this chapter, two model systems are interrogated with MD simulations and QENS experiments. Each system is representative of devices that could be used in next-generation energy storage devices. The first system is an ionic liquid confined in a nanoporous carbon and the second system is an ionic liquid intercalated into a MXene. In each system, aggressive humification was used to study the effects of added water content, including at higher concentrations than typically reported in the literature. In each system we find the addition of water increases the dynamics of the ionic liquids, especially at high water content in which these increases are particularly drastic. Informed by molecular models, we attribute this speedup not only to the inherent interactions with a mobile solvent but also rearrangement of fluids in pores. Specifically, the preferential adsorption of water at interfaces displaces cations toward other regions of the pore in which their dynamics are inherently less restricted. The work presented here has been featured in two peer-reviewed publications.[1,2] Included are contributions from numerous experimental collaborators particularly Naresh C. Osti and Eugene Mamontov of Oak Ridge National Laboratory and Boris Dyatkin, Katherine L. Van Aken and Mohamed Alhabeb of Drexel University.

5.1 Background

Ionic liquids are highly hygroscopic, even to small amounts of water. By their nature ionic liquids contain either species that are purely ionic (i.e. halide anions) or species with other charged and polar functional groups, they have strongly favorable interactions with water. As a result, the adsorption of water is virtually unavoidable in relevant contexts, i.e. synthesis and characterization of samples in labs and manufacturing and operating devices in industrial applications..[3,4] Many ionic liquids are so hygroscopic that they will adsorb water from the wapor vapor content of air in ambient conditions.[5] Unsurprisingly, the presence of water has major implications for the physiochemical properties of ionic liquids (structure, transport, thermodynamic, etc.) in bulk,[5–11] at interfaces,[4,12–14] and under confinement.[13,15]

In bulk, the addition of water has different effects at different compositions. Some simulation studies[6,16] have investigated the effects of water sorption of water over the entire range, from dilute water in ionic liquid to dilute ionic liquid in water. Starting with a neat ionic liquid, the first added water molecules are found tucked away in small pockets inside the polar domains of the ionic liquid, seeming to favor interactions with the ionic portions of the ions. At low water concentrations, many bulk properties of the ionic liquid are largely unaffected; density decreases and diffusivity increases, but only slightly. After a certain amount of water sorption, the polar domains are essentially saturated and, in many ionic liquids, the presence of large hydrophobic functional groups can result in miscibility issues. In some cases, self-assembly of clusters of various shapes and sizes has been observed.[17] Some narrow applications in catalysis and separations can leverage these micelle-like structures but they are generally not desirable for electrochemical applications. By contrast, some ionic liquids are miscible with water at all compositions; it has been proposed that hydrogen bonding is responsible for the formation of large water networks that make this possible. At some higher composition of water, these mixtures can be understood as ionic liquid salts in water solvent. There can still be some signatures of phase separation but many ionic liquids exist as single pair or free ions in dilute solutions in water.[7] In these mixtures, the diffusivity of ionic liquid molecules is drastically higher than in bulk[6,10,16] even within an order of magnitude of bulk

water. These speeedups are remarkable; neat ionic liquids typically exhibit diffusivities on order of $1 \times 10^{-12}\,\mathrm{m^2\,s^{-1}}$–$1 \times 10^{-13}\,\mathrm{m^2\,s^{-1}}$, compared to $2 \times 10^{-9}\,\mathrm{m^2\,s^{-1}}$, so these factors represents on the order of hundreds to thousands times faster transport.

Little work, comparatively, has been done to understand the effects of water sorption in ionic liquids at interfaces and in confinement. Some studies[4,13–15] have used molecular models to show water tends to preferentially adsorb at the interface relative to the bulk. Similar effects have been reported using AFM experiments.[12] These systems are naturally suited to molecular dynamics simulations, as their atomistic resolution provides enough low-level insights to inform relevant properties and sufficiently representative length and timescales are accessible with modern software and hardware. Studying the structure and dynamics of individual molecules, particularly molecules as small as water, is more difficult in simulation. AFM probes can detect the location, but not necessarily density, of structural layers at interfaces, but is not tractable for studying the structure fluids in confinement. Dynamics of individual species are accessible in the bulk phase with NMR but resolving transport in confinement is not as tractable. QENS experiments are well-equipped to study the dynamics of confined species, especially water. The scattered waves, if the sample is prepared properly, does not discern between species in confinement or in bulk.

5.2 Humidification of Ionic Liquids Confined in Nanoporous Carbon

5.2.1 Sample Preparation and Characterization

Mo_2C CDCs were synthesized by etching a Mo_2C crystal with Cl_2 gas. As molybdenum carbide-based CDCs are less common, N_2 sorption experiments were conducted to understand the pore structure of the carbon material. A Quadrasorb-I gas sorption analyzer was used to conduct these experiments and the QSDFT kernel was implemented by the associated Quadrawin softare. Measurements were conducted at 77 K. The specific surface area (SSA) was calculated by the traditional Brunauer-Emmett-Teller (BET) method, which is baed on a fit to the adsorption load in the range 0.05 - 0.3 $P/P0$. These powders were used in separate QENS and electrochemistry

experiments.

For QENS experiments, [$BMIM^+$][TF_2N^-] was synthesized as described by Hillesheim et al.[Hillesheim2013] was added into the pores of CDC using the previously described vacuum infiltration process[1] Approximately 5.0 g of the RTIL were dispersed in a glass beaker in acetonitrile (99.5+% purity, Fischer Scientific). Based on the cumulative pore volume ($1.86\,cm^3\,g^{-1}$) of CDC, as well as the bulk density of [$BMIM^+$][TF_2N^-] ($\sim 1.5\,g\,cm^{-3}$), a measured amount of the CDC powder was added to the solution in a ratio that would allow the RTIL to occupy 100% of its pore volume. The slurry was stirred (with a magnetic stir bar) at room temperature to allow acetonitrile to evaporate. Once visible liquid disappeared, the resulting powder dried under a low vacuum (0.01 Torr) at 100 °Cfor 24 h. Finally, to ensure uniformity, the powder was ground up in an agate mortar. CDC and [$BMIM^+$][TF_2N^-] samples were loaded into standard aluminum QENS sample holders of 0.25 mm thickness and left open in a plastic desiccator. A dish with excess D_2O (purchased from Sigma Aldrich) was placed next to the samples in the desiccator. The entire system was sealed and outgassed for 5 minutes to create a low vacuum. It was left to sit for 4, 8, or 10 h in order to add different amounts of water content. Each sample holder with [$BMIM^+$][TF_2N^-]-filled CDC sample was weighed prior to and after D2O vapor exposure. A baseline reference sample was sealed in an inert environment in an Ar-filled glovebox and was, therefore, devoid of water.

5.2.2 Model

To model ionic liquids confined in CDCs, a slit pore consisting of two parallel three-layer graphene sheets was constructed. Pore walls were separated by 2.5 nm, defined as the separation distance between inner planes of carbon atoms. The cross-sectional area of the pore was 2.5 nm by 5.5 nm. On either side of the pore, laterally, was a bulk region of volume 4.0 nm by 4.0 nm by 5.5 nm, which allowed for density equilibration in the pore and molecules to sample interactions in both bulk and confinement. Because the QENS signal is believed to depend primarily on fluid behavior in mesopores, micropores were not included in this model. All MD simulations were performed with the MD software package GROMACS 5.0.8.[18] Ionic liquid molecules were de-

scribed with the force field of Lopes et al.,[19–21] which is similar to OPLS but specifically tuned for ionic liquids, including [$BMIM^+$][TF_2N^-]Ċharges were scaled by a factor of 0.8 to better describe transport properties.[22] Water molecules were described with the TIP3P model.[23] A time step of 1 fs and the "v-rescale" thermostat[24] with a time constant of 1 ps were used throughout. Carbon atoms making up the graphitic slit pores were fixed in place. All nonbonded interactions were computed with a cutoff of 1.1 nm. Electrostatic interactions were computed with the PME method, using a real-space cutoff of 1.1 nm and a Fourier grid spacing of 0.1 nm. All bonds were constrained using the LINCS algorithm. The concentrations and number of molecules used are shown in Table 5.1.

Table 5.1: Concentrations and corresponding number of molecules used in MD simulations.

Water concentration (mol fraction)	Number of IL pairs or water molecules
0.203	472, 120
0.382	461, 285
0.482	452, 420
0.602	436, 660
0.792	383, 1455

Pristine graphene is highly hydrophobic, yet CDCs are hydrophilic[25] because of structural and chemical defects on the surfaces of pore walls. To simply model this water-CDC wall interaction, the energetic coefficient of the water-carbon interaction $\varepsilon_{water-wall}$ was doubled. Other cross interactions were not changed. Initial configurations for each system were generated with PACKMOL.[26] Because PACKMOL relies on geometric constraints and does not consider energetics, the first step in each simulation was to perform an energy minimization. Then, systems were annealed by heating to 600 K over 1 ns, holding at 600 K for 3 ns, and then cooling to 300 K over 5 ns. Then, a 30 ns production run of NVT simulation at 300 K was performed. Ion diffusivities were computed using the 3D Einstein diffusion equation. Region-specific diffusivities were computed by slicing the last 20 of the 30 ns trajectory into 200 slices of 100 ps length. Ion selections were updated

at the beginning of each slice and the final MSD, from which the diffusivity was computed, was generated by averaging the MSD from all slices. Cations are separated into "wall" and "center" groups by their position in the pore. Cations with a center of mass less than 0.75 nm from the pore walls make up the wall region and cations with a center of mass farther than this distance from the pore walls are considered in the center region.

5.2.3 Results

We begin by analyzing the pore structure of the CDC samples before and after filling them with ionic liquid. These pore size distributions are shown in Fig. 5.1, with peaks at approximately 0.8 nm and 3.1 nm. Unlike many CDCs, these derived from Mo_2C exhibit a bimodal pore size distribution with similar amounts of micropore (<2 nm) and mesopore (2 nm–10 nm) volume. The surface area of the bare carbon was 2275 $m^2 g^{-1}$ before loading and 0.568 $m^2 g^{-1}$ after loading, indicating that the ionic liquid complete fills the pores.

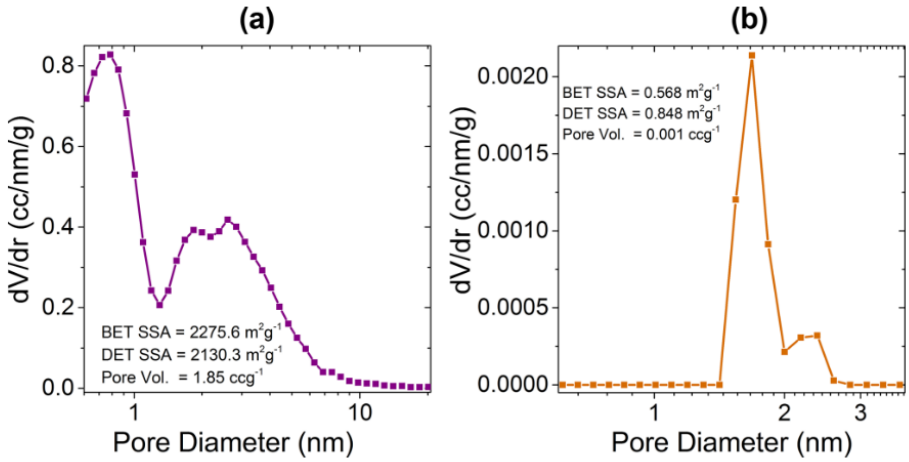

Figure 5.1: Pore size distributions of Mo_2-CDC samples via nitrogen adsorption experiments. Also included are estimates of SSA from BET and SSA and pore volume from DFT. (a) Pore size distributions before filling CDC with ionic liquid and (b) after filling. The reduction in pore volume by approximately 2000 indicates that the CDC pores are completely filled.

These samples were next analyzed using QENS. First, using the BASIS[27] backscattering spectrometer at ORNL, we measured the elastic intensity as a function of temperature. Similar to an ionic liquid confined on micropores,[28] the spectrum presented in Fig. 3(a) does not show any

abrupt changes, indicating the absence of phase transitions and confirming complete confinement of the ionic liquid inside the pores.

Next, QENS experiments were conducted at the NG-2 high flux backscattering spectrometer (HFBS)[29] at the National Institutes of Standard and Technology (NIST). Details of the experiments are enumerated in our manuscript.[30] Because the anion in this ionic liquid lacks hydrogen atoms and the water was deuterated, the QENS signal is dominated by scattering off of cations. Spectra for each sample, including without water (0h) and other amounts of water (4h, 8h, 10h) are shown in Fig. 5.2. These spectra are fit to a Lorentzian jump diffusion model from which diffusivities are backed out. These values are reported in Fig. 5.3, from which it is clear that the addition of water enhances the diffusivity of cations. These QENS experiments report an increase in cation diffusivity in response to added water content as measured by added mass and approximated by D_2O exposure time. With no D_2O in the pores, the derived value $D = 0.52 \pm 0.01 \times 10^{-10}\,\mathrm{m^2\,s^{-1}}$ is slightly higher than the diffusion coefficient reported for bulk ($D = 0.44 \pm 0.03 \times 10^{-10}\,\mathrm{m^2\,s^{-1}}$)[31] Note that the cation diffusivity in this CDC is $\sim$5 times lower than a previously reported diffusivity ($D = 2.45 \pm 0.2 \times 10^{-10}\,\mathrm{m^2\,s^{-1}}$) in mesoporous carbon with large ($\sim$8.8 nm) pores. This smaller value can be attributed to the cumulative effects of the smaller pores (0.7–3.1 nm) and the limited dynamic window of the HFBS, as evident from the raising tail of the dynamic susceptibility peak, but not its maximum (Fig. 5), as observed for all samples.

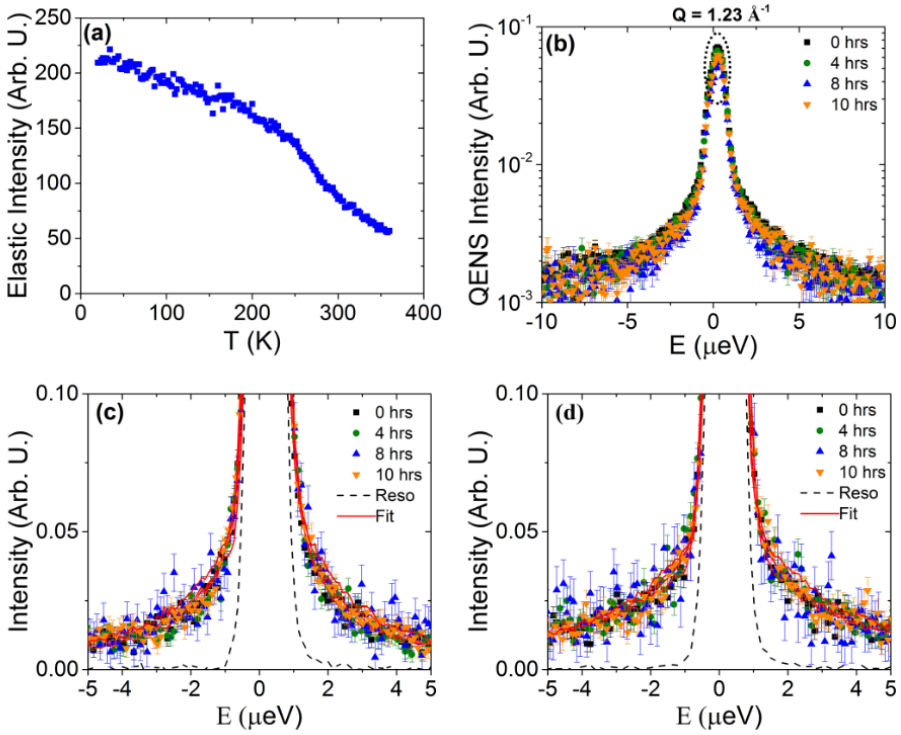

Figure 5.2: (a) Elastic scan of dry [BMIM$^+$][TF$_2$N$^-$] in CDCs. The smooth relationship with temperature indicates a lack of discrete phase transition. (b) Mass-normalized structure factor of all samples showing a drop, as marked by a dotted ellipsoid, in intensity after the addition of water. QENS spectra at (c) $Q = 0.68\,\text{Å}^{-1}$ and (d) $Q = 1.16\,\text{Å}^{-1}$ at 290 K. The symbols correspond to the data collected at different exposure times as indicated in the figure. Solid lines are fit using a Lorentzian function and the black dotted lines show the instrument resolution measured at 4 K. Data have been normalized to the highest intensity for the purpose of comparison and truncated at 0.1 arbitrary units for clarity.

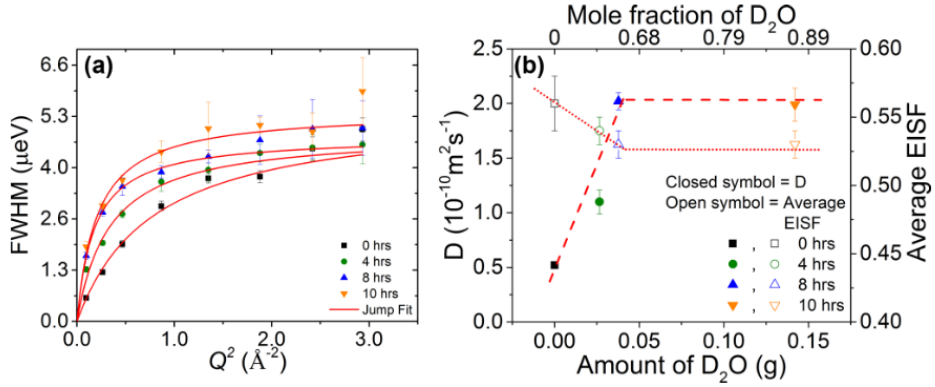

Figure 5.3: (a) FWHMs extracted from a single Lorentzian fit of the structure factors, shown in Fig. 5.2, of the confined [BMIM$^+$][TF$_2$N$^-$] as a function of added water content fitted to a jump diffusion model.(b) Corresponding diffusion coefficients of cations (left y axis) and average elastic incoherent scattering fraction (right y axis). The dotted lines are a guide to the eye.

Since the ions are sufficiently small, [$BMIM^+$][TF_2N^-] likely fills both mesopores (>1 nm) and micropores (<1 nm). On the characteristic time scale ($\sim$10 ns) of the HFBS experiment resolution,[29] the cations inside the micropores remain immobilized due to tight packing of ions inside the pore and contribute only to the elastic signal. Therefore, measured dynamics account solely for the cations confined in the 3.1 nm pores.

Narrow pores (1–3.1 nm), which preclude the formation of distinct high-density (immobilized ions at the pore wall-electrolyte interface) and low-density (center of pore) regions, may give rise to the more bulk-like diffusion behavior of confined cations compared to the larger effect on the dynamics in the pores of 8.8 nm size.[31] The current result is consistent with the relationship between diffusivity in bulk and in confinement observed for ILs in silica monoliths with the pore sizes of 5–10 nm.

Even though [$BMIM^+$] has a long hydrophobic butyl chain and absorbs 0.26 wt. % water at 59% relative humidity, remarkably, our measurements show that the confined [$BMIM^+$][TF_2N^-] absorbs significantly larger amount of water ($\sim$10 times) compared to the bulk liquid. Such water uptake yields a two-fold diffusion coefficient increase after 4 h of D2O exposure. This suggests that water molecules predominantly adsorb onto CDC surfaces and displace some of the adsorbed cations from their original sites on pore surfaces that leads to a decrease in elastic incoherent scattering fraction (EISF) (Fig. 5.3) as a function of water uptake until the CDC pores become saturated. Those [$BMIM^+$] ions, which had been previously immobilized in the system, subsequently, demonstrate higher diffusivities. It is worth noting here that even in the bulk state, addition of water increases the diffusivity of cation by reducing the cohesive attraction between the [$BMIM^+$][TF_2N^-] molecules. Therefore, overall increase in the diffusivity of cation could be the joint effect of ion displacement, as evident from a reduction in elastic intensity (Fig. 5.5), and a possible screening of the attraction between the ionic liquid molecules by water. Furthermore, nearly similar values of residence times, which is in a range of the characteristic times predicted by molecular dynamics simulations for the adsorption of ions of [$BMIM^+$][PF_6^-] on CDC,[32] illustrate that the increase in diffusivity is due to an increase in the average jump length, consistent with a

gradual decrease of cation density on the walls of the microspores.

After increasing the D2O vapor exposure time to 8 h, D2O uptake increased from 3.5wt.% (1.3 mol D2O per mol of IL) to 5.2wt.% (1.9 mol D2O per mol of IL). This yielded yet another twofold diffusion coefficient increase, likely due to the same displacement effect. However, after 10 h of D2O vapor exposure and a substantially higher heavy water uptake ($\sim$20 wt.%, or 7.6 mol D2O per mol of IL), we did not observe any further increase in cation diffusivity. We conclude that the ionic liquid-filled pore surfaces became saturated with D2O after 8 h of vapor exposure. For comparison, CDCs with unfilled pores can adsorb up to 35 wt. % of water relative to their dry mass, depending on the pore volume. Since the CDC material in this study was treated with NH_3(g) after Cl_2(g) etching, it likely retained some nitrogen-containing groups (–NH_3, –NH_2, quaternary nitrogen) and chemisorbed oxygen. Consequently, its surfaces were hydrophilic and accelerated water vapor uptake. The observed increase in the microscopic diffusivity of ionic liquid with increasing water content may explain the greater electrochemical performance of the ionic liquid observed in water-containing pores from electrochemical measurements.

Molecular dynamics (MD) simulations were used to further investigate high water uptake in confined [$BMIM^+$][TF_2N^-] and humidity effects on cation dynamics. The simulation predicts greater water composition in pores than in bulk and, for low and moderate water concentrations, preferential arrangement on the pore walls due to defects introduced interactions, in contrast to depletion of water molecules observed in defect free graphene,[4] over the center of the pore.

Figure 9 shows that, for low to moderate water concentrations, water accumulates on the pore walls and is absent from the middle regions of pores. At larger water concentrations, however, water saturates available pore surfaces and begins to accumulate in the pore centers. At such sample compositions, a relatively smaller fraction of ions is found on the pore walls. Accordingly, and similar to the QENS observation, MD simulations predict greater cation diffusivity upon addition of water. A summary is presented as an inset in Fig. 9, showing a relationship between cation diffusivity and water concentration for a model confined system.

Comparison of the experimental cation diffusivities in Fig. 4(b) and the computed cation dif-

fusivities in Fig. 9 inset reveals both the power and limitations of MD simulations, which compute system parameters in accordance with the assumed system composition. While the MD cation diffusiv- ities for Xw = 0 and Xw = 0.2, where the water molecules are near the walls (Fig. 9), are in reasonable agreement with the experimental data, the MD cation diffusivities rise very quickly once, at higher concentrations, the water molecules start occupying the middle of the pore (Fig. 9). On the other hand, the saturation of the cation diffusivities observed in the experiment at higher water concentrations suggests that, in experimental samples, the water molecules occupy sites near the walls, but not the middle of the pores, and the progressively increasing water uptake with the prolonged exposure to vapors is due to water molecules going elsewhere in the sample after saturating the near-walls sites. The likely reason for that is the strong repulsive interactions between water molecules and the ionic liquid. These repulsive interactions would indeed result in high cation diffusivities, as observed in the simulations, if the water molecules could be mixed with the ionic liquid in the middle of the pores. This can be observed in the simulation, where the system composition is set up at will, but not necessarily in real samples, where, after the saturation of the near-wall sites by water molecules, further water uptake from the vapor could not get water molecules in the middle of the pores. This is in agreement with the well-documented low miscibility of bulk ionic liquids with water. Once the water molecules in the simulation are introduced in sufficient concentrations to occupy the middle of the pores, the resulting cation diffusivities become much higher than those observed in the experiment, thus demonstrating that the water uptake in the real pores is limited to water molecules near the pore walls.

5.3 Humidification of Ionic Liquids Confined in MXene

5.3.1 Sample Preparation

MXene samples were sythesized by Mohammed Alhabeb at Drexel University. 10 g of Ti_3C_2 powder was synthesized using 10 wt % hydrofluoric acid (HF, Organic Across) according to a previous method described in detail elsewhere.[33] A mixture of 6 g of MXene, 10 mL of acetonitrile

(Alfa Aesar), and 1.2 g of 1-ethyl-3-methylimidazolium bis(trifluoromethylsulfonyl)imide (EMIm Tf2N (Sigma- Aldrich)) was sonicated for 20 min. The mixture was subsequently stirred at 60 °°C for 12 h, and then, the temperature was gradually increased to 70, 80, 100, and, finally, 120 °°C to evaporate the acetonitrile. The resulting MXene/EMIm Tf2N powder was dried in a vacuum oven at 120 °C for 12 h. The MXene powder and the MXene/ EMIm Tf2N powder were both used directly for the experiments.

5.3.2 QENS Experiments

D2O-loaded samples were prepared by storing the three samples (pristine MXene, MXene/IL, and the IL liquid in the bulk form) in open aluminum sample holders along with a cuvette with excess D_2O inside a glass desiccator for 12 h. The D_2O absorption was calculated from the weight uptake. MXene (1 g) and 1 g of EMIm Tf2N absorbed 0.019 and 0.036 g of D_2O, respectively. MXene EMIm Tf2N (1 g) absorbed 0.025 g ofD2O, which is close to the amount expected to be absorbed by 1 g of 5:1 weight ratio mixture of the MXene powder and the ionic liquid. Dry and D2O - exposed samples of MXene EMIm Tf2N, as well as pristine and D2O–exposed bulk EMIm Tf2N liquid samples, were placed into flat aluminum sample holders with inserts providing 0.25 mm thick samples and sealed with indium wire for quasi-elastic neutron scattering (QENS) measurement using a high-flux backscattering spectrometer (HFBS)[29] at the NIST Center for Neutron Research. DAVE[34] software was used for data reduction and analysis.

5.3.3 Molecular Dynamics Simulations

We employ classical molecular dynamics (MD) simulations, carried out with GROMACS 5.1.4.[18] We considered [$EMIM^+$][TF_2N^-] confined between MXene slabs 10.47 nm apart, which would be consistent with ions confined in the interstack space in MXene. The composition of the corresponding samples exposed to humidity was 25 mol % water, as estimated from the D_2O weight uptake by the ionic liquid. The SPC/E model of water[35] was used throughout. Ionic liquid interactions were described using the classical force field of Canongia Lopes and Pádua

et al..[19–21] MXene interactions were described using custom parameters largely derived from ClayFF.[36] Lorentz–Berthelot mixing rules were used throughout. After systems were built, 1000 steps of energy minimization were performed. For all molecular dynamic simulations of MXene channels, the NVT ensemble, the Nose-Hoover thermostat with a time constant of 1 ps, and a integrator timestep of 0.5 fs were used throughout. For bulk simulations, a Berendsen barostat with reference pressure 1 bar and time constant 1 ps was added and the timestep was increased to 1 fs. Because we were focused on the dynamics of the fluid and not structural changes in the carbide layer of the MXene, positions of the titanium and carbon atoms in the MXene were fixed, whereas surface atoms were integrated in a regular manner. First, an equilibration step of 10 million timesteps (5 ns) was performed. Then, a sampling trajectory of 100 million timesteps (50 ns) was generated for analysis.

5.3.4 Results

We begin with a summary of the experimental results, summarized in Fig. 5.5, Fig. 5.4, and Table 5.2, the details of which are enumerated more verbosely in the manuscript.[1] First, the elastic scans in Fig. 5.5 characterize the phase behavior of the fluids. Note again that the nature of the sample synthesis, using a hydrogen-free anion and deuterated water, means the QENS signal primarily represents the behavior of cations. Decrases in elastic intensity with increasing temperature indicate increased mobility of detected species. Smooth decreases from low temperature represent typical thermal behavior whereas stepwise or other sharp changes represent other phenomena, typically phase transitions. Elastic scans of the bulk fluids include a sharp drop that represents a melting phase transition near 275 K. In this case, the presence of water decreases the temperature of this change by approximately 5 K. The ionic liquid-intercalated MXenes, however, show two transitions. There is one at approximately the same temperatures as the bulk samples, indicating there is a relevant amount of bulk-like fluid behavior in these systems. There is also a melting transition at lower temperatures, approximately 265 K, which we attribute to the melting-like phase transition of confined fluids. In these systems, the addition of water appears to have little to no

effect on the melting temperature.

Based on the temperatures of the elastic scans, QENS spectra were collected at 270 K and 280 K. Single Lorentzian functions were fit to the data and a jump diffusion model was used to back out diffusivities. Using Table 5.2 it is clear that confinement decreases the mobility of the cations, however by a lesser amount than expected. The space between individual layers, which can be intercalated by water, is typically on the order of a few angstroms, or only enough space for a layer or two of water molecules. This degree of confinement usually produces a greater slowdown. For example, the diffusivity of water in a monolayer-like structure has been reported to be on the order of 10×10^{-11} $m^2 s^{-1}$,[37] which is less than 1% of its bulk value. Diffusivity in these samples decreased by approximatley 10% and 40% for the dry and humid samples, respectively. Therefore, we believe the primary contribution to the QENS signal is not of cations confined between individual MXene layers (nanoconfinement) but cations in larger inter-stack regions (mesoconfinement).

Table 5.2: [$EMIM^+$] diffusivities as measured by QENS experiments.

D_{cation} in $10^{-10} m^2 s^{-1}$	Dry		Humidified	
Sample	270 K	280 K	270 K	280 K
[$EMIM^+$][TF_2N^-] in bulk		0.95 ± 0.12		1.47 ± 0.21
[$EMIM^+$][TF_2N^-] in MXene	0.42 ± 0.08	0.83 ± 0.02	0.55 ± 0.07	0.89 ± 0.09

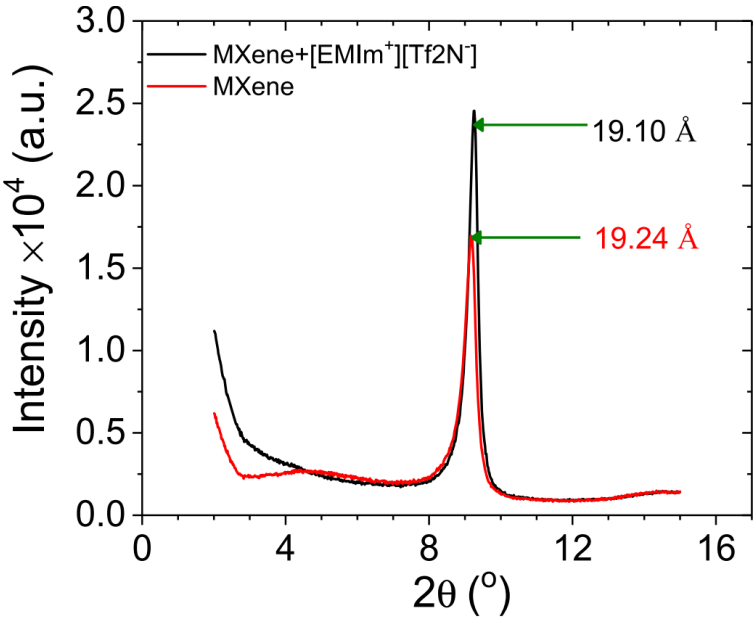

Figure 5.4: X-ray diffraction pattern of MXene samples before (red) and after (black) the addition of the ionic liquid [EMIM$^+$][TF_2N^-].

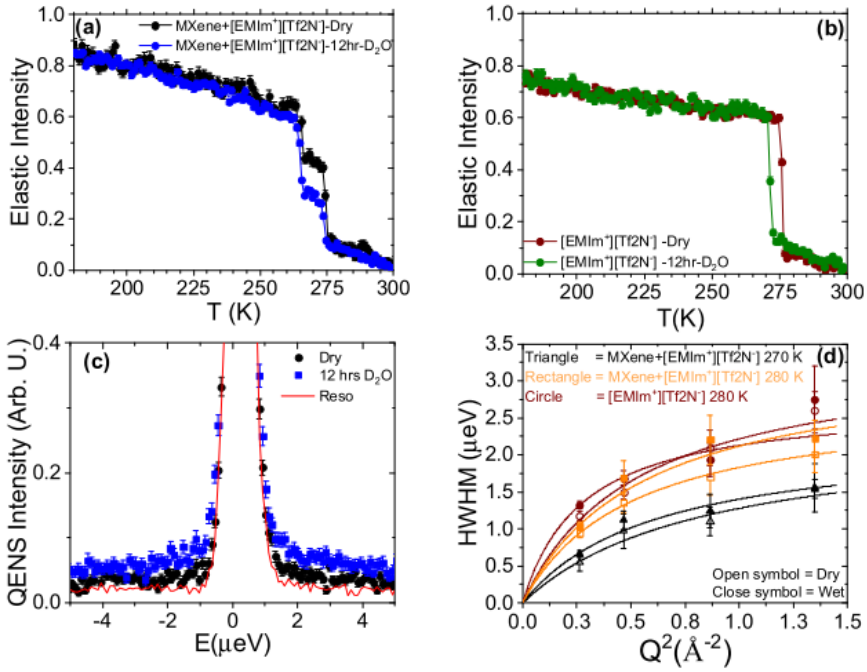

Figure 5.5: Summary of QENS experiments. Elastic scans of ionic liquids (a) confined in MXenes and (b) in bulk. (c) QENS spectra (tracking only the dynamics of the cation) of MXene systems before and after the addition of water. (d) Jump diffusion fits for ionic liquids in bulk (red circles) and confined in MXene (black triangles, yellow rectangles) before (open symbols) and after (closed symbols) the addition of water.

X-ray diffraction (XRD) patterns shown in Fig. 5.4 confirm this hypothesis. If there were changes in the interlayer spacing after intercalation of ionic liquids, the locations of the peaks would change significantly. However, we observe a minimal change, from 19.24 Å to 19.10 Å. Note that this is the difference between dry MXenes and MXenes samples intercalated with ionic liquid, before any humidification took place. The lack of any changes in the c-lattice spacing confirms that ionic liquid molecules were sorbed into inter-stack pores, not inter-layer pores.

Building off these experimental results, we used MD simulations to better understand the effects of humidification on these ionic liquids confined in mxenes. A representative snapshot of a simulation box is presented in Fig. 5.6. Based on the XRD and QENS data, there appears to be little to no nanoconfinement of ionic liquid and instead most of the interfaces were in inter-stack pores. These regions have characteristic widths on the order of a micron. At these separations, the interfaces that define pores behave independently from the perspective of molecules interacting with them. Most non-bonded interactions decay to zero within approximately 1 nm–2 nm and coulombic interactions decay slower. However, the scale of a few hundred nm or microns is much greater than any interaction in these systems. Therefore, we used a channel system in which two MXene plates are separated by a sufficiently large distance that they are not interacting and the fluid in the middle of the box exhibits bulk-like behavior. Here we chose a distance of 10.47 nm and filled the pore with either $[EMIM^+][TF_2N^-]$ or $[EMIM^+][TF_2N^-]$ and water at a composition in accordance with the measurements in experiment.

The structure of the fluids inside MXene channels was characterized in Fig. 5.7. In the dry system, the ionic liquids exhibit strong ordering at the surface that decays along oscillations to bulk-like structure in the middle of the channel. This is broadly consistent with the structure of ionic liquids at interfaces with other planar solids such as graphene.[13,38,39] In the case of strongly humidified ionic liquid, however, the water is preferentially found on the surface. This is evident in the number density profiles but also clearly observed in the simulation snapshots. This was done without any modifications to the force fileds and is generally consistent with the bulk of experimental literature focused on MXene chemistry, which indicates surface groups are believed

to be hydrophilic. Therefore, the absorbed water molecules tend to occupy space on Ti_3C_2 walls, thereby displacing the ions that can now contribute to faster diffusion in the interstack space away from the wall.

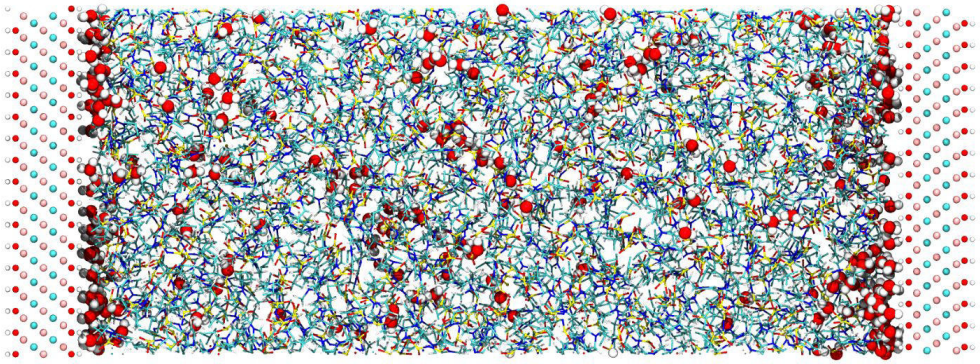

Figure 5.6: Snapshot of a humidified ionic liquid in a MXene channel simulation. To highlight the dilute water compoment, atoms in water molecules are drawn at approximately their Van der Waals radii and ionic liquids are drawn with only thin bonds. The separation distance between the two channels is approximately 10 nm.

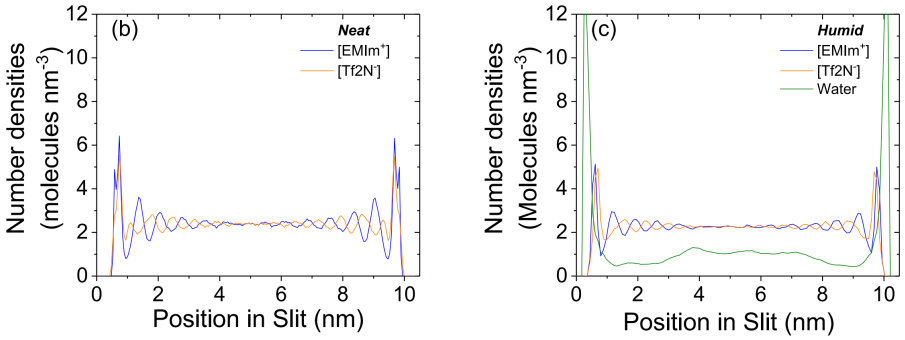

Figure 5.7: Number density profiles for molecules in MXene channel simulations of ionic liquids before (left) and after (right) the addition of water.

5.4 Conclusions

In this chapter we have explored, primarily with QENS experiments and MD simulations, the effects of added water content on the behavior of ionic liquids as electrolytes in interaction with common supercapacitor electrode materials. In each system, an imidazolium-based ionic liquid ($[BMIM^+][TF_2N^-]$ or $[EMIM^+][TF_2N^-]$) was confined in an nanomaterial, large quantities of water were added, and the dynamics of the confined ions were enhanced as a result. In each system,

QENS experiments observed these increases in ion dynamics and MD simulations helped explain these increases by describing the structure of the ionic liquid and water molecules in confinement. In the first system, $[BMIM^+][TF_2N^-]$ was confined in a micro/mesoporous CDC and the addition of water displaced some ions from the pore wall, where they are relatively immobile, to the center of the pores, where they are more mobile. A similar process was observed in the second system in which $[EMIM^+][TF_2N^-]$ was confined in the inter-stack regions of MXene. Water molecules primarily sorbed to the surface of the MXene and displaced some cations from the MXene surface to the bulk-like fluid phase of the inter-stack regions, where the ions are more mobile. These results indicate that, provided some electrochemical issues are mitigated, the addition of water can be used to design supercapacitors with greater power density and rate-handling capabilities.

5.5 Bibliography

[1] Naresh C. Osti et al. "Evidence of molecular hydrogen trapped in two-dimensional layered titanium carbide-based MXene". In: *Physical Review Materials* 1.2 (2017), p. 024004.

[2] Naresh C. Osti et al. "Humidity Exposure Enhances Microscopic Mobility in a Room-Temperature Ionic Liquid in MXene". In: *The Journal of Physical Chemistry C* 122 (2018), pp. 27561–27566.

[3] Rui Qiao. "Water at ionic liquids-solid interfaces". In: *Current Opinion in Electrochemistry* 13 (2019), pp. 11–17.

[4] Guang Feng et al. "Water in Ionic Liquids at Electrified Interfaces: The Anatomy of Electrosorption". In: *ACS Nano* 8.11 (2014), pp. 11685–11694.

[5] Radhika S Anaredy, Anthony J Lucio, and Scott K Shaw. "Adventitious Water Sorption in a Hydrophilic and a Hydrophobic Ionic Liquid: Analysis and Implications". In: *ACS Omega* 1.3 (2016), pp. 407–416.

[6] Wei Jiang, Yanting Wang, and Gregory A. Voth. “Molecular dynamics simulation of nanostructural organization in ionic liquid/water mixtures”. In: *Journal of Physical Chemistry B* 111.18 (2007), pp. 4812–4818.

[7] Patrick Yee, Jindal K. Shah, and Edward J. Maginn. “State of hydrophobic and hydrophilic ionic liquids in aqueous solutions: Are the ions fully dissociated?” In: *Journal of Physical Chemistry B* 117.41 (2013), pp. 12556–12566.

[8] Anirban Sharma and Pradip Kr. Ghorai. “Effect of water on structure and dynamics of [BMIM][PF 6] ionic liquid: An all-atom molecular dynamics simulation investigation”. In: *The Journal of Chemical Physics* 144.11 (2016), p. 114505.

[9] Wenjing Li et al. “Effect of water and organic solvents on-the ionic dissociation of ionic liquids”. In: *Journal of Physical Chemistry B* 111.23 (2007), pp. 6452–6456.

[10] Amrish Menjoge et al. “Influence of water on diffusion in imidazolium-based ionic liquids: A pulsed field gradient NMR study”. In: *Journal of Physical Chemistry B* 113.18 (2009), pp. 6353–6359.

[11] Anne-Laure Rollet et al. “Anomalous Diffusion of Water in [BMIM][TFSI] Room-Temperature Ionic Liquid”. In: *The Journal of Physical Chemistry B* 111.41 (2007), pp. 11888–11891.

[12] Tong Cui et al. “Influence of Water on the Electrified Ionic Liquid/Solid Interface: A Direct Observation of the Transition From a Multilayered Structure to a Double Layer Structure”. In: *The Journal of Physical Chemistry C* (2016), acs.jpcc.6b02549.

[13] Borja Docampo-Álvarez et al. “Molecular dynamics simulation of behaviour of water in nano-confined ionic liquid–water mixtures”. In: *Journal of Physics: Condensed Matter* (2016). arXiv: 1604.02788.

[14] Fei Zhang, Chao Fang, and Rui Qiao. “Effects of Water on Mica-Ionic Liquid Interfaces”. In: *Journal of Physical Chemistry C* 122.16 (2018), pp. 9035–9045.

[15] Oscar Y Fajardo et al. “Water in Ionic Liquid Lubricants: Friend and Foe”. In: *ACS Nano* (2017), acsnano.7b01835.

[16] Amir A. Niazi, Brooks D. Rabideau, and Ahmed E. Ismail. “Effects of water concentration on the structural and diffusion properties of imidazolium-based ionic liquid-water mixtures”. In: *Journal of Physical Chemistry B* 117.5 (2013), pp. 1378–1388.

[17] Shimou Chen et al. “Ionic liquid clusters: structure, formation mechanism, and effect on the behavior of ionic liquids”. In: *Phys. Chem. Chem. Phys.* 16.13 (2014), pp. 5893–5906. arXiv: NIHMS150003.

[18] Mark James Abraham et al. “Gromacs: High performance molecular simulations through multi-level parallelism from laptops to supercomputers”. In: *SoftwareX* 1-2 (2015), pp. 19–25.

[19] José N. Canongia Lopes, Johnny Deschamps, and Agílio A. H. Pádua. “Modeling Ionic Liquids Using a Systematic All-Atom Force Field”. In: *The Journal of Physical Chemistry B* 108.6 (2004), pp. 2038–2047.

[20] José N. Canongia Lopes and Agílio A. H. Pádua. “Molecular Force Field for Ionic Liquids III: Imidazolium, Pyridinium, and Phosphonium Cations; Chloride, Bromide, and Dicyanamide Anions”. In: *The Journal of Physical Chemistry B* 110.39 (2006), pp. 19586–19592.

[21] José N. Canongia Lopes and Agílio A. H. Pádua. “CL&P: A generic and systematic force field for ionic liquids modeling”. In: *Theoretical Chemistry Accounts* 131.3 (2012), p. 1129.

[22] Yong Zhang and Edward J. Maginn. “A Simple AIMD Approach to Derive Atomic Charges for Condensed Phase Simulation of Ionic Liquids”. In: *The Journal of Physical Chemistry B* 116.33 (2012), pp. 10036–10048.

[23] William L. Jorgensen et al. “Comparison of simple potential functions for simulating liquid water”. In: *The Journal of Chemical Physics* 79.2 (1983), p. 926. arXiv: arXiv : 1011 . 1669v3.

[24] Giovanni Bussi, Davide Donadio, and Michele Parrinello. “Canonical sampling through velocity rescaling”. In: *Journal of Chemical Physics* 126.1 (2007), pp. 1–7. arXiv: arXiv: 0803.4060v1.

[25] Boris Dyatkin et al. “Capacitance, charge dynamics, and electrolyte-surface interactions in functionalized carbide-derived carbon electrodes”. In: *Progress in Natural Science: Materials International* 25.6 (2015), pp. 631–641.

[26] L. Martínez et al. “PACKMOL: A package for building initial configurations for molecular dynamics simulations”. In: *Journal of Computational Chemistry* 30.13 (2009), pp. 2157–2164. arXiv: NIHMS150003.

[27] Eugene Mamontov, Huimin Luo, and Sheng Dai. “Proton Dynamics in N,N,N,N-Tetramethylguanidinium Bis(perfluoroethylsulfonyl)imide Protic Ionic Liquid Probed by Quasielastic Neutron Scattering”. In: *The Journal of Physical Chemistry B* 113.1 (2009), pp. 159–169.

[28] Shannon M. Mahurin et al. “Relationship between pore size and reversible and irreversible immobilization of ionic liquid electrolytes in porous carbon under applied electric potential”. In: *Applied Physics Letters* 109.14 (2016), p. 143111.

[29] A. Meyer et al. “The high-flux backscattering spectrometer at the NIST Center for Neutron Research”. In: *Review of Scientific Instruments* 74.5 (2003), pp. 2759–2777. arXiv: 0209153 [cond-mat].

[30] Naresh C. Osti et al. “Influence of humidity on performance and microscopic dynamics of an ionic liquid in supercapacitor”. In: *Physical Review Materials* 1.3 (2017), p. 035402.

[31] S. M. Chathoth et al. “Fast diffusion in a room temperature ionic liquid confined in mesoporous carbon”. In: *EPL (Europhysics Letters)* 97.6 (2012), p. 66004.

[32] Clarisse Péan et al. “Confinement, desolvation and electrosorption effects on the diffusion of ions in nanoporous carbon electrodes”. In: *Journal of the American Chemical Society* (2015), p. 150929003048004.

[33] Mohamed Alhabeb et al. “Guidelines for Synthesis and Processing of Two-Dimensional Titanium Carbide (Ti 3 C 2 T x MXene)”. In: *Chemistry of Materials* 29.18 (2017), pp. 7633–7644.

[34] Richard Tumanjong Azuah et al. “DAVE: A Comprehensive Software Suite for the Reduction, Visualization, and Analysis of Low Energy Neutron Spectroscopic Data”. In: *Journal of Research of the National Institute of Standards and Technology* 114.6 (2009), p. 341.

[35] H J C Berendsen, J R Grigera, and T P Straatsma. “The Missing Term in Effective Pair Potentials”. In: *Journal of Physical Chemistry* 91.24 (1987), pp. 6269–6271.

[36] Randall T Cygan, Jian-Jie Liang, and Andrey G Kalinichev. “Molecular Models of Hydroxide, Oxyhydroxide, and Clay Phases and the Development of a General Force Field”. In: *The Journal of Physical Chemistry B* 108.4 (2004), pp. 1255–1266.

[37] Naresh C. Osti et al. “Effect of Metal Ion Intercalation on the Structure of MXene and Water Dynamics on its Internal Surfaces”. In: *ACS Applied Materials & Interfaces* 8.14 (2016), pp. 8859–8863.

[38] Guang Feng, J. S. Zhang, and Rui Qiao. “Microstructure and capacitance of the electrical double layers at the interface of ionic liquids and planar electrodes”. In: *Journal of Physical Chemistry C* 113.11 (2009), pp. 4549–4559.

[39] Nav Nidhi Rajput, Joshua Monk, and Francisco R. Hung. “Ionic Liquids Confined in a Realistic Activated Carbon Model: A Molecular Simulation Study”. In: *The Journal of Physical Chemistry C* 118.3 (2014), pp. 1540–1553.

Chapter 6

Evaluation of Molecular Models for Ionic Liquids at Interfaces

A major barrier to the widespread adoption of molecular simulation, particularly classical molecular dynamics and Monte Carlo simulations, is the availability of reliable force fields.[1] As a matter of computational necessity, classical models describe major simplifications of complex computational chemistry yet attain an acceptable level of accuracy in describing physical properties. The history of molecular simulation includes a push-and-pull relationship between the desire to employ accurate models and the costs associated with developing and implementing them. Capturing physically diverse properties (i.e. simultaneously describing the density and viscosity of a liquid) is difficult to do in a general and transferable manner. Some molecular sciences, particularly well-funded and older fields like biophysics, have more viable force fields than others. Molecular simulation of ionic liquids is still a young topic; the first studies are 20 years old, which are especially young compared to early the first model of liquid argon published in 1964. Because ionic liquids have fundamentally different physics than other salts or fluids, foundational work needs to be done to build the relevant force field infrastructure.[1]

This chapter describes some of our efforts in this direction. We interrogate two toy systems in an effort to understand how, if at all, force field-related shortcomings in simple physical properties affect higher-level properties and application-scale trends. We also describe a method for tuning fluid-solid interactions in leiu of expensive first-principles calculations. Many of the simulations described in this chapter were prepared and run by Felix Tiet, an undergraduate researcher in our lab from Summer 2016 to Spring 2019, under my direction.

6.1 Background

Many applications of ionic liquids involve exploiting their unique properties at interfaces and confinement. Molecular simulation is a powerful tool and is now almost ubiquitously used for

understanding the fundamentals that govern ion structure and dynamics at interfaces and under. In particular, molecular dynamics is well-suited to study these systems: their slow dynamics nearly require classical models to study transport properties and their nanoscale clustering on the order of a few nanometers provides limitations to use first-principles methods that, for other systems, would provide macroscopic information with unit cells of a few molecules.

However, the necessary reliance on empirical force fields casts some doubt on their conclusions. The generalizability and transferability of classical force fields has been an issue for as long as they have been used; a force field may be tuned to match one particular physical property, and successfully so, but its accuracy with respect to another physical property is far from guaranteed; in fact, for fundamentally different properties such as liquid density and enthalpy of vaporization, it seems that accuracy is the exception, not the rule. Recently for some simple fluids there have been advancements in force field derivation methodologies that do a better job at simultaneously describing disparate properties, i.e. structure, transport, and thermodynamics. However, for models of larger, more interesting, and chemically complex systems, such as ionic liquids, this work lags behind. A popular force field, herein referred to as KPL (named after the authors Koddermann, Paschek, and Ludwig), has achieved this for a set of common ionic liquids, some 1-alkyl-3-methylimidazoles with the bistriflamide anion. A major driver of interest in ionic liquids is their extremely diverse chemical space; the amount of work required to develop a good model for one ionic liquid makes it difficult to make but small progress in direction of describing much of this space. Ionic liquid force field suffer from these same limitations. The popular CL&P force field, for example does a good job describing liquid and crystal structure but its transport properties are not accurate. Another difficulty with application-relevant systems is that it is difficult to treat fluid-solid interactions with care. Most commonly, simulation engines use Lorentz–Berthelot mixing rules to describe cross-interactions; not only are there limitations for chemically heterogeneous fluids but there is little theoretical basis for using this in fluid-solid interactions. Force fields are typically derived from simple systems, such as bulk fluids, but are applied to complex systems with different components and heterogeneities. Even for some that do a generally good job of describing

bulk fluid properties, there is little confidence they describe interfaces with similar accuracy. Here, we employ a number of simple toy systems to investigate some fundamentals of the behavior of relevant interfacial ionic liquid simulations.

6.2 Methods

6.2.1 Molecular Simulation Design Framework

Simulations were conducted using the Molecular Simulation Design Framework (MoSDeF) suite of software tools. The process is comprised of four main steps: First, systems are built with mBuild, placing molecules in a simulation box at random while avoiding overlapping molecules by utilizing PACKMOL. Next, force fields are applied with foyer. Then, simulations are run, composed of three main steps detailed in the next section. Finally, analyses are run using a variety of python packages and custom scripts.

6.2.2 Channel Simulations

Channel and droplet simulations were performed with GROMACS 5.1.4, while AWH simulations were performed with GROMACS 2018.5. Despite the difference in version numbers (GROMACS changes from semantic versioning to calendar versioning midway through this study) there are minimal differences between the releases. After initialization of the systems and application of forcefields, three main simulation steps are run: energy minimization, equilibration, and sampling. For energy minimization, all systems proceeded using 1000 steps of the steepest descent algorithm. To generate the charged channel systems, ionic liquids were randomly placed inside a box bounded on either side in the x-y plane by three graphene sheets. Partial charges were manually added onto each carbon atom for the sheets in direct contact with the fluid, varying from 0 to ±0.02 e- in increments of 0.001. These surface charges correspond to macroscopic charge densities of -0.7 to 0.7 $\mathrm{C\,m^{-2}}$. To drive the channel systems toward equilibrium, a 20 ns NVT simulation was performed using the Berendsen thermostat with a reference temperature of 300 K

and a 1 fs timestep. Then, systems were sampled for 150 ns in the NVT ensemble, with a longer timestep of 1.5 fs using the v-rescale thermostat with a reference temperature of 300 K. Multiple force fields were explored through these simulations - graphene was described using the Amber and Steele force fields, while the ionic liquids were described using KPL, Lopes, and Lopes with scaled charges. Charge density and potential for the charged channel systems was then obtained using the `gmx potential` command provided by GROMACS. To obtain diffusivity data, the sampling trajectory was converted to a center of mass trajectory in which each molecule is tracked by a single point representing its center of mass. Then, diffusion was calculated from MSD values obtained from using the mtools software package.

6.2.3 Droplet Systems

To build the droplet systems, a sphere of ionic liquids was generated based on the desired radius. Then, molecules were removed to achieve the specified initial contact angle. Finally, the spherical cap was translated as needed to rest above three sheets of graphene. To equilibrate the droplet systems, a 1.5 ns NVT simulation was performed using the Berendsen thermostat and a 1 fs timestep. The systems were initialized at 50 K for the first 0.5 ns, and was then annealed to 300 K over the next 0.9 ns, ending in a constant temperature of 300 K over the last 0.1 ns. Then, systems were sampled for 225 ns in the NVT ensemble, with a longer timestep of 1.5 fs using the v-rescale thermostat with a reference temperature of 300 K. Graphene was described using the Amber force field, while the ionic liquids were described using Lopes with scaled charges and KPL. Contact angles were calculated using a custom Python analysis script. First, a center of mass trajectory is computed and transformed from cartesian coordinates to [r,z] coordinates. Then, a 2D histogram is generated based on the r and z values. After normalizing the histogram and removing values below a certain threshold, a contact angle is calculated by fitting a sphere to the edges of the histogram based.

6.2.4 AWH Systems

Channel simulations were also interrogated with free energy calculations using the Accelerated Weight Histogram (AWH) method, similar to as described in Chapter 4. These systems were built using the same graphene sheets as the previous charged channel systems. Two boxes were defined: a smaller box near the surface for the ionic liquid molecule, and a larger box for the solvent molecules. Then, mBuild was used to fill in these regions using PACKMOL, which prevents any overlaps between the ionic liquid and solvent. Next, an index file is generated to define the two groups to be pulled for the AWH simulation - for our purposes, we specified the EMIM cation to be pulled away from the graphene surface. Position restraints are utilized and further detailed below to prevent significant lateral diffusion of the cation. Before any pulling occurred, the AWH channel systems were first equilibrated through a 1 ns NVT simulation using the Berendsen thermostat and a 1 fs timestep. Then, systems were sampled for 300 ns in the NVT ensemble, with a longer timestep of 1.5 fs using the v-rescale thermostat with a reference temperature of 300 K. Pulling occured along the z-axis, with an EMIM being pulled from distances of 0.3 to 3.0 nm from the graphene surface. The nitrogen atom connected to the longer chain was position restrained with a force constant of 100 $\mathrm{kJ\,nm^{-2}}$ in the x and y directions. The Amber force field was used to describe the graphene sheets, while KPL was used for the ionic liquids and OPLS for the solvents. PMF data for the system was then obtained using the ‘gmx awh‘ command provided by GROMACS.

6.3 Results

6.3.1 Channel Simulations

The first toy system we studied was the channel simulation, which is frequently used to study the properties of fluid-solid interfaces broadly and has been proposed as a model system for supercapacitors not based on nanoporous electrodes. It consists of two parallel planar electrodes separated by some distance and filled in between with fluid. In the supercapacitor literature the surfaces are sheets of graphene but in other fields can be other materials, i.e. silica or mica. The

separation distance is typically 5 nm–10 nm, large enough for the fluid to reach a bulk-like state in the middle of the channel and, therefore, large enough for the electrodes to be considered independent. A representative snapshot of such a system is presented in Fig. 6.1

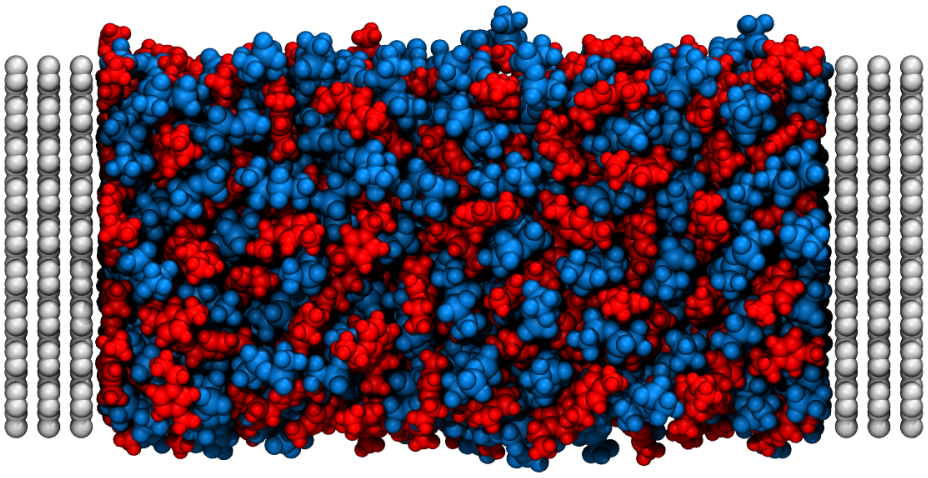

Figure 6.1: Representative snapshot of a channel simulation. Graphitic carbons are colored grey, [$EMIM^+$] cations colored red, and [TF_2N^-] anions colored blue.

These simulations have been employed in some hundreds of studies in the supercapacitor literature, forming much of our molecular understanding of these systems. It is therefore worth studying the details of how our force fields are implemented in them. We selected three common ionic liquid force fields (CL&P, CL&P with scaled charges, and KPL) and two carbon parameter sets commonly used to model graphene interactions. Some methods have been proposed to tune the cross-interactions to a particular target. However, these are not commonly employed in MD studies so we did not consider them. Our objective is to investigate how, if at all, the selection of force fields affects the measured capacitance. Note that these force fields predict different values of basic physical properties (liquid density, molecular diffusivity, enthalpy of vaporizaiton).

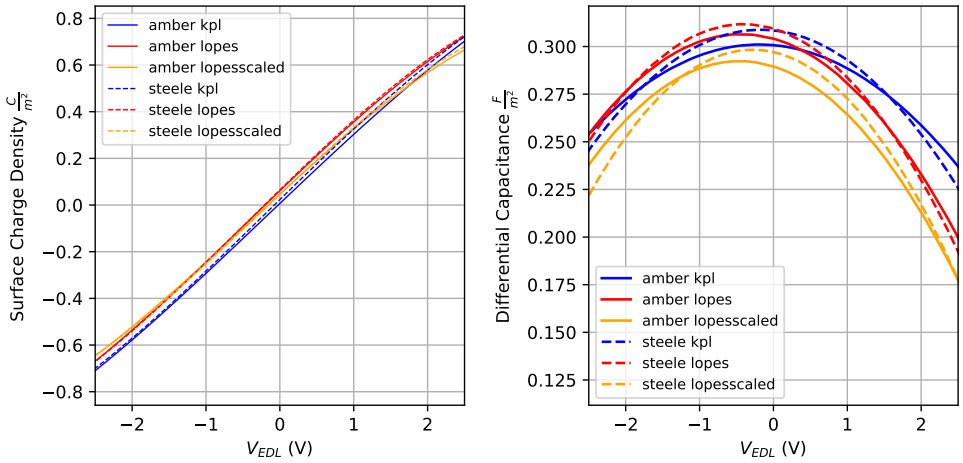

Figure 6.2: Electrochemical behavior of a model supercapacitor as predicted by different force fields. Solid lines use Amber parameters for graphitic carbon atoms and dashed lines use Steele parameters. Colors represent the use of the KPL, Lopes, and Lopes-scaled force fields. The relationship between surface charge density and the potential drop at the EDL (left) is used to compute the differential capacitance (right).

The results of these channel simulations are summarized in Fig. 6.2. We observe for the set of six unique force field models remarkably similar capacitance curves. This implies that the development of rigorous force fields, while of broad interest to the field as a whole for the prediction of other physical properties, may not be impactful for the prediction of capacitive performance in simple model systems. Alternatively, it may be the case that these models — all classical in nature — each fail in some common manner as a result of their not handling other relevant physics, i.e. the polarizability of the electrode and/or electrolyte, hydrogen bonding, charge transfer effects, and/or long-range coulombic forces. Some efforts have been made to capture the polarizability of the electrode applying a constant electric potential (as distinct from the common technique of applying a constant charge) but most of these groups have not chosen to publicly release these their code, making it difficult for other researchers to use this method in their own studies.

6.3.2 Droplet Simulations

Our next toy system is the droplet simulation (or nanodroplet, given its typical size). At the macroscale, simply placing a fluid on a surface and — provided the liquid beads up to form dorplets

— describing the shape of the liquid droplets has been used for decades as a simple yet powerful technique to characterize the interacitons between the fluid and surface. They can be used to capture simple qualitative trends, i.e. if a surface is hydrophilic or hydrophobic, or more quantitative measures using Young's equation. Here, we use nanoscale droplets to characterize the interaction between ionic liquid molecules and a graphene interface, given how common this interaction is in supercapacitor studies. A representative snapshot of such a system is presented in Fig. 6.3

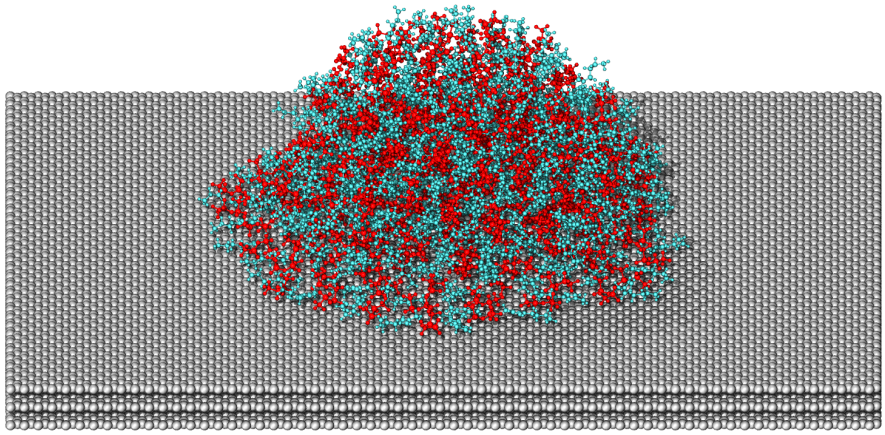

Figure 6.3: Representative snapshot of a droplet simulation. The surface is three-layer graphene, represented by silver spheres. The ionic liquid is $[BMIM^+][TF_2N^-]$ represented by cyan and red ball-and-stick models, respectively.

Given that most studies to not concern themselves with tuning fluid-solid interactions, we begin by using "out-of-the-box" force fields and treatment of cross-interactions. A summary is presented below.

As one may expect, given how sensitive the wetting behavior of droplets is to the fluid-solid interaction, the choice of force field strongly impacts the wetting behavior of $[EMIM^+][TF_2N^-]$. If one was selecting force fields based purely on simple physical properties, which are used to derive and evaluate force fields, KPL would be the clear choice. One may also select the carbon

parameters of Steele which are popular in the adsorption literature. The result of such choices, however, is a droplet that rapidly wets the surface. While it is not clear precisely what contact angle should be gleaned from experiment as a target, there is no disputing that a stable droplet should be formed.

Next, we choose some other parameter sets and observe the results. First, we switch from the KPL force field to the CL&P force field, which is the most commonly used ionic liquid force field in literature (and was used extensively in this thesis). Then, we switch from the carbon parameters of Steele to the sp^2 carbon parameters in the General Amber force field (GAFF), which are commonly used in the supercapacitor studies and similar to other commonly parameters. The results of these switches is the formation of more stable droplets that that settle around 50° and 60° after 200 ns of simulation. Again, it is not clear precisely what value should be taken as a representative experimental measurement, but these two results are more consistent with the existing literature.

Ionic liquids characteristically have slow transport properties, which can cast some doubt on how accurate the above results are. Simulations of length 200 ns are on the longer end of what is casually accessible with classic molecular dynamics (these simulations took approximately four days on our local cluster). From experimental studies, there is broad evidence indicating ionic liquids have slow and perhaps complex relaxation behavior taking place on longer timescales (i.e. compared to water). To investigate this, we biased our droplet simulations toward the final state by initializing the droplets at different contact angles. The GAFF and CL&P parameters were used here. We previoulsy initialized our droplets at a contact angle of approximately 90° and observed the wetting behavior as a function of time. Given that these droplets exclusively moved toward wetting behavior (decreasing $\theta_{contact}$) we initialized analogous simulations with droplets of smaller contact angles (100°, 80°, and 60°) and ran each for 200 ns. The results, shown in Fig. 6.4, indicate that previously results had not reached an equilibrium state. The droplet initialized at 100° appeared to stablize near 40° after 100 ns but later wetted the surface further. The droplet initalized at 80° exhibited similar behavior at lower contact angles and completely we the surface

at longer times. The droplet initalized at 60° wetted the surface more rapidly, fully wetting after approximately 50°. These results indicate, at least for a particular parameter set, that nanodroplets with a small $\theta_{contact}$ may be metastable and, at longer timescales, completely wet the surface.

With these limitations in mind, we seek to investigate how much control we have the wetting behavior of an ionic liquid nanodroplet on graphene. We use the same system as above but modulate the fluid-solid interaction by varying the ε_C parameter — that is, the energetic term of the Lennard-Jones potential used to describe the carbon atoms in the graphene surface. GROMACS, like most molecular simulation engines, uses Lorentz–Berthelot mixing rules[2,3] by default. In leiu of custom $i-j$ interactions, which are typically not included in common force fields, the Lennard-Jones interactions between atoms i and j are

$$\sigma_{ij} = \frac{\sigma_i + \sigma_j}{2} \tag{6.1}$$

and

$$\varepsilon_{ij} = \sqrt{\varepsilon_j \varepsilon_j}. \tag{6.2}$$

Recall from the general form of the Lennard-Jones potential

$$V_{LJ} = 4\varepsilon \left[\left(\frac{\sigma}{r} \right)^{12} - \left(\frac{\sigma}{r} \right)^{6} \right] \tag{6.3}$$

that the parameter ε largely controls the depth of the potential energy curve and σ controls the location (or, similarly, the size of the atom). In most atomistic force fields, particularly those used to model ionic liquids, there can be dozens of unique atom types and an equal number of potential cross-interactions to tune. More rigourous techniques can leverage all of these parameters toward control of physical properties (i.e. $\theta_{contact}$) but would be more difficult for other researchers to adapt in their simulations. Our approach involves changing only one value in the GROMACS input files. In varying ε_C, all fluid-solid interactions, and therefore the overall description of the interface, are controled with a single parameter.

We scaled ε_C by three values: 0.1, 0.01, 0.002, and 0.001. Note that because of the mixing rule (), the potential energy scales as the square root of these values, or 0.3162, 0.1, 0.0447, and 0.03162. To hedge against any metastability issues, we also initialized each nanodroplet, subject to each scaling, at angles of 80°, 100°, and 120°, for a total of 12 unique simulations. The wetting behavior of each nanodroplet as a function of time, measured by $\theta_{contact}(t)$, is summarized in Fig. 6.4

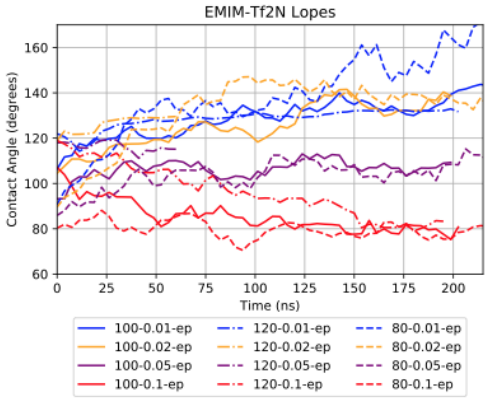

Figure 6.4: Wetting behavior of droplets with different initial contact angles and fluid-solid interaction parameters

It is clear that scaling the parameter ε_C has robust control over the wetting behavior of the nanodroplet. As evidenced by the convergence of contact angles at long time regardless of their initial contact angles, this control also appears to be insensitive to the contact angle of the initial configuration. The values of $\theta_{contact}(t)$ also appear to be largely stable as a function of time, especially when the initial and equilibrium contact angles do not differ by large amounts. While the extremely ionophobic surfaces of $\varepsilon_C = 0.001\varepsilon_{C,GAFF}$ are not realistic, these results indicate that, particularly for large contact angles, molecular interactions can be stably tuned toward a target value by scaling only one parameter. Without these modifications, wetting processes may not be captured within the timescales accessible by atomistic molecular dynamics simulations.

6.4 Conclusions

Molecular simulation in the past decade has become a commonly used tool for modeling supercacitors and has been used to study other interfaces for decades prior. As with its use in most other fields, the design, derivation, and selection of of force field is crucial to accurately model relevant physical phenomena. In this chapter, we evaluated this relationship with a focus on ionic liquids at interfaces. We used toy systems of graphene channels and nanodroplets to study the relationships between simple and higher-level physical properties as predicted by some force fields. We found that the differential capacitance predicted via channel simulations — and considering no other properties — is not noticably sensitive to the selection of force fields, at least within the context of classical, atomistic molecular dynamics simulations using the constant charge method. This is notable given that the force fields exhibit remarkably different physical properties in the bulk ionic liquid phase. We next employed simple nanodroplets to focus on the fluid-solid interactions modeled by these force fields. We found that the force field with the best bulk ionic liquid properties (KPL) provides physically unrealistically behavior (rapid and complete wetting) and other force fields provide more realistic behavior (wetting to contact angles near 50°) but may be susceptible to being trapped in metastable states. Finally, we proposed a simple method by which a force field can be tuned to a fit a target contact angle, which is a proxy for fluid-solid interactions more broadly.

6.5 Bibliography

[1] Edward J. Maginn. “From discovery to data: What must happen for molecular simulation to become a mainstream chemical engineering tool”. In: *AIChE Journal* 55.6 (2009), pp. 1304–1310. arXiv: arXiv:1402.6991v1.

[2] H. A. Lorentz. “Ueber die Anwendung des Satzes vom Virial in der kinetischen Theorie der Gase”. In: *Annalen der Physik* 248.1 (1881), pp. 127–136.

[3] Daniel Berthelot. “Sur le mélange des gaz”. In: *Compt. Rendus* 126 (1898), pp. 1703–1706.

Chapter 7

Molecular Simulation of MXenes

MXenes are a new class of 2D materials with excellent physical properties and broad relevance to many energy applications. In this chapter, we describe the development and testing of software that implmements a classical model of MXenes and intercalated fluids for use in molecular simulation.

7.1 Introduction

Much like graphene a decade ago and carbon nanotubes a decade prior, MXenes are a new and exciting class of 2D materials. They are metal carbides composed of alternating layers of carbon (or nitrogen) and transition metals. Their discovery was reported in 2011 by Michael Naguib and Yury Gogotsi[1] and has spawned some thousands of papers in years since. Their potential applications are numerous, but early work has been focused on energy storage and catalysis.

To illustrate this point, simple analytics of MXene publications were compared to other popular, arguably revolutionary nanomaterials. The number of unique manuscripts over time, according to Web of Science searches, are compared in Fig. 7.1 and Fig. 7.2. While MXenes currently occupy an early position on the technology pipeline, it is difficult to overstate the amount of interest in them. It is clear that the number of papers concerning MXenes is growing rapidly, but as evidenced by Fig. 7.2. Many other materials have stalled in interest, as measured by the number of new papers published each year, but interest in MXenes is still growing by this measure. Many novel materials have shown promise in the lab but stalled out before making a significant impact on society. It is a decade or so too early to evaluate MXenes on such a basis, but the early excitement is at least on par, if not greater than, any other innovation in this generation of materials science.

MXenes are synthesized by etching the A phase out of a "MAX" precursor. These "MAX" materials typically follow the form $M_{n+1}AX_n$ where M is an early transition metal, X is carbon

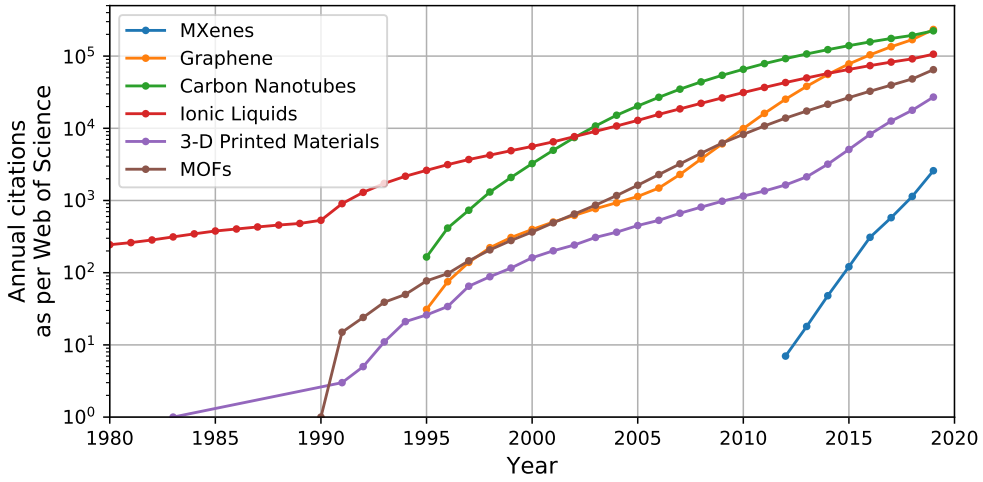

Figure 7.1: Cumulative number of references to some popular nanomaterials, as per a Web of Science search.

and/or nitrogen, and A is a group 13 or 14 element and n is 1, 2, or 3. The most common MXene is Ti3C2, which comes from chemically etching the Al from a Ti3AlC2 precursor. The resulting structure includes alternating and well-defined layers of metal and carbon (and/or nitrogen). One layer of MXene is defined as a grouping of typically five (sometimes three or seven) of these atomic layers. The Ti atoms that define the outer atomic layers are functionalized with surface termination groups. The chemical etchant is typically HF, so these surface terminations groups are typically F, OH, and some drpronotated OH (O). The composition of these groups appears to be highly sensitive to synthesis conditions, as various experimental probes have provided remarkably different stoichiometric estimates.[2–4]

Nonetheless, the overall nature of the surfaces appears to be hydrophilic. Upon exposure to water, these interlayer spacings are readily intercalated with small amounts of fluid, often as small as a monolayer quantity of water. Many experimental probes have characterized the overall structure of the resulting system by observing changes in the c-lattice parameter that can be attributed to this intercalation.

MXenes can also be intercalated with electrolytes, both aqueous and organic in nature. The naturally high conductivity of the carbide phase, the inherently high surface area of the 2D MXene

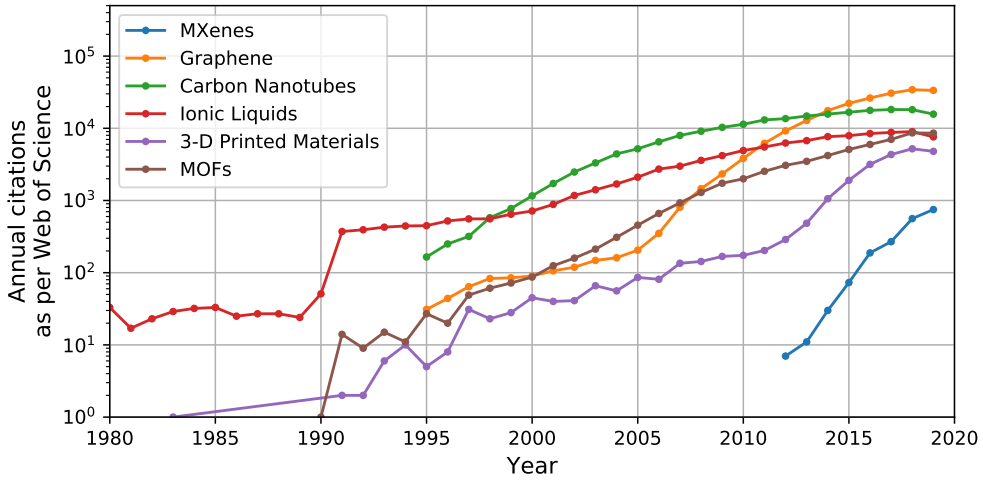

Figure 7.2: Annual number of references to some popular nanomaterials, as per a Web of Science search.

sheets, and the rich chemistry of the surfaces and adsorbed fluids have spurred interest in a variety of applications ranging from energy storage (Faradaic, non-Faradaic, and semi-Faradaic in nature), electrocatalysis, gas sensing and storage, lubricaiton, and water purification. Underlaying most of these properties are the structure and transport of intercalated species (water, ions, or other species). Provided this and the difficult nature of comphrenesively studying these systems with experiments, it is therefore of fundamental interest to develop and deploy molecular models of MXenes in order to understand the structure and dynamics of these confined species.

Metals in general can be tricky to study with classical molecular dynamics since their chemistry is more diverse and their physics are not as well-described by simple potentials that work well for organic and biological compounds. Similarly, there is a limited scope of what can be studied by classical molecular dynamics. Many of the relevant properties, such as reaction energetics, electronic structure, and thermal and electrical conductivity must be studied by first-principles methods. However, classical molecular dynamics is an invaluable tool in a narrow scope, primarily focused on the structure and dynamics of fluids and electrolytes confined in layers or "stacks" of MXenes. To facilitate robust and reproducible applications of classical models to study the properties of these systems, we developed a Python package in the MoSDeF ecosystem. It provides

users, with only a few lines of Python code, the capability of building MXene systems with vast complexity in the design space of these materials. Such parameters include system size, crystal structure of the base lattice, chemical composition of the surface termination groups, and interlayer spacing.

To this end, we have implemented this force field into a larger package, MXenes, to aid in the reproducible generation of these systems for molecular simulation. Included are functions that handle the generation of the atomistic structure, including different surface terminations, the parametrization according to our force field, and the writing to various file formats. This can all be done in a scalable, scriptable manner.

7.1.1 Model

The force field was developed by Lukas Vlcek at Oak Ridge National Laboratory. He used a rigorous fitting procedure he previously developed[5] that is based on optimizing the statistical distance between statistical mechanical systems. It attempts to capture the overall thermodynamic description of a system with a single measure, much like an objective function, instead of selecting a few (1-3) physical properties and tuning force field parameters to those. The target data was a set of *ab initio* molecular dynamics (AIMD) simulations generated by Yu Xie, also at Oak Ridge National Laboratory.

7.1.2 Example systems

7.1.2.1 Dry MXenes

There is some uncertainty about the surface chemistry of MXenes, particularly because synthesis procedures were not standardized until recently, and still there are a number of techniques to choose from. A comphrensive list can be found in.[6] Because of this, there is some disagreement in the few experimental studies that have attempted to quantitatively characterize the composition of different surface chemistries.[2–4] However, the general picture is that the surfaces are primarily

hydroxylated, with some deprotonated hydroxyl groups and fluorine groups, and also sometimes sorbed water molecules. This is similar to the surface of metal oxide materials, which have been studied for decades.

Given that the surface chemistry is of broad interest to molecular simulation studies, it is useful to consider model systems having surfaces of different composition. To this end, we considered four model systems, enumerated in Table 7.1. To ensure the systems are stable, we report the *c*-lattice parameter for each system. Experimental studies tend to report values near 2 nm. We see in Fig. 7.3 that each system equilibrates to similar values. The system with 100% hydroxyl termination has a smaller value, perhaps artificially low due to strong hydrogen bonding between layers. Note that despite the wide variety of surface compositions reporting in experimental measurements, a purely hydroxylated surface, or anything close to it, has never been reported. The system with a surface composition as reported by Wang *et al.*[2] is close to the reported value of 1.934 nm, which is believed to correspond to a dry (i.e. no intercalated water) system.

Table 7.1: Example systems of dry MXenes

Name	xOH	xO	xF
Pure OH	1.0	0	0
Pure F	1.0	0	0
Mixed	0.5	0.25	0.25
Wang, 2015[2]	0.52	.06	0.42

7.1.2.2 Water in MXenes

Given that most MXene synthesis routines involve water-based etchants and many applications rely on water-based fluids like aqueous electrolytes, it is of fundamental interst to study water confined in MXenes. As a simple step in this direciton, we considered different amounts of water intercalated between MXene layers: 8, 10, 15, and 20 water molecules per lattice repeat units. We used the SPC/E water model and followed a similar procedure as above. First, we evaluate the

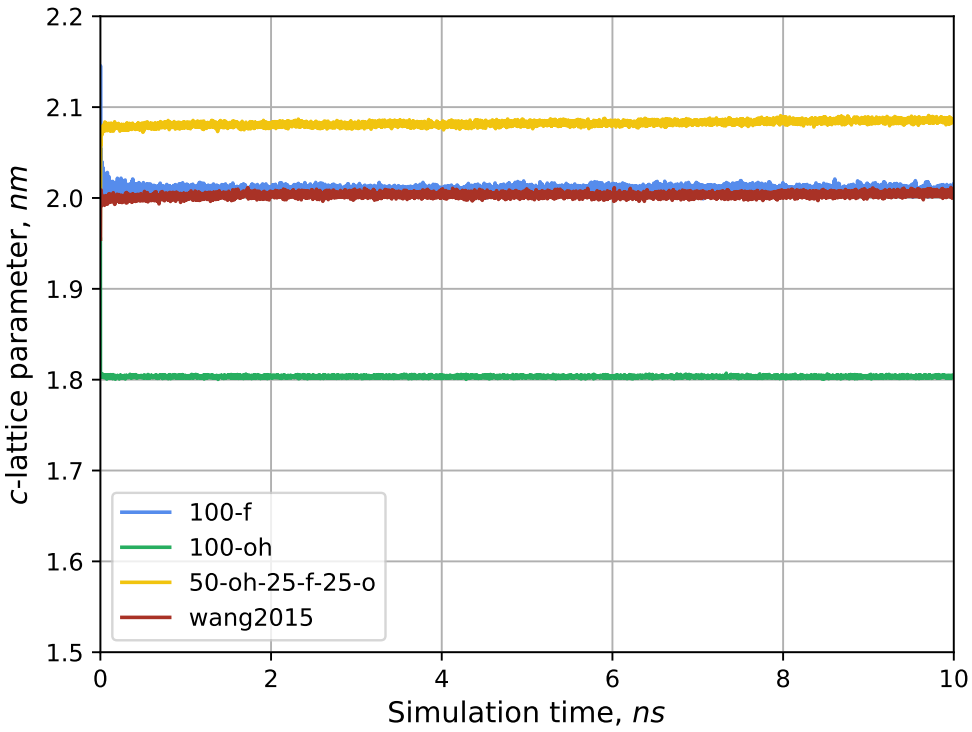

Figure 7.3: Simulation box sizes over the course of a 10 ns trajectory.

structure of these systems by considering again the c-lattice parameter. It is clear from Fig. 7.4 that the layers expand with the addition of more water content and that all systems are stable.

Next we consider the mobility of the confined waters by measuring their diffusivity in the x and y directions. Diffusivities extracted from the MSDs shown in Fig. 7.5 are, for water quantities 8, 10, 15, and 20 waters per lattice repeat unit, $2.9 \times 10^{-12}\,\mathrm{m^2\,s^{-1}}$, $1.1 \times 10^{-11}\,\mathrm{m^2\,s^{-1}}$, $6.7 \times 10^{-11}\,\mathrm{m^2\,s^{-1}}$, and $1.3 \times 10^{-10}\,\mathrm{m^2\,s^{-1}}$. Fluids generally exhibit slower transport properties on confinement, particularly nanoconfinement, and these systems are no exception.

7.1.2.3 Large MXenes

The nature of these builder functions, the MoSDeF ecosystem, and scriptable Python-based tools more generally is the scalability of any process. The modification of a single argument (`periods`) allows for scaling to arbitrary system size with minimal modifications of downstream scripts and interfaces with other engines and tools. To illustrate the point, we have generated a

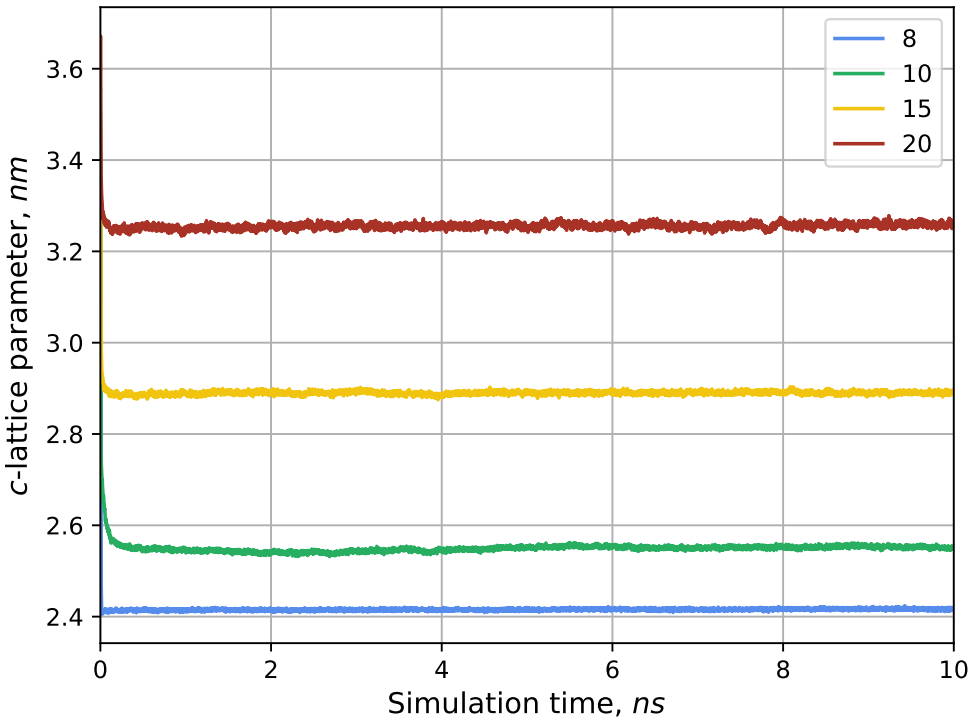

Figure 7.4: Simulation box sizes over the course of a 10 ns trajectory.

single large MXene system by using `periods=[40, 40, 3]`, which generate in a matter of minutes a large MXene system. This can then be passed to a molecular simulation engine (i.e. LAMMPS, GROMACS, OpenMM, etc.) for equilibration and production runs. A snapshot of this simulation is presented below.

7.1.2.4 Mixed Electrolytes Confined In MXenes

Given the broad interest in MXenes as electrodes for energy storage applications, it is useful to consider molecular simulations of electrolytes confined in MXenes. We consdier a mixed eletrolyte similar to the focus of Chapter 4. The ionic liquid [EMIM$^+$][TF$_2$N$^-$] was mixed in acetonitrile at a molar ratio of 1 ionic liquid per 10 solvent molecules. A total of 40 ionic liquid pairs and 400 solvent molecules were placed across 4 layers of a hydroxyl-functionalized Ti_3C_2 MXene. Our force field was applied to the MXene and the CL&P and OPLS-AA force fields were applied to the ionic liquids and solvent molecules, repsectively. We ran a single 10 ns simulation with generally

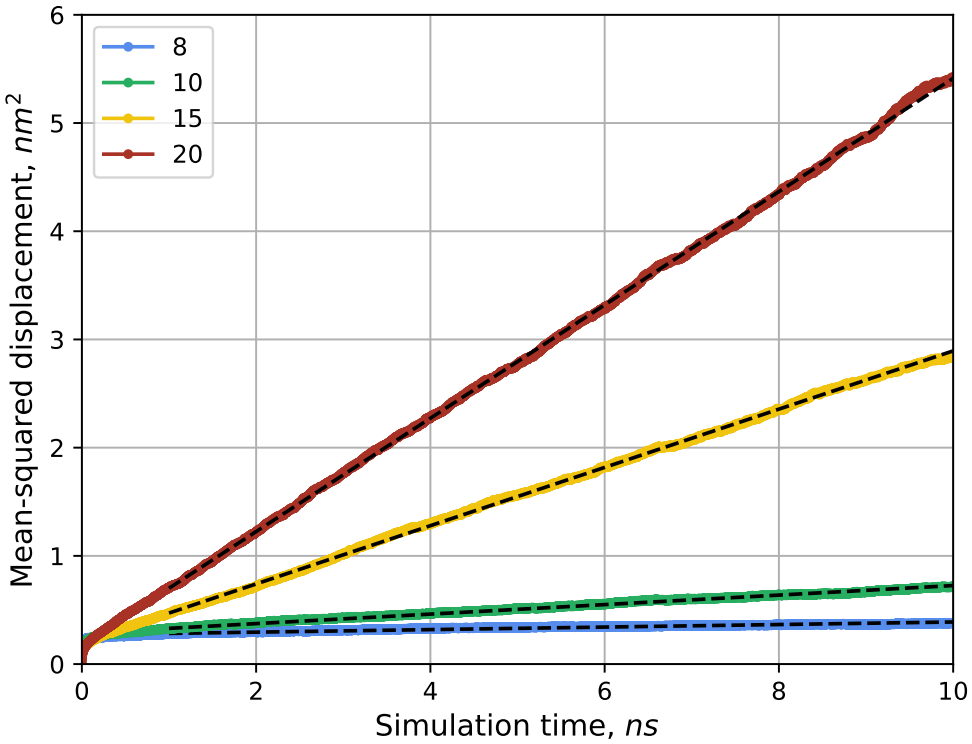

Figure 7.5: Mean-squared displacement of water molecules molecules in the x and y directions as a function of water content.

standard simulation parameters.

First we verify that the simulation is stable by considering the simulation box lengths in each dimension. Unstable systems typically blow up quickly or exhibit unphysical volume changes when in the *NPT* ensemble. As shown in Fig. 7.8, the system is stable in each dimension, quickly reaching steady-state values that remain constant over the length of the 10 ns simulation. Next we consider the diffusivity of the ionic liquid by a simple MSD analysis. Because of the nature of confinement in a 2-D material, we consider only diffusion in the x and y dimensions. A summary is presented below in Fig. 7.9. The linear fit to the MSD produces a diffusion coefficient of $3.3 \times 10^{-9}\,\mathrm{m^2\,s^{-1}}$ which is both in line with the mobility of other dilute ionic liquids and drastically higher than comparable neat ionic liquids. The properties of energy soraged devices based on MXenes and solvated ionic liquids have been studied more in-depth by our collaborators.[7]

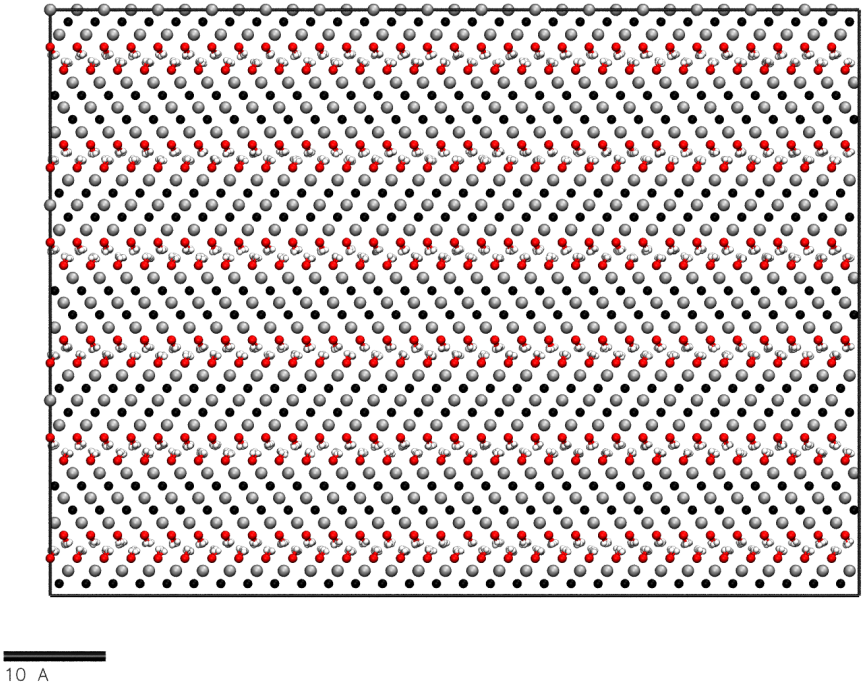

Figure 7.6: Snapshot of a large MXene system. The unit cell is replicated 40 times in the x and y directions and 3 times in the z direction producting a system of 43,232 atoms and a box lengths of approximately 9.144 nm, 7.9 nm, and 5.7 nm in the x, y, and z directions, respectively. Here the x axis points into the page, the y axis points to the right, and the z axis points down. A scale bar of 10 Å or 1 nm is included for reference. Atoms are colored as follows: Ti: silver, C: black, O: red, H: white.

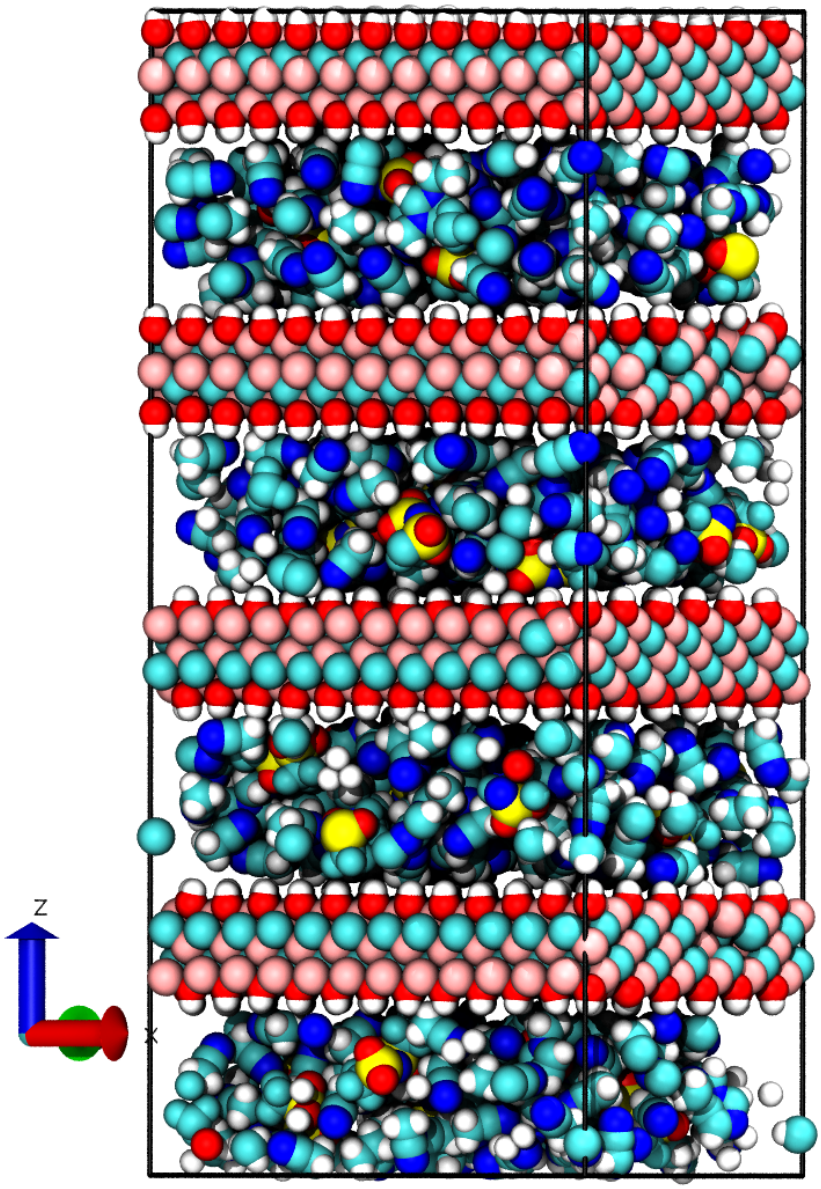

Figure 7.7: Snapshot of a solvated ionic liquid confined in a MXene. The system includes 40 pairs of the ionic liquid [$EMIM^+$][TF_2N^-] and 400 acetonitrile molecules. Atoms are colored approximately with the CPK scheme: Ti: pink, C: cyan, O: red, H: white, N: blue, S: yellow.

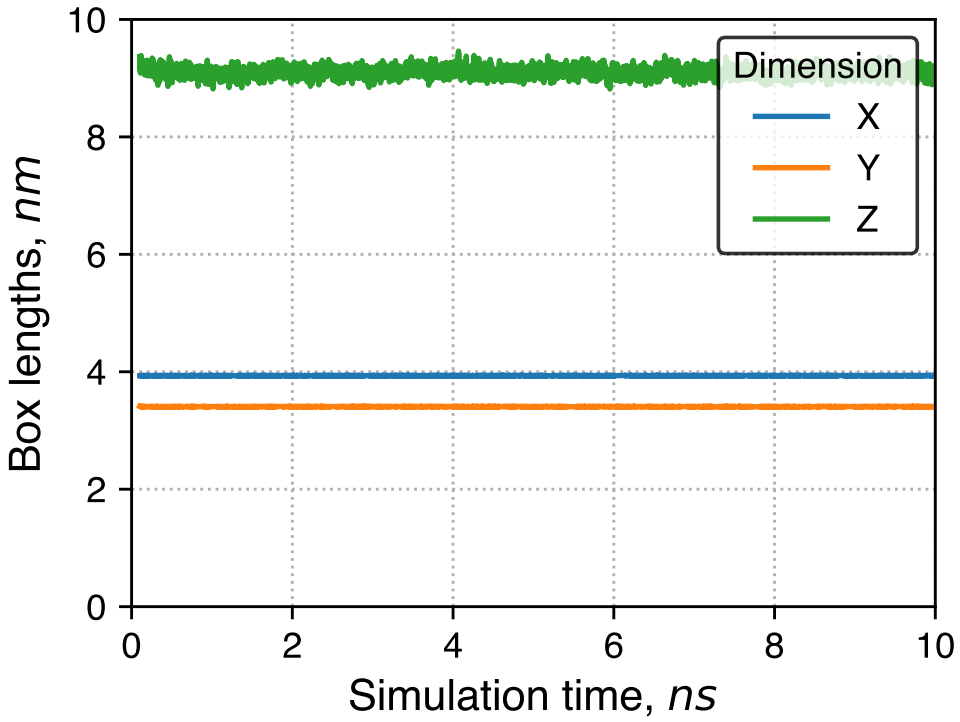

Figure 7.8: Simulation box sizes over the course of a 10 ns trajectory.

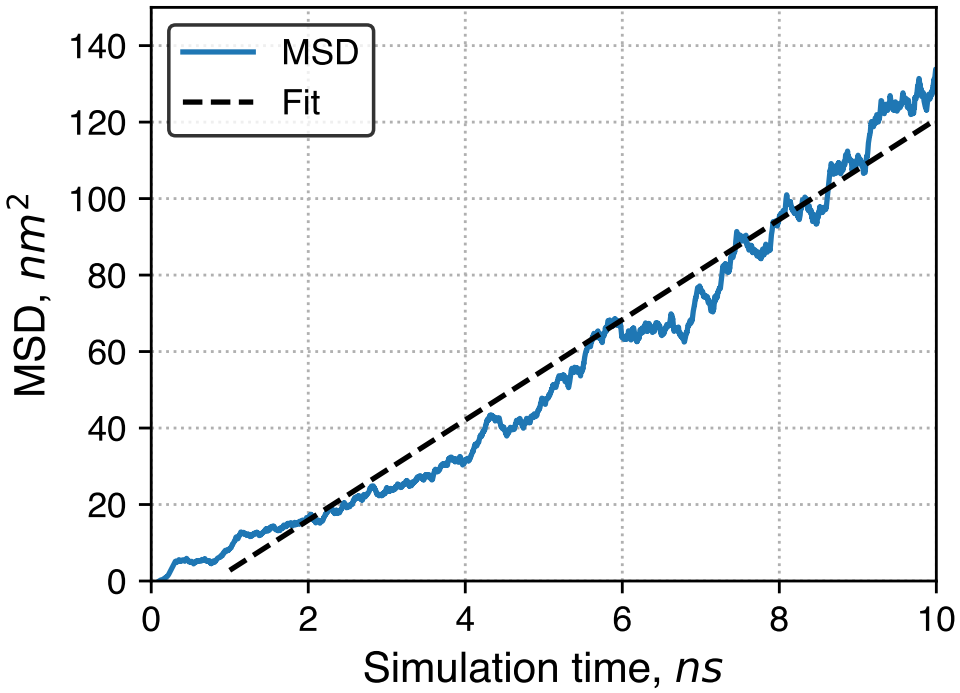

Figure 7.9: Mean-squared displacement of ionic liquid molecules in the x and y directions.

7.2 Conclusions

This chapter reports a classical model of MXenes that can be used to study a variety of systems relevant to many applications. To our knowledge, there is no such model currently available in the literature. Most of the computational work on MXenes has, for good reason, relied on first-principles methods. Some groups have reported the use of classical models in some studies but none have shared their models in detail. To validate the stability of this model, we built a few systems that are simple, yet form the basis of basic energy research. This includes dry MXenes with different surface termination groups, MXenes with different amounts of water intercalated between the layers, a large MXene system, and a MXene intercalated with a solvated ionic liquid. Thus, we have demonstrated that this model can cover a majority of the current design space in MXenes: the selection of surface termination chemistry and intercalated fluid or electrolyte.

7.3 Bibliography

[1] Michael Naguib et al. "Two-dimensional nanocrystals produced by exfoliation of Ti 3AlC 2". In: *Advanced Materials* 23.37 (2011), pp. 4248–4253.

[2] Hsiu-Wen Wang et al. "Resolving the Structure of Ti 3 C 2 T x MXenes through Multilevel Structural Modeling of the Atomic Pair Distribution Function". In: *Chemistry of Materials* 28.1 (2016), pp. 349–359.

[3] Michael A. Hope et al. "NMR reveals the surface functionalisation of Ti 3 C 2 MXene". In: *Phys. Chem. Chem. Phys.* 18.7 (2016), pp. 5099–5102.

[4] Minmin Hu et al. "Surface Functional Groups and Interlayer Water Determine the Electrochemical Capacitance of Ti 3 C 2 T x MXene". In: *ACS Nano* 12.4 (2018), pp. 3578–3586.

[5] Lukas Vlcek and Ariel A Chialvo. "Rigorous force field optimization principles based on statistical distance minimization". In: *The Journal of Chemical Physics* 143.143 (2015).

[6] Mohamed Alhabeb et al. “Guidelines for Synthesis and Processing of Two-Dimensional Titanium Carbide (Ti 3 C 2 T x MXene)”. In: *Chemistry of Materials* 29.18 (2017), pp. 7633–7644.

[7] Xuehang Wang et al. “Influences from solvents on charge storage in titanium carbide MXenes”. In: *Nature Energy* 4.3 (2019), pp. 241–248.

Chapter 8

Conclusions

Although Walden's discovery of ionic liquids dates back more than a century, the field is still young and a comprehensive understanding of the physics of ionic liquids is not yet mature. Both molecular simulation and novel experimental techniques will continue to develop as ionic liquids progress in the technological pipeline; to date, few companies have been formed around ionic liquids. As molecular simulations become more robust and accurate (with the development of advanced sampling techniques and molecular force fields) and as experimental probes are better able to simultaneously resolve the structure and dynamics at molecular scales (Å to nm and fs to ns) a more clear understanding of the fundamental physiochemical properties of ionic liquids will emerge. This progress cannot currently take place with either computational models or experimental probes alone. The work presented in this thesis includes several such examples of how iterations between simulations and experiments can synergistically promote better understaning of how ionic liquids behave in contexts releveant to energy storage and other applications.

These previous chapters have presented contributions to a broad array of applications in which ionic liquids present opportunities but need to be studied more. Chapter 3 detailed the development and validation of a routine for generating atomistic models of porous carbons that can be used in molecular simulations in not only energy storage devices but other applications such as gas adsorption and separation. Chapter 6 tested the reliability of "out of the box" uses of classical molecular models, to mixed results, and provided some recommendations for general use. In Chapter 4, we rigorously evaluated how solvents impact ion mobilities in mixtures of ionic liquids and organic solvents and demonstrated that solvents with greater diffusivities and, secondarily, with greater capacity to screen ion-ion interactions produce the greatest enhancement of ion mobilities. Chapter 5 showed that the addition of large amounts of water to ionic liquids confined in microporous carbon or MXene electrodes can increase ion diffusivity by displacing ions from pore walls, where they

are generally least mobile. Finally, Chapter 7 reports the development of a MXene model that has been used in some simple systems and can be the basis of many future studies on MXenes.

Appendix A

Appendix to Chapter 3

A.1 Selection of of Compression Pressure

The compression procedure described in the main text was repeated at pressures 1000 atm, 10,000 atm, 30,000 atm, 50,000 atm in addition to the selected pressure of 20,000 atm. System densities over the course of these compressions are shown in Figure Fig. A.1. It is observed that pressures of 1000 atm and 10,000 atm are too low to largely impact the density. A barostat of 50,000 atm is too large, as it compresses the system nearly to the graphitic limit of $2.26\,\mathrm{g\,cm^{-3}}$. Intermediate pressures of 20,000 atm and 30,000 atm increase the density of the system above the density observed in experiment but not so high that they could not be found in certain nanostructures found in CDCs.

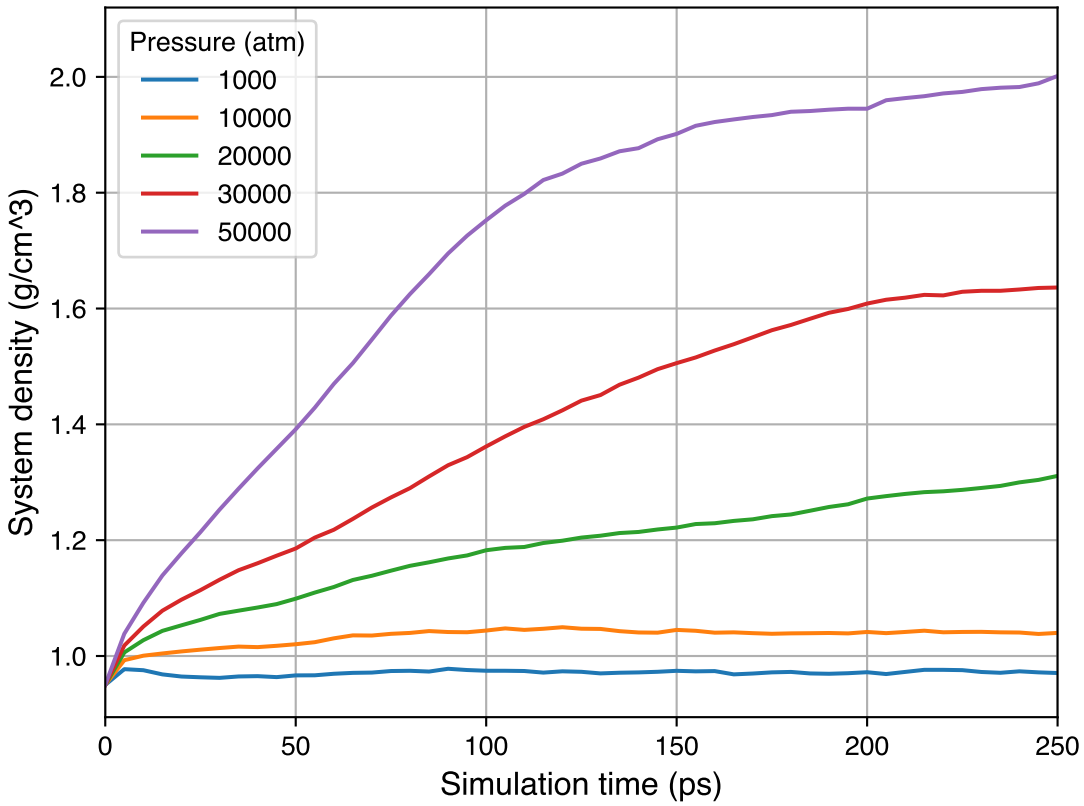

Figure A.1: System densities over the length of compression simulations with different reference pressures.

A.2 Electron Energy Loss Spectroscopy

Aberration Corrected Scanning Transmission Electron Microscopy (ADF-STEM) and Electron Energy Loss Spectroscopy (EELS) data were collected on CDC samples. Data collected on a SiC-CDC sample vacuum annealed at 700 °C is shown in Figure Fig. A.2. A number of bright spots are observed are further investigated with EELS. An EEL spectra was collected on the region highlighted in a red box and a K-edge as 99 eV was observed. This corresponds to Si, indicating that bright spots in the sample are residual Si atoms not fully processed during material synthesis.

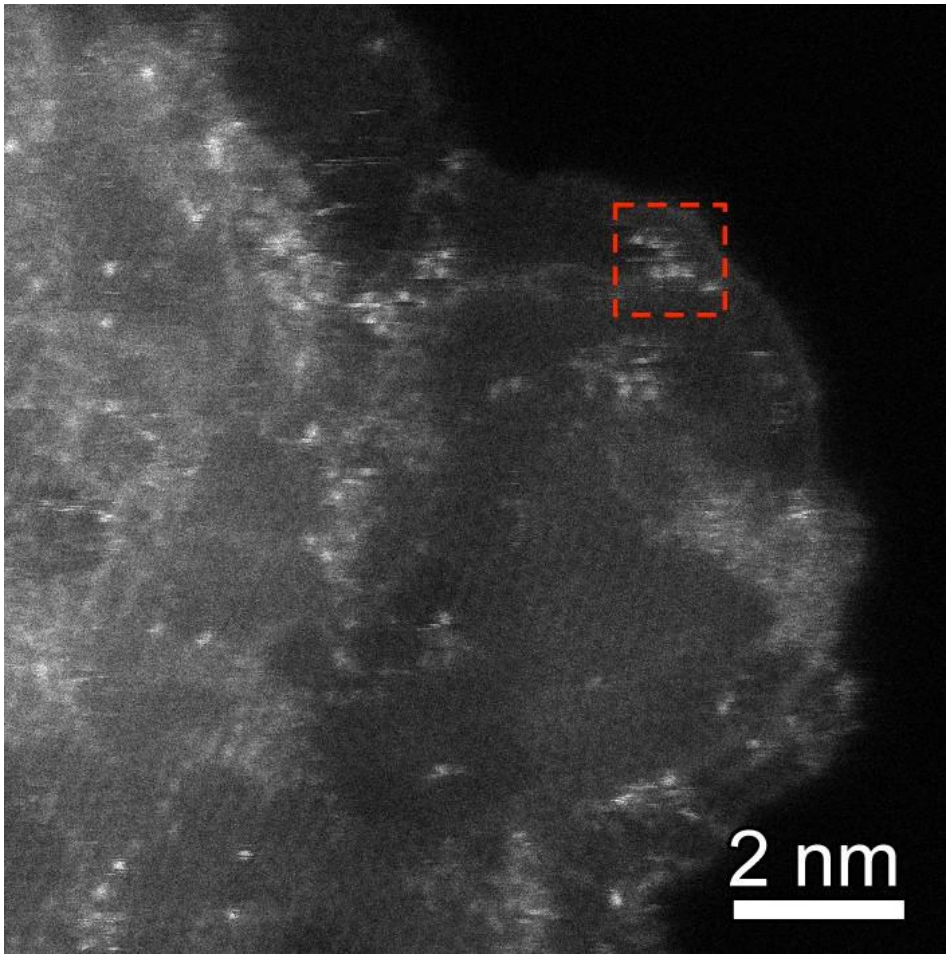

(**a**)

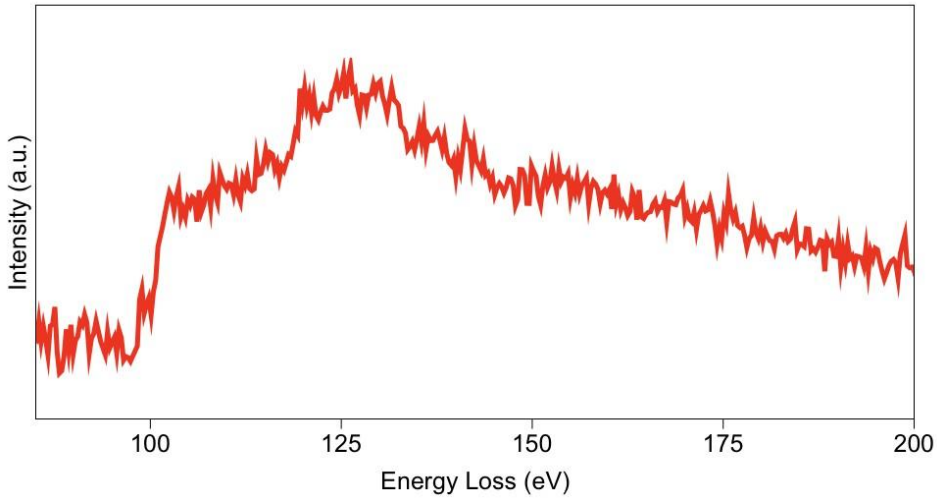

(**b**)

Figure A.2: Annular Dark-Field (ADF) Abberation-Corrected Scanning Transmission Electron Microscopy (STEM) image and Electron Energy Loss (EEL) spectra collected on a SiC-CDC sample after vacuum annealing at 700 °C. (**a**) ADF STEM image of SiC-CDC vacuum annealed at 700 °C; (**b**) Corresponding EEL spectra from SiC-CDC vacuum annealed at 700 °C. The K-edge at 99 eV confirms that the bright spots located in the region highlighted with a red box are Si atoms.

A.3 Raman Spectroscopy

A Raman spectrum is included in Figure Fig. A.3. The data is characteristic of disordered carbon and shows prominent D and G bands.

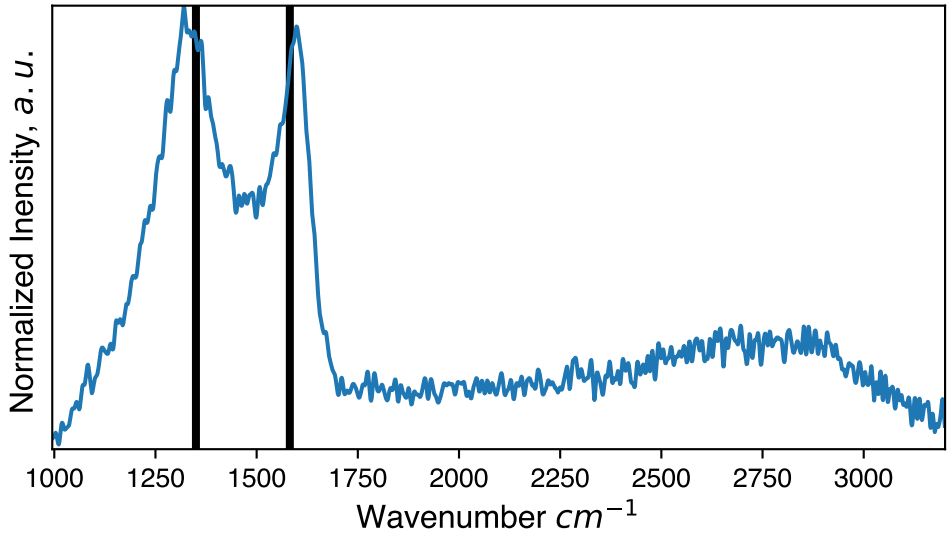

Figure A.3: Raman spectrum of experimental sample of SiC-CDC synthesized by vacuum annealing at 700 °C

A.4 Effects of Compression Pressure

Effects of compression pressure on pore size distribution are also explored, using methods described in the main text and shown in Figure Fig. A.4. As implied in the densities of systems compressed above 20,000 atm, overall pore volume is greatly reduced in systems compressed at these pressures. Therefore, in order to minimize the loss of pore volume as a result of compression but benefit from the reduction in average pore size, a pressure of 20,000 atm was selected.

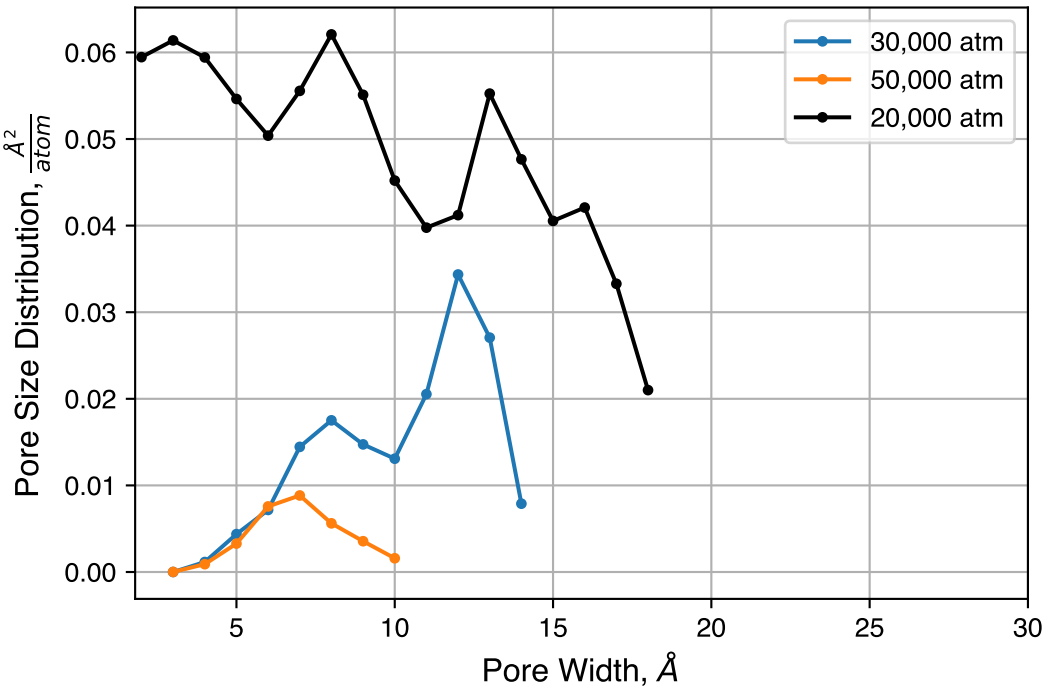

Figure A.4: Pore size distributions resulting from the use of barostats with high reference pressure.

A.5 Large Systems

System size effects are a common, if typically minor issue in molecular simulation. The use of periodic boundary conditions is typically of little or no consequence, sometimes after correction terms are included to certain analysis equations, but the use of a nanoscale simulation box can sometimes distort molecular simulations toward non-physical states. To verify that this was not the case, we repeated the procedure described in Chapter 3 with 200,000 atoms, or ten times as many as was used to derive and characterize the model. I am unaware of any work in the literature considering systems of anything close to 200,000 atoms with atomistic resolution. This is an advantage of the ReaxFF force field; while it is more expensive than a classical model, it is not prohibitively expensive for large systems. It is clear from Figs. A.5 and A.6 that the general structure features are the same in systems of 20,000 and 200,000 atoms. We conclude that system size effects do not majorly impact this model.

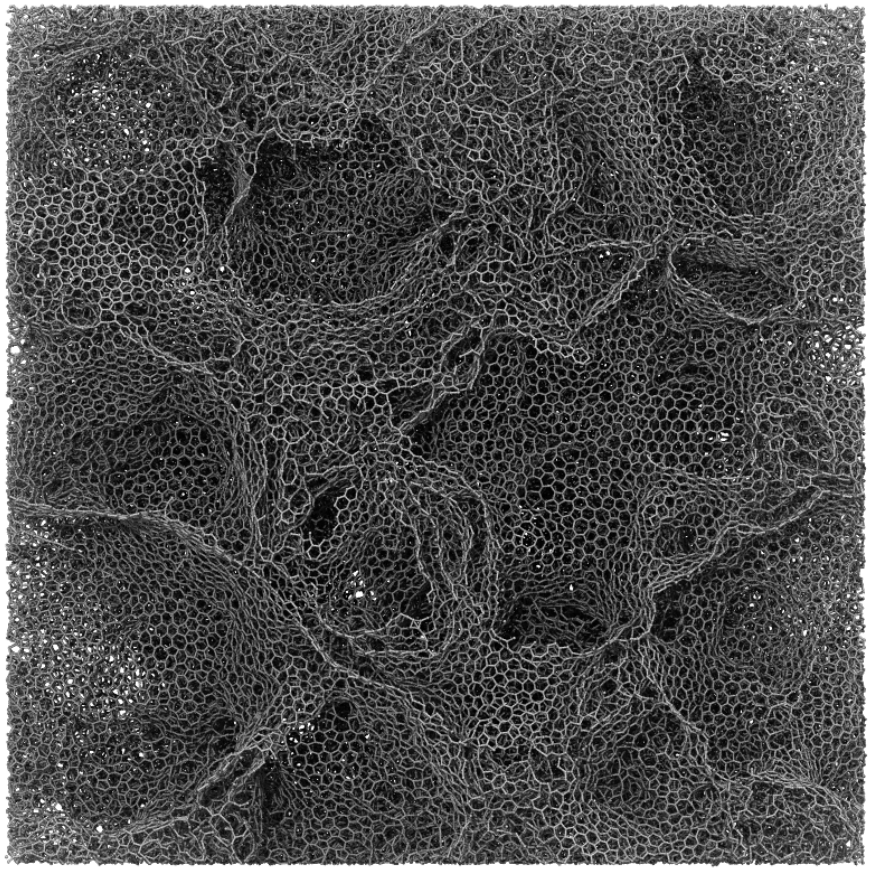

Figure A.5: Large QMD-generated structure including 200,000 carbon atoms in a system size of approximately 16 nm. Some messiness around the edges is the result of drawing bonds with the DynamicBonds representation in VMD, which does not consider bonds crossing periodic boundaries.

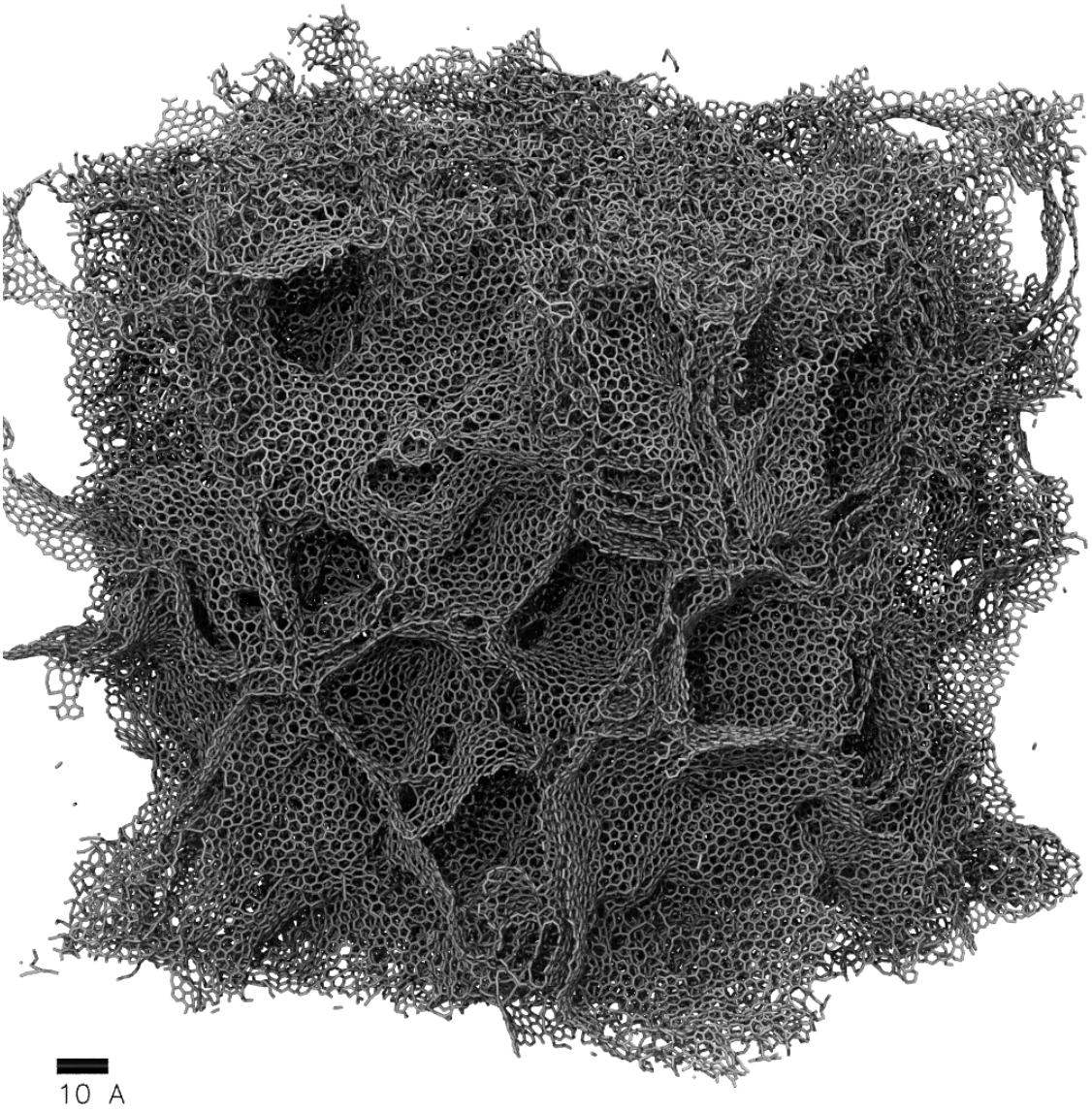

Figure A.6: The same structure as in Fig. A.5 but with a rotated view.

Appendix B

Appendix to Chapter 4

B.1 Comparison of ion diffusivities

As discussed in the main text, diffusivities were computed with two methods: an MSD of the entire trajectory and the average of MSDs from smaller sub-trajectories of the same trajectory. Each trajectory is 30 ns (20 million timesteps of 1.5 fs) and slices of 1.5 ns were considered. As shown in Fig. B.1, these methods produce nearly identical results. For all but a small number of data points, the diffusivity values produced from a single trajectory falls within the errorbars of values from multiple sub-trajectories. While 1.5 ns may not be enough for complete decorrelation between configurations in all systems, we select the average diffusivity from multiple shorter MSDs as the values to report in all other sections of this study. A more rigorous approach would be to compute multiple independent simulations for each statepoint.[1]

A comparison of individual ion diffisivities, *i.e.* cations and anions, is shown in Fig. B.2. In our previous work,[2] the nature of neutron experiments restricted our focus to only the cations. Here, we considered all ions at once, although the diffusivities of each ion are qualitatively (and nearly quantitatively) interchangeable.

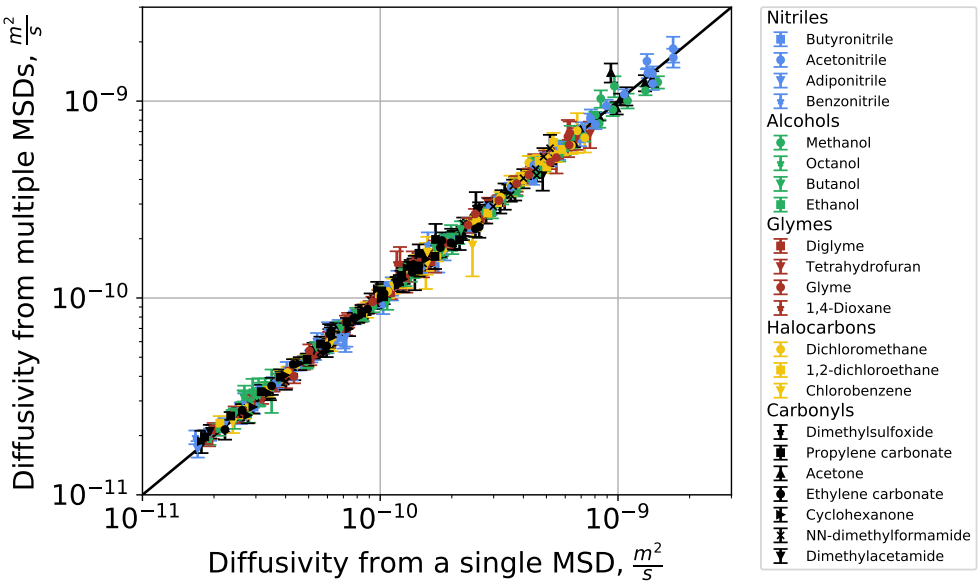

Figure B.1: Comparison between diffusivity values from a single MSD and values from averaging over MSDs obtained from smaller sub-trajectories of the same trajectory. The diagonal line at $y = x$ is to guide the eye.

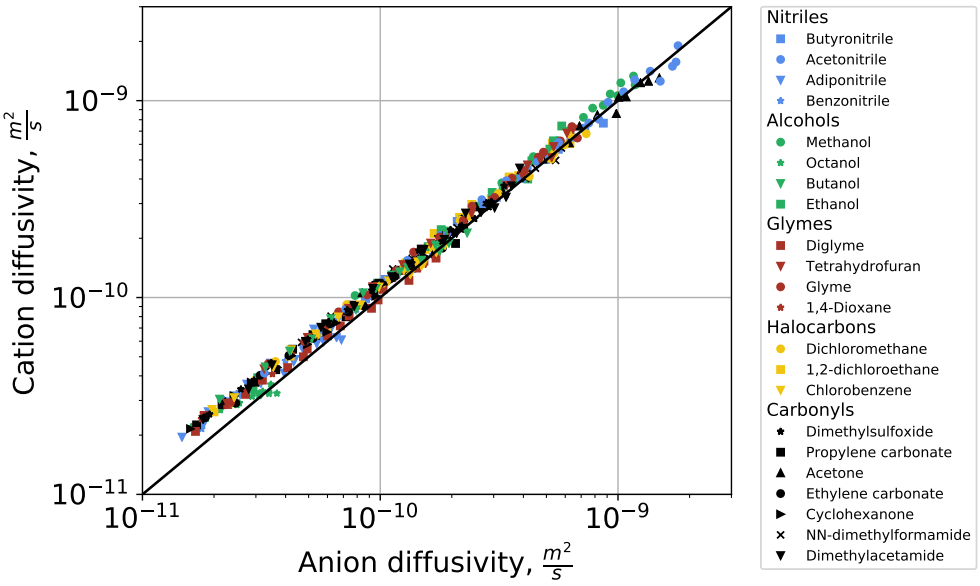

Figure B.2: Comparison of cation and ion diffusivities. The diagonal line at $y = x$ is to guide the eye.

B.2 Computation of Ion Correlation Lifetimes

The calculation of ion pairing and caging lifetimes were discussed briefly in the main text. This is done so by computing the number of ion pairs in the first frame, and then computing which of these pairs remains in the subsequent pairs. The distance criteria use to calculate pairs was determined by the first peak displayed in the radial distribution functions (RDFs) between [$BMIM^+$] and [TF_2N^-]. Rather than display hundreds of RDFs, the first peak positions of the [$BMIM^+$] and [TF_2N^-] RDF for all systems are shown in Fig. B.3. The ratio of remaining pairs is plotted against time, and the curve is fitted with a stretch expoential function get the pairing/caging lifetimes. These plots are shown in Fig. B.4 and Fig. B.5. For statistical averaging, the 30 ns trajectory (20,000 frames) is broken up into 750 frame chunks. We have experimented with longer and shorter chunks, but the fits of the stretched exponential functions are not significantly affected.

Addtionally, the slope of the fraction of free ions as a function of [$BMIM^+$][TF_2N^-] composition was computed for all solvents. The slopes are compiled into Table B.1.

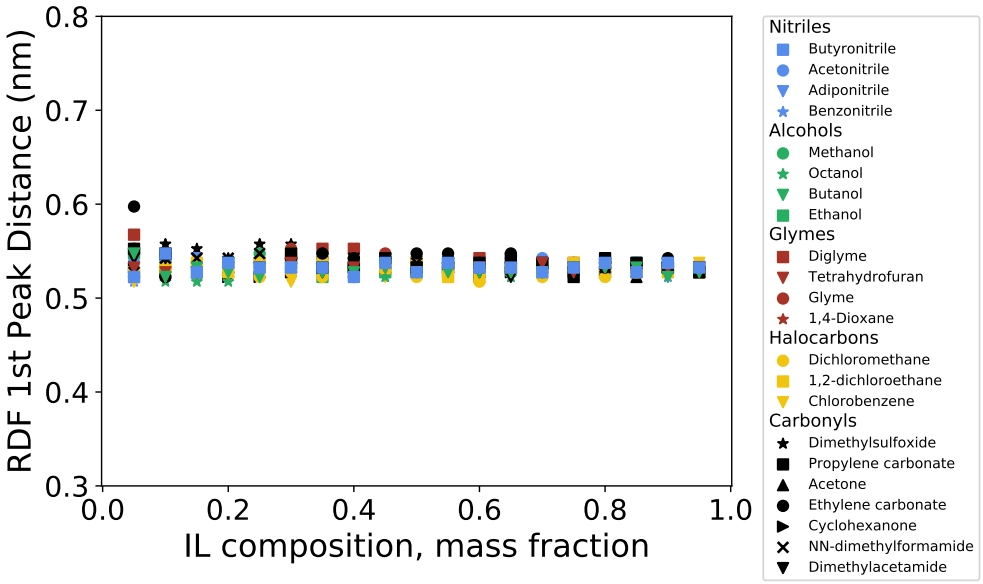

Figure B.3: Radial distribution function first peak position (nm) between [$BMIM^+$] and [TF_2N^-].

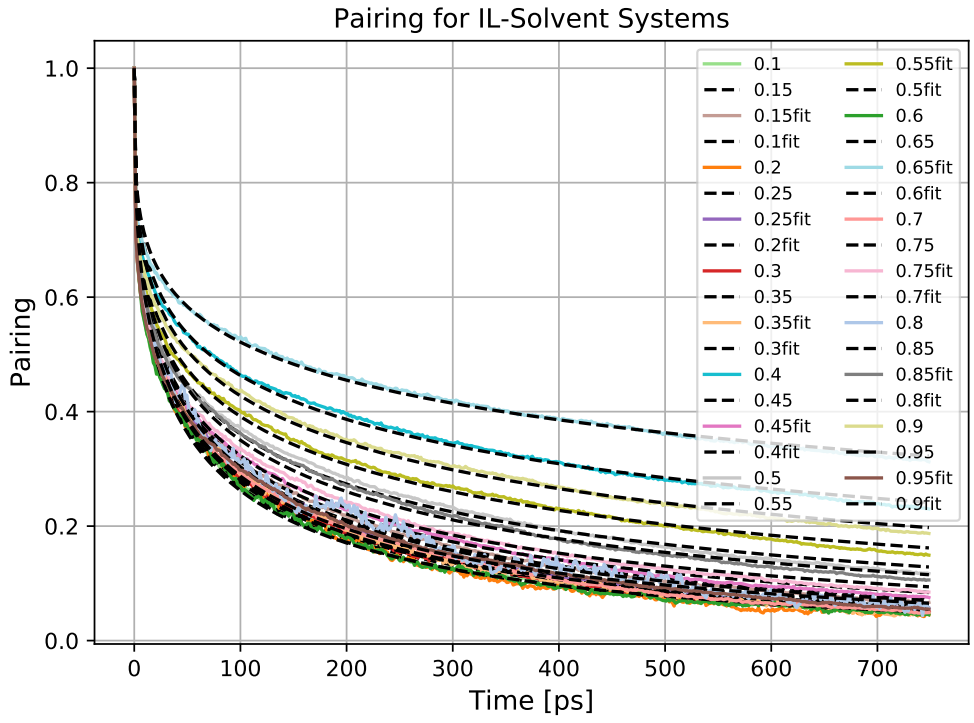

Figure B.4: Time decay of [$BMIM^+$][TF_2N^-] ion pairs in methanol.

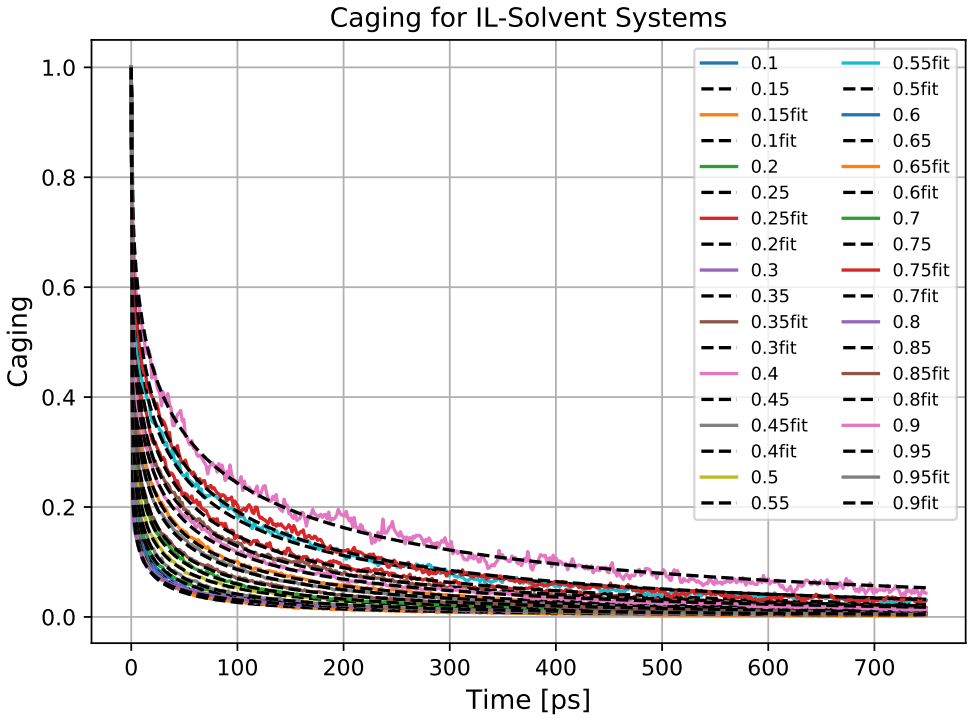

Figure B.5: Time decay of [BMIM$^+$][TF_2N^-] ion cages in methanol.

Solvent	Free Ions Slope
Ethylene carbonate	-0.88
Acetonitrile	-0.82
Adiponitrile	-0.81
Ethanol	-0.82
1,2-dichloroethane	-0.76
Dimethylsulfoxide	-0.91
Methanol	-0.84
Glyme	-0.85
Acetone	-0.85
Dimethylacetamide	-0.86
NN-dimethylformamide	-0.87
Butyronitrile	-0.77
Butanol	-0.71
Diglyme	-0.88
Cyclohexanone	-0.72
Tetrahydrofuran	-0.67
Benzonitrile	-0.60
Dichloromethane	-0.46
Chlorobenzene	-0.38
Octanol	-0.56
1,4-dioxane	-0.53
Propylene carbonate	-0.80

Table B.1: Table of solvents and slopes of free ions as a function of $[BMIM^+][TF_2N^-]$ composition.

B.3 Bibliography

[1] Gaurav Pranami and Monica H. Lamm. “Estimating Error in Diffusion Coefficients Derived from Molecular Dynamics Simulations”. In: *Journal of Chemical Theory and Computation* 11.10 (2015), pp. 4586–4592. arXiv: /www.pubmedcentral.nih.gov/articlerender.fcgi?artid=3006164{\&}tool=pmcentrez{\&}rendertype=abstract. [Figures, S., 2010. Supplementary information. Nature, 1(c), pp.1–7. Available at: http:].

[2] Naresh C. Osti et al. “Solvent Polarity Governs Ion Interactions and Transport in a Solvated Room-Temperature Ionic Liquid”. In: *The Journal of Physical Chemistry Letters* 8.1 (2017), pp. 167–171.

Appendix C

Appendix to Chapter 6

C.1 General Structure of the OPLS-AA Force Field

The Optimized potential for liquid systems (OPLS) force field, an in particular its all-atom form (OPLS-AA) follows the typical structure of a classical force field. Interactions are the sum of many terms, typically divided into intermolecular (non-bonded) and intramolecular (bonded) terms. The structure of this force field was followed exacgtly or approximately for all work in this thesis except for the ReaxFF potentials of Chapter 3.

$$E_{total} = E_{non-bonded} + E_{non-bonded} \tag{C.1}$$

$$E_{non-bonded} = E_{Lennard-Jones} + E_{coulomb} \tag{C.2}$$

$$E_{Lennard-Jones} = \sum_{i} \sum_{j>i} \left[4\varepsilon_{ij} \left(\left(\frac{\sigma_{ij}}{r_{ij}} \right)^{12} - \left(\frac{\sigma_{ij}}{r_{ij}} \right)^{6} \right) \right] \tag{C.3}$$

$$E_{coulomb} = \sum_{i} \sum_{j>i} \left[\frac{q_i q_j e^2}{r_{ij}} \right] \tag{C.4}$$

$$E_{bonded} = E_{bond} + E_{angle} + E_{torsion} \tag{C.5}$$

$$E_{bond} = \sum_{bonds} K_b \left(r - r_0 \right)^2 \tag{C.6}$$

$$E_{angle} = \sum_{angles} K_\theta \left(\theta - \theta_0 \right)^2 \tag{C.7}$$

$$E_{torsion} = \sum_{torsions} \frac{1}{2} [K_1(1+\cos\phi) + K_2(1-\cos 2\phi) + K_3(1+\cos 3\phi) - K_4(1-\cos 4\phi)] \quad \text{(C.8)}$$

The non-bonded interactions are the sum of a Lennard-Jones potential, which handles short-range Pauli repulsion and attractive long-range dispersion forces, and a coulombic potential that describes electrostatic interactions. Intramolecular forces are the sum of harmonic springs that represent bond stretching and bond bending and a sum of sinusoids that describe more complex molecular twisting (torsions). Sums over i and j correspond to pairwise sums over all particles in a system (three-body and higher-order interactions are not considered). At each step these equations are evaluted based on r_{ij} (the distance between atoms i and j), r (the separation distance of of a bond), θ (the internal angle between any set of three atoms) and ϕ (the angle of a torsion between four atoms, defined by the angles between planes defined by the first and last three atoms of the quartet). Fitted parameters specific to particular interactions include Lennard-Jones parameters ε_{ij} and σ_{ij}, the partial charges q_i on any atom i, equilibrium bond distances r_0, equilibrium angles θ_0, bond and angle spring constants K_b and K_θ, and diehdral force constants K_1, K_2, K_3, and K_4.

C.2 Calculation of Nanodroplet Contact Angle

To characterize the interaction of ionic liquids with a graphene surface, nanodroplets were formed, equilibrated, and their resulting structure was analyzed. We assume that the nanodroplet forms a well-defined droplet structure that can be approximated as a spherical cap. This approach is commonly-used in the analysis of nanodroplets because molecular ordering at the interface prevents the formation of a well-defined contact angle directly on the interface; however, the rest of the droplet follows this approximation. This is distinct from droplets at the macro scale, in which this molecular ordering is far too small to be noticed by cameras, and the contact angle at the interface can be directly measured. Here we define a spherical cap as a segment of a sphere of radius r formed by slicing it in a plane in xy, resulting in a spherical cap of height h. This implies the

surface is perpindicular to the z axis, the that the droplet is smooth and well-rounded in the x and y directions.

A simple way to implement this technique is to collect an atomistic density profile of the droplet in the lateral (z) direction from a molecular dynamics trajectory and fit it to a spherical cap to this density profile. Note that data within approximately the first nanometer off of the surface must be discarded due to molecular ordering (for water or other smaller molecules, less data must be discarded). This fit provides the radius of the sphere including the spherical cap. The height of the cap can be computed directly from the difference between the maximum z coordinate of the spherical cap and the z coordinate of the surface. With these two values alone, the contact angle, in °, can be computed as

$$\theta_{contact} = \arccos\left(\frac{R-h}{R}\right) \tag{C.9}$$

This method has been implemented in a Python package, hosted on GitHub and distributed under the MIT license.[1]

C.3 Bibliography

[1] Matthew W. Thompson and Felix Tiet. *droplet*. 2019.